A FINITE ELEMENT MODEL OF THE HUMAN LEFT VENTRICULAR SYSTOLE, TAKING INTO ACCOUNT THE FIBRE ORIENTATION PATTERN

FARSHAD DORRI

Diss. ETH No. 15484

Diss.ETH No. 15484

A FINITE ELEMENT MODEL OF THE HUMAN LEFT VENTRICULAR SYSTOLE, TAKING INTO ACCOUNT THE FIBRE ORIENTATION PATTERN

A dissertation submitted to the

SWISS FEDERAL INSTITUTE OF TECHNOLOGY ZURICH

for the degree of

DOCTOR OF TECHNICAL SCIENCES

presented by

FARSHAD DORRI

Dipl. Phys. ETH Zurich

born on February 20, 1966

citizen of Iran

accepted on the recommendation of

Prof. Dr. Peter Niederer, examiner

Prof. Dr. Paul P. Lunkenheimer, co-examiner

2004

Abstract

The healthy human myocardium represents a global syncytium consisting of myocytes or fibres which are attached to each other to form a spatial network with a well-defined mechanical functionality. In order that upon stimulation of the fibres and subsequent contraction a physiologic ejection volume of blood is reached, the arrangement of the fibres exhibits a systematic architecture, in particular, the fibrous network wraps both ventricles in a characteristic, rope-like fashion. Thereby, no beginning and end of fibre strands can be found in the myocardium; in contrast to the skeletal muscles where fibre strands are attached to ligaments, cardiac contractile pathways are essentially closed.

In this work the fibre structure of the human heart is studied and finite element models are presented which were developed to simulate the contraction of the left ventricle in three dimensions. The anisotropy associated with the fibre arrangement within the myocardium is thereby included and the active fibre contraction processes are described. Finally, the relation between the local fibre structure in the myocardium and the systolic deformation patterns are studied.

The first step in constructing the finite element models was to define the geometry of the human heart. Three geometrical models were created for the left ventricle, *viz.*, a model derived from measurements performed on a real heart and two models representing two different levels of approximation. The endocardial and epicardial surfaces of the real model were reconstructed from thousands of digitized surface points from a human *post mortem* heart. The three FE models were then generated in the form of three spatial meshes whose coarseness was designed to include the desired amount of geometrical detail.

The SPOT method (fibre Strand Peel-Off Technique) was applied to obtain a representative fibre architecture of the human heart. The data contained the coordinates of several thousand myocardial fibres, whereby each fibre, in turn, was represented by a number of points. The fibre orientation in the myocardium was derived from a point wise determination of the fibre direction, whereby the points were interpolated with the help of splines. From this, a three dimensional vector field was built, which defined the local fibre orientation. In addition, three dimensional representations of the global fibre structure of the left ventricle were created.

The myocardium is modelled as a material, composed of a weakly compressible matrix and active fibres. The matrix has nonlinear and anisotropic characteristics according to the configuration of the myocardium. The active forces are modelled by an additive stress tensor including the effect of the transversely branching of the fibres.

For the implementation of the anisotropic constitutive equation, it is necessary to determine the spatial fibre orientation in each element. To achieve this goal, an algorithm was developed such that for any arbitrary mesh with sufficiently small elements, an average and representative fibre orientation is defined.

Another feature of the implemented software is the possibility to produce two dimensional representations of layers with a defined thickness and viewpoints from an

arbitrary perspective within the myocardium. This feature was used, among other, for the verification of the fibre orientation in different regions of the myocardium.

Three finite element models for the left ventricle were implemented successfully. The sensitivities of the models with respect to the most important quantities, especially the fibre orientation, were studied by variation of the parameters.

The inhomogeneities of the systolic wall thickening, which is an important diagnostic criterion, were studied by variation of the local fibre structure, constitutive equation, boundary conditions and geometry.

A pathologic situation, *i.e.*, a localised infarction of the heart was modelled by inactivating the associated fibre areas. The results show a good agreement with the reports of MRI measurements and clinical observations.

Zusammenfassung

Das gesunde menschliche Herzmuskelgewebe besteht aus einem homogenen Aufbau von Myozyten oder Fasern, welche untereinander verbunden sind und ein Netzwerk mit einer wohldefinierten mechanischen Funktionalität bilden. Damit bei Stimulation und anschliessender Kontraktion der Fasern ein physiologisches Auswurfvolumen von Blut erreicht wird, weist die Anordnung der Fasern eine systematische Architektur auf, insbesondere umschliesst das fibröse Netzwerk beide Ventrikel in einer charakteristischen, seilartigen Weise. Dabei ist bemerkenswert, dass kein Anfang und Ende von Fasersträngen im Myokard gefunden werden können; im Gegensatz zu Skelettmuskeln, welche in Sehnen beginnen und enden, sind kontraktile Pfade im Herzmuskel geschlossen.

In der vorliegenden Arbeit wurde die Faserstruktur des menschlichen Herzens analysiert und Modelle auf der Basis der Finiten Elemente (FE) konstruiert, um räumliche Kontraktionsmuster des linken Ventrikels zu simulieren. Die Anisotropie, welche sich aus der Faserstruktur des Myokards ergibt, wurde dabei berücksichtigt und der Verlauf der aktiven Faserkontraktion miteinbezogen. Damit wurde es möglich, den

Zusammenhang zwischen der lokalen Faserarchitektur des Myokards und dem systolischen Deformationsmuster zu untersuchen.

Der erste Schritt bei der Konstruktion der FE Modelle war die Definition der Geometrie des menschlichen Herzens. Drei geometrische Modelle wurden für die linken Ventrikel gestaltet, nämlich ein reales Modell und zwei Modelle, welche durch schrittweise Glättung und Approximation der Oberflächen gewonnen wurden. Die endokardialen und epikardialen Oberflächen des realen Modells entstanden dabei aus Tausenden von digitalisierten Oberflächenpunkten eines menschlichen *post mortem* Herzens. Daraus ergaben sich drei räumliche Netze für das linken Ventrikel, welche die Geometrie des Herzens in unterschiedlicher Detailauflösung wiedergeben.

Die SPOT-Methode (fibre Strand Peel-Off Technique) wurde angewandt um eine repräsentative Faserarchitektur des menschlichen Herzens zu erzeugen. Die dabei entstandenen Daten enthielten die Koordinaten von mehreren Tausend Myokardfasern, wobei jede Faser durch eine Reihe von Punkten dargestellt wurde. Die Faserorientierung im Myokard ergab sich zunächst punktweise aus den Differenzen benachbarter Punkte, sodann wurde der Verlauf mit Hilfe von Splines interpoliert und daraus ein dreidimensionales Vektorfeld gebildet, das die lokale Faserorientierung definiert. Räumliche Darstellungen der globalen Faserstruktur entstanden als Faservektorfeld des linken Ventrikels.

Das Myokard wurde modelliert als ein Material, welches aus einer leicht kompressiblen Matrix und aktiven Fasern besteht. Die Matrix hat entsprechend dem Aufbau des Myokards nichtlineare und anisotrope Eigenschaften. Die aktiven Faserkräfte wurden durch einen additiven Spannungstensor modelliert, in welchem der Effekt der Quervernetzung der Fasern mitberücksichtigt ist.

Für die Implementierung des anisotropen Stoffgesetzes ist es notwendig, die räumliche Faserorientierung in jedem Element des FE Netzes zu bestimmen. Um diese Ziel zu erreichen, wurde ein Algorithmus entwickelt, welcher gestattet, für beliebige Netze von

genügend kleinen Elementen eine mittlere und repräsentative Faserorientierung zu erhalten.

Eine weitere Möglichkeit der implementierten Software besteht darin, zweidimensionale Darstellungen von Schichten vorgegebener Dicke und aus beliebiger Perspektive im Myokard zu erzeugen. Dies gestattete unter anderen die Verifizierung der Faserorientierung in verschiedenen Bereichen des Myokards.

Drei FE Modelle des linken Ventrikels wurden erarbeitet. Die Untersuchung und Dokumentation der Sensitivität der Modelle in Bezug auf die wichtigsten Einflussgrössen, insbesondere den Faserverlauf, erfolgte aufgrund von Parametervariationen.

Wichtige diagnostische Hinweise ergeben sich häufig aus der systolischen Wanddickenzunahme und deren inhomogenen räumliche Verteilung. Die Veränderungen der lokalen Wanddicken wurden durch Variation durch Veränderung der lokalen Faserstruktur, des Stoffgesetzes, der Randbedingungen und der Geometrie untersucht.

Durch Inaktivierung einzelner Faserbezirke konnte ein pathologischer Zustand, d.h. ein Herzinfarkt modelliert werden. Die Resultate zeigen eine gute Übereinstimmung mit den Ergebnissen von MRI Messungen und klinischen Beobachtungen.

CONTENTS

Introduction

The heart fulfils a vital role in the human body. It pumps blood, thereby delivering oxygen and nutrients to the body and removing waste products. It is constantly adjusting and adapting its activity to meet the body's needs regardless whether we are sleeping or engaging in physical activities. It works continuously for the entire time of our life and pumps blood at a rate varying from 5 to 25 litters per minute in a healthy, not particularly trained adult. Due to the importance of the heart to human health, it has been studied extensively by medical scientists. Especially in earlier times, however, many researches in cardiac physiology had an essentially nonmathematical basis. In contrast, mechanical and electrical studies of the heart aiming at a quantitative analysis of the cardiovascular system have been performed only more recently. During the last decades, physical scientists have thereby made numerous experimental measurements and developed mathematical models in view of a better understanding of the heart function. Even though there is still a long way before us to understand the complicated microstructure and details of the mechanisms of the heart, these attempts have opened new ways for investigators and brought new insights into the sophisticated structure and machinery of the heart.

The first three chapters of this dissertation are concerned with the physiology and architecture of the heart.

In chapter 1 we make a short review of the physiology of the heart. We begin with the basic concepts of the anatomy and functional role of the heart in the body as a blood pump. Then the electrical activities, the heart rate and selected principles of the mechanism of contraction are outlined.

In chapter 2 various theories regarding the architecture of the heart are discussed. After some historical remarks, more recent theories about the fibre and laminar structure of the myocardium are reviewed. These theories have been developed during the last decades; yet, further investigations are needed to arrive at a comprehensive view of the heart structure.

A novel approach for the determination and documentation of the fibre structure is introduced in chapter 3. This chapter plays a central role in the dissertation; however, since the procedures are based on a manual digitisation process, there is still a margin for improvement with respect to accuracy and completeness of the recovered fibre field. Nevertheless, the fibre structure of a human heart in short axis and long axis sections can be discussed adequately and the statistical nature of the fibre distribution documented.

In the second part of the dissertation the heart tissue is studied from a continuum mechanical point of view and models of the ventricle are presented.

In chapter 4 selected elements of continuum mechanics are outlined. After a short summary of the fundamental concepts of continuum mechanics, mathematical formulations of the hyperelastic, especially transversely isotropic materials are given.

In chapter 5 various approaches for the formulation of the material behaviour of myocardial tissue are discussed and constitutive equations of passive and active myocardium which were proposed in the past are reviewed.

A finite element model of the left ventricle is implemented in chapter 6. To this end, a relatively smooth geometrical shape for the ventricle is chosen as a first level of approximation. Appropriate boundary conditions are furthermore imposed, the constitutive behaviour including the vector field describing the fibre orientation pattern is prescribed and the mathematical approach used for the formulation of the contraction is substantiated.

Results of the FE implementation are discussed in chapter 7. In particular, the sensitivity of selected important quantities such as wall thickening and stroke volume with respect to the fibre orientation and constitutive equation is analysed and discussed.

In chapter 8, finally, the geometry is refined and an exemplary model derived from a real geometry of the left ventricle is implemented. As an application of the model, the effects of an infarction are simulated.

CHAPTER 1

SELECTED ASPECTS OF HEART PHYSIOLOGY

1.1 Anatomy and function

The heart is located between the lungs and the diaphragm, exhibits a blunt cone shape and has the size of about our clenched fist. The interior of the heart is divided into four chambers. These chambers receive and pump the blood from and to the vascular system by performing rhythmic contractions. The two upper chambers are called left and right atrium while the two lower ones are the left and right ventricles, respectively.

The heart is divided into two functional halves, left and right, according to the two vascular systems it has to feed, viz. the large or systemic circulation (left) and the small or pulmonary circulation (right). While through the systemic system the entire body is supplied with blood, the pulmonary tree perfuses the lungs. The left and right sides, i.e., the left atrium and ventricle and right atrium and ventricle are often referred to as the left and right heart. A muscular wall, called septum, serves as a partition and separates the heart into the right and left sides (Figure 1.1).

The heart has to make available a sufficient amount of blood to allow the organs to perform their function. The performance of the heart is thereby measured as cardiac output (CO), defined as heart rate times the stroke volume, or cardiac index (CI), which is the CO per body surface area. The CO of a healthy adult heart is able to cover a wide

range of operating conditions, from typically 5 Lit/min at rest to some 25 Lit/min under heavy physical activity, even in an untrained person. In order to meet such demands, both heart rate and stroke volume are controlled individually which will be discussed later.

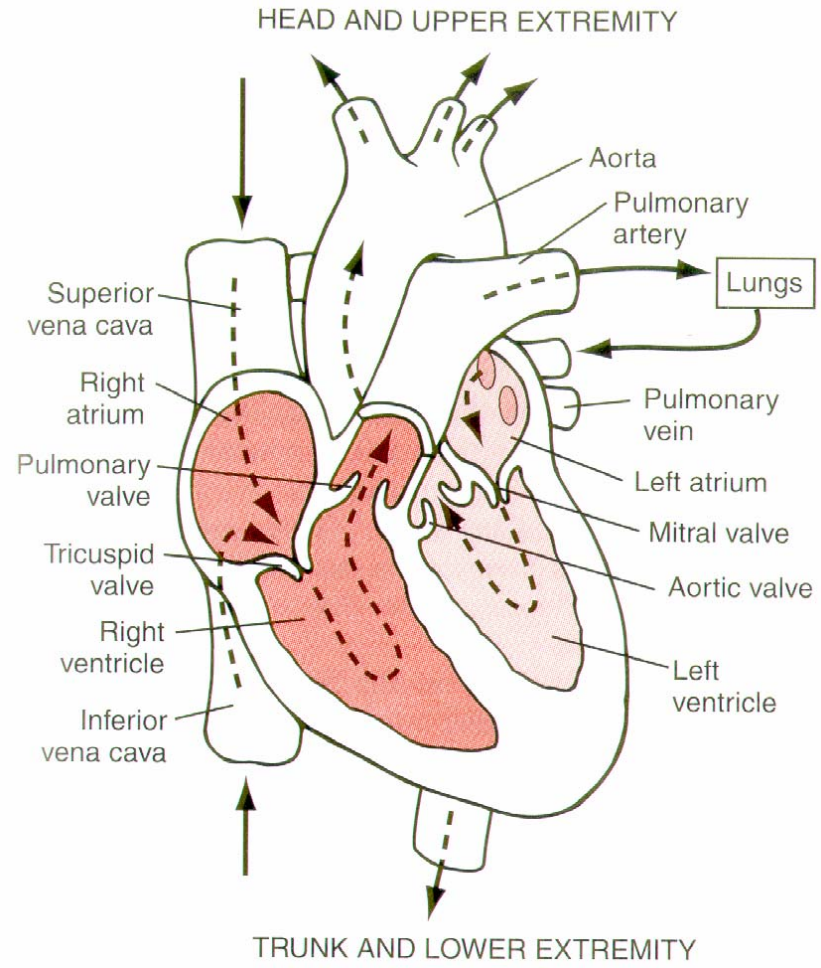

Figure 1.1 Structure of the heart and course of blood flow through the heart chambers (Guyton and Hall 2000)

The left ventricle is the main pumping chamber of the heart and has a thick muscular wall (typically about 1 cm in the relaxed state) which is responsible to generate the high pulse pressures (12 – 16 kPa peak under healthy conditions) necessary to pump blood throughout the systemic circulation. The pressures on right side, in turn, are about 3 – 4 times smaller, accordingly, the wall is only about half as thick as the right ventricle has to drive the blood through the pulmonary system for O_2-CO_2 exchange solely. The walls of

atria, finally, are thin in comparison to the ventricular walls because their main function consists of moving blood over the short distance and against a low resistance from the atria to the ventricles. With each contraction of the heart, blood is pumped from the atria into the ventricles and then out of the heart through the aorta and pulmonary artery.

The heart is contained within a special sac called the pericardium (Figure 1.2). The pericardium has two layers, whereby the outer layer is fibrous and the inner one serous. The fibrous pericardial sac has a smooth and well lubricated lining which serves as a protection against infection, helps to anchor the heart within the chest, and allows the heart to move freely inside the sac. The serous pericardium consists also of two layers, the parietal layer that adheres to the fibrous pericardium and the visceral layer that adheres to the heart. The space between the heart and the pericardium is called pericardial space. This space contains a small amount of pericardial fluid that is secreted by the serous membrane. This fluid provides lubrication between the membranous layers.

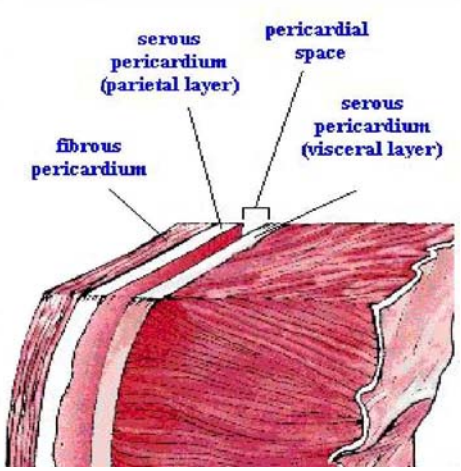

Figure 1.2 Structure of pericardial sac

The walls of the ventricles consist of three layers. The epicardium is the outermost layer consisting mainly of connective tissue and a serous surface. The myocardium represents the driving muscle layer responsible for the heart's ability to contract and pump blood. The endocardium is the thin lining of the inner surface and cavities. The valves of the heart and the tendons that hold them open are also covered by the endocardium. The heart

wall consists mainly of cardiac muscle or myocardium; several blood vessels called coronary arteries supply the myocardium with oxygen and nutrients.

The heart has four valves in order to keep blood from flowing backward. These valves are one-way doors that control the flow of blood through the heart. The heart valves in turn are controlled and operated by pressure changes in the ventricles as well as by the papillary muscles which are part of the myocardium (Figure 1.3).

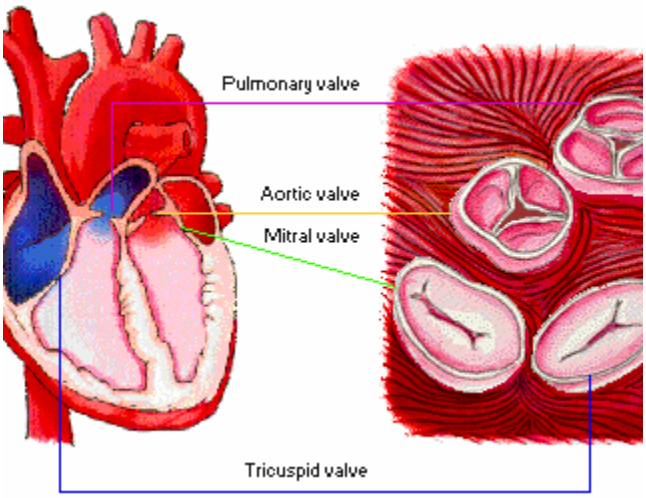

Figure 1.3 Valves of the heart

A cardiac cycle comprises one complete heart beat, where the atria and ventricles contract and then relax. Contraction of the ventricles is called systole, filling is denoted as diastole. Just before the beginning of systole, the two atria contract simultaneously, then, the two ventricles contract. Relaxation of the atria occurs during the first phase of systole, while relaxation of the ventricles marks the beginning of diastole.

1.2 Electrical activity and heart rate

Each heart beat starts with an electrical impulse which is automatically released by a special group of cells concentrated in a node called the sinusatrial (SA) node. The SA node is located above the right atrium. At the beginning of a heart cycle, an action

potential originating from the SA node propagates over the two atria and induces contraction. The activity of the SA node, i.e., the heart rate, is in essence controlled by three sources. First, like all myocytes (muscle fibres of the heart, see below), the SA node has its own intrinsic rhythm (more than 60 beats per minute). Second, the sympathetic as well as the parasympathetic nervous system are directly coupled to the SA node and have an increasing or decreasing effect on the heart rhythm, respectively. Third, the activity of the SA node is influenced by a number of hormones, such as adrenalin.

After contraction of the atria, the electrical impulse reaches another conducting structure, the atrioventricular or AV node which is located at the base of the right atrium. Since a set of connective tissue associated with the valves separates the atria from the ventricles, the AV node is the only conductive link between the atria and the ventricles. The cells of the AV node are specialized to delay the conduction of electrical excitation from the atria to the ventricles. This node acts as a filter to permit the atrial contraction to fill the ventricles with blood before the ventricles begin to contract (Figure 1.4).

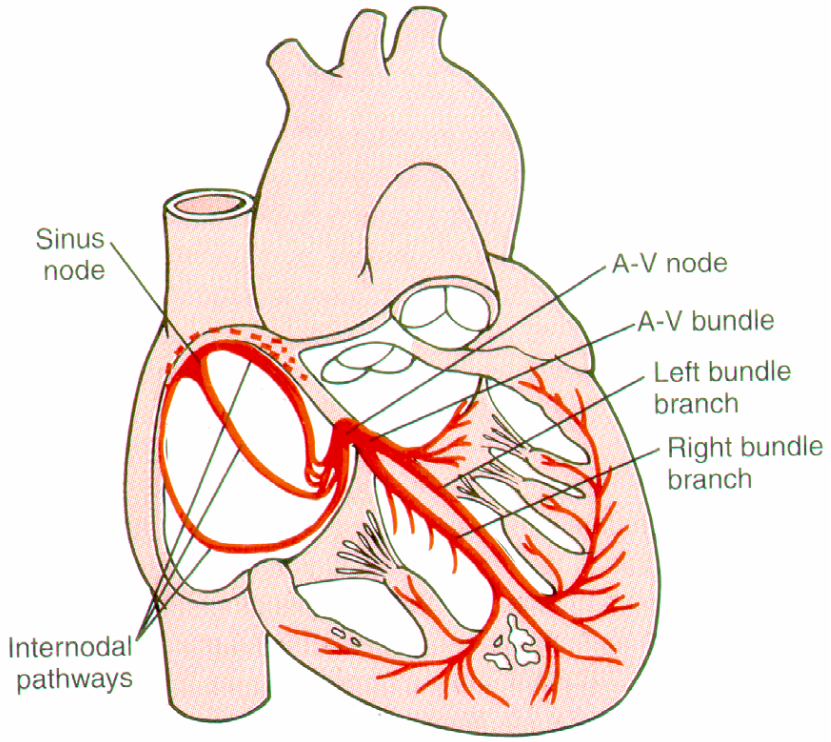

Figure 1.4 Sinus node, A-V node and the Purkinje system of the heart (Guyton and Hall 2000)

The bundle of His represents a continuation of the AV node and provides the electrical connection to the ventricles. It separates into two branches called right and left bundle branches. These branches descend on either side of the septum and divide into hundreds of tiny nerve fibrils called Purkinje fibres throughout the wall of each ventricle. Purkinje fibres are conductile cells that conduct action potentials very rapidly, as such, they act like a network in order to spread the electrical excitations quickly throughout the cells of the ventricular walls.

The electrical currents occurring during de- and repolarisation (contraction and relaxation, see below) of the myocytes are sufficiently strong that the electrical activity generated by the heart's contractile system during each cycle can be recorded at the surface of the body using conductive adhesive patches. The obtained recording is called the electrocardiogram (ECG). In Figure (1.5) we see three examples of typical ECGs. They are all regular but with different heart rates.

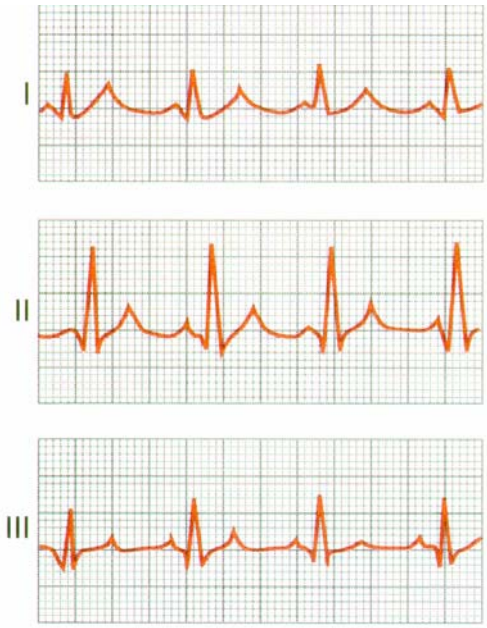

Figure 1.5 Normal electrocardiograms recorded from the three standard electrocardiograph leads (Guyton and Hall 2000)

The ECG is subdivided into two segments, separated by three waves (Figure 1.6). The first wave, called P wave, is due to the atrial contraction. Subsequent to electrical stimulation, the right and left atria depolarise and contract. After the P wave, there is a straight line called the PR segment. It represents the time delay of the electrical stimulation of the AV node. The second and largest wave of the cardiac cycle is the QRS wave complex. This wave represents the depolarisation of the ventricles. The third wave of the cardiac cycle is denoted as T wave which is due to the repolarisation of the ventricles. The second segment, between the QRS wave complex and the T wave, is referred to as the ST segment. This segment represents the time delay between the end of ventricular contraction and the beginning of full relaxation of the ventricles. The P wave is much smaller than the following two waves according to the smaller muscle mass of the atria. The atria also have a repolarisation wave, but because it is much smaller and occurs at the same time as the QRS wave complex, it can usually not be detected.

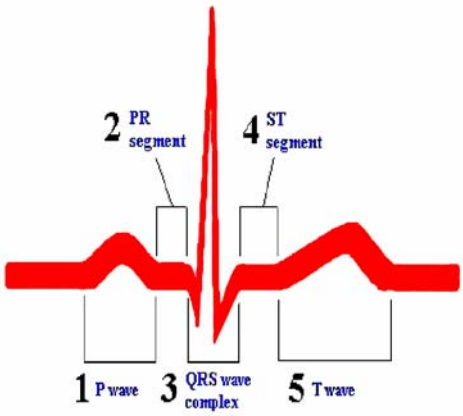

Figure 1.6 Normal electrocardiogram

The various quantities which can be observed and measured during a cardiac cycle are summarized in Figure (1.7). The phonocardiogram which is a recording of the sounds produced by the beating heart is shown in this figure too.

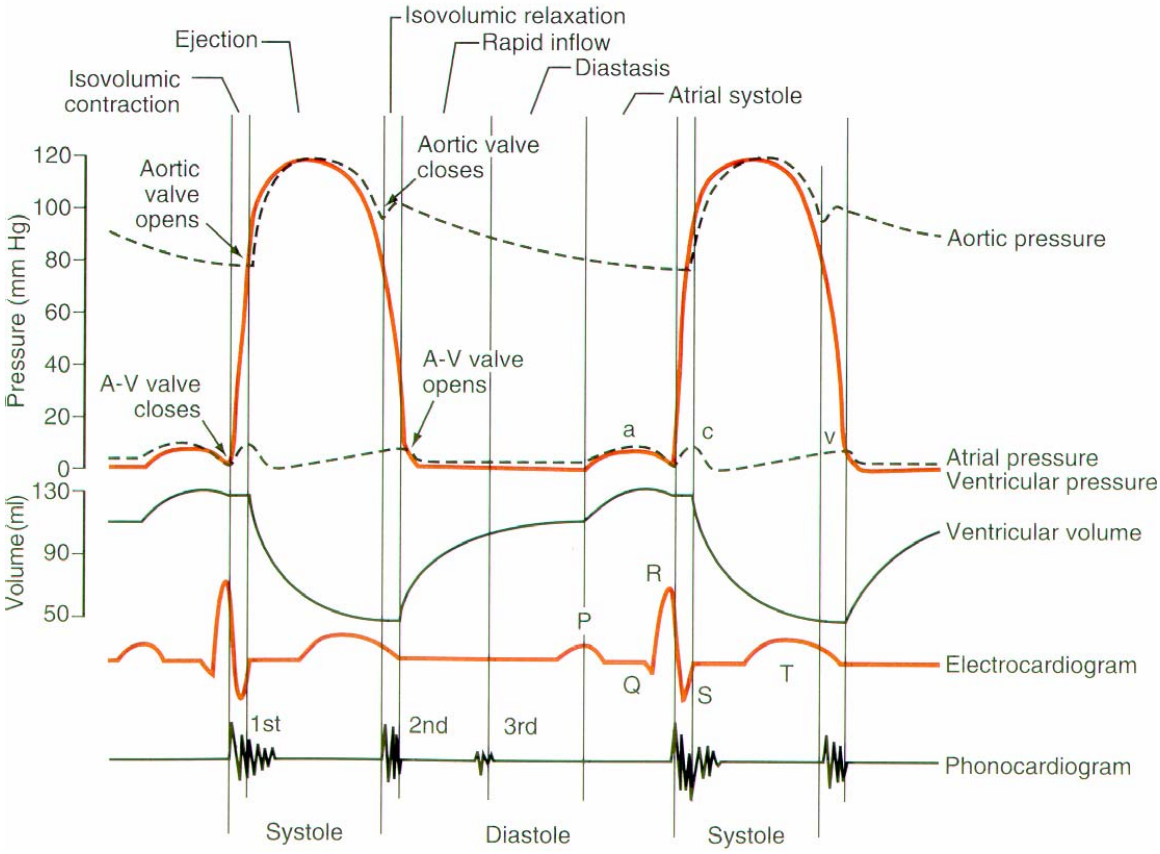

Figure 1.7 Cardiac cycle for left ventricle function (Guyton and Hall 2000)

1.3 Contraction and stroke volume

It is instructive in view of our goal to review the process of contraction shortly. Many of the mechanisms of contraction of cardiac and skeletal muscle are similar. For simplicity, we begin with skeletal muscle and then indicate some of the differences to cardiac muscle. In Figure (1.8) we see the organisation of a skeletal muscle from the gross to the molecular level.

Muscle fibres are built of parallel arrays of myofibrils. Myofibrils are the functional units of the muscle. A typical muscle fibre may contain from several hundreds to several thousands parallel myofibrils. Surrounding the fibre is a plasma membrane called sarcolemma. This membrane defines the fibre as a single cell. Each myofibril is

composed of several hundred myosin and actin filaments, which are large polymerized protein molecules. Titin, which is one of the largest proteins in the body, keeps the myosin and actin molecules side by side. The proteins actin and myosin are arranged in a highly organised lattice and provide the basis of the force-generating apparatus. The myofibrils are suspended inside the muscle fibre in an intracellular matrix called sarcoplasm, which is mainly composed of the usual intracellular constituents. The fluid of the sarcoplasm contains large quantities of potassium, magnesium, phosphate, plus multiple protein enzymes. As in all cells a potential difference across the membrane arises from a trans-membrane ion gradient.

The electrical signal inducing the contraction process causes a reversal of this potential. In skeletal muscle the initiating signal comes from the attached nerve fibre which arrives at the endplate and decreases the muscle-cell-membrane potential. Once a certain threshold is reached, a chain of events is triggered. The action potential causes the sarcoplasmic reticulum to release large quantities of calcium ions Ca^{2+} that rapidly penetrate myofibrils and enter the cells. Ca^{2+} ions activate the actin and myosin filaments and cause the contraction. The energy which is needed for the contraction is supplied by adenosine triphosphate (ATP) formed by the mitochondria, which is degraded to adenosine diphosphate (ADP).

The mechanisms of muscle contraction have not yet been resolved entirely; nevertheless, there is a theory which is composed of two parts, the sliding filament theory and the cross-bridge theory. A short summery of myosin-actin interaction is described in the following.

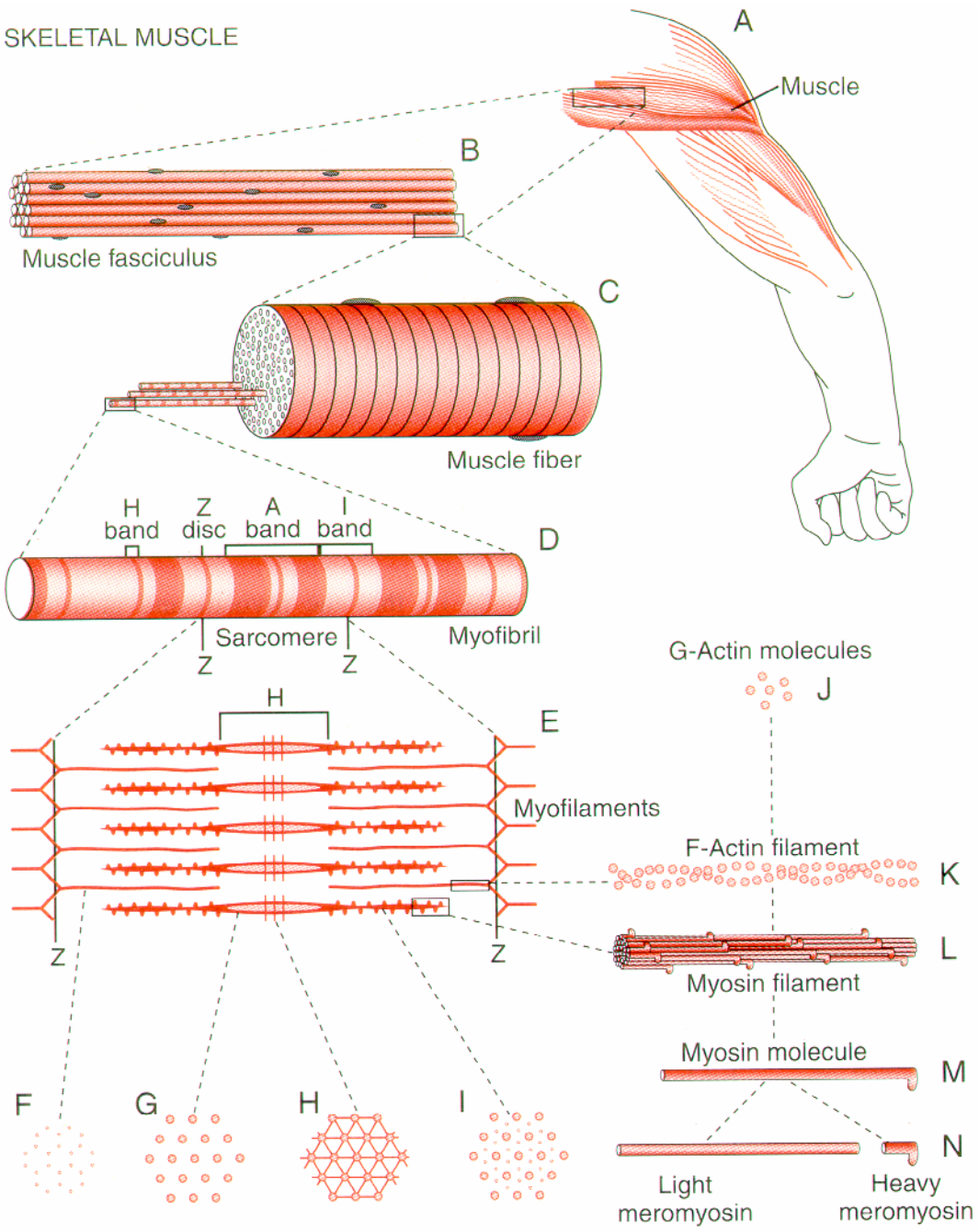

Figure 1.8 Organization of skeletal muscle, from the gross to the molecular level (Guyton and Hall 2000)

The myosin filament is composed of hundreds of myosin molecules. The myosin molecule, in turn, is composed of six chains, two heavy chains and four light chains. The two heavy chains wrap spirally around one another to form a double helix which makes up the large tail of the myosin molecule. One end of each chain is folded into a structure

called the myosin head where two of the light chains are attached. Thus, a double helix myosin molecule has two free heads lying side by side at one end (Figure 1.9A). At the other end, the tails of the myosin molecules are bundled together to form the body of the filament. Each head includes a leverarm that extends outward from the body to enable a connection which is flexible at two points called hinges, one where the lever leaves the body of the myosin filament and the other where the head is attached. The hinged leverarms allow the heads to be extended outward or close to the body (Figure 1.9B).

The angle under which the lever points outward with respect to the body is, among other, a function of the local calcium ion concentration and can change rapidly under excitation.

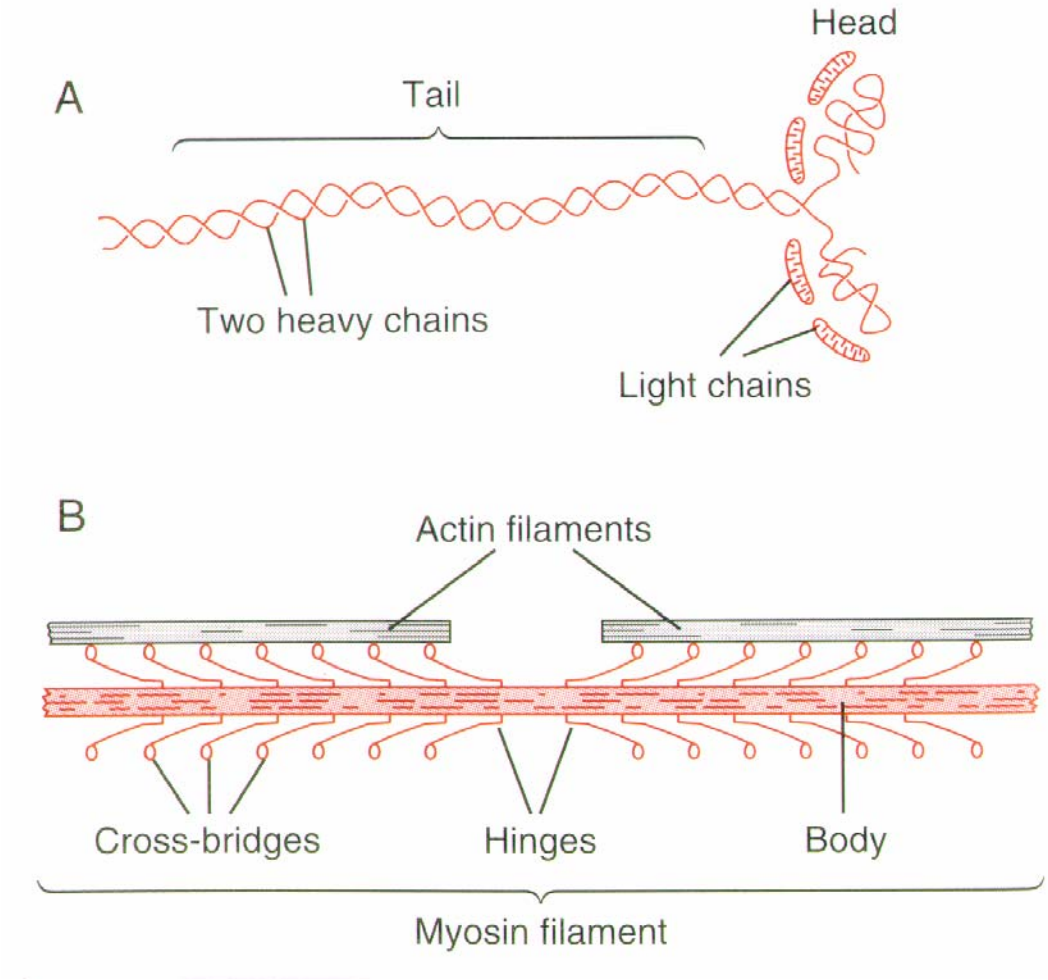

Figure 1.9 (A) Myosin molecule (B) Myosin filament (Guyton and Hall 2000)

The second molecule involved in the contraction process, the actin filament is composed of three protein components. According to the experimental observations, during the contraction, the actin filaments are being pulled together along the myosin filaments. It is thereby suggested that the contraction is associated with a sliding mechanism, i.e., the filaments slide and pass along each other (Figure 1.10). This sliding is facilitated by regularly spaced binding sites on the actin molecule where the myosin heads can connect (crossbridges). As the hinges, i.e., the leverarms are activated by calcium ions, the heads jump from binding site to binding site.

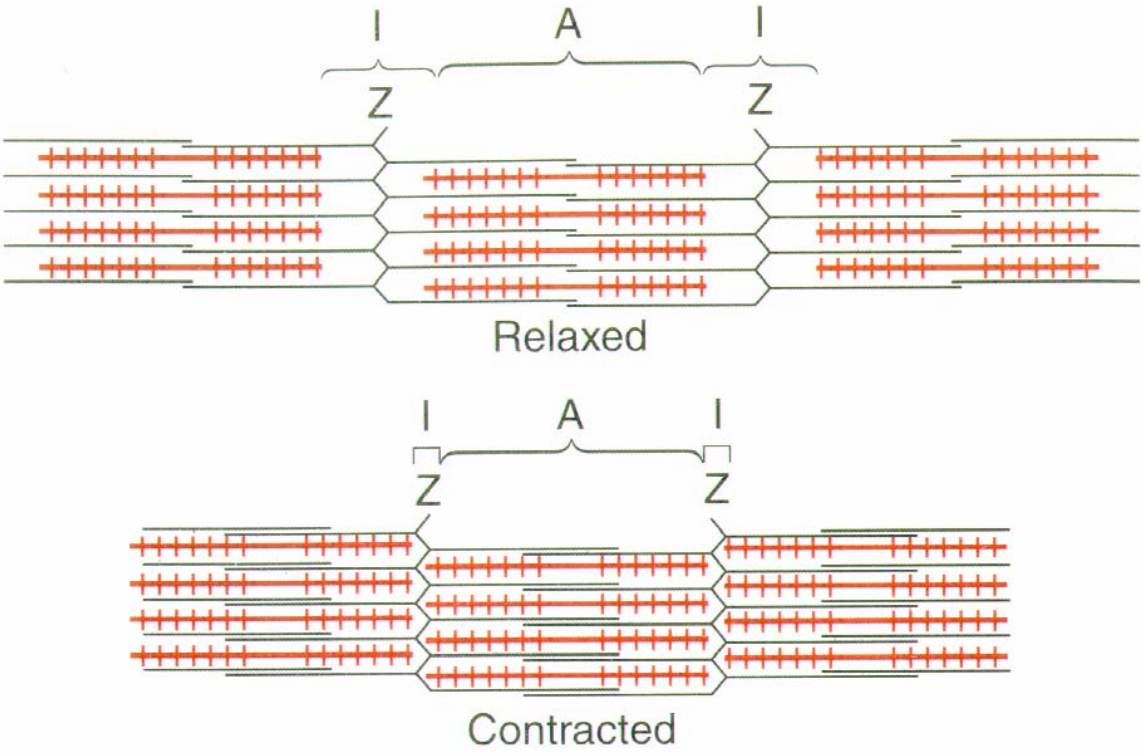

Figure 1.10 Relaxed and contracted states of a myofibril (Guyton and Hall 2000)

Cardiac muscle has some similarities and some differences with skeletal muscle. Figure (1.11A) shows the myofibrils of a skeletal muscle of a frog and Figure (1.11B) the myofibrils of a mammalian heart. The similar structure can be seen clearly in these figures. Yet, a major and important difference consists of the ubiquitous and dense crosslinking of the cardiac muscle fibres (Figure 1.12). Dark areas oriented across the

cardiac muscle fibres indicate cell membranes that separate individual cells from one another and provide connections by way of gap junctions. Electrical resistance through these junctions is only about $\frac{1}{400}$ of the resistance through the outside membranes. Accordingly, ions can move almost freely in the intracellular fluid along the cardiac muscle fibres. Thus, the cardiac muscle works as a syncytium comprising numerous muscle cells.

A further difference derives from the fact that the cardiac action potential is not initiated at an endplate but by the specialized conduction system of the heart itself which was mentioned earlier. Because of the gap junctions between adjacent cardiac muscle cells, the electrical activation spreads from muscle cell to muscle cell.

Furthermore, the duration of a cardiac action potential is about 300 msec, whereas an action potential of a typical nerve lasts only about 1 msec. As a result, a single action potential maintains tension development throughout systole and neural activities have only a modulatory effect on the heart rate (through interaction with the SA node) and hardly influence the length of systole.

The actin-myosin structures exhibit a regular geometry and are arranged in a well-organized pattern. Accordingly, the Z-bands (Figure 1.12) can well be discerned microscopically. The distance between the Z-bands is called sarcomere length.

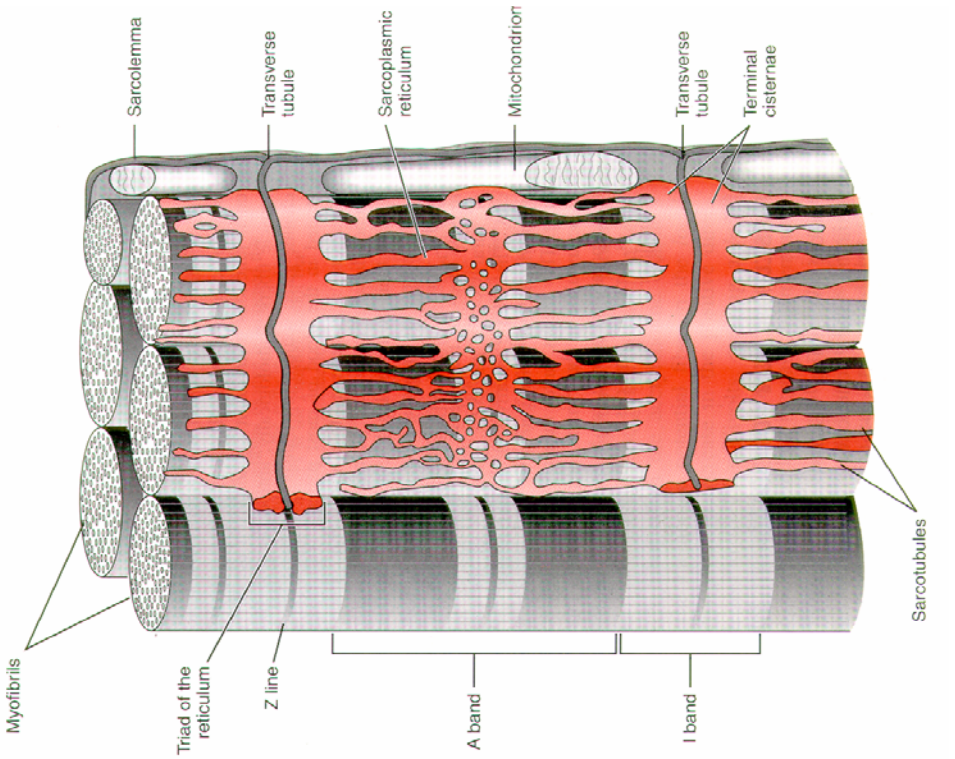

A

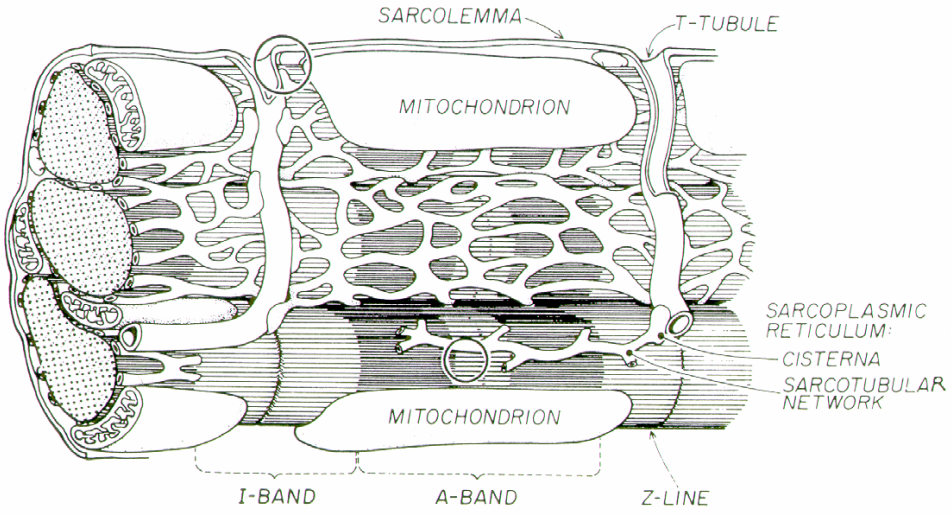

B

Figure 1.11 Transverse tubule-Sarcoplastic Reticulum system from (A) frog muscle (B) mammalian heart muscle (Guyton and Hall 2000; Sperelakis 2001)

Contraction of the heart occurs in response to a single action potential transmitted to all fibres. Thereby, the metabolism of cardiac muscle cells allows the intensity of contraction to be modulated from beat to beat.

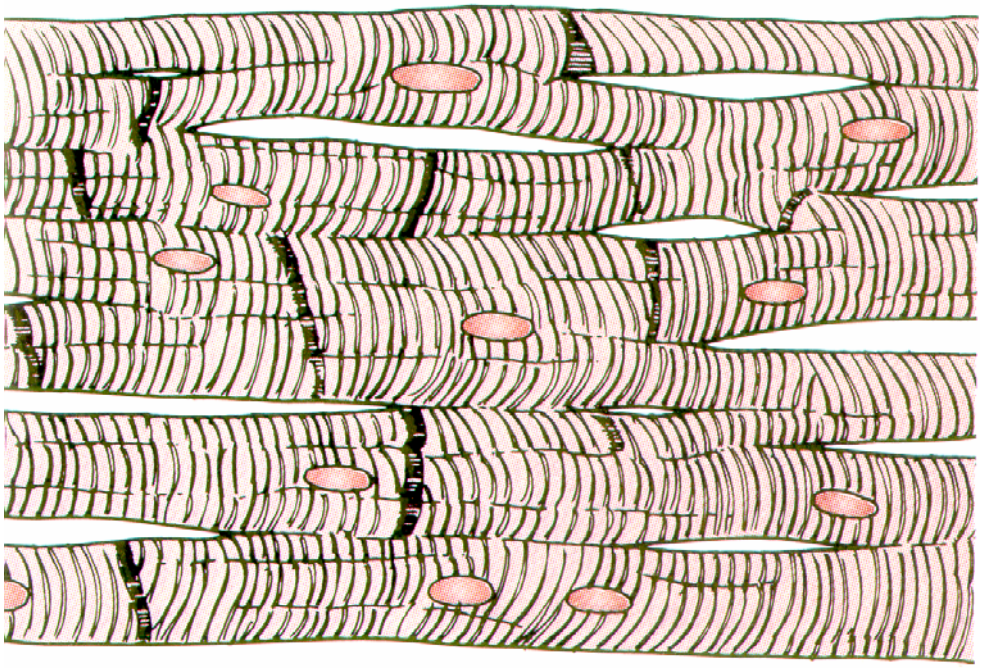

Figure 1.12 Interconnecting nature of cardiac muscle fibres “Syncytial” (Guyton and Hall 2000)

Finally, a muscle is more complex than a mere fibre bundle. In the myocardium the fibres are not only crosslinked, but they form an architecture which includes surface-parallel and oblique fibre strands (see chapter 3). In particular, due to the hollow shape of the ventricles, fibre paths are closed, i.e., in contrast to skeletal muscle, fibre trajectories have no beginning and no end as a general rule. Because of such complexities, the analysis of the cardiac muscle as a whole is considerably more intricate than the analysis of single fibre function.

The particular dynamics associated with the attachment and separation processes of the crossbridges along with the properties of the calcium ion channels, lead to the well known behaviour of the fibers according to which the force developed after stimulation increases with increasing sarcomere length. As a consequence, the stroke volume is controlled in a natural fashion, in that the venous return governs the amount of filling of

the ventricles, thereby the stretching of the sarcomeres at end-diastole and subsequently the intensity of contraction (Frank-Starling's law).

1.4 *In vivo* imaging of the heart

An *in vivo* monitoring of the motion and deformation of the heart is important for the work described here. A number of techniques, mostly based on ultrasound, x-ray, PET and MRI/MRS are available today for this purpose. These methods can be characterized as follows.

Ultrasound: True real-time, low resolution, limited 3D capabilities, non-invasive.

X-ray: Real-time, ionizing, one or two 2D projections only (except for ciné-CT).

PET: Measurement extends over many heart beats, ionizing, low resolution, provides functional information (metabolism of the heart muscle).

MRI: Requires averaging over a number of heart beats, non-invasive, high resolution, tagging allows measurement of deformation (see chapter 8).

When cardiac fibres contract, the wall of the left ventricle begins to rotate and move inward, the wall becomes thicker and the heart becomes shorter. The question arises (and is the subject of the next two chapters) how the simple axial shortening of individual sarcomeres transforms into the complex deformation pattern required for an efficient ejection of blood from heart. E.g., fibre shortening is accompanied by thickening as a result of incompressibility. However, it is known that the increase in the cross section of the myocytes associated with the fibre shortening can not account for the local wall thickening which is more than 40%. Neither can the longitudinal shortening of the heart be explained in a straightforward fashion. Some investigators suggested that there occurs some fibre rearrangement during contraction which cause, among other, these complex deformations of myocardium. From *in vivo* imaging and mathematical modelling we expect to be able to elucidate some of these questions.

References

Carmeliet E, Vereecke J. 2002. Cardiac cellular electrophysiology. Boston: Kluwer Academic Publishers. 421 S. p.

Das DK. 1999. Heart in stress. New York: New York Academy of Sciences. 438 S. p.

Goldstein DS. 2001. The autonomic nervous system in health and disease. New York: M. Dekker. xii, 618 p.

Guyton AC, Hall JE. 2000. Textbook of medical physiology. Philadelphia: Saunders. xxxii, 1064 S. p.

Holubarsch CJF. 2002. Mechanics and energetics of the myocardium. Boston: Kluwer Academic Publishers. 216 S. p.

Sperelakis N. 2001. Heart physiology and pathophysiology. San Diego: Academic Press. 1261 S. p.

CHAPTER 2

ARCHITECTURE OF THE HEART

2.1 Introduction

The study of the heart has a long history, and numerous investigations have been made through the centuries by anatomists and medical scientists. Available reports from the 16th century document that already at that time investigators attempted to explain the structure and the function of the heart along with the analysis of the anatomy. Some of their developed methods or suggestions about the function or structure of the heart are still useful or motivating for current studies. For example, Vesalius (1514-1564) and later Lower (1669) who developed the blunt unwinding technique (BUT) claimed that the ventricles were made up of distinct bands of muscle.

Actually, the blunt unwinding technique (BUT) is still being used today for preparations of the heat-denatured heart muscle. In this method, the heart is boiled for about two hours in water with acetic acid, then the atria, the epicardium and the subepicardial fat is removed. The superficial myocardial fibre coat wrapping both ventricles are subsequently peeled off from the biventricular body and the muscle band which builds up the main bulk of the structure can then be unrolled.

Later Borelli (1681) postulated that the heart has a rope structure which is twisted.
Borelli's ideas have been further developed in the 20th century by Torrent-Guasp (Torrent-Guasp and others 1997). In his anatomical approach he put forward the notion that the ventricular myocardial mass consists of a band, curled in a helical way, which

extends from the pulmonary artery to the aorta and forms the figure of the number “8” (Figure 2.1). He reconstructed a silicone rubber model which was cast from an actual unrolled myocardial band to demonstrate and to provide an understanding of this idea (Figure 2.2). Unfortunately, the functional role of this hypothetical band structure in the motion of the heart is not clear, moreover, the preparation of the band as such contradicts the morphology of the myocardium in that a separation of the left ventricular wall into two concentric layers is not possible without severe damage (Lunkenheimer and others 1997b). Moreover, the heart muscle, unlike skeletal muscle, does not exhibit a beginning and an end, as is suggested by Torrent-Guasp’s model. Nevertheless, if interpreted carefully, it can be helpful for a general anatomical understanding.

Figure 2.1 Postulated rope structure of the heart. The figure 8 does not constitute a unique layer or winding (Torrent-Guasp and others 1997)

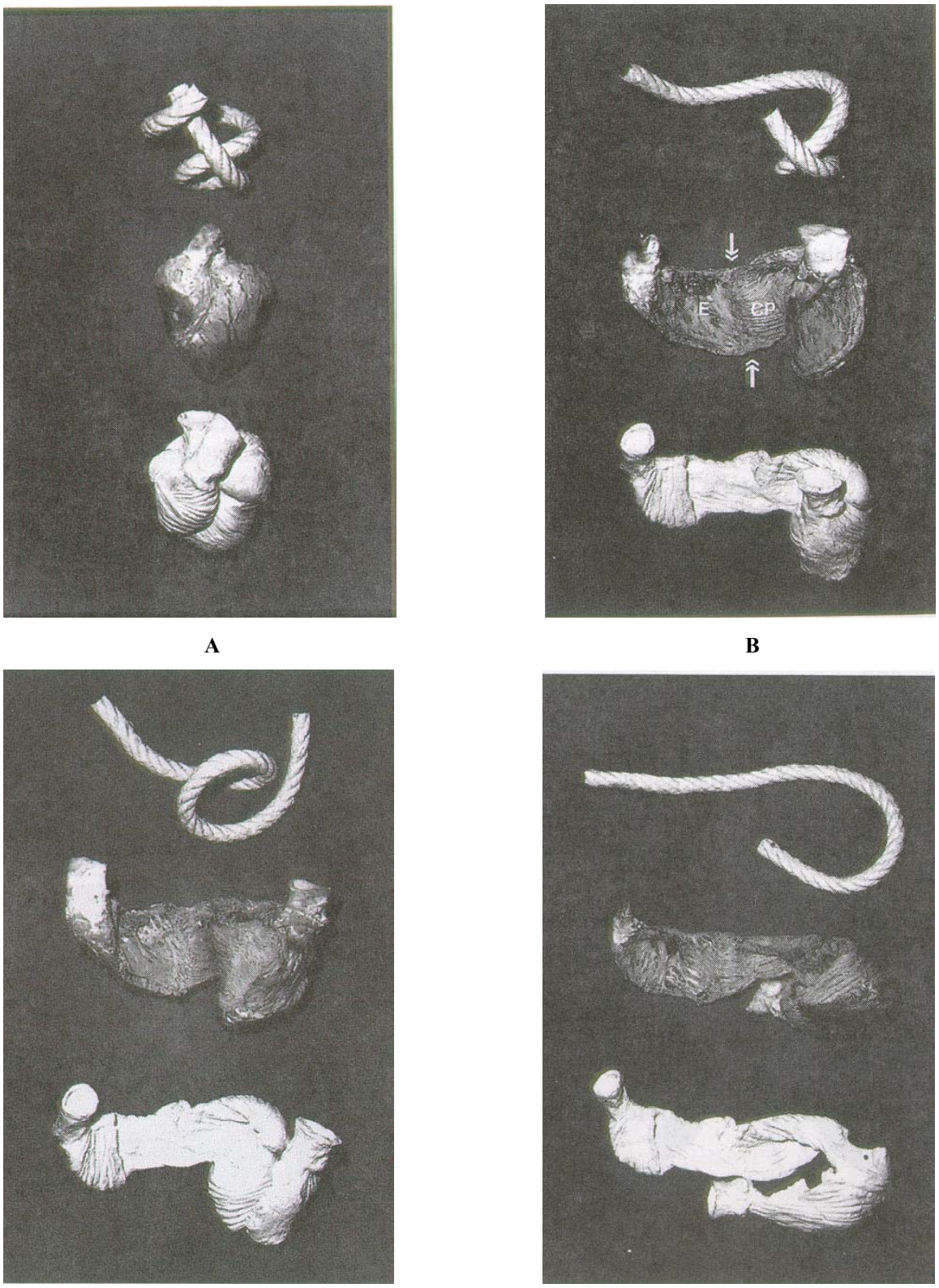

A **B**

C **D**

Figure 2.2 A rope model, an intact heart, the silicone rubber mould of the ventricular band, before and after unwinding (Torrent-Guasp and others 1997)

2.2 Fibre structure

In the 20th century, investigators paid particular attention to the fibre structure of the myocardium and its possible role in the functionality of the heart.

Hort (1960) prepared frozen sections in planes parallel to the epicardial surface and measured the fibre orientation in each section. He reported that the fibres were locally parallel and that the fibre orientation changed smoothly through the myocardium. Contrary to skeletal muscle, he observed nowhere separating boundaries in the myocardium which would allow distinguishing between different layers of muscle strands. He reported also that the network of muscle fibres was interrupted at many points but generally, the fibres were closely parallel to the external surface. They were oriented obliquely in the outer half of the myocardium, circumferentially at midwall and obliquely in the opposite sense in the inner half of the myocardium. He also observed that the number of cells along a radial line through the wall of the left ventricle when it was arrested and immobilized in systole was up to about 50% higher than in the diastole phase. He therefore concluded that the fibres might rearrange themselves during contraction of the ventricle.

Streeter and co-workers (1966; 1969) further developed the work of Hort in order to verify the hypothesis that there exist discrete muscle bundles in the myocardium which exhibit well-defined helical fibre paths running from the apex to the base. For the measurements they used a light microscope at magnification 400, which was equipped with an eyepiece hairline reticle and rotating stage calibrated in degrees. At this magnification, they could see the myofilaments within the fibres. They identified the orientation of the myofilament array in the cell with the fibre orientation.

Streeter followed the method of Hort for the measurements of the fibre angles in serial tangential sections of myocardium and extended it to three dimensions. The sections were obtained from a through-the-wall block of tissue (Figure 2.3).

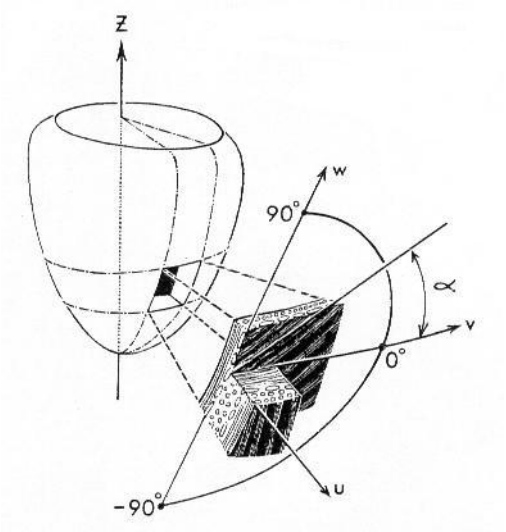

Figure 2.3 Schematic drawing of the left ventricle, showing a full-thickness specimen (Streeter 1983)

Their attempts failed to confirm the existence of any band or layer organization in the ventricular wall. Since the work of Streeter, myocardium has been widely viewed as a continuous structure in which muscle fibre orientation varies smoothly. Whether Streeter and his coworkers with their method would have been able to verify the existence of various kinds of possible more complicated fibre organizations in cardiac muscle than they documented is a question that cannot easily be determined and is not further discussed here. In their earlier work, following Hort and others, they assumed that the fibres lie in a plane parallel to the epicardial surface (Streeter and Basset 1966; Streeter and others 1969) . They suggested that the left ventricle, for the purpose of stress analysis, can be characterized as a cross-linked, fibrous ellipsoidal or paraboloidal pressure vessel with a fibre angle changing smoothly from about $60°$ inside to about $-60°$ outside. Since Streeter this pattern has been adopted in almost all mathematical models of the left ventricle. Streeter and coworkers reported also that during the transition from diastole to systole in areas not near the apex and base, there was an almost constant increase in all fibre angles through the wall. But in areas near the apex they observed significant fibre angle differences between diastole and systole. In his later work, Streeter conceded that the fibres are not everywhere in a plane parallel to the epicardium, and that for the complete determination of the fibre orientation an additional

angle which relates to the inclination of fibres with respect to the epicardial surface must be measured.

The inclination angle of the fibres (deviation from a plane parallel to the epicardium) is in literature sometimes also called imbrication angle.

Even though the estimates of the inclination angle which is denoted in Figure 2.4 by α_3 had a large variance, Streeter and co-workers (1978) reported that α_3 tends to remain small everywhere in the wall with a magnitude of the order of a few degrees. According to these measurements, almost all mathematical models were built upon this assumption, which significantly simplifies the mathematical construction (Bovendeerd and others 1992; Hunter and others 1992).

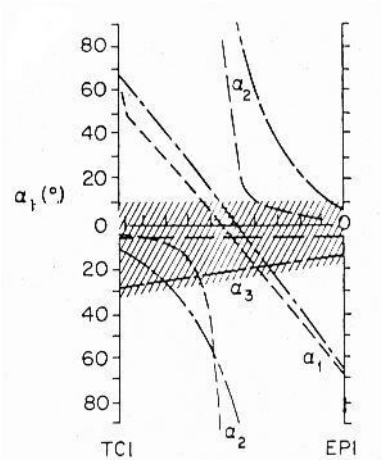

Figure 2.4 Dependence of inclination angle α_3 on position in the wall. Shaded area encompasses all obtained data for α_3 (Streeter and others 1978)

2.3 Laminar structure of the heart

After the works of Streeter, the idea of a continuous structure of the myocardium dominated for more than two decades. Yet, during the past decade, some investigators revived the notion of a discrete architecture of the myocardial tissue, but at a higher level of magnification.

LeGrice and co-workers (1997; 1995a) studied the transmural variations in the structure of the ventricular myocardium. Their work supported the view that the ventricular myocardium exhibits a discrete laminar structure in which at any point three distinct material axes can be identified, *viz.*, the fibre axis in the direction of the muscle fibres, the sheet axis which is transverse to the fibres in the plane of the muscle layer and the sheet-normal axis which is perpendicular to that plane (Figure 2.5).

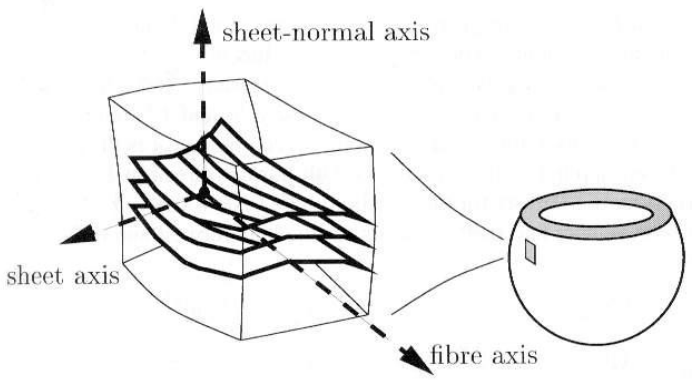

Figure 2.5 Schematic of discrete laminar structure of the left ventricle (Nash and Hunter 2000)

In their experiments, dog hearts were arrested in diastole, rapidly excised, and fixed in an unloaded state. The right ventricle, the interventricular septum, and the left ventricle free wall were divided into a series of wedge-shaped segments by means of radial-transmural cuts along meridians spaced at 12° intervals around the heart (Figure 2.6). A series of sections were obtained from the base to the apex. Ten wedges of the ventricular myocardium were sectioned at 36° spacing. With this method a full set of transmural

sections at 12° steps around the heart was provided. Transmural segments of the left ventricle were cut parallel to the base and in each segment five serial slices were cut parallel to the epicardial tangent plane. The samples were imaged with a scanning electron microscope.

They reported that longitudinal-transmural sections showed a laminar structure, in particular, that the myocardium consisted of an array of discrete layers running across the ventricular wall from the endocardium to the epicardium in an approximately radial direction (Figure 2.7).

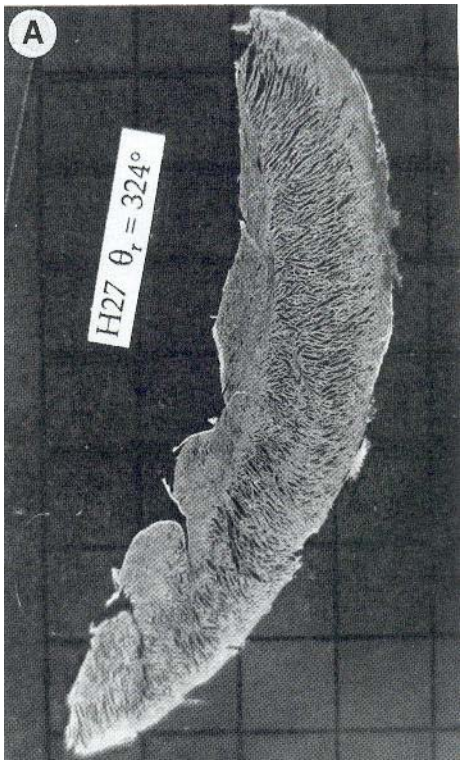

Figure 2.6 Micrograph of longitudinal-transmural section of left ventricle (LeGrice and others 1995a)

They furthermore found that branching between adjacent layers was relatively sparse and each layer consisted of tightly packed groups of myocytes aligned so that the cell axis was approximately parallel to the edge of the layer. Adjacent muscle layers were connected with collagen fibres (struts). Capillary vessels were observed within layers and not in the cleavage planes that separate them.

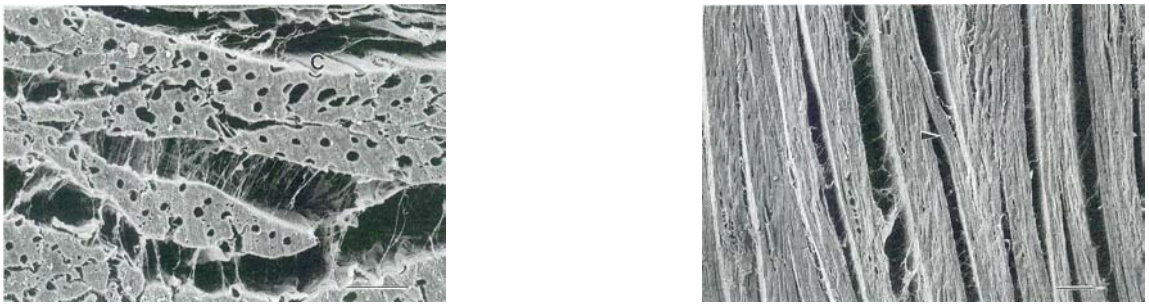

A **B**

Figure 2.7 Micrograph of (A) transverse (B) tangential surface of specimen (LeGrice and others 1995a)

They also observed that, despite the uniformity of the muscle layer organization, the architecture of ventricular myocardium was not homogeneous and that there was a clear transmural variation in the extent of coupling between adjacent layers (Figure 2.8). Accordingly, they suggested an arrangement of the muscle layers as shown in Figure 2.9.

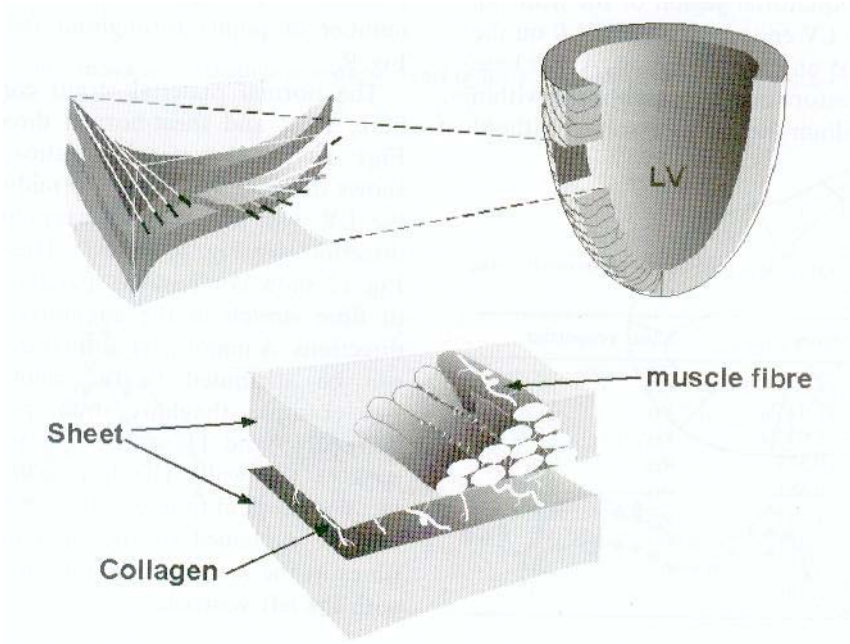

Figure 2.8 Schematic of fibrous-sheet structure of cardiac microstructure (LeGrice and others 1995a)

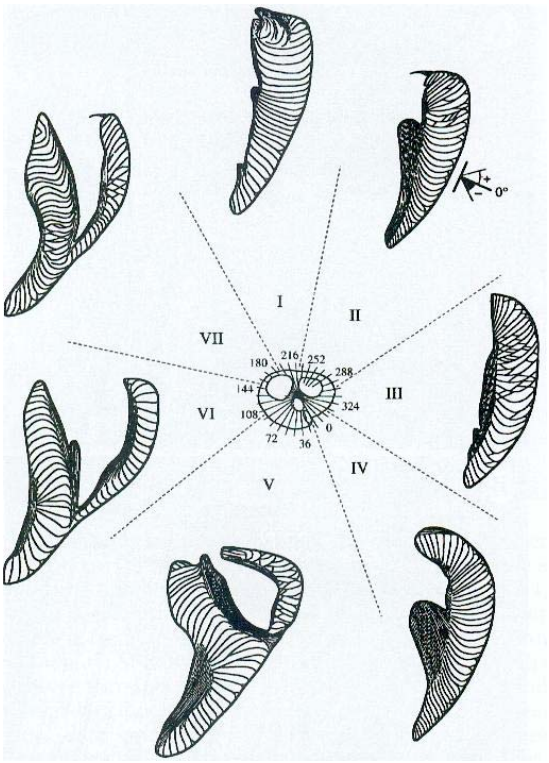

Figure 2.9 Suggested arrangement of the muscle layers (LeGrice and others 1995a)

Some investigators (LeGrice and others 1995b) argued that cleavage planes in the ventricular myocardium could support a lateral movement of muscle layers with respect to each other and permit the rearrangement of muscle fibres during contraction of the ventricle. Thus, this mechanism favours changes in wall thickness which is a decisive factor in the process of systolic ejection of blood.

2.4 Fibre orientation

The notion of a laminar structure of the ventricle is not yet widely accepted and more investigations are necessary to develop a complete theory for the orthotropic architecture of the ventricular myocardium. Especially three dimensional stress and strain measurements would be needed to confirm the orthotropic material behaviour of myocardial tissue. However, such measurements are difficult or even impossible to perform with presently available instrumentation, in particular under *in vivo* conditions.

Lunkenheimer and co-workers (1997a) developed an alternative method to assess the orientation of the ventricular muscle fibres in three dimensions. They used the myocardial fibre strand peel-off technique (SPOT) on the biventricular wall of the heart for digitizing the fibre architecture. In their approach, different mammalian hearts were fixed in formalin (10%) by coronary perfusion. The subepicardial fat, the coronary vessels and the epicardial coating were removed. At first, the epicardial surface was digitized using a three dimensional magnetic field digitizing system. Then, both ventricles including the septum were prepared strand by strand from base to apex and from epicardium to endocardium. The contractile pathway alignments were digitized manually using the fibre strand peel-off technique (SPOT) (Figure 2.10).

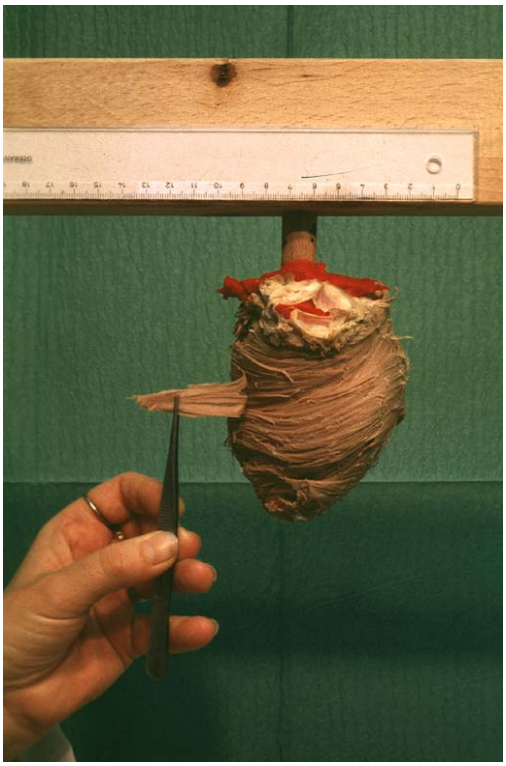

Figure 2.10 Fibre strand peel-off technique (Lunkenheimer *et al*.)

Several thousands points on the epicardium and endocardium surfaces, respectively, and likewise several thousands points of almost randomly selected fibres were recovered for mathematical analysis. With this method they were able to follow the natural course of

the fibres, and thereby they could distinguish between two gross types of fibre populations. The first kind of fibres was parallel to the epicardial surface, and the second was inclined in an oblique transmural direction towards the endocardial surface. They observed that the inclination angle was not everywhere in the myocardium smaller than 10°, as Streeter *et al.* reported, but they found a wide spectrum of angles which increased with depth in the ventricular wall. They reported also that in general, the inclination angle in the subepicardium was smaller than in the midwall and subendocardium (Lunkenheimer and others 1997a).

Cryer and co-workers (1997) developed an algorithm to calculate the epicardial surface and the inclination angle of the fibre strands using the digitized data of Lunkenheimer *et al.* They made a statistical study and presented the distribution of inclination angles as histograms (Figure 2.11). In order to obtain these distributions, the length of the digitized fibres was used as a weighting factor, so that for each fibre the length of that part whose inclination angle lay within a specified range of 10° was determined. In the histogram shown in Figure 2.11 the ordinate value is proportional to the number of the individual contractile pathways and the abscissa shows the angle of inclination.

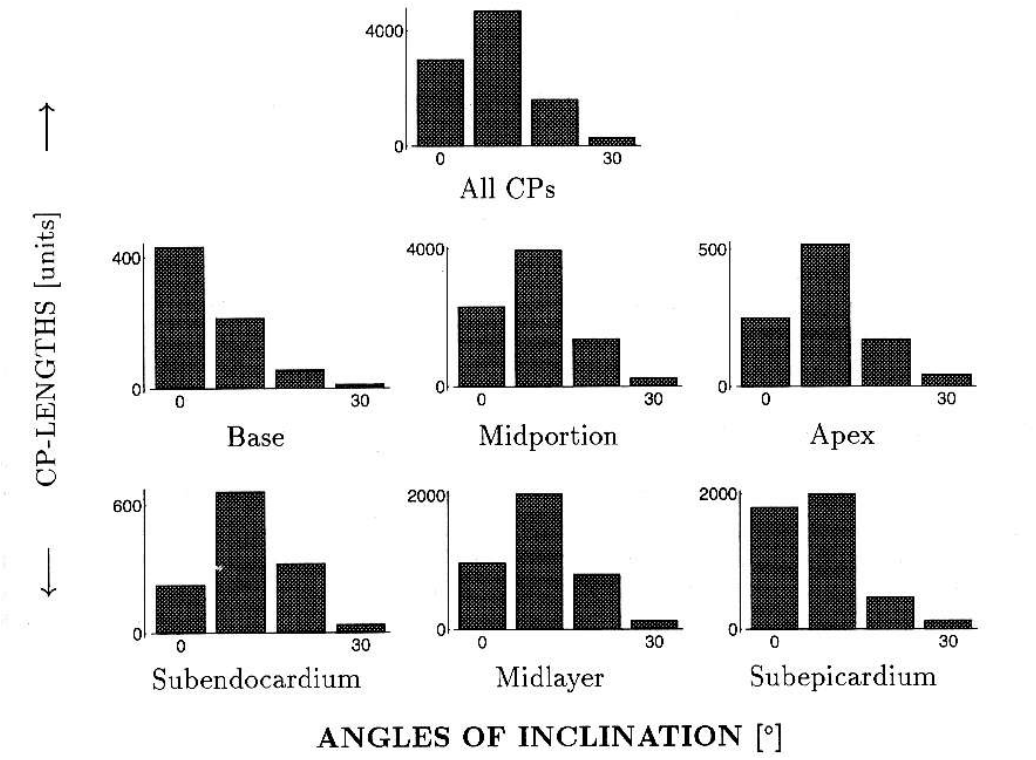

Figure 2.11 Distribution of the angle of inclination in a pig heart (Cryer and others 1997)

In the next chapter we will see how the digitized fibre orientations can be converted into fibre vector fields in three dimensions. In chapter 6 we will then use these fibre vector fields for the implementation of finite element models of the left ventricle.

References

Borelli HS. 1681. De Muto Animalium. Rome.

Bovendeerd PH, Arts T, Huyghe JM, van Campen DH, Reneman RS. 1992. Dependence of local left ventricular wall mechanics on myocardial fiber orientation: a model study. J Biomech 25(10):1129-40.

Cryer CW, Navidi-Kasmai H, Lunkenheimer PP, Redmann K. 1997. Computation of the alignment of myocardial contractile pathways using a magnetic tablet and an optical method. Technology and Health Care 5:79-93.

Hort W. 1960. Makroskopische und mikrometrische Untersuchungen am Myokard verschieden stark gefüllter linker Kammern. Virchows Arch. path. Anat. Physiol. 333:569-581.

Hunter PJ, Nielsen PM, Smaill BH, LeGrice IJ, Hunter IW. 1992. An anatomical heart model with applications to myocardial activation and ventricular mechanics. Crit Rev Biomed Eng 20(5-6):403-26.

LeGrice IJ, Hunter PJ, Smaill BH. 1997. Laminar structure of the heart: a mathematical model. Am J Physiol 272(5 Pt 2):H2466-76.

LeGrice IJ, Smaill BH, Chai LZ, Edgar SG, Gavin JB, Hunter PJ. 1995a. Laminar structure of the heart: ventricular myocyte arrangement and connective tissue architecture in the dog. Am J Physiol 269(2 Pt 2):H571-82.

LeGrice IJ, Takayama Y, Covell JW. 1995b. Transverse shear along myocardial cleavage planes provides a mechanism for normal systolic wall thickening. Circ Res 77(1):182-93.

Lower R. 1669. Tractatus de Corde. London.

Lunkenheimer PP, Redmann K, Dietl K-H, Cryer C, Richter K-D, Whimster WF, Niederer P. 1997a. The heart's fibre alignment assessed by comparing two digitizing systems. Methodological investigation into the inclination angle toward wall thickness. Technology and Health Care 5:65-77.

Lunkenheimer PP, Redmann K, Scheld H, Dietl K-H, Cryer C, Richter K-D, Merker J, Whimster WF. 1997b. The heart muscle's putative 'secondary structure'.

Functional implications of a band-like anisotropy. Technology and Health Care 5:53-64.

Nash MP, Hunter PJ. 2000. Computational mechanics of the heart. journal of Elasticity 61(1-3):113-141.

Streeter DD, JR. 1983. Gross morphology and fibre geometry in the heart wall. Handbook of Physiology, Section 2: The Cardiovascular System Vol. 1:pp. 61-109.

Streeter DD, JR., Basset DL. 1966. An engineering analysis of myocardial fibre orientation in pig's left ventricle in systole. The Anatomical Record 155:503-511.

Streeter DD, JR., Power WE, Ross MA, Torrent-Guasp F. Three-Dimentional fiber orientation in the mammalian left ventricular wall. In: Vally Forge P, 1975, Baan, j., A. Noordergraaf, J. Raines (eds.), editor; 1978; London. The MIT Press, Cambridge (Massachusets). p 73-84.

Streeter DD, JR., Spotnitz DPP, Ross JJ, Sonnenblick EH. 1969. Fiber orientation in the canine left ventricle during diastole and systole. Circ Res 24:339-347.

Torrent-Guasp F, Whimster WF, Redmann K. 1997. A silicone rubber mould of the heart. Technology and Health Care 5:13-20.

CHAPTER 3

A THREE-DIMENTIONAL MODEL OF THE FIBER ORIENTATION OF THE HUMAN LEFT VENTRICLE

3.1 Introduction

Anisotropy is one of the most important aspects of the tissue of the heart (chapters 6 and 7). It plays an essential role in heart function, especially with respect to contraction and dilatation. Due to the fibrous structure of the heart muscle, the study of anisotropy could be interpreted as local determination of the fibre orientation in the heart muscle. To date, there is no method to find out the fibre orientation *in vivo*. In this work, the fibre strand peel-off technique (SPOT) was used to determine the spatial orientation of the muscle fibres in a human *post mortem heart*. The measured fibres were not evenly distributed throughout myocardium and the pattern had to be completed accordingly. To achieve this goal an algorithm was developed and a new software package was implemented. The major result of this study is: The local anisotropy of the heart is determined as a 3D fibre orientation field which can be used for the future mechanical analyses of the heart.

The architecture of the ventricular muscle fibres (cardiomyocytes) along with their contraction and relaxation behaviour is the main determinant of cardiodynamics. As

mentioned above, the possibilities of determining the fibre orientations in the myocardium in vivo are however very limited. Experimental measurements, in particular MRI imaging and tagging methods (Stuber 1997), provide mostly global information about the motion of the heart during contraction. Nevertheless, the technique of Tensor Diffusion Imaging (DTI) which has recently been introduced (Basser and others 1994; Pierpaoli and others 1996) reveals a powerful future potential with respect to an analysis of the fibre arrangement in the beating heart.

Our knowledge of human cardiac morphology is mostly based on *ex vivo* preparations (Streeter 1983). A hierarchy of structures has thereby been found, *viz.*, from a macroscopic global rope-like architecture (Torrent-Guasp and others 1997) to a submicroscopic sheet and fibre arrangement (LeGrice and others 1997; LeGrice and others 1995). To this end, a large body of morphological analysis has been made also on those animal hearts which exhibit a high similarity with human hearts (swine, dog). Besides the cardiomyocytes, the endomysial collagen network, the vasculature and interstitial fluid are of further importance. In a comprehensive understanding of cardiodynamics, the interplay between the active and passive solid and fluid elements throughout the heart cycle has to be taken into account.

In most published heart models (Bovendeerd and others 1992; Nielsen and others 1991) the muscle fibres are assumed to be parallel to the endocardial and epicardial surfaces, respectively. A uniform structure, density and global architecture of the fibre strands wrapping both ventricles without local irregularities are furthermore assumed. Both assumptions may deviate in part considerably from the reality, in particular in pathologic cases (Lunkenheimer and others 1997). A major goal of this work was to obtain representative fibre architectures of human hearts under representative healthy and selected pathologic conditions.

3.2 Preparation of the Heart

A fresh human heart in rigor mortis weighing around 500 g typically was perfused via the coronary arteries for 24 hours with saline at a pressure of 120 mm Hg. The perfusate was subsequently replaced by a 10 % formaldehyde solution and the perfusion was continued for another 24 hours. The atria were trimmed down to the ventricular base and the heart was submerged for two weeks in a 10% formaldehyde solution. The ventricles were then filled with Technovit (Haereus-Kulzer, Germany) such that mouldings of the ventricular cavities were obtained. Together with the two-component resin a wooden rod was axially anchored in the left ventricular cavity which served to fix the heart in a jig on top of the electromagnetic digitizing tablet (3 Draw Digitizer System, 3 SD 005, Polhemus, Cochester VTO 5446, USA).

3.3 Peeling of the ventricular muscle body and digitization

After having removed the epicardium together with the perivascular fat, one leg of a fine forceps was inserted 1 to 2 mm deep into the left ventricular wall. The enclosed fibre bundle was detached from its surroundings and then pulled along its prevailing longitudinal direction, thus sequestering it from its bed. In so doing, we aimed to restrict the strands neither in length nor in their self-organized pathway. Accordingly, minute fibres portions were removed sequentially which were typically between 1 – 2 cm long and 1 – 2 mm across until the ventricle was essentially peeled. During this process, a stepwise digitization was performed by using a manual stylus. Care was furthermore taken to perform the combined peeling and digitizing procedure as fast as possible to keep the evaporation minimal (Figure 3.1).

While strands were removed from their grooved bed, numerous connections with the neighbouring fibres were disrupted which is an inevitable consequence of the ubiquitous cross linking of the cardiomyocytes. Histology however confirms that a preferred fibre

direction prevails throughout the ventricular wall such that our procedure reproduced in essence this preferred orientation pattern. While the detached strands were of limited length, contractile pathways in the ventricular wall have, strictly speaking, no beginning and no end. The strands therefore characterize local main fibre trajectories and as such mark the fibre architecture pattern segment wise.

Close to the epicardium where the main fibre weave exhibits a primarily surface-parallel orientation, the peeled strands were quite uniform in thickness. In deeper zones, however, strands usually grew in thickness as they were pulled out of the myocardial continuum. Therefore, opposing surfaces of the strands were found to be slightly wedge-shaped.

Both ventricles including the septum were prepared in the described fashion, strand by strand, from base to apex and from the epicardium to the endocardium. Thereby, sequential peeling steps exposed progressively more uneven surfaces, because in distinct areas of the left ventricular wall the carved–out strands were more and more inclined towards the endocardium.

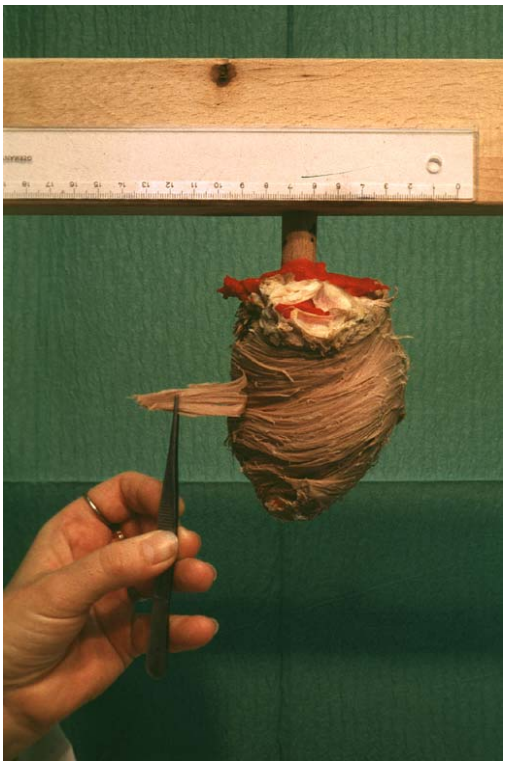

Figure 3.1 Peeling of the fibre muscles (SPOT)

While following the well defined grooves and crests on the sequentially exposed surfaces with the stylus, a data set characterizing the contractile pathways was obtained. No further data processing for the identification of these structures was performed, *i.e.*, the strands were considered to represent short segments of the continuous fibre orientation field.

The density of the cloud varied throughout the ventricular wall because, for practical reasons, the peeling process could not be performed uniformly. *E.g.*, the wedge shape of the strands differed from location to location such that consecutive strands had variable dimensions. Care was taken, however, to digitize the base of both ventricles with maximal resolution. In the following paragraph, the data processing procedure is demonstrated with a typical heart.

3.4 Geometry

The first step in (re-)constructing the cardiac anatomy consisted of the determination of the left ventricular epi- and endocardium from the point clouds containing typically 2000 points representing the endocardial and some 4'500 points the epicardial surface. In order to derive closed and smooth surfaces from these sets, the software system Raindrop Geomagic® was applied. The mathematical procedure thereby utilized was based on Nonuniform Rational B-Splines (NURBs) (Rogers 2001). The result of the procedure is seen in Figure (3.2).

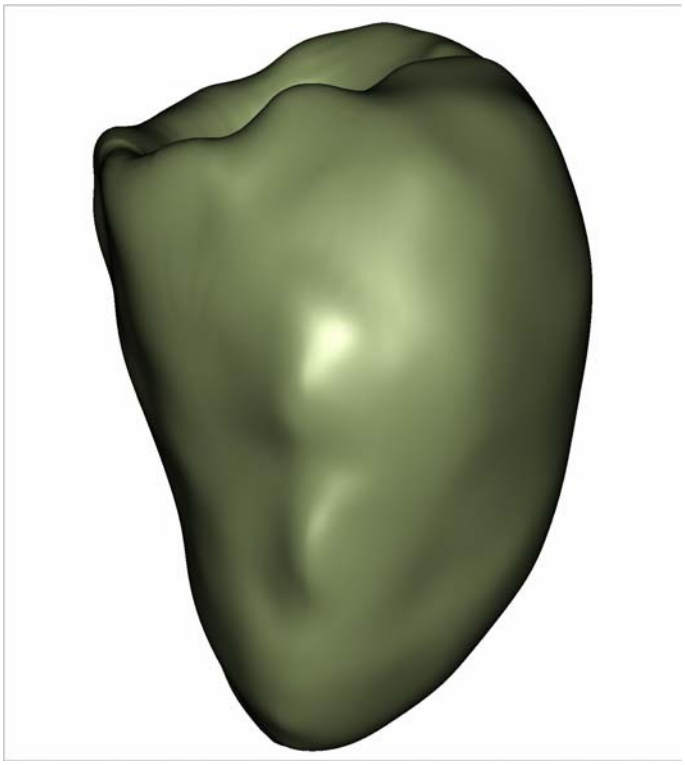

Figure 3.2 Real geometry of a typical left ventricle

3.5 Fibre orientation field

Second, the fibre pattern had to be built into the ventricular wall now outlined by two surfaces. Due to the method of peeling the measured strands were not evenly distributed throughout the myocardium, as mentioned previously (Figure 3.3). While at certain locations a dense pattern could be documented, others are almost devoid of fibre traces or trajectories. We hypothesize that the characteristics of myocardial tissue exhibits little variation within a healthy heart and that therefore the fibre density is quite uniform throughout the ventricle. In case of hearts with an infarcted region or with extended fibrosis, however, this proposition cannot be applied. A particularly careful peeling is necessary in such cases. Nevertheless, even if there are inactive (akinetic) areas or if fibrosis is present, the myocardium is anisotropic. The fibre orientation field constructed

here can therefore be regarded as a representation of global anisotropy in the sense of continuum mechanics. Accordingly, the terms fibre, strand, trajectory and axis of anisotropy are used synonymously.

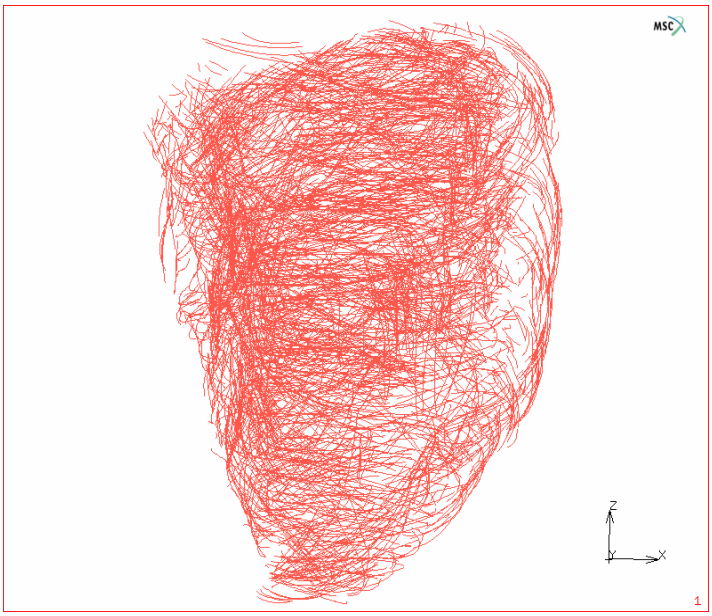

Figure 3.3 Fibre trajectories of a typical left ventricle

An extrapolation was in all cases necessary to complete the fibre pattern. For this goal an algorithm was developed with which the fibre orientation pattern was determined in the form of a uniform fibre field. This field was discretized and defined in a sufficiently large number of points in myocardium. The density of points was considered sufficient if it was comparable to the one that might be chosen to create a typical Finite Element (FE) mesh because such a mesh is expected to include all geometrical details of importance. Accordingly, we used the hex-mesh generator of the FE software system MSC Marc-Mentat to subdivide the volume given by the two surfaces. A mesh with about 47'000 eight-node hexahedral elements resulted. All of the nodes were numbered and the coordinates of all nodes were defined in a global rectangular Cartesian coordinate system (Figure 3.4).

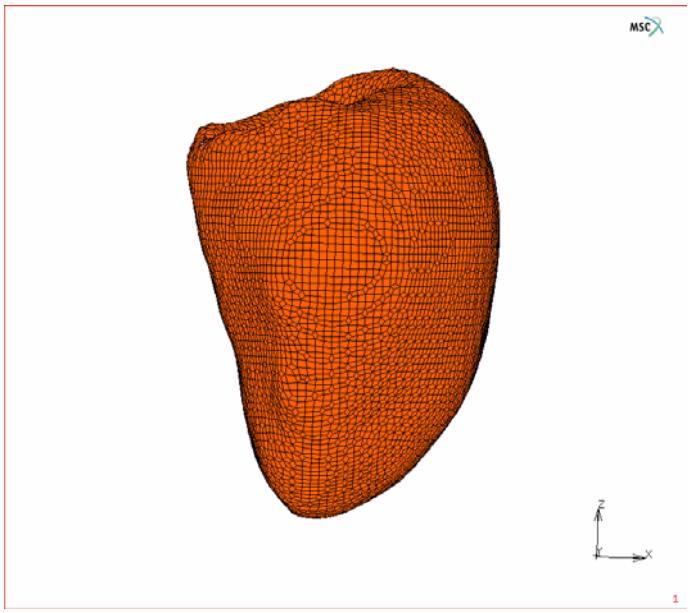

Figure 3.4 Mesh of a typical left ventricle

More than 2,700 point sequences containing up to 19 individual points defining fibre trajectories were available for the left ventricle. In each sequence, the first and last points were discarded because these points were often inaccurate due to the manual peeling procedure. Accordingly, sequences consisting of less than 4 points were omitted. The trajectories were smoothed and converted into cubic splines [NAG, Oxford]. At least 4 and at most 90 regularly spaced points were interpolated on each spline and utilized to represent a trajectory; the number of points thereby depended primarily on the length of the curve (Figure 3.3).

If we choose an arbitrary line between two points, P_i and P_{i+1}, on an arbitrary trajectory F (Figure 3.5), with the position vectors (bold characters are used to denote vectors) $\mathbf{r}_F(P_i)$ and $\mathbf{r}_F(P_{i+1})$, respectively, the middle point Z_i can be calculated as

$$\mathbf{r}_F(Z_i) = \frac{1}{2}\left\{\mathbf{r}_F(P_i) + \mathbf{r}_F(P_{i+1})\right\} \tag{3.1}$$

These consecutive points, P_i and P_{i+1}, in turn, define a direction vector,

$$\mathbf{v}_F(Z_i) = \mathbf{r}_F(P_{i+1}) - \mathbf{r}_F(P_i) \tag{3.2}$$

Since the points on the trajectory are chosen sufficiently close together and the trajectory is a smooth curve, we can utilize this vector as an approximation for the tangent vector at the middle point of the arc between the two points.

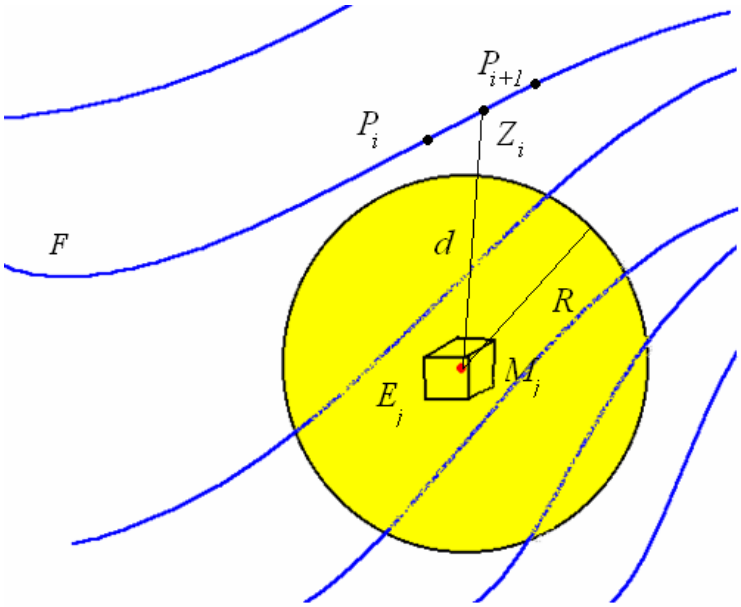

Figure 3.5 fibre distribution in the near of an element E_j

Next, we considered an arbitrary hexahedral element, E_j obtained from the meshing procedure mentioned above, and identified an interior point so that there existed always a neighbourhood which was inside the hexahedral element (Figure 3.5).

A straightforward choice is the middle point M_j of the hexahedral element with coordinates that are defined as the average value of the coordinates of eight nodes in the corners. Let us now consider a spherical neighbourhood of radius R around M_j and calculate the distance $d\left(Z_i, M_j\right)$ between all points Z_i on the arbitrary trajectory F and M_j. In case that $R \succ d$, the point Z_i is within the sphere, if the next point, *i.e.*, Z_{i+1} is within the sphere too, we conclude that the vector $\mathbf{v}_F\left(Z_i\right)$ is likewise within the sphere. This procedure was repeated for all trajectories and for all of their points Z_i to find the

number of curves which cross the sphere. The radius R has to be estimated suitably at the beginning; if the number of curves which cross the sphere was zero or too small, R was increased and the procedure repeated until there were at least three curves in the chosen sphere around point M_j.

A geometrically accurate model of the left ventricle may consist of up to about 50'000 elements and 70'000 points on the fibre trajectories. If the described algorithm is implemented, computing time becomes rather long. A considerable reduction was achieved by two modifications of the algorithm. First, the computation of the square root associated with the criterion involving the test sphere with radius R is not necessary if d is much larger than R. Most of the fibre trajectories lie outside, often even far away from our chosen element.

Instead of a sphere, we can therefore use at first a rectangular neighbourhood of M_j with the edge length $2R$ and determine the fibres of interest. Because

$$Sup\left\{\left|x_1 - x_2\right|, \left|y_1 - y_2\right|, \left|z_1 - z_2\right|\right\} \leq d\left(1,2\right) \tag{3.3}$$

we evaluate

$$Sup\left\{\left|x_1 - x_2\right|, \left|y_1 - y_2\right|, \left|z_1 - z_2\right|\right\} \succ R \tag{3.4}$$

and discard the corresponding fibres. A further improvement results if we skip a number of consecutive points and repeat the test for point Z_{i+k}, $k \succ 1$ only if

$$Sup\left\{\left|x_1 - x_2\right|, \left|y_1 - y_2\right|, \left|z_1 - z_2\right|\right\} \gg R \tag{3.5}$$

If we define $\left|\mathbf{v}_F\right|_{\max}$ as the maximal distance of points Z_i and Z_{i+1} on the trajectory F, we can estimate k from following relation

$$k = Int\left\{\frac{Sup\left\{\left|x_1 - x_2\right|, \left|y_1 - y_2\right|, \left|z_1 - z_2\right|\right\} - R}{\left|\mathbf{v}_F\right|_{\max}}\right\} \tag{3.6}$$

If $k \prec 1$ we use $k = 1$.

From all direction vectors $\mathbf{v}_F(Z_i)$ which are inside the spherical neighbourhood of M_j, an average fibre direction vector for the element E_j has now to be determined (Figure 3.6).

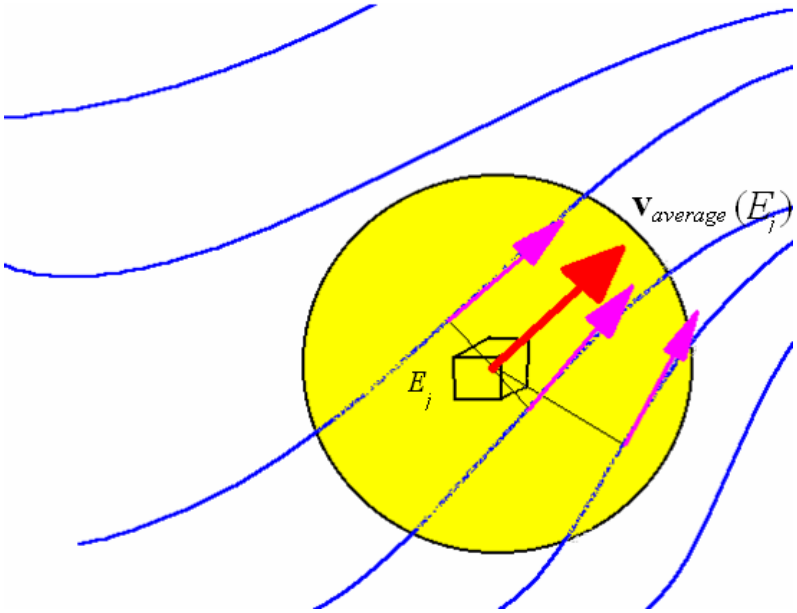

Figure 3.6 Average direction vector defined as fibre orientation for element E_j

For this purpose, we define a weighting function W, and postulate that the vectors which are closer to the centre of the element have a heavier weight, such that we can write

$$\mathbf{v}_{average}(E_j) = \sum_i W_i \cdot \mathbf{v}_F(Z_i) \tag{3.7}$$

Upon normalization we obtain

$$\mathbf{N}(E_j) = \frac{\mathbf{v}_{average}(E_j)}{\left|\mathbf{v}_{average}(E_j)\right|} \tag{3.8}$$

For the weighting function W we used the form

$$W_i = \frac{1}{\left\{c_t \cdot (d_t)^n + c_n \cdot (d_n)^m\right\}^p} \tag{3.9}$$

and

$$d\left(Z_i, M_j\right) = \sqrt{\left(d_t\right)^2 + \left(d_n\right)^2} \tag{3.10}$$

Here, d_t and d_n are the tangential and normal distances of M_j and Z_i, respectively, furthermore, c_t and c_n are constant coefficients which determine the relationship between d_t and d_n, and n, m and p are exponents. With the help of these factors we can determine the influence of the spatial distribution of the trajectories on the average direction. For this purpose, a software package was developed which allowed reconstructing the fibre vector field from the digitized fibre trajectories (Figure 3.7).

Figure 3.7 3D-represantation of fibre orientation field

A number of further features were thereby implemented, in particular:

(a) Visualization of the fibre structure in the form of a two dimensional representation of layers with defined thickness and viewpoints from an arbitrary perspective within the myocardium.

(b) Interpolation of the fibre orientation in the myocardium. As input, the program uses not evenly distributed digitized data without any assumption about the distribution of the fibres.

(c) Construction of a rectangular Cartesian coordinate system in the middle point of each arbitrary element in myocardium, so that the first axis of this coordinate system is along the fibre orientation in that point. This feature will be used for implementation of a transversely isotropic finite element model of the left ventricle in chapters 6, 7 and 8.

(d) The program performs a statistical evaluation of the interpolated fibre orientation.

3.6 Transverse fibres

A first focus was aimed at the repartition of oblique transmurally aligned pathways (transverse fibre trajectories) throughout the myocardium (Cryer and others 1997). Although transverse fibres may have a significant influence on the performance of the ventricle, this aspect received little attention in previous mathematical models [transverse fibres were considered, *e.g.*, by Bovendeerd *et al.* (1994)]. It turns out that the tendency of the contractile pathways to incline towards the endocardium is quite unevenly distributed all over the left ventricular wall. While at certain locations, such as the *margo obtusus*, transmural fibres are encountered frequently, others are almost devoid. The spatial angulations of all contractile pathways which have been digitized in this heart are summarized as histograms in Figure (3.8).

3.7 Short axis sections

In Figure (3.9) the fibre trajectories are shown in thirty short axis slices of the heart. We found a pronounced concentration of transverse fibres in the apical eight slices (ca. 2.5 cm), Figure (3.9-23 to 30). Thereby, the angles with respect to the epicardial surface were particularly large exceeding in some areas of the five most apical slices (1.5 cm) an angle of 45 degrees. In the base, the first three slices (ca. 1 cm) displayed the highest extent of variations in fibre angulations, all around the circumference, resembling in some areas to a fishbone-like pattern (Figure 3.9-1 to 3). From there up to slice fifteen (ca 3.5 cm) still some deviations from the strictly tangential alignment were found, however, angles bigger than 20 degrees were never recorded (Figure 3.9-3 to 15). The highest amount of transverse fibres in this area was mainly located around the obtuse margin of the free wall. From slice sixteen to twenty-two (ca. 2 cm) an almost strictly tangential fibre alignment prevailed (Figure 3.9-16 to 22).

The question arises with respect to the significance of transverse contractile pathways. In agreement with the classical literature (Hunter and others 1988; Laplace 1806; Mirsky 1969; Mirsky and others 1981; Mirsky and Krayenbühl 1981) we conclude that the subbasal 3.5 cm along with the adjoining 2 cm of the ventricle's midportion represent the main hemodynamic pump unit of the left ventricle. The upper part of the left ventricle is in particular supposed to sustain ventricular ejection by contraction of its circular muscle mass. Its most basal part (ca. 1 cm) might furthermore be involved in the operation of the complex dynamics of the mitral valve apparatus (Boehme 1936). Transverse fibres which are located in this section might be of use in controlling circumferential constriction in terms of amount and timing (Shapiro and Rademakers 1997).

The highest amounts of contractile pathways which are not aligned parallel to the epicardial surface were however found in the apex. This structural particularity has been associated with the cyclic wringing motion of the apex (Ingels 1997). Yet, the functional significance of this motion has recently been questioned since Boesiger *et al.* (Stuber 1997; Stuber and others 1999) and other investigators have shown that apical twisting and its reversal are strictly confined to the period of ventricular ejection. Therefore, at present, we do not attribute much functional importance to the marked transverse fibre

presence in the apex in particular with respect to their hypothetical contribution to early diastolic filling of the ventricle (Torrent-Guasp and others 2001), but they might in fact contribute to homogenize the bioelectric signal transmission as part of the conduction of excitation.

3.8 Long axis sections

In longitudinal sections the course of the contractile pathways was seen to deviate substantially more from a surface-parallel alignment than in short axis sections (Figure 3.10). This fact might in part be explained by the overall prevailing longitudinal orientation of the contractile pathways within the left ventricular wall. Upon comparing the septum with the free walls, it was found that in any section the obliqueness was more pronounced in the septum. This is particularly true in the border segments of the septum, *i.e.*, near the junctions with the free walls where transmural components accumulated especially near its inferior junction. Quite generally, the oblique transmural striation of the contractile pathways in the free walls appeared to be less pronounced because of the shortness of the segments which we were able to digitize. Nevertheless, it turned out that the inferior wall is densely interspersed with short segments which are inclined towards the endocardium at an angle which largely exceeds 45 degrees.

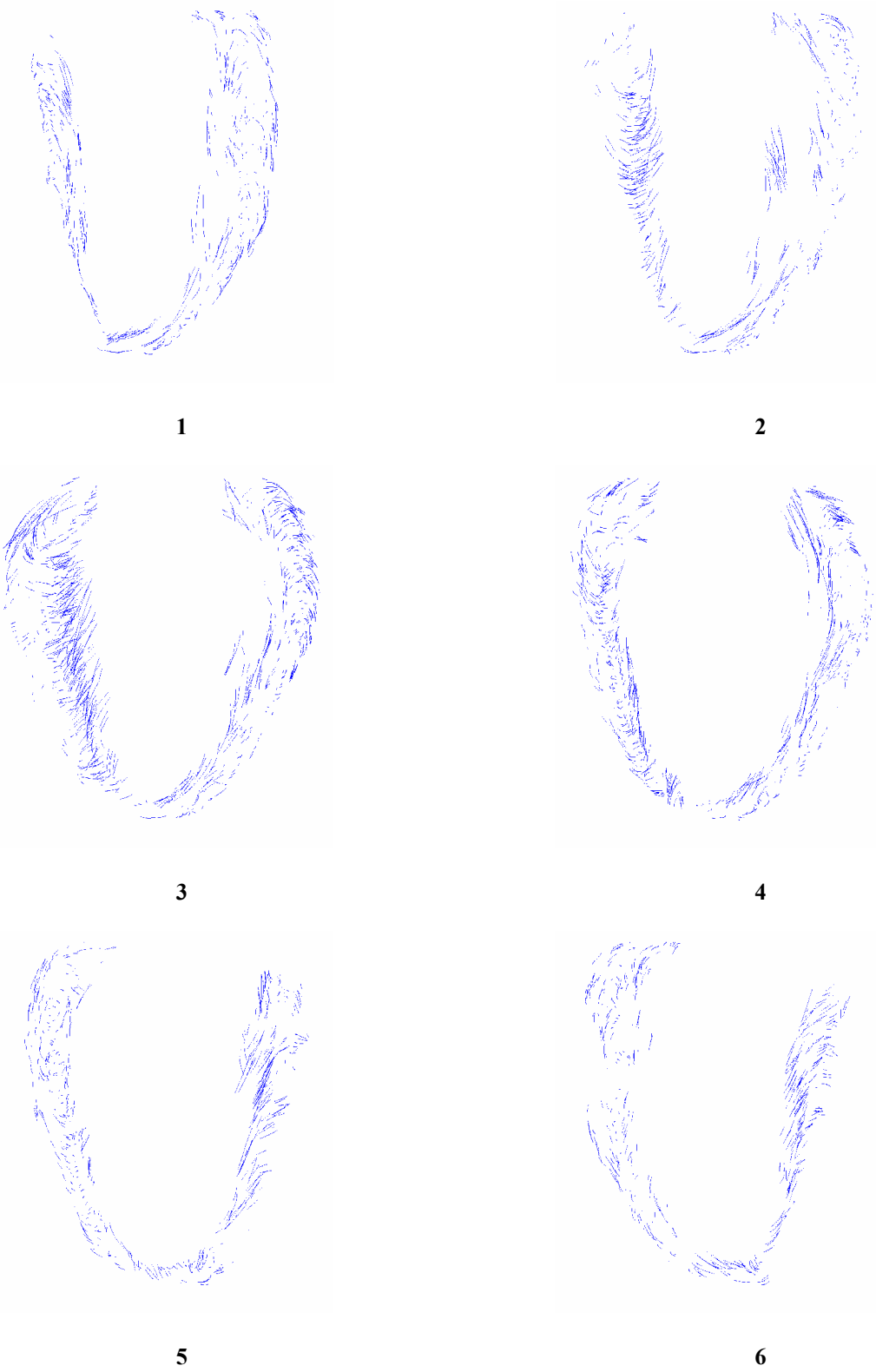

Figure 3.10 2D-represantations of fibres in defined layers (long-axis view)

3.9 Radius of fibre curvature

An important underestimated aspect in ventricular mechanics is related to the fact that the radius of curvature of the fibres varies widely over the ventricular wall. In part, this explains the local inhomogeneities of the systolic contraction pattern which is measured by various methods (Brutsaert 1987; Brutsaert and others 1984; Brutsaert and Sonnenblick 1969; Lunkenheimer and others 2004).

In ventricular length sections the radius of curvature more or less continuously increases from the ventricular base to the apex. This observation has widely been discussed in the literature in context with models used for the calculation of ventricular wall stress (spheres or ellipsoids). Due to the confined resolution, echocardiography furthered the impression that the short axis cross section of the left ventricle is essentially circular (Mandarino and others 1998). More advanced imaging methods such as MRI taught us however that this assumption is not valid (Stuber 1997; Stuber and others 1999).

Digitized individual contractile pathways demonstrate the considerable amount of regional deviation from a constant average radius of curvature of the ventricle. This holds both for vicinal pathways as well as along individual trajectories and becomes particularly apparent in ventricular cross sections. Here, each of the three segments of the free wall (inferior, posterior and superior) and the septum show their typical modulation in curvature when proceeding from base to apex.

3.10 Shape of the cross section

The two most basal slices (0.6 cm) exhibit a fairly circular contour. This is the typical cross section seen in echocardiography. From the third slice onward, the ventricular cavity progressively flattens whereby the largest radius of curvature is found in the

septum while the curvature is greatest in the superior and inferior walls. The posterior wall around the obtuse margin also flattens out without however reaching the large radius of the septum. Beginning with the seventh slice, the posterior wall progressively bends more and its bending exceeds that of the inferior wall from the ninth slice onward. Here, the bending of the superior wall definitely prevails. From the twelfth slice onward, the ventricular cross section assumes a horse shoe shape with its base in the septum and the smallest radius of curvature in the posterior wall. Descending further towards the apex the cross section looses even more of its sphericity as it changes into a shape with an almost continuous bending of the posterior and superior wall and with a flat septum and inferior wall. Both are almost at right angles to one another. From the nineteenth slice onward, the inferior wall regains in bending while the posterior wall progressively flattens. The highest degree in bending nevertheless prevails in the superior wall. Between the twenty-first and twenty-fourth slice the horse shoe-like cross section is dominant with the smallest radius of curvature in the posterior wall. Between the twenty-fifth and twenty-seventh slice the posterior and superior wall exhibit again an almost continuous curvature while the inferior wall flattens and aligns at right angle to the septum. The very apical slices, finally, show an almost circular cavity.

In summary, the basal ring and the very apical lumen show a circular shape. The subbasal lumen assumes a more or less rectangular shape, then, from 1.8 cm downwards an oval, from 3.3cm on a horse shoe-like, from 4.5 cm downwards an irregularly triangular contour with the posterior and superior walls merging to one long, continuously curved structure. From 5.4 cm onward, the horse shoe-like cross section is found again, from 6.3 to 8.1 cm the shape is triangular again, and in the apical 9 mm the cross section returns to circular. It is worth mentioning that, although the wall thickness varies between the various regions this aspect quite generally applies to the shape of the ventricular cavity as well as to its outer dimensions.

3.11 Limitations

The human heart investigated here had previously undergone a process of fixation devised to fill up the interstitial space with water such that, after formalin fixation, the peeling procedure could be performed. Yet, any extended time of manipulation on the heart before it is fixed furthers the process of degradation. Therefore, the shape of the heart which we assessed during the peeling procedure must be expected to differ somewhat from its intravital configuration. However, it might be argued that Hort *et al.* have shown (1957; 1960a) that the contour and compliance of the heart are essentially determined by its connective tissue scaffold rather than by the contractile tissue.

Finally, the combined peeling and digitization procedure described here is quite selective in that certain fibre strands, *i.e.*, those which can be reached by the forceps are documented, while others are omitted. In fact, the greater part of the ventricular muscle mass is not peeled. Therefore, if the same heart could be treated twice in this fashion, a somewhat different result in terms of alignment of the trajectories would be obtained, however, the essential aspects of the overall architecture would be maintained.

3.12 Mathematical procedure

The developed computer procedure has a number of options which can be used for further evaluations. E.g., a perspective plot from an arbitrary viewpoint can be created and the fibre architecture of a particular layer represented (Figure 3.10). This facility is instructive because it can show how the trajectories are distributed in different areas of the heart and we can in particular compare the measured with the calculated directions (Figure 3.11).

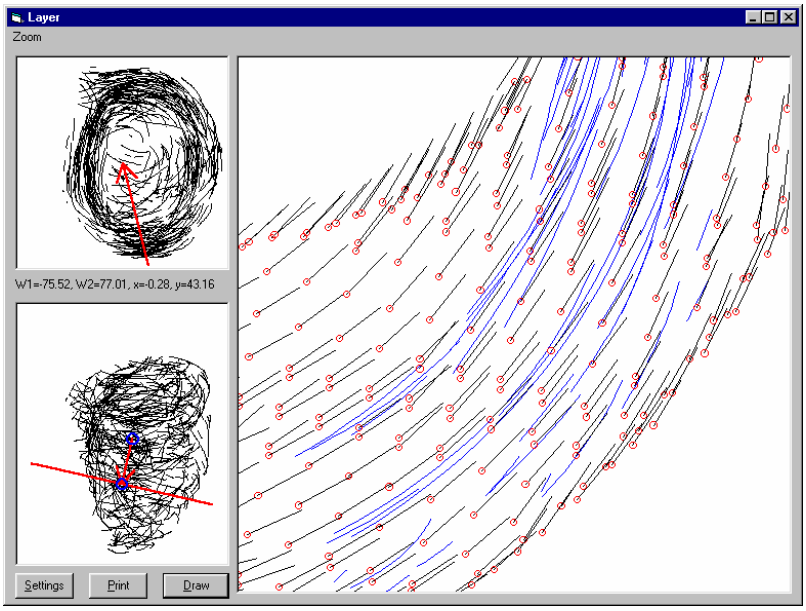

Figure 3.10 Comparison of digitized (blue) and calculated (black) fibre directions

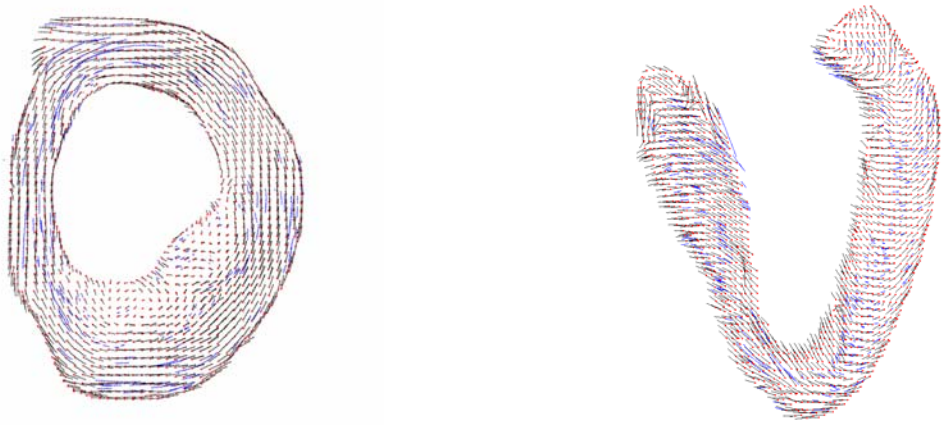

Figure 3.11 Comparison of digitized (blue) and calculated (black) fibre directions from different view points

Furthermore, certain statistical evaluations can be made: We calculate the average of the $\mathbf{v}_F(Z_i)$ vectors in all Z_i points inside a spherical neighbourhood of M_j and attribute it as the fibre direction vector to the element E_j. It is interesting to know how large the average deviations of $\mathbf{v}_F(Z_i)$ with respect to $\mathbf{v}_{average}(E_j)$ are (Figure 3.12). It is found that for the heart which was analyzed here the peak of the diagram is located around 15

degrees. The maximal deviation of $\mathbf{v}_F(Z_i)$ with respect to $\mathbf{v}_{average}(E_j)$ can be determined; for our typical heart sample the result is shown in Figure (3.13). In Figure (3.14) we see moreover how many trajectories were in each spherical neighbourhood on the average. It turns out that in our sample most of the elements included between 3 and 15 trajectories for the chosen radius $R = 5\,mm$ of the spherical neighbourhood. For most of the elements the trajectories were inside this neighbourhood and only for a small percentage it was necessary to make it larger.

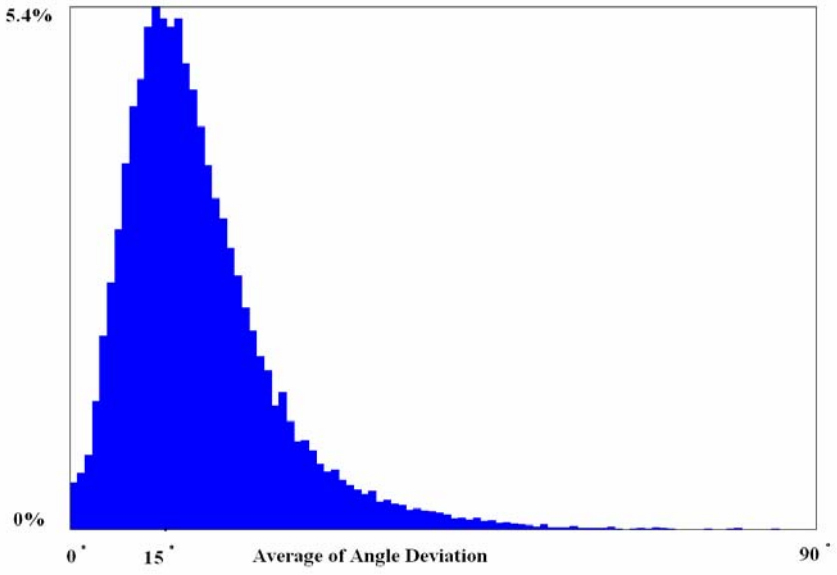

Figure 3.12 Average of angle deviation

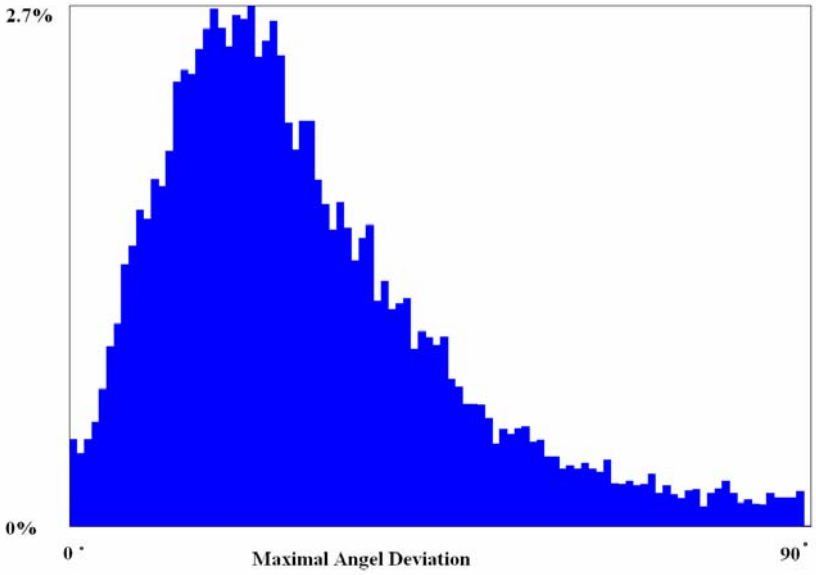

Figure 3.13 Maximal angle deviation

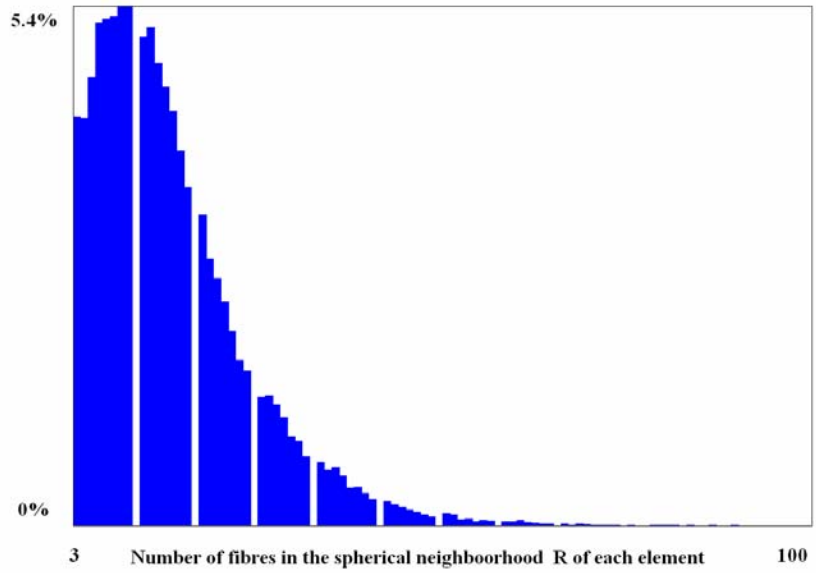

Figure 3.14 Number of fibres in the spherical neighbourhood R of each element

3.13 Other hearts

The results shown in this work were derived from a typical healthy human heart. The question arises with respect to the biological variability in case of healthy as well as diseased hearts. To this end, more samples should be studied, however, in view of the time which is necessary for a full statistical study; such a project has to be deferred to the future. In this work we have rather concentrated on the development of the basic methods which are needed to investigate the fibrous structure of the heart. The functionality and significance of the procedures are demonstrated on a sample specimen.

A further interesting aspect is related to the differences in the fibre orientations which occur in the systolic in comparison with the diastolic phase of the heart cycle. For this purpose, a sample should be studied in different phases of contraction. From such a study would bring further insight into the functional significance of the fibre structure of the heart.

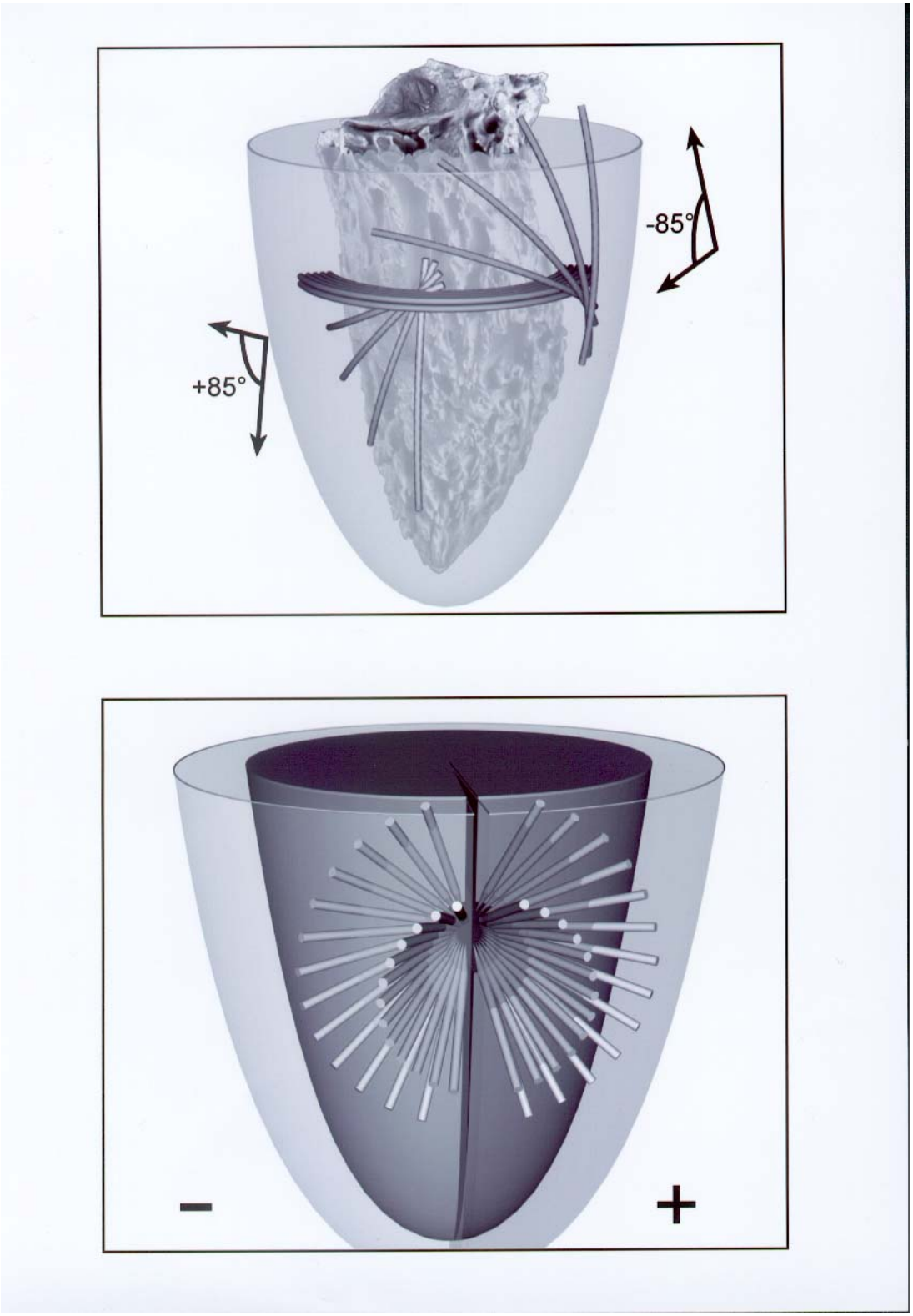

Figure 3.8A Helix and angle of inclination are defined according to Streeter, positive and negative values of these angels are shown here schematically

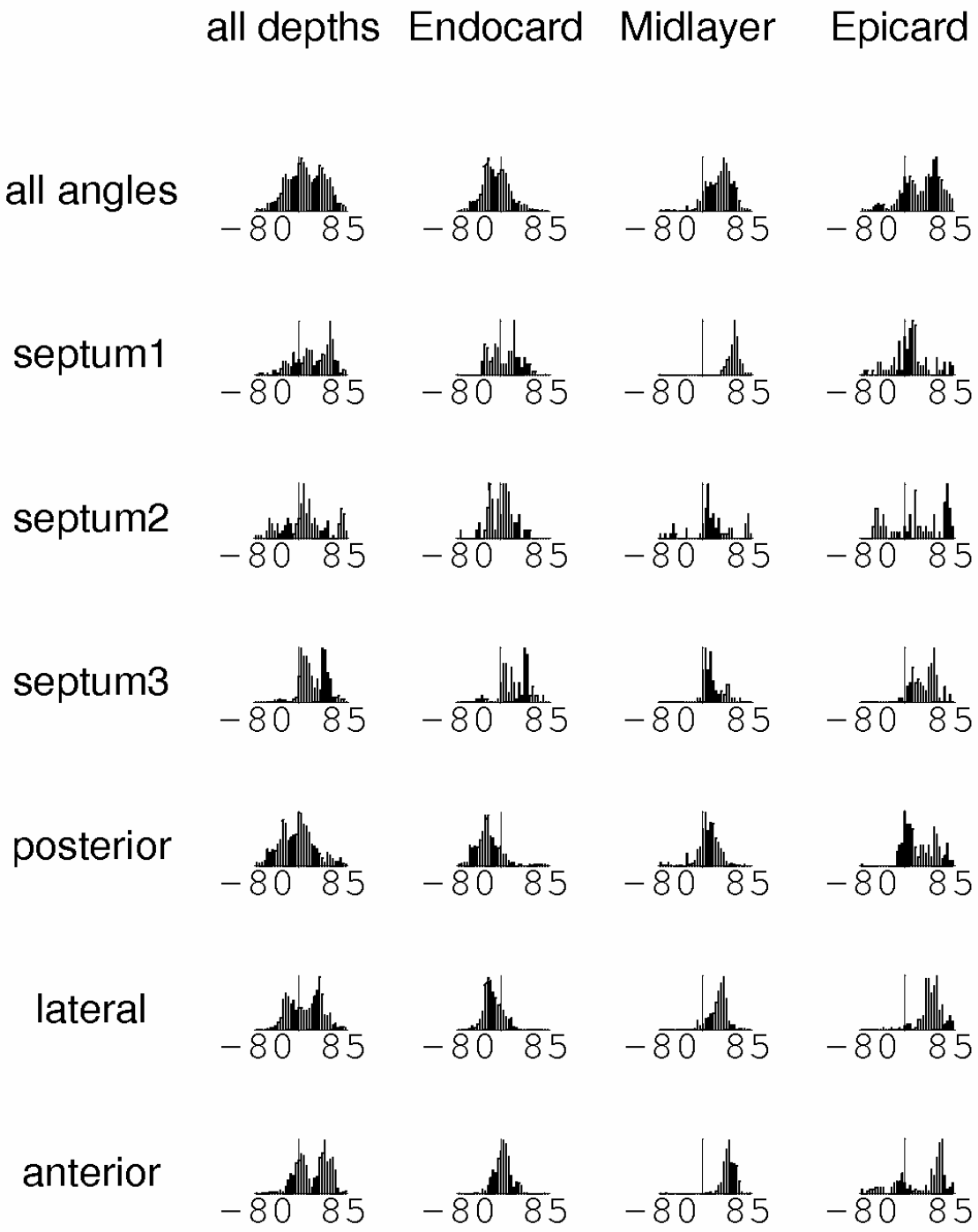

Figure 3.8B Histograms of the digitized human heart, Helix angle Base (Cryer *et al*.)

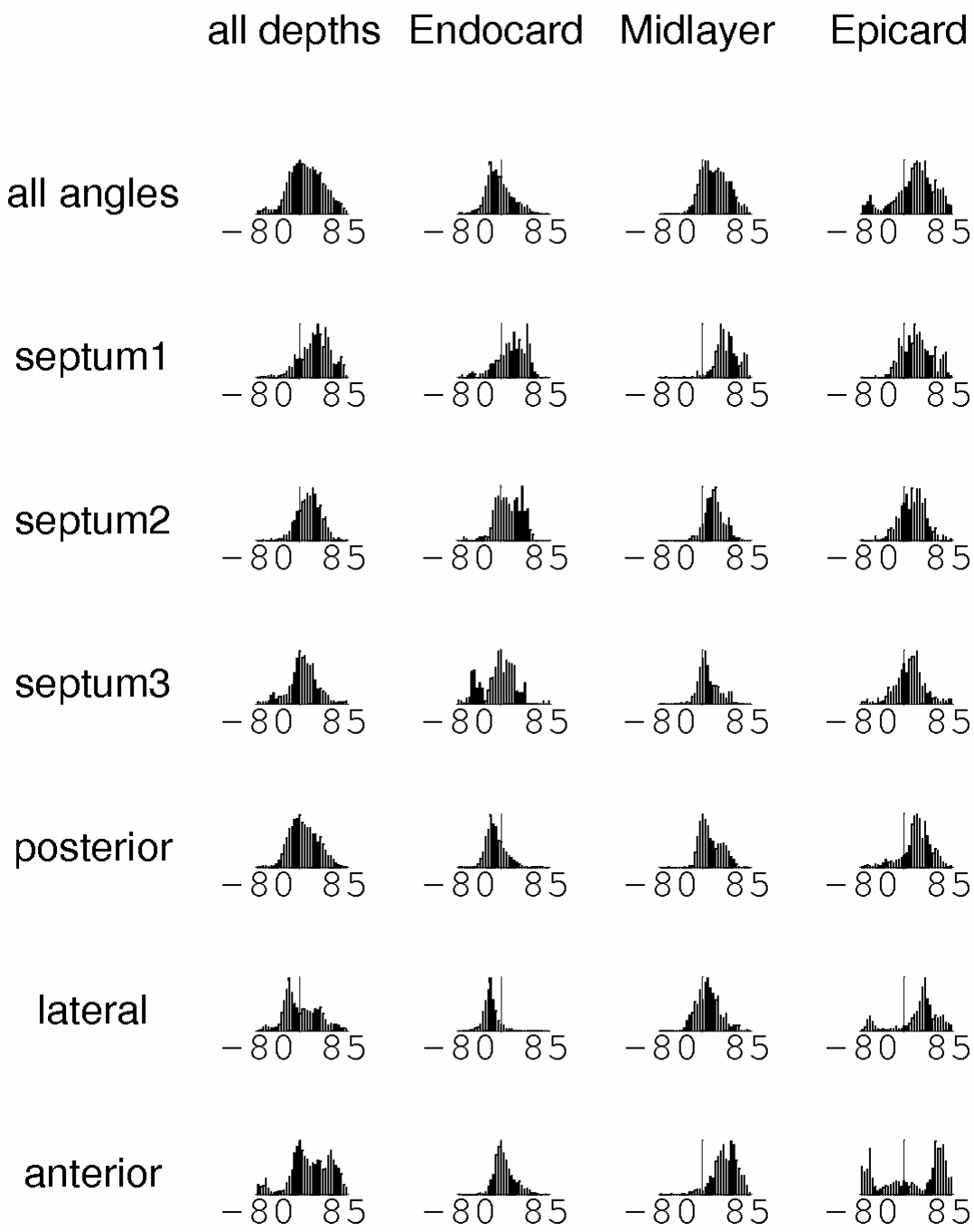

Figure 3.8C Histograms show the distribution of digitized fibres of the human heart with respect to helix angle in midportion (Cryer *et al*.)

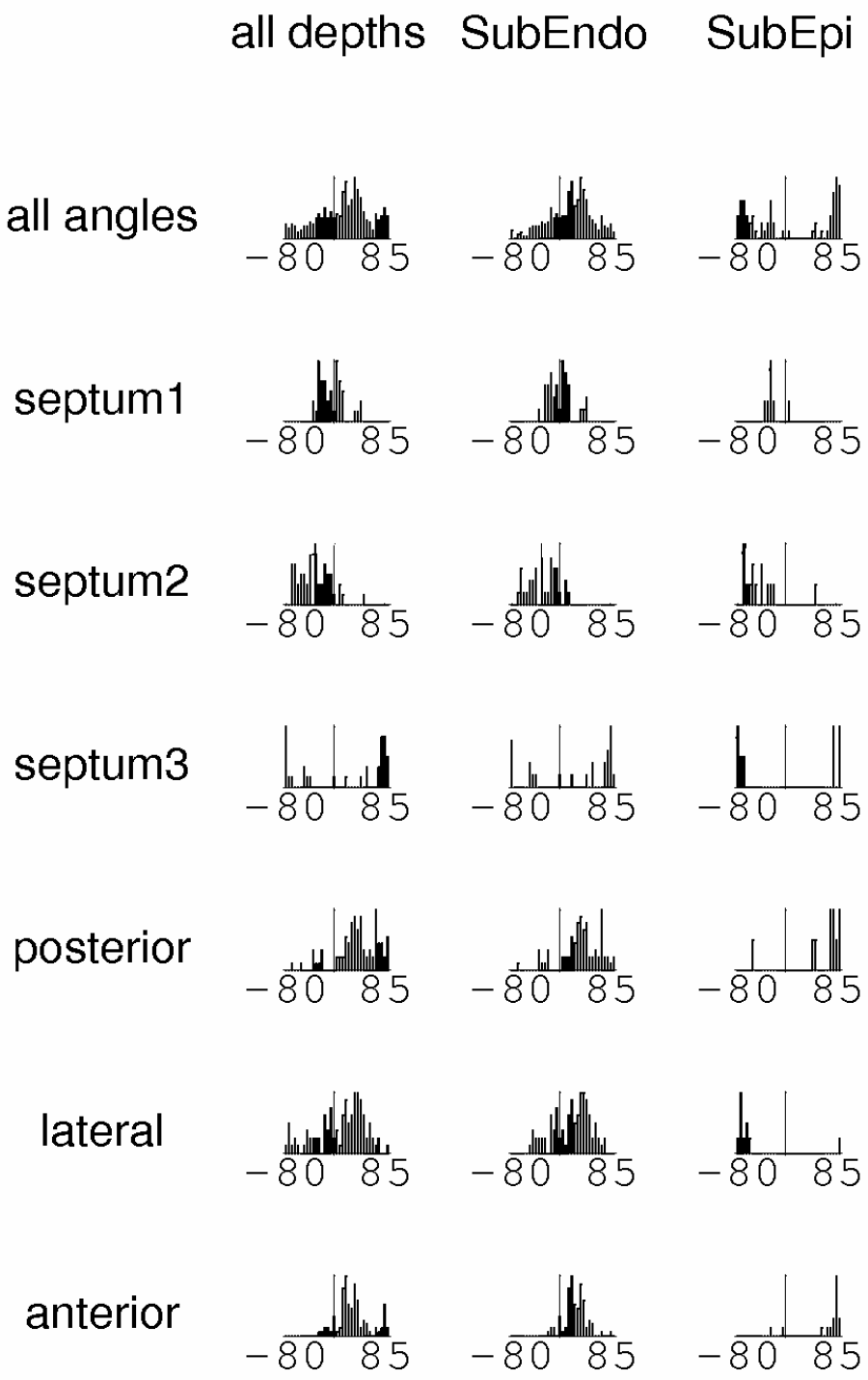

Figure 3.8D Histograms show the distribution of digitized fibres of the human heart with respect to helix angle in apex (Cryer *et al*.)

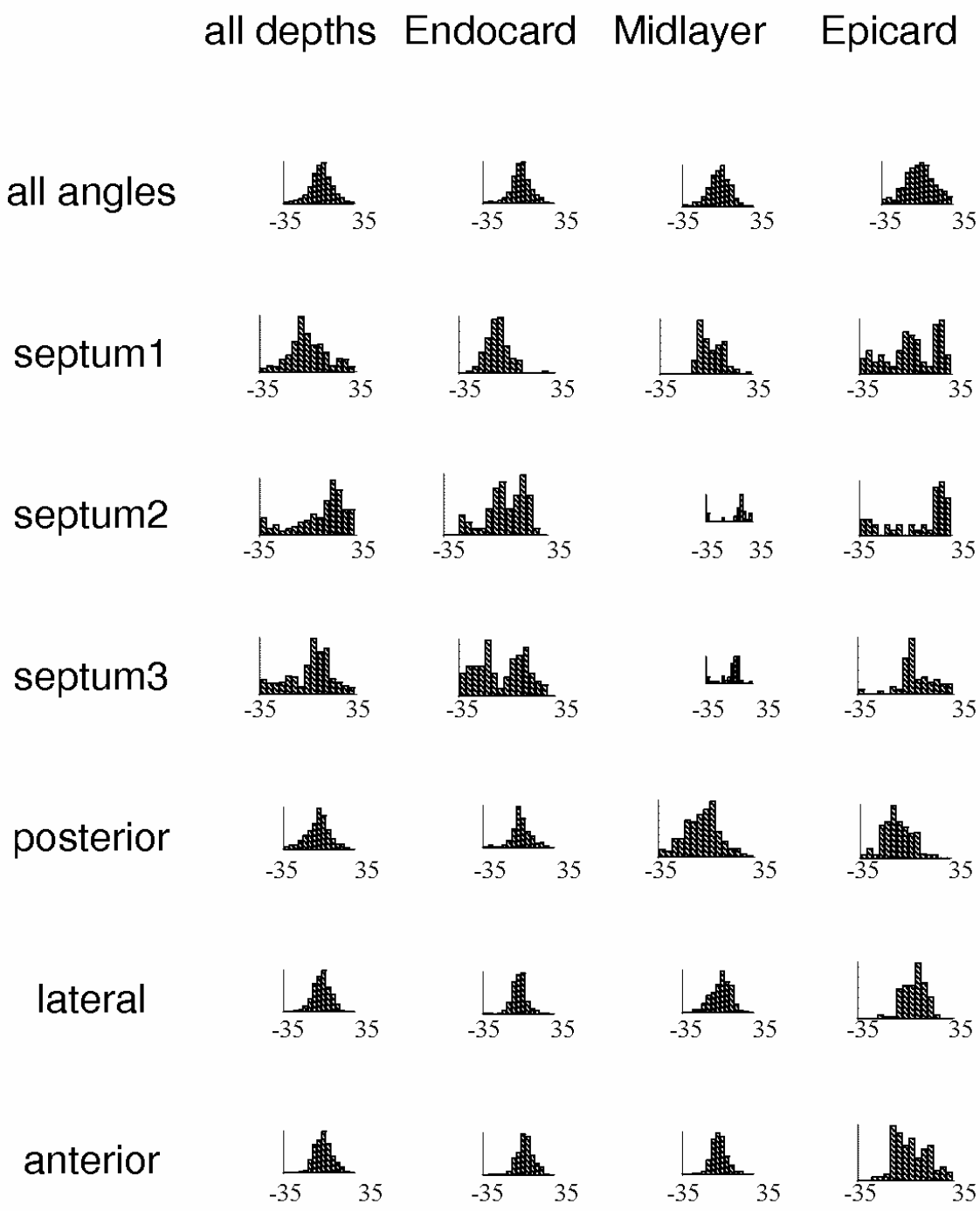

Figure 3.8E Histograms show the distribution of digitized fibres of the human heart with respect to inclination angle in base (Cryer *et al*.)

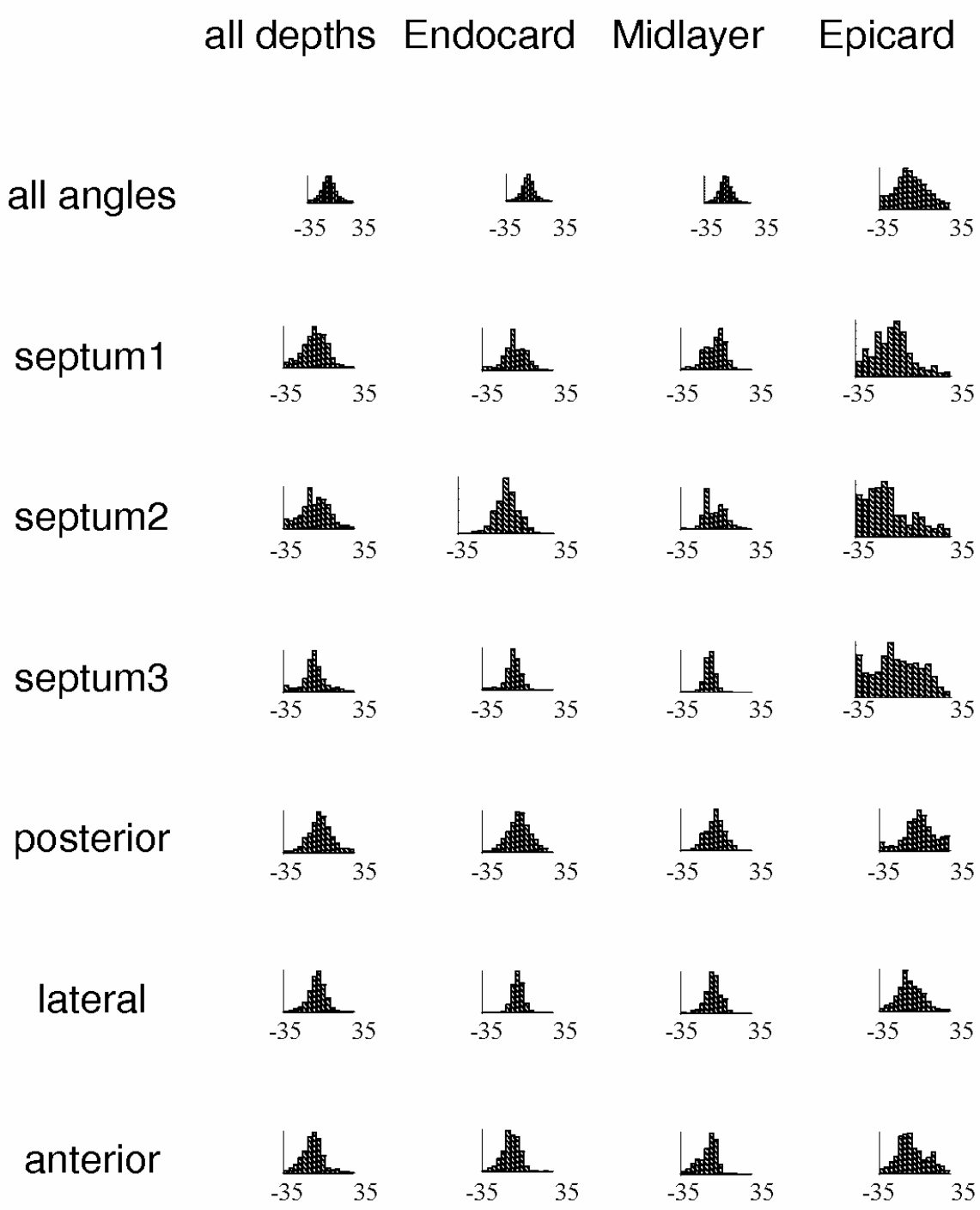

Figure 3.8F Histograms show the distribution of digitized fibres of the human heart with respect to inclination angle in midportion (Cryer *et al*.)

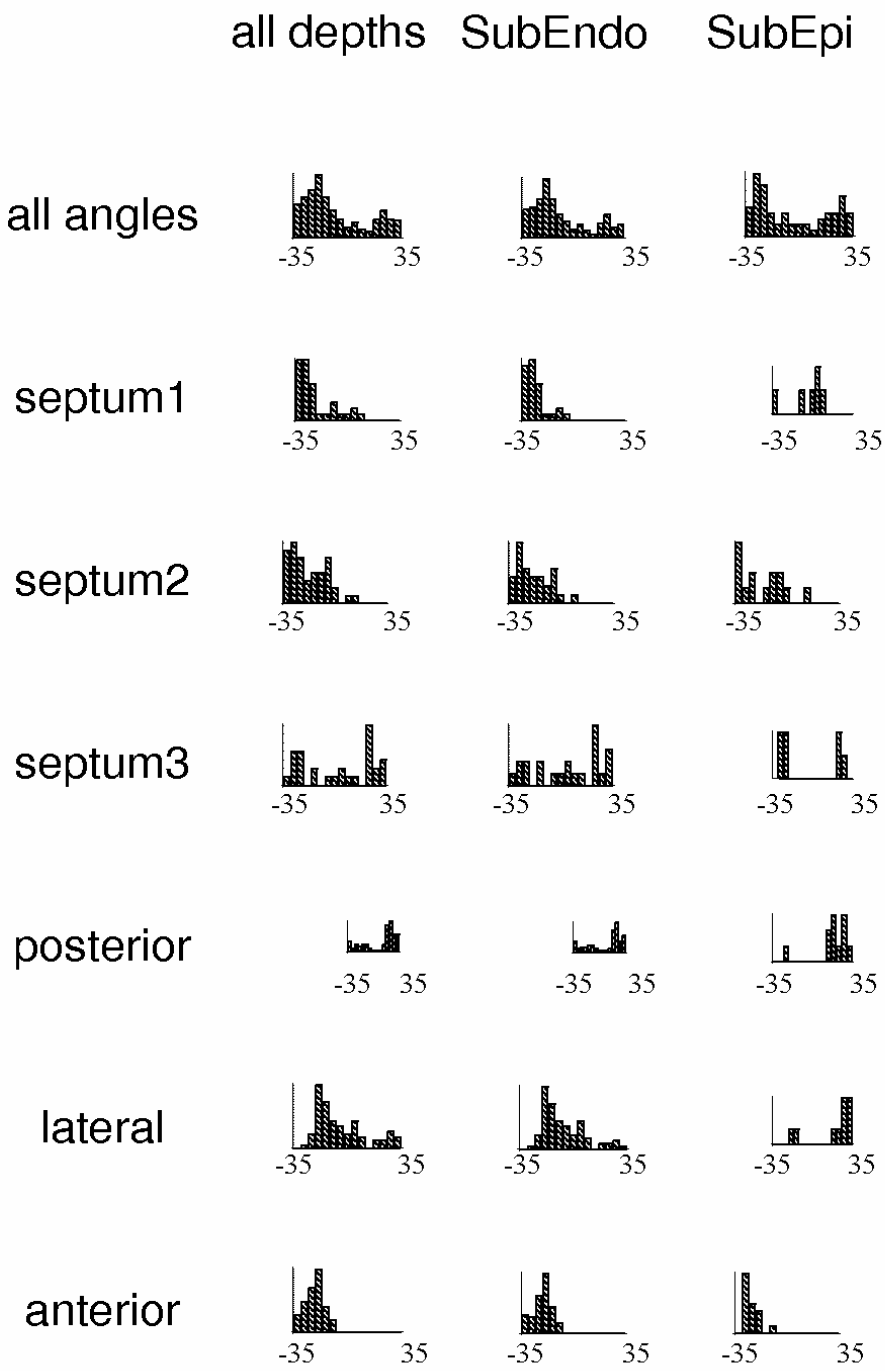

Figure 3.8G Histograms show the distribution of digitized fibres of the human heart with respect to inclination angle in apex (Cryer *et al*.)

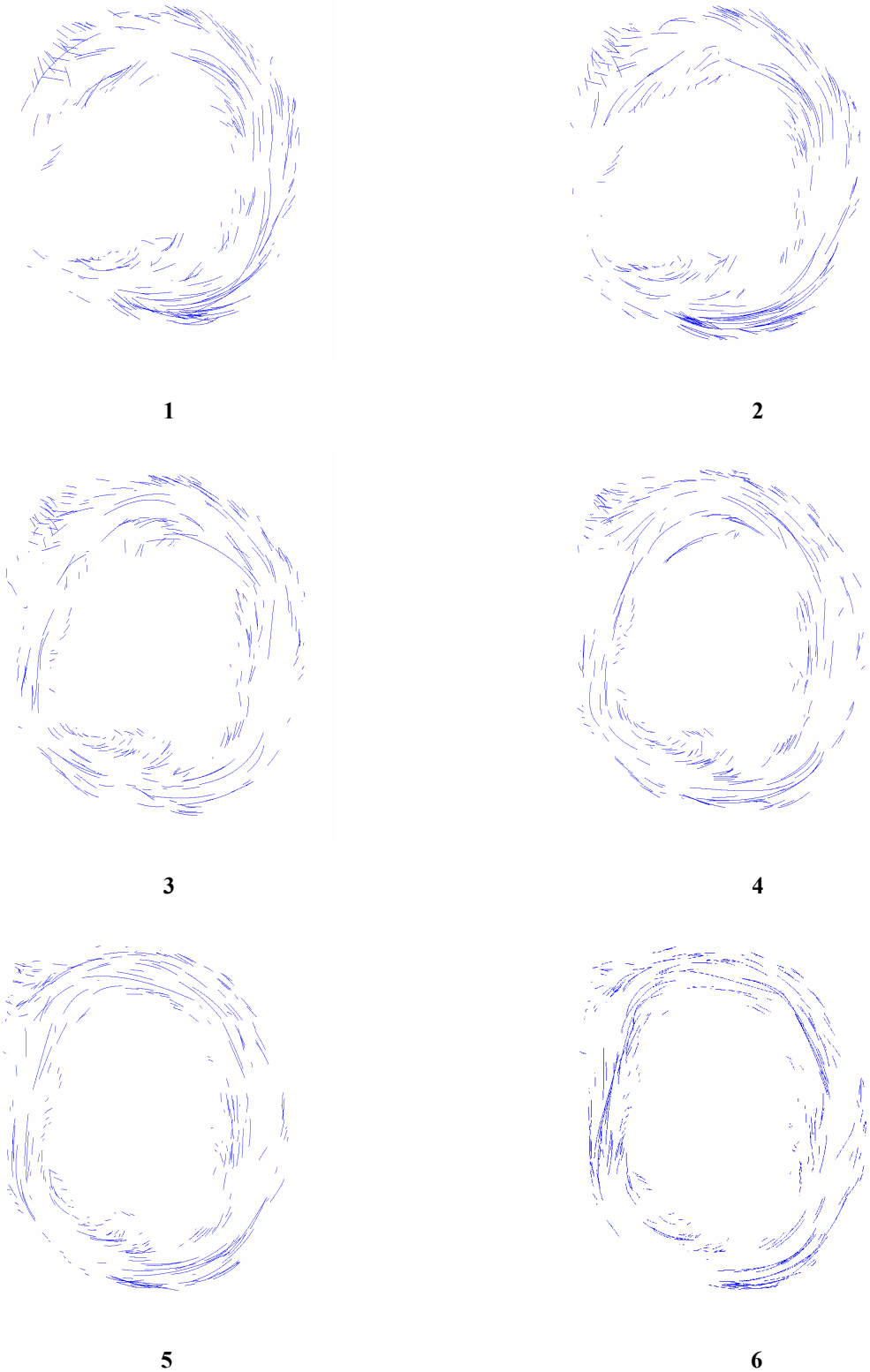

Figure 3.9 2D-represantations of fibres in defined layers (short-axis view)

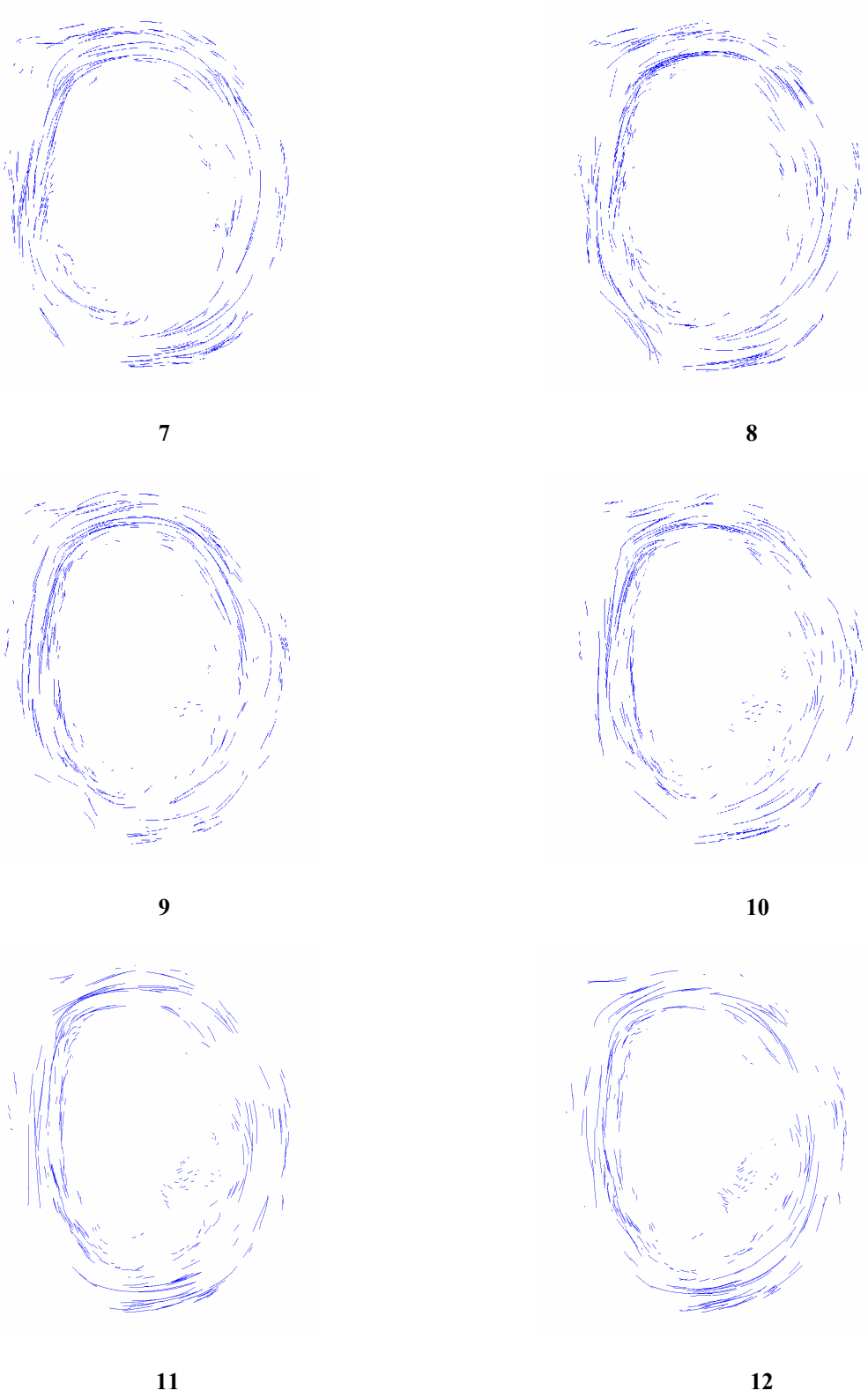

Figure 3.9 2D-represantations of fibres in defined layers (short-axis view)

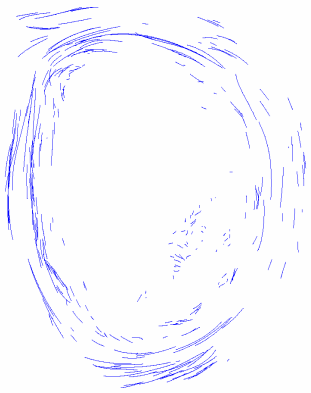

13

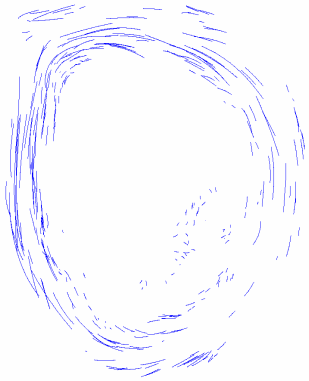

14

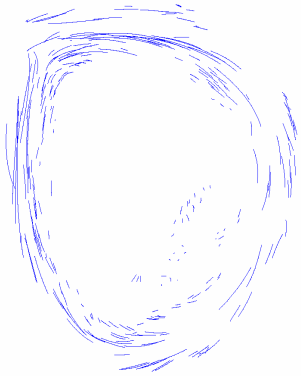

15

16

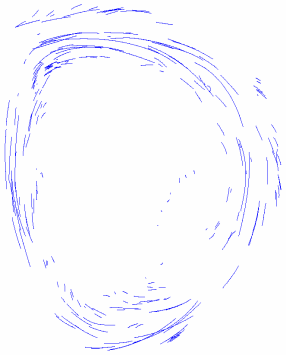

17

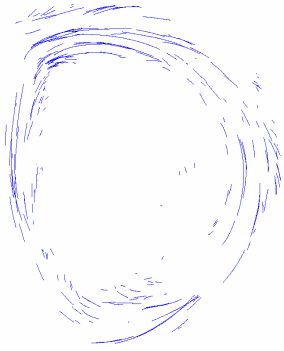

18

Figure 3.9 2D-represantations of fibres in defined layers (short-axis view)

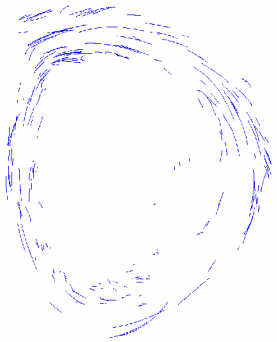

19

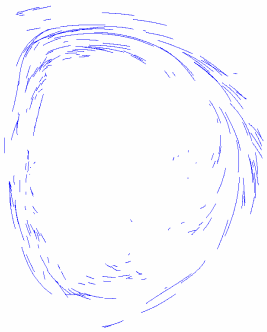

20

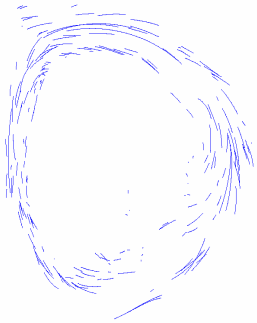

21

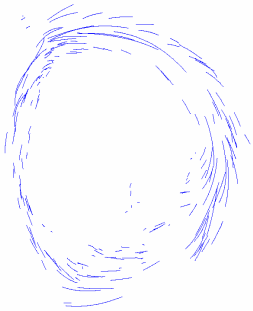

22

23

24

Figure 3.9 2D-represantations of fibres in defined layers (short-axis view)

25

26

27

28

29

30

Figure 3.9 2D-represantations of fibres in defined layers (short-axis view)

References

Basser PJ, Mattiello J, LeBihan D. 1994. MR diffusion tensor spectroscopy and imaging. Biophys J 66(1):259-67.

Boehme W. 1936. Ueber den aktiven Anteil des Herzens an der Förderung des Venenblutes. Ergebn. Physiol. 38:252-338.

Bovendeerd PH, Arts T, Huyghe JM, van Campen DH, Reneman RS. 1992. Dependence of local left ventricular wall mechanics on myocardial fiber orientation: a model study. J Biomech 25(10):1129-40.

Bovendeerd PH, Huyghe JM, Arts T, van Campen DH, Reneman RS. 1994. Influence of endocardial-epicardial crossover of muscle fibers on left ventricular wall mechanics. J Biomech 27(7):941-51.

Brutsaert DL. 1987. Nonuniformity: a physiologic modulator of contraction and relaxation of the normal heart. J. Am. Coll. Cardiol. 9:341-348.

Brutsaert DL, Rademakers F, Sys SU. 1984. Triple control of relaxation: implications in cardiac disease. Circulation 69:190-196.

Brutsaert DL, Sonnenblick EH. 1969. Force-velocity-length-time relations of the contractile elements in heart muscle of the cat. Circ Res 24:137-149.

Cryer CW, Navidi-Kasmai H, Lunkenheimer PP, Redmann K. 1997. Computation of the alignment of myocardial contractile pathways using a magnetic tablet and an optical method. Technology and Health Care 5:79-93.

Hort W. 1957. Untersuchungen über die Muskelfaserdehnung und das Gefüge des Myokards in der rechten Herzkammerwand des Meerschweinchens. Virchows Arch. path. Anat. Physiol. 239:694-731.

Hort W. 1960a. Makroskopische und mikrometrische Untersuchungen am Myokard verschieden stark gefüllter linker Kammern. Virchows Arch. path. Anat. Physiol. 333:569-581.

Hort W. 1960b. Untersuchungen zur funktionellen Morphologie des Bindegewebsgerüstes und der Blutgefässe der linken Herzkammerwand. Virchows Arch. path. Anat. Physiol. 33:565-581.

Hunter PJ, McCulloch AD, Nielsen PMF, Smaill BH. 1988. A finite element model of passive ventricular mechanics. Computational Methods in Bioengineering 9:387-397.

Ingels NB. 1997. Myocardial fiber architecture and left ventricular function. Technology and Health Care 5:45-52.

Laplace PS. 1806. Marquis de Supplément au Livre X du Traité de Méchanique Céleste.

LeGrice IJ, Hunter PJ, Smaill BH. 1997. Laminar structure of the heart: a mathematical model. Am J Physiol 272(5 Pt 2):H2466-76.

LeGrice IJ, Smaill BH, Chai LZ, Edgar SG, Gavin JB, Hunter PJ. 1995. Laminar structure of the heart: ventricular myocyte arrangement and connective tissue architecture in the dog. Am J Physiol 269(2 Pt 2):H571-82.

Lunkenheimer PP, Redmann K, Dietl K-H, Cryer C, Richter K-D, Whimster WF, Niederer P. 1997. The heart's fibre alignment assessed by comparing two digitizing systems. Methodological investigation into the inclination angle toward wall thickness. Technology and Health Care 5:65-77.

Lunkenheimer PP, Redmann K, Florek J, Fassnacht U, Cryer CW, Wübbeling F, Niederer P, Anderson RH. 2004. The forces generated within the musculature of the left ventricular wall. Heart 90:(in press).

Mandarino WA, Pinsky MR, Gorcsan J. 1998. Assessment of left ventricular contractile state by preload-adjusted maximal power using echocardiographic automated border detection. JACC 31(861-868).

Mirsky I. 1969. Left ventricular stresses in the intact human heart. Biophys J 9:189-208.

Mirsky I, Ellison RC, Hugenholtz PG. 1981. Assesment of myocardial contractility in children and young adults from ventricular pressure recordings. Am. J.Cardiol. 27:359-367.

Mirsky I, Krayenbühl HP. 1981. The role of wall stress in the assessment of ventricular function. Herz 6:288-299.

Nielsen PM, Le Grice IJ, Smaill BH, Hunter PJ. 1991. Mathematical model of geometry and fibrous structure of the heart. Am J Physiol 260(4 Pt 2):H1365-78.

Pierpaoli C, Jezzard P, Basser PJ, Barnett A, Di Chiro G. 1996. Diffusion tensor MR imaging of the human brain. Radiology 201(3):637-48.

Rogers DF. 2001. <<An>> introduction to NURBS with historical perspective. San Francisco, Calif.: Morgan Kaufmann Publ. 322 S. p.

Shapiro EP, Rademakers FE. 1997. importance of oblique fiber orientation for left ventricular wall deformation. Technology and Health Care 5:21-28.

Streeter DD, JR. 1983. Gross morphology and fibre geometry in the heart wall. Handbook of Physiology, Section 2: The Cardiovascular System Vol. 1:pp. 61-109.

Stuber M. 1997. Quantification of the human heart wall motion by ultra-fast magnetic resonance myocardial tagging techniques [Ph.D. Thesis]. Zurich: Ph.D. Thesis, Swiss Federal Institute of Technology. ethz-bib 12208 p.

Stuber M, Scheidegger MB, Fischer SE, Nagel E, Steinemann F, Hess OM, Boesiger P. 1999. Alternations in the local myocardial motion pattern in patients suffering from pressure overload due to aortic stenosis. Circulation 100:361-368.

Torrent-Guasp F, Buckberg GD, Clemente C, Cox JL, Coghlan HC, Gharib M. 2001. The structure and function of the helical heart and its buttress wrapping. I. The normal macroscopic structure of the heart. Seminars in Thoracic and Cardiovascular Surgery 13:301-319.

Torrent-Guasp F, Whimster WF, Redmann K. 1997. A silicone rubber mould of the heart. Technology and Health Care 5:13-20.

CHAPTER 4

SELECTED ELEMENTS OF CONTINUUM MECHANICS

Biological materials exhibit an inhomogeneous and complex microscopic structure and are generally composed of various solid and fluid constituents with in part very different mechanical properties. For many applications, however, we do not need to know all the details and mechanical characteristics about the microscopic structure to study the macroscopic behaviour of a biological object.

Continuum mechanics lends itself for a description of the macroscopic behaviour of materials where many details of the internal microscopic structure are at least partly disregarded or substantially simplified. To what extent the inhomogeneities of biological materials have to be taken into account thereby depends on the requirements of the model to be developed.

In this chapter we review some basic features of continuum mechanics which will be needed for our modelling efforts.

4.1 Fundamental concepts

We introduce a rectangular Cartesian coordinate system $(\mathbf{i}, \mathbf{j}, \mathbf{k})$ with the origin O at an arbitrary point in space (Figure 4.1). We denote the reference configuration of the body at the initial time $t = 0$ with R_0 and the configuration of the body at any later time $t \succ 0$

with R_t. In the reference configuration, R_0, every point of the body is identified with a position vector $\mathbf{X}$ in the reference frame $(\mathbf{i},\mathbf{j},\mathbf{k})$. If the body moves or deforms with the time, its configuration changes continuously from R_0 to R_t and the point under consideration is located at the position $\mathbf{x}$ in the reference frame $(\mathbf{i},\mathbf{j},\mathbf{k})$.

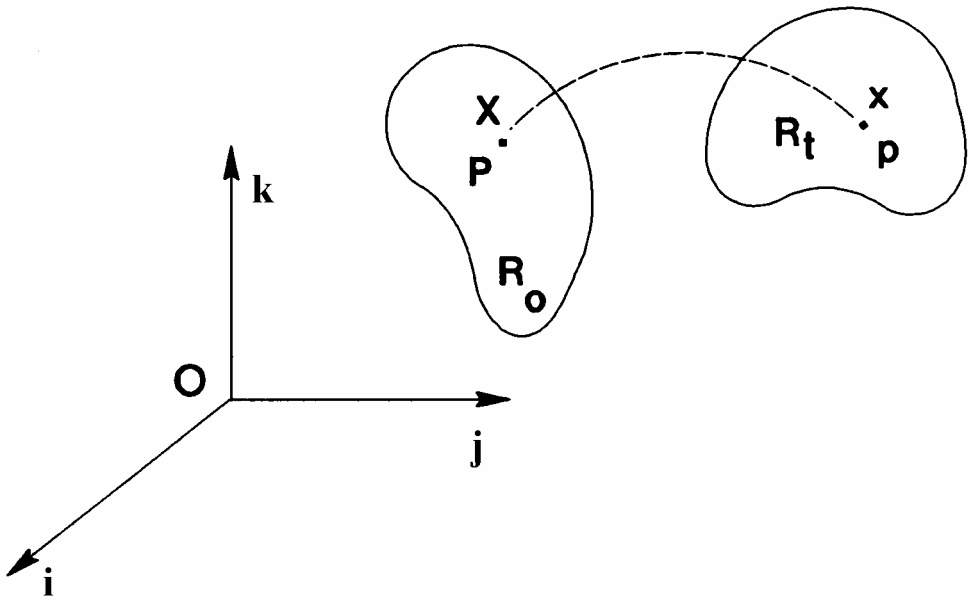

Figure 4.1 Coordinate system (**i**,**j**,**k**)

We assume that there is a one-to-one mapping from the reference configuration R_0 to the deformed configuration R_t so that for every point of the body we can write

$$\mathbf{x} = \mathbf{x}(\mathbf{X}, t) \tag{4.1}$$

Further, we can assume that this mapping is invertible so that

$$\mathbf{X} = \mathbf{X}(\mathbf{x}, t) \tag{4.2}$$

because for physically realistic problems the Jacobian of the transformation

$$J = \det\left(\frac{\partial x_i}{\partial X_j}\right) \tag{4.3}$$

must never be zero for $t \succ 0$.

The displacement for the point under consideration is defined as

$$\mathbf{u} = \mathbf{x} - \mathbf{X} \tag{4.4}$$

Note that displacement **u** can be written in both configurations R_0 and R_t, but **u** has always the same value in R_0 and R_t.

From (4.1) we can define the deformation gradient tensor as

$$d\mathbf{x} = \mathbf{F}d\mathbf{X} \tag{4.5}$$

or with respect to the components

$$F_{ij} = \frac{\partial x_i}{\partial X_j} \tag{4.6}$$

From (4.3) it is clear that

$$J = \det \mathbf{F} \tag{4.7}$$

and from (4.5), for the inverse of the deformation gradient tensor, we can write

$$\mathbf{G}d\mathbf{x} = d\mathbf{X} \tag{4.8}$$

$$\mathbf{G} = \mathbf{F}^{-1} \tag{4.9}$$

Now, we can derive the relation between displacement and deformation gradient tensor as follows

$$\mathbf{x} = \mathbf{u} + \mathbf{X} \tag{4.10}$$

$$d\mathbf{x} = d\mathbf{u} + d\mathbf{X} \tag{4.11}$$

$$\mathbf{F} = \text{grad}\mathbf{u} + \mathbf{I} \tag{4.12}$$

or

$$F_{ij} = \frac{\partial u_i}{\partial X_j} + \delta_{ij} \tag{4.13}$$

The deformation gradient tensor is important because it characterizes the state of motion and deformation in the neighbourhood of any point of the body.

Equation (4.5) shows the transformation of any infinitesimal line element in the neighbourhood associated with an arbitrary point of the body. It is interesting to know how volume elements or surface elements transform during deformation. Let dV be an infinitesimal volume element in the reference configuration R_0. Due to deformation this

element will have the volume dv in deformed configuration R_t. It is easy to prove that (Holzapfel 2000)

$$dv = JdV \tag{4.14}$$

and with the use of

$$dv = d\mathbf{s} \cdot d\mathbf{x} = Jd\mathbf{S} \cdot d\mathbf{X} \tag{4.15}$$

$$d\mathbf{s} \cdot \mathbf{F}d\mathbf{X} = \mathbf{F}^T d\mathbf{s} \cdot d\mathbf{X} \tag{4.16}$$

and (4.5) we can derive the relation between the surface elements in R_0 and R_t

$$d\mathbf{s} = J\mathbf{F}^{-T} d\mathbf{S} \tag{4.17}$$

or

$$d\mathbf{s} = J\mathbf{G}^T d\mathbf{S} \tag{4.18}$$

We define the right Cauchy-Green tensor as

$$\mathbf{C} = \mathbf{F}^T \mathbf{F} \tag{4.19}$$

and the left Cauchy-Green tensor

$$\mathbf{B} = \mathbf{F}\mathbf{F}^T \tag{4.20}$$

respectively.

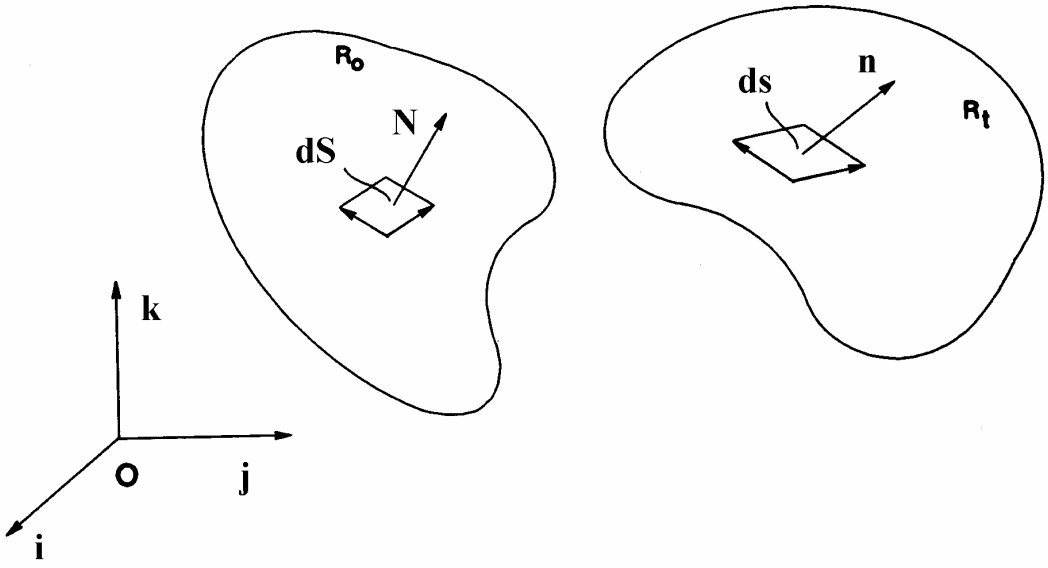

Figure 4.2 Deformation of a surface element

Now we introduce a unit vector $\mathbf{N}$ which has an arbitrary direction in configuration R_0. $\mathbf{n}'$ is the corresponding vector of $\mathbf{N}$ in R_t. From (4.5) it is seen that $\mathbf{N}$ will deform to $\mathbf{n}'$ according to

$$\mathbf{n}' = \mathbf{F}\mathbf{N} \tag{4.21}$$

The stretch ratio λ corresponds to the length of $\mathbf{n}'$

$$\lambda = \sqrt{\mathbf{F}\mathbf{N} \cdot \mathbf{F}\mathbf{N}} \tag{4.22}$$

or

$$\lambda = \sqrt{\mathbf{N} \cdot \mathbf{F}^T\mathbf{F} \cdot \mathbf{N}} \tag{4.23}$$

and from (4.19) we can write

$$\lambda = \sqrt{\mathbf{N} \cdot \mathbf{C} \cdot \mathbf{N}} \tag{4.24}$$

From definition of the unit vector we have, in turn,

$$\mathbf{n} = \frac{\mathbf{n}'}{\lambda} = \frac{\mathbf{F}\mathbf{N}}{\lambda} \tag{4.25}$$

This is an important relation and shows how a unit vector $\mathbf{N}$ in R_0 transforms to the unit vector $\mathbf{n}$ in R_t (Figure 4.2).

A further useful tensor is the Green-Lagrange strain tensor which is defined as

$$\mathbf{E} = \frac{1}{2}\left(\mathbf{C} - \mathbf{I}\right) \tag{4.26}$$

Since $\mathbf{F}$ is nonsingular, it can be decomposed into a pure stretch tensor $\mathbf{U}$ and a pure rotation tensor $\mathbf{R}$

$$\mathbf{F} = \mathbf{R}\mathbf{U} \tag{4.27}$$

so that

$$\begin{aligned} \mathbf{R}^T\mathbf{R} &= \mathbf{I} \\ \mathbf{U} &= \mathbf{U}^T \end{aligned} \tag{4.28}$$

implying that

$$\mathbf{U}^2 = \mathbf{U}\mathbf{U} = \mathbf{C} \tag{4.29}$$

$\mathbf{U}$ and $\mathbf{C}$ are symmetric and positive definite. From (4.26) we see furthermore that the Green-Lagrange strain tensor depends only on the stretch tensor $\mathbf{U}$ and that it is

independent of the rotation tensor **R**, or, in other words, independent of the rotation of the body during deformation.

Next, we review the concept of stress. Let the body under consideration be cut hypothetically by a plane surface. We look at an infinitesimal surface element $d\mathbf{s}$ of this hypothetical plane in an arbitrary point **x** in the body in deformed configuration R_t. If $d\mathbf{f}$ denotes the infinitesimal force acting on surface element $d\mathbf{s}$, the Cauchy stress or true stress $\sigma(\mathbf{x},t)$ can be determined by definition from the following relation

$$d\mathbf{f} = \sigma(\mathbf{x},t)\, d\mathbf{s} \tag{4.30}$$

In the reference configuration R_0 we introduce the first Piola-Kirchhof stress tensor $\mathbf{P}(\mathbf{X},t)$ by writing

$$d\mathbf{f} = \mathbf{P}(\mathbf{X},t)\, d\mathbf{S} \tag{4.31}$$

From (4.30) , (4.31) and (4.17) we can derive the relation between the Cauchy stress tensor and first Piola-Kirchhoff stress tensor as

$$\sigma(\mathbf{x},t)\, d\mathbf{s} = \mathbf{P}(\mathbf{X},t)\, d\mathbf{S} \tag{4.32}$$

$$\sigma = J^{-1}\mathbf{P}\mathbf{F}^T \tag{4.33}$$

$$\mathbf{P} = J\sigma\mathbf{F}^{-T} \tag{4.34}$$

The second Piola-Kirchhoff stress tensor **S** can be found from the first Piola-Kirchhoff stress tensor as follows

$$\mathbf{P} = \mathbf{F}\mathbf{S} \tag{4.35}$$

This implies that

$$\sigma = J^{-1}\mathbf{F}\mathbf{S}\mathbf{F}^T \tag{4.36}$$

$$\mathbf{S} = J\mathbf{F}^{-1}\sigma\mathbf{F}^{-T} \tag{4.37}$$

σ and **S** are both symmetric, but **S**, as opposed to σ, does not admit a straightforward physical interpretation.

4.2 Elastic and hyperelastic materials

In this paragraph we consider only deformations of a special, but very important class of materials. We thereby assume that the temperature remains constant, i.e., all processes are isothermal as is by and large the case in biological systems. A material is called elastic if the stress at time *t* depends only on the state of deformation at this instant of time and not on the deformation history, in other words, the stress tensor σ is completely determined by the instantaneous value of the deformation gradient tensor **F** at any point of the body and at any time *t* and is not affected by the previous values of **F** (Ogden 1984).

A constitutive equation describes the mechanical behaviour of a material in terms of stress and strain (in case of non elastic materials, there may be other quantities of importance such as the strain rate). The equation defines the state of stress at any point of the body and at any time *t* as a function of the deformation. For elastic materials, the general form of the constitutive equation can be expressed as

$$\sigma(\mathbf{x},t) = \mathbf{g}(\mathbf{F}) \tag{4.38}$$

Although we confine ourselves here to homogeneous materials only, the stress tensor σ depends explicitly on the coordinates **X**, and the constitutive equation may vary from point to point within the body thereby including the possibility of spatial inhomogeneity. Axiomatically we accept that physical processes are independent of the observer, which implies that the mathematical representation of all processes of interest must be written in an invariant formulation under transformation of the reference frame.

It can be easily proven (Truesdell and Noll 1992) that the necessary and sufficient condition for the invariance of (4.38) is that stress tensor σ takes the following form

$$\sigma = \mathbf{F}\mathbf{f}(\mathbf{C})\mathbf{F}^T \tag{4.39}$$

or, from (4.37), the second Piola-Kirchhoff stress tensor

$$\mathbf{S} = J\mathbf{f}(\mathbf{C}) \tag{4.40}$$

E.g., for an isotropic material, which is a material whose mechanical properties do not exhibit any preferred direction, $\mathbf{f}(\mathbf{C})$ is often expanded in a power series

$$\mathbf{f}(\mathbf{C}) = a_0\mathbf{I} + a_1\mathbf{C} + a_2\mathbf{C}^2 + \cdots + a_N\mathbf{C}^N \tag{4.41}$$

and the stress tensor σ takes the following form

$$\sigma = \alpha_0\mathbf{I} + \alpha_1\mathbf{B} + \alpha_2\mathbf{B}^2 \tag{4.42}$$

where $\alpha_0, \alpha_1, \alpha_2$ are functions of invariants of **B**.

σ can also be expressed in an alternative form as

$$\sigma = \beta_0\mathbf{I} + \beta_1\mathbf{B} + \beta_{-1}\mathbf{B}^{-1} \tag{4.43}$$

where again $\beta_0, \beta_1, \beta_{-1}$ are functions of invariants of **B**.

If the material is incompressible, we find from (4.14) that $J = 1$. Accordingly, the relations (4.38), (4.39) and (4.40) must be corrected to

$$\sigma = -p\mathbf{I} + \mathbf{g}(\mathbf{F}) \tag{4.44}$$

$$\sigma = -p\mathbf{I} + \mathbf{F}\mathbf{f}(\mathbf{C})\mathbf{F}^T \tag{4.45}$$

$$\mathbf{S} = -p\mathbf{C}^{-1} + \mathbf{f}(\mathbf{C}) \tag{4.46}$$

where p is an undetermined scalar called the hydrostatic pressure (Eringen 1962; Eringen 1980). It can be found from equilibrium and boundary conditions. The relation (4.42) for an isotropic and incompressible material then reads

$$\sigma = -p\mathbf{I} + \alpha_1\mathbf{B} + \alpha_2\mathbf{B}^2 \tag{4.47}$$

or

$$\sigma = -p\mathbf{I} + \beta_1\mathbf{B} + \beta_{-1}\mathbf{B}^{-1} \tag{4.48}$$

In order to proceed, we assume that there exists a function $W(\mathbf{F})$, known as strain–energy function that is a single-valued function of the deformation gradient tensor **F** at any point of the body and any time**,** which is independent of the rate of deformation or its history. $W(\mathbf{F})$ is the internal mechanical energy due to deformation that is stored in the body. It is measured per unit reference volume.

Hyperelastic materials represent a subclass of elastic materials which are defined such that the first Piola-Kirchhoff stress tensor can be derived from the strain-energy function $W(\mathbf{F})$ as

$$\mathbf{P} = \frac{\partial W(\mathbf{F})}{\partial \mathbf{F}} \tag{4.49}$$

or from (4.33) the Cauchy stress tensor as

$$\sigma = J^{-1} \frac{\partial W(\mathbf{F})}{\partial \mathbf{F}} \mathbf{F}^T \tag{4.50}$$

From the invariance of W with respect to arbitrary rigid motions it can be proven (Green and Adkins 1970) that W is a function of the right Cauchy-Green tensor **C**

$$W(\mathbf{F}) = W\left(\mathbf{C}^{\frac{1}{2}}\right) \tag{4.51}$$

Furthermore, from (4.26), it can be written as a function of the Green-Lagrange strain tensor, **E.** In order to avoid the introduction of other symbols, we denote these functions of C and E by $W(\mathbf{C})$ and $W(\mathbf{E})$. Then $\mathbf{P}, \sigma$ and **S** can be written as follows

$$\mathbf{P} = 2\mathbf{F} \frac{\partial W(\mathbf{C})}{\partial \mathbf{C}} \tag{4.52}$$

$$\sigma = 2J^{-1}\mathbf{F} \frac{\partial W(\mathbf{C})}{\partial \mathbf{C}} \mathbf{F}^T \tag{4.53}$$

$$\mathbf{S} = 2\frac{\partial W(\mathbf{C})}{\partial \mathbf{C}} = \frac{\partial W(\mathbf{E})}{\partial \mathbf{E}} \tag{4.54}$$

Due to the simple form of (4.54), in many cases it is easier to work with second Piola-Kirchhof stress tensor **S**.

For an isotropic material $W(\mathbf{C})$ must be invariant under arbitrary rotational motions **Q,** from which follows

$$W(\mathbf{C}) = W\left(\mathbf{Q}\mathbf{C}\mathbf{Q}^T\right) \tag{4.55}$$

If we choose **Q** such that $\mathbf{Q}\mathbf{C}\mathbf{Q}^T$ is diagonal (which is always possible), we conclude that W must be a function of the invariants of **C**. Denoting them by $I_1(\mathbf{C}), I_2(\mathbf{C}), I_3(\mathbf{C})$ we have

$$W = W\left(I_1(\mathbf{C}), I_2(\mathbf{C}), I_3(\mathbf{C})\right) \tag{4.56}$$

$$I_1(\mathbf{C}) = \mathrm{tr}\mathbf{C} \tag{4.57}$$

$$I_2(\mathbf{C}) = \frac{1}{2}\left[\left(\mathrm{tr}\mathbf{C}\right)^2 - \mathrm{tr}\mathbf{C}^2\right] \tag{4.58}$$

$$I_3(\mathbf{C}) = \det\mathbf{C} = J^2 \tag{4.59}$$

and for the second Piola-Kirchhoff stress tensor follows

$$\mathbf{S} = 2\sum_{i=1}^{3} \frac{\partial W(\mathbf{C})}{\partial I_i}\frac{\partial I_i}{\partial \mathbf{C}} \tag{4.60}$$

$$W_i = \frac{\partial W(\mathbf{C})}{\partial I_i} \tag{4.61}$$

$$\frac{\partial I_1}{\partial \mathbf{C}} = \mathbf{I} \tag{4.62}$$

$$\frac{\partial I_2}{\partial \mathbf{C}} = I_1\mathbf{I} - \mathbf{C} \tag{4.63}$$

$$\frac{\partial I_3}{\partial \mathbf{C}} = I_3\mathbf{C}^{-1}. \tag{4.64}$$

Accordingly, we can write

$$\mathbf{S} = 2\left[\left(W_1 + I_1W_2\right)\mathbf{I} - W_2\mathbf{C} + I_3W_3\mathbf{C}^{-1}\right] \tag{4.65}$$

With (4.65) we furthermore deduce from (4.36) for the Cauchy stress tensor

$$\sigma = 2J^{-1}\left[\left(I_2W_2 + I_3W_3\right)\mathbf{I} + W_1\mathbf{B} - I_3W_2\mathbf{B}^{-1}\right] \tag{4.66}$$

Considering the concept of strain energy function W we see that we arrive at the same relation as (4.43).

For an isotropic incompressible material the relation $J = \sqrt{I_3} = 1$ holds. This condition can be treated as an internal constraint for the material. Upon introducing an indeterminate Lagrange multiplier, p, corresponding to the hydrostatic pressure, and writing the strain-energy function as

$$W = W\left(I_1(\mathbf{C}), I_2(\mathbf{C})\right) - \frac{1}{2}p\left(I_3 - 1\right) \tag{4.67}$$

$\mathbf{S}$ and σ obtain the following forms

$$\mathbf{S} = -p\mathbf{C}^{-1} + 2\frac{\partial W(\mathbf{C})}{\partial \mathbf{C}} \tag{4.68}$$

$$\sigma = -p\mathbf{I} + 2\mathbf{F}\frac{\partial W(\mathbf{C})}{\partial \mathbf{C}}\mathbf{F}^T \tag{4.69}$$

Finally, with the use of equations (4.60) to (4.64), we can write

$$\mathbf{S} = -p\mathbf{C}^{-1} + 2\left(W_1 + I_1 W_2\right)\mathbf{I} - 2W_2\mathbf{C} \tag{4.70}$$

$$\sigma = -p\mathbf{I} + 2\left(W_1 + I_1 W_2\right)\mathbf{B} - 2W_2\mathbf{B}^2 \tag{4.71}$$

or alternatively

$$\sigma = -p\mathbf{I} + 2W_1\mathbf{B} - 2W_2\mathbf{B}^{-1} \tag{4.72}$$

The scalars p in (4.71) and (4.72) differ by the term $2I_1W_2$.

4.3 Transversely isotropic two-phase materials

Next we consider a class of materials that are composed of two phases, *viz.*, a matrix material or ground substance and a family of continuously and systematically arranged fibres in the matrix. Such materials exhibit a preferred direction or axis and we expect that their material properties depend on this direction. If the response of the material along directions which are orthogonal to this preferred axis is isotropic, we say that the material is transversely isotropic (Figure 4.3).

In case that the material is moreover hyperelastic there exists a strain-energy function which not only depends on **C** but also on the preferred direction, **N**. Whenever the material undergoes deformation, the vector **N** will deform with the body. From (4.25) we can write for the new direction **n**

$$\lambda\mathbf{n} = \mathbf{F}\mathbf{N} \tag{4.73}$$

$$\lambda^2 = \mathbf{N}\cdot\mathbf{C}\cdot\mathbf{N} \tag{4.74}$$

It can be proven (Spencer 1984) that under these conditions the strain energy function must be of the form

$$W = W\left(\mathbf{C}, \mathbf{N}\otimes\mathbf{N}\right) \tag{4.75}$$

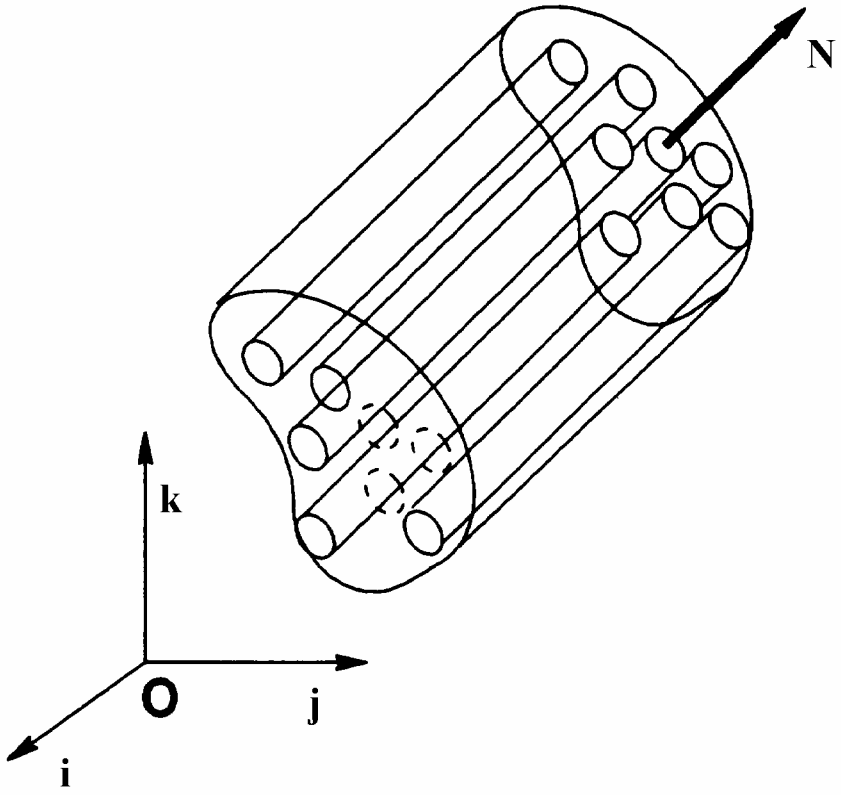

Figure 4.3 Transversely isotropic material

Similar to (4.56), it must be a function of the invariants $I_1(\mathbf{C}), I_2(\mathbf{C}), I_3(\mathbf{C}), I_4(\mathbf{C},\mathbf{N})$ and $I_5(\mathbf{C},\mathbf{N})$ as follows

$$W = W\left[I_1(\mathbf{C}), I_2(\mathbf{C}), I_3(\mathbf{C}), I_4(\mathbf{C},\mathbf{N}), I_5(\mathbf{C},\mathbf{N})\right] \tag{4.76}$$

where $I_1(\mathbf{C}), I_2(\mathbf{C})$ and $I_3(\mathbf{C})$ are given by (4.57), (4.58) and (4.59). $I_4(\mathbf{C},\mathbf{N})$ and $I_5(\mathbf{C},\mathbf{N})$ are defined by

$$I_4(\mathbf{C},\mathbf{N}) = \mathbf{N}\cdot\mathbf{C}\cdot\mathbf{N} \tag{4.77}$$

$$I_5(\mathbf{C},\mathbf{N}) = \mathbf{N}\cdot\mathbf{C}^2\cdot\mathbf{N} \tag{4.78}$$

while the second Piola-Kirchhof stress tensor is defined by

$$\mathbf{S} = 2\frac{\partial W\left(\mathbf{C}, \mathbf{N}\otimes\mathbf{N}\right)}{\partial \mathbf{C}} \tag{4.79}$$

or

$$\mathbf{S} = 2\sum_{i=1}^{5}\frac{\partial W\left(\mathbf{C}, \mathbf{N}\otimes\mathbf{N}\right)}{\partial I_i}\frac{\partial I_i}{\partial \mathbf{C}} \tag{4.80}$$

$\frac{\partial I_1}{\partial \mathbf{C}}$, $\frac{\partial I_2}{\partial \mathbf{C}}$ and $\frac{\partial I_3}{\partial \mathbf{C}}$ are given by (4.62), (4.63) and (4.64), respectively. $\frac{\partial I_4}{\partial \mathbf{C}}$, $\frac{\partial I_5}{\partial \mathbf{C}}$, in turn, and are defined by

$$\frac{\partial I_4}{\partial \mathbf{C}} = \mathbf{N}\otimes\mathbf{N} \tag{4.81}$$

$$\frac{\partial I_5}{\partial \mathbf{C}} = \mathbf{N}\otimes\mathbf{C}\mathbf{N} + \mathbf{N}\mathbf{C}\otimes\mathbf{N} \tag{4.82}$$

Analogous to (4.65) and (4.66), the constitutive equations of an transversely isotropic material can be written. For S we have accordingly

$$\begin{aligned}\mathbf{S} = {} & 2\left[\left(W_1 + I_1 W_2\right)\mathbf{I} - W_2\mathbf{C} + I_3 W_3\mathbf{C}^{-1}\right] \\ & + 2\left[W_4\mathbf{N}\otimes\mathbf{N} + W_5\left(\mathbf{N}\otimes\mathbf{C}\mathbf{N} + \mathbf{N}\mathbf{C}\otimes\mathbf{N}\right)\right]\end{aligned} \tag{4.83}$$

and with the definition $\mathbf{n} = \frac{\mathbf{F}\mathbf{N}}{\lambda}$ follows

$$\sigma = 2J^{-1}\mathbf{F}\frac{\partial W\left(\mathbf{C}, \mathbf{N}\otimes\mathbf{N}\right)}{\partial \mathbf{C}}\mathbf{F}^{T} \tag{4.84}$$

$$\begin{aligned}\sigma = {} & 2J^{-1}\left[I_3 W_3\mathbf{I} + \left(W_1 + I_1 W_2\right)\mathbf{B} - W_2\mathbf{B}^2\right] \\ & + 2J^{-1}\left[I_4 W_4\mathbf{n}\otimes\mathbf{n} + I_4 W_5\left(\mathbf{n}\otimes\mathbf{B}\mathbf{n} + \mathbf{n}\mathbf{B}\otimes\mathbf{n}\right)\right]\end{aligned} \tag{4.85}$$

For a transversely isotropic material with an incompressible matrix, we postulate for W an expression of the form

$$W = W\left[I_1\left(\mathbf{C}\right), I_2\left(\mathbf{C}\right), I_4\left(\mathbf{C}, \mathbf{N}\right), I_5\left(\mathbf{C}, \mathbf{N}\right)\right] - \frac{1}{2}p\left(I_3 - 1\right) \tag{4.86}$$

where p is again the hydrostatic pressure. From this formulation one obtains for $\mathbf{S}$ and σ

$$\mathbf{S} = -p\mathbf{C}^{-1} + 2\frac{\partial W\left(\mathbf{C}, \mathbf{N}\otimes\mathbf{N}\right)}{\partial \mathbf{C}} \tag{4.87}$$

$$\sigma = -p\mathbf{I} + 2\mathbf{F}\frac{\partial W\left(\mathbf{C}, \mathbf{N}\otimes\mathbf{N}\right)}{\partial \mathbf{C}}\mathbf{F}^{T} \tag{4.88}$$

Furthermore, it follows

$$\begin{aligned}\mathbf{S} = &-p\mathbf{C}^{-1} + 2\left(W_1 + I_1 W_2\right)\mathbf{I} - 2W_2\mathbf{C} \\ &+ 2\left[W_4\mathbf{N}\otimes\mathbf{N} + W_5\left(\mathbf{N}\otimes\mathbf{C}\mathbf{N} + \mathbf{N}\mathbf{C}\otimes\mathbf{N}\right)\right]\end{aligned} \tag{4.89}$$

$$\begin{aligned}\sigma = &-p\mathbf{I} + 2\left(W_1 + I_1 W_2\right)\mathbf{B} - 2W_2\mathbf{B}^{2} \\ &+ 2\left[I_4 W_4\mathbf{n}\otimes\mathbf{n} + I_4 W_5\left(\mathbf{n}\otimes\mathbf{B}\mathbf{n} + \mathbf{n}\mathbf{B}\otimes\mathbf{n}\right)\right]\end{aligned} \tag{4.90}$$

Finally, the alternative form for σ is

$$\begin{aligned}\sigma = &-p\mathbf{I} + 2W_1\mathbf{B} - 2W_2\mathbf{B}^{-1} \\ &+ 2\left[I_4 W_4\mathbf{n}\otimes\mathbf{n} + I_4 W_5\left(\mathbf{n}\otimes\mathbf{B}\mathbf{n} + \mathbf{n}\mathbf{B}\otimes\mathbf{n}\right)\right]\end{aligned} \tag{4.91}$$

Again, the scalars *p* in (4.90) and (4.91) differ by the term $2I_1 W_2$.

In order to arrive at a useful description for biological materials, these general formulations have to be adapted accordingly. A number of approaches have been proposed in the literature to this end. In the next chapter we will first discuss some of the constitutive equations which have been developed during the last twenty years to describe the properties of the fibrous structure of the heart tissue. In our model we will then substantiate that transversely isotropic constitutive equations are essential for a realistic description of the mechanics of the myocardium.

References

Eringen AC. 1962. Nonlinear theory of continuous media. New York: McGraw-Hill. 477 p.

Eringen AC. 1980. Mechanics of continua. Huntington, N.Y.: R. E. Krieger Pub. Co. xv, 592 p.

Green AE, Adkins JE. 1970. Large elastic deformations. Oxford,: Clarendon Press. xiv, 324 illus. p.

Holzapfel GA. 2000. Nonlinear solid mechanics : a continuum approach for engineering. Chichester ; New York: Wiley. 455 p.

Ogden RW. 1984. Non-linear elastic deformations. Chichester
New York: E. Horwood ;Halsted Press. xiv, 532 p.

Spencer AJM. 1984. Continuum theory of the mechanics of fibre-reinforced composites. Wien: Springer. viii, 284 -- p.

Truesdell C, Noll W. 1992. The non-linear field theories of mechanics. Berlin ; New York: Springer-Verlag. x, 591 p.

CHAPTER 5

CONSTITUTIVE MODELS FOR MYOCARDIUM

Biological materials are heterogeneous, of a multiphase nature and exhibit viscoelastic behaviour. Myocardial tissue is furthermore anisotropic and nearly incompressible. Anisotropy, which is due to the fibrous structure of the tissue, causes directional dependency of the material behaviour to the applied loads. It is particularly important for any useful constitutive equation describing myocardial tissue that the dependency of the behaviour on the direction along with local variations thereof be included in the analysis. The simplest anisotropic material, called transversely isotropic material, has a single preferred direction or axis of symmetry. This type of anisotropy can be described by a vector field so that in each point of the material a vector shows the preferred direction.

A further important property is due to viscoelasticity in that the load-elongation and relaxation curves of biological tissue specimens show a hysteresis. After an initial conditioning phase, however, the difference between loading and unloading curves of successive cycles is often found to exhibit a decreasing tendency, i.e., the hysteresis becomes smaller (Figure 5.1). After a number of successive cycles, the hysteresis stabilizes asymptotically. At this stage, one says that the tissue has reached a preconditioned state. Experimental investigations show moreover that the hysteresis of living tissues is rather insensitive to the strain rate ("structural damping"). Even under a wide rage of frequencies, such as in an extreme situation in ultrasound experiments when the frequency changes from 1 KHz to 10 MHz, the energy dissipation per cycle usually changes not more than by a factor of 2 or 3 (Fung 1993).

Every hysteresis consists of two curves, *viz*., one for loading and one for unloading which are essentially independent from the strain rate in case of biological tissues. If one derives from this fact an approximation and assumes that in the preconditioned state the viscoelastic material can be treated as one elastic material under loading and another elastic material under unloading conditions. Then methods of the theory of elasticity can be used to describe the energy dissipation or damping properties of the tissue. Several authors denote this procedure as pseudoelastic approximation in order to remind that the material is actually inelastic but under the special conditions considered here, we can deal with it as an elastic material. For each of these pseudoelastic loading and unloading curves, a strain-energy function can be defined that is named pseudostrain-energy function. It means that the preconditioned tissue can be treated approximately as two hyperelastic materials.

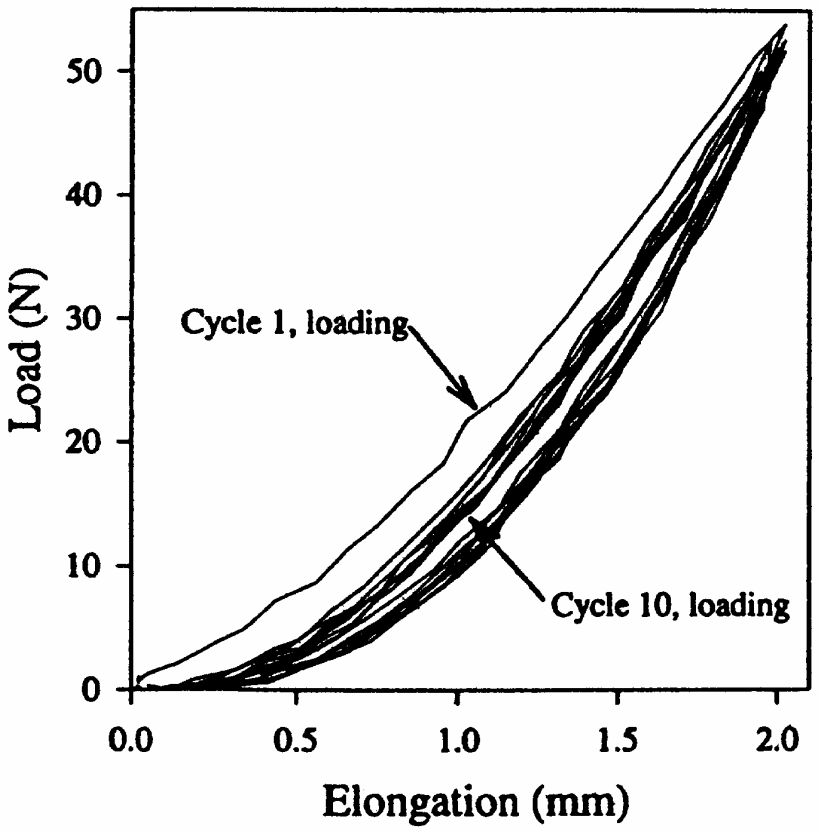

Figure 5.1 Load-elongation behaviour of human fascia lata tested along the fibre direction (Weiss and others 1996)

For an anisotropic material the pseudostrain-energy function must be formulated so that it includes the dependency of the material properties on the preferred direction. Because of the complex and multiphase structure of biological materials this dependency is not trivial and during the last years a considerable amount of research has been devoted to the investigation of the directional dependency of the constitutive equation for various biological materials. A number of investigators have studied especially the fibrous structure of the heart and tried to find suitable constitutive equations for the myocardial tissue. These attempts can be categorised into two approaches.

In the first approach one uses the symmetry of the structure to choose a local coordinate system. The strain energy function in this local coordinate system is determined so that the dependency on the strain tensor reflects the symmetry. In the second approach one introduces a strain energy function in the global coordinate system, which depends explicitly on a vector field **N** that represents the preferred direction of the material in each point.

5.1 Constitutive equations in a local coordinate system

This approach is in widespread use by many investigators. The principle of this approach derives from the fact that for an anisotropic material in each point a local coordinate system can be defined so that one of the axes of the coordinate system is collinear with the direction of anisotropy (In case of a more complex anisotropy than the transverse isotropy considered here, the alignment of the local coordinate system is chosen such that other symmetry axes are taken into account). In this coordinate system the strain energy can be expressed as a quadratic function of the components of the Green-Lagrange strain tensor. Thus, all computations must be performed in this local coordinate system. This approach has been used by various investigators who studied cardiac and cardiovascular mechanics. A transversely isotropic structure for the tissue is thereby often assumed and a formulation for the material behaviour is chosen which is based on the available experimental information.

Chuong and Fung (1986) proposed the following form of the strain energy function to describe the mechanical properties of arteries in three dimensions assuming orthotropic symmetry

$$W = \frac{1}{2} C \left(e^{Q} - 1 \right) \tag{5.1}$$

where Q is a quadratic function of the three principal strain components. C is a suitably chosen constant.

Guccione and co-workers (1991) used this idea for developing a cylindrical model for the left ventricle and presented an explicit form for Q to describe the special case of three dimensional fibre structure of the myocardium. They thereby assumed a thick-walled cylindrical geometry for the left ventricle with a transversely isotropic structure for the myocardium that is incompressible. They defined a local coordinate system $\left(X_R, X_F, X_C \right)$ which was orthogonal in the stress-free state. The X_R axis was aligned with the radial direction; the fibre axis X_F was oriented along the fibres and laid in a plane normal to the radial axis while the X_C axis was chosen along the cross-fibre direction. The form is

$$\begin{aligned} Q = {} & 2b_1 \left(E_{RR} + E_{FF} + E_{CC} \right) \\ & + b_2 E_{FF}^2 + b_3 \left(E_{CC}^2 + E_{RR}^2 + E_{CR}^2 + E_{RC}^2 \right) \\ & + b_4 \left(E_{RF}^2 + E_{FR}^2 + E_{FC}^2 + E_{CF}^2 \right) \end{aligned} \tag{5.2}$$

where the E_{ij} are the components of the Green-Lagrange strain tensor in the local coordinate system and the coefficients C, b_1, b_2, b_3, b_4 are material constants and independent of the deformation and position in the body.

Bovendeerd and co-workers (1992) developed a finite element model with prolate spheroidal geometry for the left ventricle under the assumption of transverse isotropy and incompressibility of the tissue. They defined an orthonormal local coordinate system $\left(X_1, X_2, X_3 \right)$ with the axis X_3 parallel to the fibre direction and X_1 and X_2 as cross-fibre axes (Figure 5.2). They introduced a form for Q as follows

$$Q = a_1\left(I_1\left(\mathbf{E}\right)\right)^2 + a_2 I_2\left(\mathbf{E}\right) + a_3 E_{33}^2 + a_4\left(E_{31}^2 + E_{32}^2\right) \tag{5.3}$$

where E_{ij} are the components of the Green-Lagrange strain tensor $\mathbf{E}$. $I_1\left(\mathbf{E}\right)$ and $I_2\left(\mathbf{E}\right)$ are the following set of strain invariants

$$\begin{aligned} I_1\left(\mathbf{E}\right) &= \mathrm{tr}\mathbf{E} \\ &= E_{11} + E_{22} + E_{33} \end{aligned} \tag{5.4}$$

$$\begin{aligned} I_2\left(\mathbf{E}\right) &= \frac{1}{2}\left[\left(\mathrm{tr}\mathbf{E}\right)^2 - \mathrm{tr}\left(\mathbf{E}^2\right)\right] \\ &= E_{12}^2 + E_{23}^2 + E_{31}^2 - E_{11}E_{22} \\ &\quad - E_{22}E_{33} - E_{33}E_{11} \end{aligned} \tag{5.5}$$

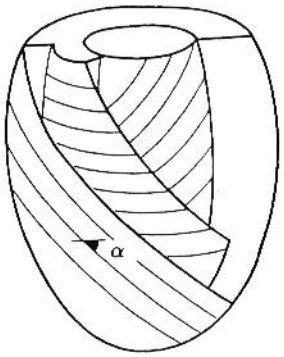

Figure 5.2 X_3 axis is assumed parallel to the muscle fibres in each point (Bovendeerd and others 1992)

In both of the above models the assumption of transverse isotropy is the key to the formulation of the strain energy function. In chapter 2 it was however reported that according to the most recent investigations the ultrastructure of the myocardium exhibits distinct cleavage planes (LeGrice and others 1997; LeGrice and others 1995). Each plane is thereby defined by a sheet of interconnected muscle fibres invested in a sheath. Sheaths, in turn, are separated from adjacent planes by perpendicularly arranged strands of collagen. This structural arrangement, which suggests an orthotropic material symmetry, motivated some authors to develop a generalized form of the Guccione's

formulation for Q (Costa and others 2001; Usyk and others 2000). Suppose that the orthonormal local coordinate system $\left(X_{\mathrm{F}}, X_S, X_N\right)$ is defined so that X_F is parallel to the muscle fibres, X_S is parallel to the sheets and perpendicular to the fibres and X_N is normal to the sheet plane. Then Q is defined for this orthotropic and incompressible structure as

$$\begin{aligned} Q = b_{FF}E_{FF}^2 + b_{SS}E_{SS}^2 + b_{NN}E_{NN}^2 + b_{FS}\left(E_{FS}^2 + E_{SF}^2\right) \\ + b_{FN}\left(E_{FN}^2 + E_{NF}^2\right) + b_{NS}\left(E_{NS}^2 + E_{SN}^2\right) \end{aligned} \tag{5.6}$$

where again E_{ij} are the components of Green-Lagrange strain tensor and b_{ij} the material constants.

Recently, Nash and Hunter (2000) proposed a 'pole-zero' formulation of the pseudo-strain energy function with eighteen material constants in the local coordinate system $\left(X_{\mathrm{F}}, X_S, X_N\right)$ to describe the orthotropic behaviour of myocardium (Figure 5.3).

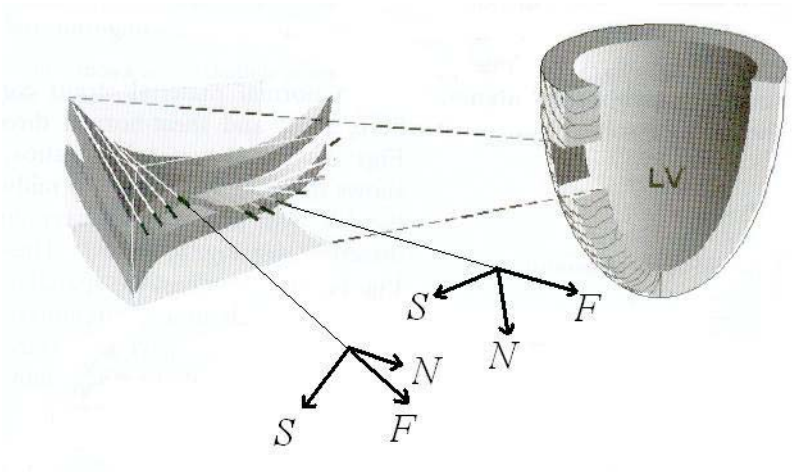

Figure 5.3 Local coordinate system (X_{F},X_{S},X_{N}) (LeGrice and others 1997)

This particular form was chosen to reproduce the highly nonlinear increase of the stiffness of the myocardium as the elongation reaches some practical upper limit (Figure 5.4). The derivation of the explicit form of such a constitutive law requires three dimensional stress and strain measurements to provide sufficient experimental data. Because these histological measurements are not yet completed, they reduced the number of independent unknown material parameters on the basis of a number of assumptions about the microstructure of myocardium. They suggested in particular that the strain energy function is separable into individual expressions in terms of the stretch along each of the material axes and gave the following form for the pole-zero strain energy function

$$W = k_{11}\frac{E_{11}^2}{\left|a_{11}-E_{11}\right|^{b_{11}}} + k_{22}\frac{E_{22}^2}{\left|a_{22}-E_{22}\right|^{b_{22}}} + k_{33}\frac{E_{33}^2}{\left|a_{33}-E_{33}\right|^{b_{33}}} + k_{12}\frac{E_{12}^2}{\left|a_{12}-E_{12}\right|^{b_{12}}} + k_{13}\frac{E_{13}^2}{\left|a_{13}-E_{13}\right|^{b_{13}}} + k_{23}\frac{E_{23}^2}{\left|a_{23}-E_{23}\right|^{b_{23}}} \tag{5.7}$$

where the a_{ij}, b_{ij} and k_{ij} are material constants.

It is clear from the above examples that this first type of approach is based on phenomenological and microstructural aspects and has the advantage of mathematical simplicity. The other advantage consists of the fact that there is a direct physical interpretation of the various material parameters and that they can therefore be used, among other, as controlling tools for certain aspects of the material behaviour, for example, the rigidity of the material in a defined direction.

In the literature the use of local coordinate systems has often been accompanied by assumptions about the fibre architecture of the ventricular wall. On the one hand, this can be very helpful for the simplicity of numerical calculations but, on the other, it is not necessarily in agreement with the reality. For example, a prolate spheroidal coordinate system has been applied and it was assumed that the inclination angel is zero, i.e., the fibres are always parallel to the epicardial surface.

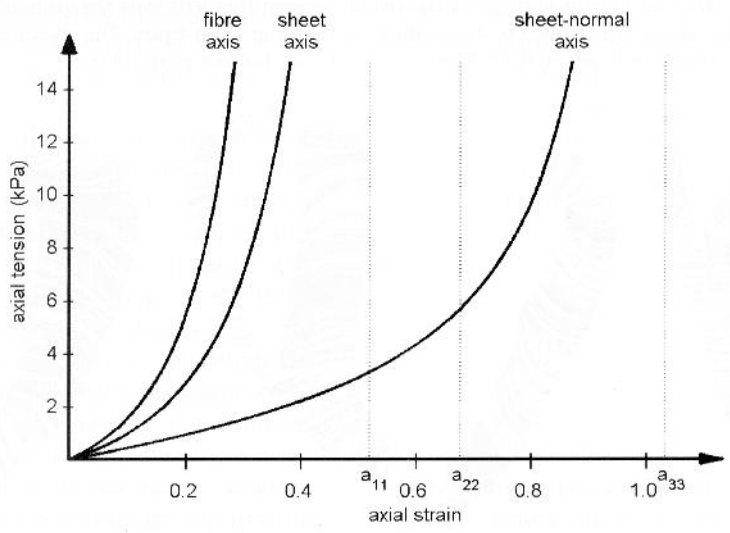

Figure 5.4 suggested stress-strain curves for each of the material axes (Stevens and others 2003)

A disadvantage of this approach is that for finite element implementation stress and elasticity tensors must be transformed to the global coordinate system. It requires the transformation of a rank two and rank four tensor at every integration point for every element and at each iteration of the nonlinear solver which is computationally very expensive, especially if a large number of elements are needed to describe details of the geometry(Weiss 1994).

5.2 Constitutive equations in the global coordinate system

The important point when choosing this approach is that at first the fibre directions must be determined in the global coordinate system as a vector field throughout the entire myocardium. We thereby assume again that the tissue is in a preconditioned state and that the preferred direction of the tissue is determined by a vector field throughout the body. Additionally, we assume that the material is hyperelastic and that there exist a strain energy function that depends on the vector field.

In the last chapter we saw that for a hyperelastic material the strain energy function can be expressed as a function of strain invariants taking into account the vector field which

determines the preferred direction of the material in each point. In the case of a transversely isotropic material we had the following form which depends on five scalars I_1, I_2, I_3, I_4, I_5

$$W = W\left[I_1(\mathbf{C}), I_2(\mathbf{C}), I_3(\mathbf{C}), I_4(\mathbf{C},\mathbf{N}), I_5(\mathbf{C},\mathbf{N}) \right] \tag{5.8}$$

The scalars I_1, I_2, I_3, I_4, I_5 are defined in section 4.3 and $\mathbf{N}$ is the vector field of fibre orientation.

Models are documented in the literature where the authors proposed an explicit form for W and determined the material parameters with the use of experimental data. For practical reasons the determination of a specific form of the strain energy function which depends on five invariants is difficult, nevertheless, attempts have been made to define W for a subclass of transversely isotropic materials. It is thereby hypothesized that the tissue can be idealized as being composed of a noninteracting bundle of fibres and a matrix. The fibres are continuously distributed and there can be interactions between fibres and the matrix. Furthermore it is assumed that the material is incompressible which implies that $J^2 = I_3 = 1$, and that the matrix is isotropic. Upon postulating that the strain energy function can be written as the sum of three separated parts we have

$$W = W_{\text{matrix}}(I_1, I_2) + W_{\text{fibres}}(I_4) + W_{\text{interaction}}(I_1, I_2, I_4) \tag{5.9}$$

W_{matrix} is the strain energy function of the matrix, W_{fibres} the one of the fibres and $W_{\text{interaction}}$ is related to the interaction of matrix and fibres.

Due to the lack of experimental data, the dependency on I_5 has been omitted in the above formulation because it has the smallest influence. It is intended to keep the functional form of W as simple as possible and the number of invariants compatible with the experimental evidence. A form for W is chosen which depends on a minimal number of invariants and which can yield a good fit with experimental data. The dependency on I_4 can moreover be replaced from the relation $\lambda = \sqrt{I_4} = \sqrt{\mathbf{N}\cdot\mathbf{C}\cdot\mathbf{N}}$, which is sometimes more useful for the determination of the material coefficients from experimental data.

Along these lines, Humphrey and co-workers (I,II1990b) proposed a specific functional form for the strain energy function whereby they took into account the information they established experimentally with respect to geometrical structure and multiaxial mechanical properties for passive myocardium. Accordingly, they chose a polynomial form which depended only on two invariants I_1 and λ as follows

$$\begin{aligned} W(I_1,\lambda) &= C_1(\lambda-1)^2 + C_2(\lambda-1)^3 + C_3(I_1-3) \\ &+ C_4(I_1-3)(\lambda-1) + C_5(I_1-3)^2 \end{aligned} \tag{5.10}$$

They estimated mean values for the material parameters C_1, C_2, C_3, C_4, C_5 from biaxial deformation experiments. With this form of W, the Cauchy stress tensor can be calculated from

$$\sigma = -p\mathbf{I} + 2\frac{\partial W}{\partial I_1}\mathbf{B} + \frac{1}{\lambda}\frac{\partial W}{\partial \lambda}\mathbf{FN}\otimes\mathbf{NF}^T \tag{5.11}$$

where in agreement with the equation (4.90), I_4 is replaced with λ.

Later, Novak and co-workers (1994) performed further biaxial tests observing similar protocols as Humphrey *et al.* and used the same functional form for the strain energy. They showed that the proposed constitutive equation could be used to describe the nonlinear and anisotropic behaviour found in the four regions, i.e., the middle portion of the interventricular septum, furthermore the inner, middle and outer layers of the lateral left ventricular free wall of the canine heart equally well with material parameters chosen appropriately for these four regions. In particular, specimens from the inner and outer portions of the LV free wall tended to be stiffer than those from the middle of the LV free wall and the septum. This finding suggests that the mechanical properties of the heart are qualitatively similar from region to region, but quantitatively different.

Lin and co-workers (1998) performed biaxial tests using a similar protocol as Humphrey *et al*. on passive and activated specimens. They reported that the simplest polynomial energy function which fitted the experimental data for the passive material and which had zero energy in the unloaded state had 14 parameters. To reduce this number they used an exponential function rather than a polynomial one and gave the following form for the passive strain energy function

$$W\left(I_1, I_4\right) = C_1\left(e^Q - 1\right) \tag{5.12}$$

where

$$Q = C_2\left(I_1 - 3\right)^2 + C_3\left(I_1 - 3\right)\left(I_4 - 1\right) + C_4\left(I_4 - 1\right)^2 \tag{5.13}$$

They were furthermore able to perform for the first time similar measurements on activated thin sheets of myocardium. In their tests, the active stress-strain responses were more linear than the passive ones. This finding suggested that the passive and actively contracting myocardium represent functionally two different types of materials which therefore require different strain energy functions to describe their properties. Yet, unlike the passive state, the best fit for the experimental data could be reached with the polynomial form. A peculiarity derived however from the active material behaviour. Upon activation, the muscle shortened. The strains during activation were referenced to the dimensions in the passive unloaded state, such that there could be active stress, and hence a nonzero energy developed at zero passive strain level (i.e. at stretch ratios = 1). They proposed the following form for the active strain energy function

$$\begin{aligned} W\left(I_1, I_4\right) = {} & C_0 + C_1\left(I_1 - 3\right)\left(I_4 - 1\right) + C_2\left(I_1 - 3\right)^2 \\ & + C_3\left(I_4 - 1\right)^2 + C_4\left(I_1 - 3\right) + C_5\left(I_4 - 1\right) \end{aligned} \tag{5.14}$$

Due to the large amount and relative comprehensiveness of *in vitro* biaxial test data which has been used for the determination of the functional form and the estimation of material parameters described above, we expect that the constitutive equations (5.10), (5.12) and (5.14) might be employed in analyses of the intact heart with more confidence than previous relations which were based on uniaxial experiments solely.

The first advantage of the second approach involving the global reference system is that we do not need to make any *a priori* assumption or definition with respect the global geometry of the myocardium or the orientation of the fibres. A second advantage is related to the finite element implementation in that the stress and elasticity tensors can be computed in the global coordinate system without transformation. We can therefore use a fine mesh to describe details of the geometry and still expect a reasonable computation time.

Nevertheless, there is a disadvantage associated with the second approach. The mathematical dependence of the strain energy function on invariants is rather formal and it is not straightforward to give a direct and simple physical interpretation of the material constants. Nevertheless, in the next chapters we will see that the use of a strain energy function in the global coordinate system has significant practical advantages. E.g., it makes the use of commercial FE codes and their widely developed facilities possible.

References

Bovendeerd PH, Arts T, Huyghe JM, van Campen DH, Reneman RS. 1992. Dependence of local left ventricular wall mechanics on myocardial fiber orientation: a model study. J Biomech 25(10):1129-40.

Chuong CJ, Fung YC. 1986. Residual stress in arteries. In: Schmid-Schönbein GW, Woo Sl-Y, Zweifach BW, editors. Frontiers in Biomechanics. New York: Springer-Verlag. p pp. 117-129.

Costa KD, Holmes JW, McCulloch AD. 2001. Modelling cardiac mechanical properties in three dimentions. The Royal Society 359:1233-1250.

Fung YC. 1993. Biomechanics : mechanical properties of living tissues. New York: Springer-Verlag. xviii, 568 p.

Guccione JM, McCulloch AD, Waldman LK. 1991. Passive material properties of intact ventricular myocardium determined from a cylindrical model. J Biomech Eng 113(1):42-55.

Humphrey JD, Strumpf RK, Yin FC. 1990a. Determination of a constitutive relation for passive myocardium: I. A new functional form. Journal of Biomechanical Engineering 112:333-339.

Humphrey JD, Strumpf RK, Yin FC. 1990b. Determination of a constitutive relation for passive myocardium: II. Parameter estimation. Journal of Biomechanical Engineering 112:340-346.

LeGrice IJ, Hunter PJ, Smaill BH. 1997. Laminar structure of the heart: a mathematical model. Am J Physiol 272(5 Pt 2):H2466-76.

LeGrice IJ, Smaill BH, Chai LZ, Edgar SG, Gavin JB, Hunter PJ. 1995. Laminar structure of the heart: ventricular myocyte arrangement and connective tissue architecture in the dog. Am J Physiol 269(2 Pt 2):H571-82.

Lin DHS, Yin FC. 1998. A Multiaxial Constitutive law for Mammalian Left Ventricular Myocardium in Steady-State Barium Contracture or Tetanus. Journal of Biomechanical Engineering 120:504-517.

Nash MP, Hunter PJ. 2000. Computational mechanics of the heart. journal of Elasticity 61(1-3):113-141.

Novak VP, Yin FC, Humphrey JD. 1994. Regional mechanical properties of passive myocardium. J Biomech 27(4):403-12.

Stevens C, Remme E, LeGrice I, Hunter P. 2003. Ventricular mechanics in diastole: material parameter sensitivity. J Biomech 36(5):737-48.

Usyk TP, Mazhari R, McCulloch AD. 2000. Effect of Laminar Orthotropic Myofiber Architecture on regional Stress and Strain in the Canine Left Ventricle. Journal of Elasticity 61:143-164.

Weiss, j. A., Maker BN, Govindjee S. 1996. Finite element implementation of incompressible, transversely isotropic hyperelasticity. Computer methods in applied mechanics and engineering 135:107-128.

Weiss JA. 1994. A constitutive model and finite element representation for transversely isotropic soft tissue. Ph.D. Thesis: The University of Utha.

CHAPTER 6

FINITE ELEMENT MODELING OF THE LEFT VENTRICLE – GEOMETRICAL APPROXIMATIONS

6.1 Introduction

In the last chapters the fibrous architecture and the constitutive properties of the heart were discussed. But, in addition to the sophisticated fibre structure and material behaviour, the heart has a quite irregular geometry. Especially the structure of the highly trabeculated endocardium does not easily allow for a mathematical description. Accordingly, to gain an initial access to the study of heart mechanics, some radical simplifications of the geometry are helpful and actually necessary to obtain basic general results. The most important approximation consists of the assumption of an axisymmetric geometry for the left ventricle which was popular in early studies of the heart and was helpful for a better basic understanding of the heart function. Thereby, some investigators approximated the geometry of the left ventricle by a thin-walled cylinder, sphere or ellipsoid (Falsetti and others 1970; Sandler and Dodge 1963). In this case, the wall stress can be calculated analytically as a function of the inside pressure and of the geometrical dimensions, and the results can be regarded as a first approximation for the average stress in the heart wall (Huisman and others 1980). Other authors developed somewhat more complicated models. They modelled the left ventricle as a thick-walled cylinder, sphere or ellipsoid to estimate the transmural stress distribution in the wall (Ghista and Sandler

1969; Mirsky 1969; Wong and Rautaharju 1968). Usually, in particular in models treated analytically, it was supposed that the symmetry was preserved during the deformation.

These simplifications of the geometry were usually accompanied by other approximations with respect to the material behaviour. For example, in early attempts for the modelling of the heart, assumptions like isotropy and linear elasticity of the material were widely used. Depending on the assumptions about the geometry, the material behaviour and the boundary conditions, these models yielded sometimes quite different predictions of the circumferential or longitudinal distribution of the wall stress in the myocardium (Huisman and others 1980; Yin 1985). These different predictions which sometimes could not be verified experimentally were the reason for partly controversial conclusions about the structure of the myocardium and heart function and emphasised the necessity for more investigations about the microstructure of the myocardium.

Later experimental studies confirmed the nature of the fibre structure in the myocardium (Streeter and others 1966; Streeter and others 1969). Thereby, the existence of an interwoven network of the circumferential and transmural fibres was verified, but due to the complicated nature of the fibrous network, its structure could not be determined in detail. A number of investigators gave a mathematical formulation for the fibre architecture on the basis of certain simplifying assumptions. They supposed in particular that the fibres were distributed in separate thin layers parallel to the endocardial and epicardial surfaces (Arts and Reneman 1989; Arts and others 1982), and in each layer the fibres ran parallel to one another in a specified surface-parallel direction (Beyar and Sideman 1984a; Beyar and Sideman 1984b). Once the fibre direction field was given, transversely isotropic constitutive equations in the associated local coordinate system were developed to model the material behaviour.

Analytic procedures are only possible with extremely limiting assumptions. More refined constitutive models and complicated geometries have to be treated numerically. Thereby, the Finite Element (FE) method lends itself for this purpose, as it is suited to treat

irregular solid geometries, boundary conditions and nonlinear multiphase constitutive properties. During the last twenty years there were a number approaches involving FE techniques in combination with experimental attempts including MRI measurements to formulate advanced models of the heart. A short review of the most important published finite element models of the left ventricle and their results is given in the following (Yin 1985).

Gould and co-workers (1972) defined a nonsymmetric geometry and showed that the transmural stress distribution depends on local wall curvature.

Janz and co-workers (1978) used an axisymmetric geometry and emphasised the necessity to apply a finite deformation theory. They showed furthermore that material anisotropy and regional heterogeneity may exert a substantial influence on the stress and strain distribution in the myocardial wall.

Pao and co-workers (1976) applied a nonsymmetric geometry and demonstrated that even for an isotropic linear elastic material model, local wall curvature and varying wall thickness can influence the distribution of wall stress considerably.

Panda and Natarajan (1977) formulated an anisotropic linear elastic material model along with a nonsymmetric geometry and verified that the form of the assumed anisotropy may have an appreciable effect on the transmural stress distribution.

Vinson and co-workers (1979) studied the effect of various regional heterogeneities of material properties on the basis of a nonsymmetric ventricular geometry.

Arts and co-workers (1989; 1982) and also Beyer and Sideman (1984a; 1984b) worked with a symmetric geometry. They developed a model for the myocardium in which the tissue was assumed to be composed of a contractile fibre structure embedded in an incompressible fluid. Contractile fibre stress thereby depended on time, sarcomere length and velocity of sarcomere shortening.

Horowitz and Perl (Horowitz and others 1986; Perl and others 1986) created a nonsymmetric model in the form of a three dimensional reconstruction of the left ventricle which was based on the geometric data derived by Ritman et al. from computed tomography. The myocardial material consisted of a matrix in which fibres were embedded. It was thereby assumed that the matrix had a Poisson's ratio of 0.45 and a constant Young's modulus while the Young's modulus and the stiffness of the fibres increased with increasing strain. The surface-parallel fibre structure included a linear variation of the fibre angle, from $+60°$ to the circumferential direction at the endocardium to $-60°$ at the epicardium.

Huyghe and co-workers (1992) proposed a two phase axisymmetric FE model which allowed torsion about the axis of symmetry. They implemented an anisotropic quasi-linear viscoelastic constitutive relation (Fung 1993) for myocardium which was considered to be saturated with intracoronary blood. Incompressibility was assumed, yet, the volume of the ventricular wall was variable since blood could be squeezed out of the wall. Active fibre stress depended on time, strain and strain rate and a transmural variation of the otherwise surface-parallel muscle fibre orientation was included.

Bovendeerd and co-workers (1996; 1992; 1994) studied the dependence of local left ventricular mechanics on myocardial muscle fibre orientation. They used a thick-walled truncated ellipsoid of revolution for the geometry of the left ventricle. During a simulated ventricular cycle rotational symmetry was maintained, as a result of rotationally symmetric input parameters. Passive material behaviour included incompressibility and transverse isotropy. The muscle fibre orientation in the left ventricle wall was quantified by the helix fibre angle (here denoted as inclination angle), defined as the angle between the local circumferential direction and the projection of the fibre path on the plane perpendicular to the local radial direction. A transmural variation of the helix fibre angle from $+60°$ at the endocardium to $-60°$ at the epicardium was assumed. In addition, a transverse fibre angle (here oblique or crossover angle) was used to model the continuous course of the muscle fibres between the inner and the outer layers of the ventricular wall.

This angle was defined as the angle between the circumferential direction and the projection of the fibre path on the plane perpendicular to the local longitudinal direction (Figure 6.1). The model for the contractile properties of the myocardium was similar to the approach presented by Arts (1982).

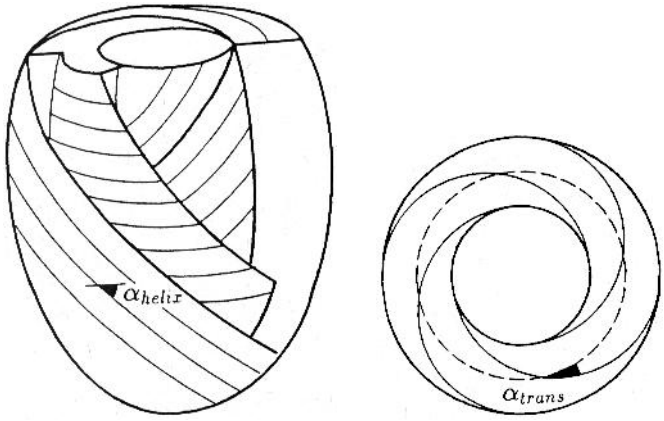

Figure 6.1 Fibre orientations is quantified by two angles α_{helix} and α_{trans} (Bovendeerd and others 1994)

Extensive work on the mechanics and microstructure of the heart has been performed by the bioengineering research group at the University of Auckland, Auckland, New Zealand (P. J. Hunter and co-workers). They developed various three dimensional finite element models of the canine heart which were based on a prolate spheroid coordinate system and a defined fibre structure (Hunter and others 1992). The orientation of the fibres at and between the epicardial and endocardial surfaces was measured and interpolated throughout the ventricular wall (Figure 6.2). In their early models they used transversely isotropic constitutive equations. The FE code was derived from a high order Hermitian element formulation (Nielsen and others 1991a; Nielsen and others 1991b).

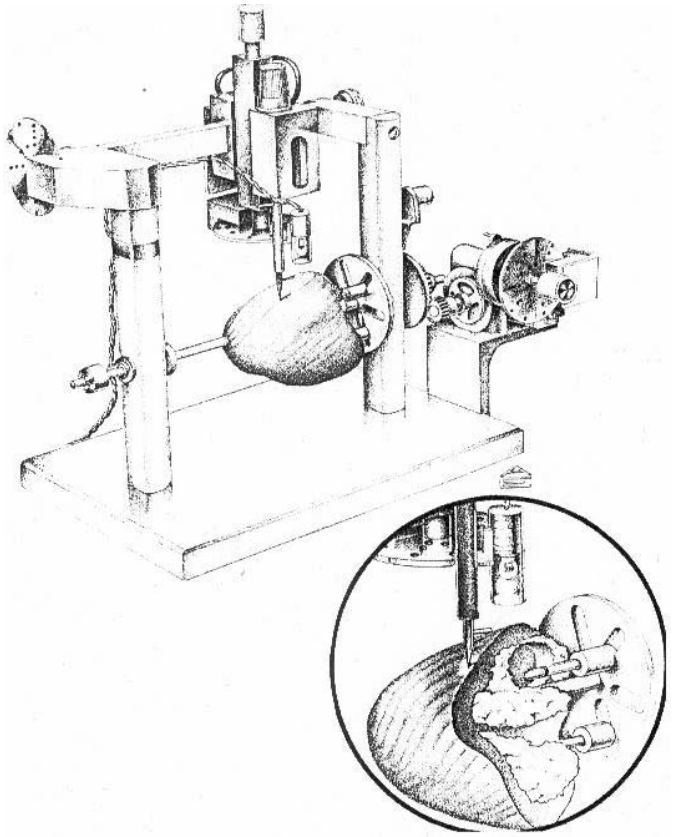

Figure 6.2 Schematic diagram of specially designed apparatus for the measurement of fibre orientation (Nielsen and others 1991a)

Later they analysed the three dimensional arrangement of the ventricular muscle cells and the associated extracellular connective tissue matrix in dog hearts. The existence of an ordered laminar arrangement of the myocytes with extensive cleavage planes between the muscle layers was reported. Thereby, these planes were found to run radially from the endocardium toward the epicardium in transmural sections and to coincide with the local muscle fibre orientation in tangential sections. They concluded that the ventricular myocardium is not a uniformly branching continuum but is organised in a laminar hierarchy in which it is possible to identify three axes of material symmetry at any point (LeGrice and others 1995). They gave in particular a mathematical formulation for the laminar structure of the heart (LeGrice and others 1997) and formulated an orthotropic material model called “pole-zero” law which is discussed in chapter five (Figure 6.3).

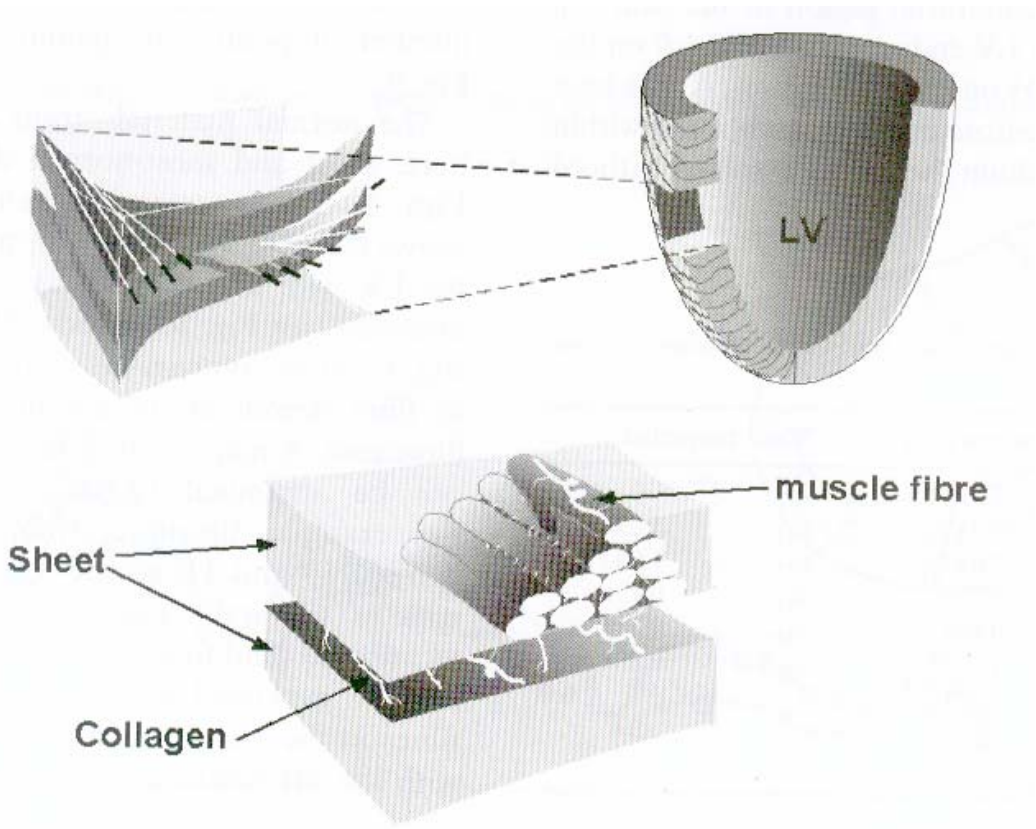

Figure 6.3 Schematic of fibrous-sheet structure of cardiac tissue (LeGrice and others 1995)

Another group, at the University of California, San Diego (A. D. McCulloch and co-workers) followed the work of Hunter et al. and developed a finite element model of the rabbit ventricular anatomy in a prolate spheroidal coordinate system. They studied among other its fibre architecture, as before with this assumption that the fibres were distributed in parallel layers (Vetter and McCulloch 1998). Recently, they have used a three dimensional finite element model to investigate the effects of material orthotropy on the regional mechanics of the canine left ventricular wall at end-diastole and end-systole (Usyk and others 2000).

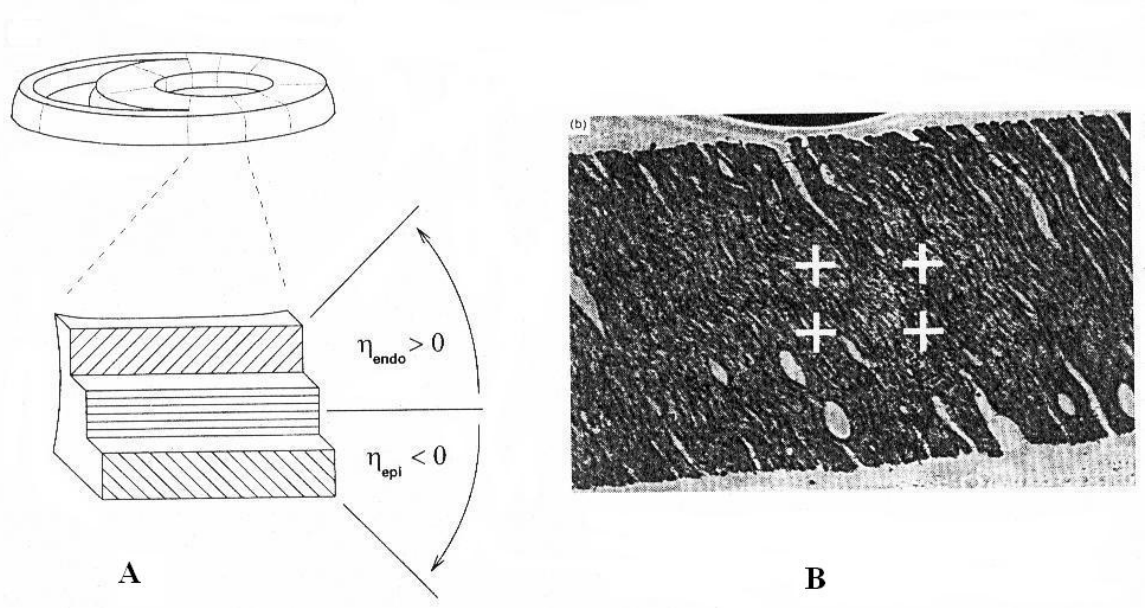

Figure 6.4 (A) Schematic of a block cut from a tissue slice. (B) Micrograph of unstained cryosectioned tissue showing fibre orientations (Vetter and McCulloch 1998).

The results published so far are based on more or less idealised models of the heart which enable an understanding of general cardiovascular physiology. They are furthermore mostly derived from animal preparations. In order to provide further insight into cardiodynamics, local deformation patterns of the myocardium as function of time and in particular pathologic developments including fibre disarray, accurate information about the three dimensional motion of the human heart as well as on the detailed fibre architecture and a constitutive equation which mimics the material behaviour of the myocardium and the dependence of it on time are necessary (Yin 1985).

In this chapter we use the method of finite elements to construct a mathematical model for the left ventricle. We begin with an idealized geometry and attempt to implement the constitutive equation introduced in the last chapter with an artificially generated orientation vector field, which is comprehensively discussed in chapter 3. In chapter 8 we will further develop the model on the basis of a realistic geometry obtained from a post mortem human heart.

6.2 Geometry and mesh

As a first attempt for the simulation of contraction process of the heart we start with a simple geometry and investigate how the change of the components of the active stress tensor influence the deformation and stress distribution in the heart wall. There are several methods to fit a geometry to digitized data representing a fibre orientation field (Cryer and others 1997; Hunter and others 1992). In this chapter we use a graphical method for the sake of simplicity. A real geometry of the left ventricle will be discussed in chapter 8.

Consider the equation of an ellipse in a global Cartesian coordinate system (X, Y, Z) in the $Z = 0$ plane and in the region $x \geq 0, y \leq 0$

$$\frac{x^2}{a^2} + \frac{y^2}{b^2} = 1 \tag{6.1}$$

we choose the values

$$\begin{aligned} a &= 0.5 \\ b &= 1.0 \end{aligned} \tag{6.2}$$

with constant parameters *a* and *b* and create a first curve. Then we choose

$$\begin{aligned} a &= 0.3 \\ b &= 0.9 \end{aligned} \tag{6.3}$$

and create a second curve.

If we connect these two curves with the lines $x = 0$ and $y = 0$, subsequently rotate the associated surface around the Y-axis (Figure 6.5A), the resulting object is an ellipsoid. The values of parameters *a* and *b* are quite arbitrary at this time, but the geometry and mesh can be scaled later on with graphical tools.

In this fashion a prolate spheroidal geometry was produced, then, a mesh consisting of more than 11,700 eight-node hexahedral elements was introduced with the help of hex-mesh generator of the commercial software package MSC-Marc Mentat® (Figure 6.5B).

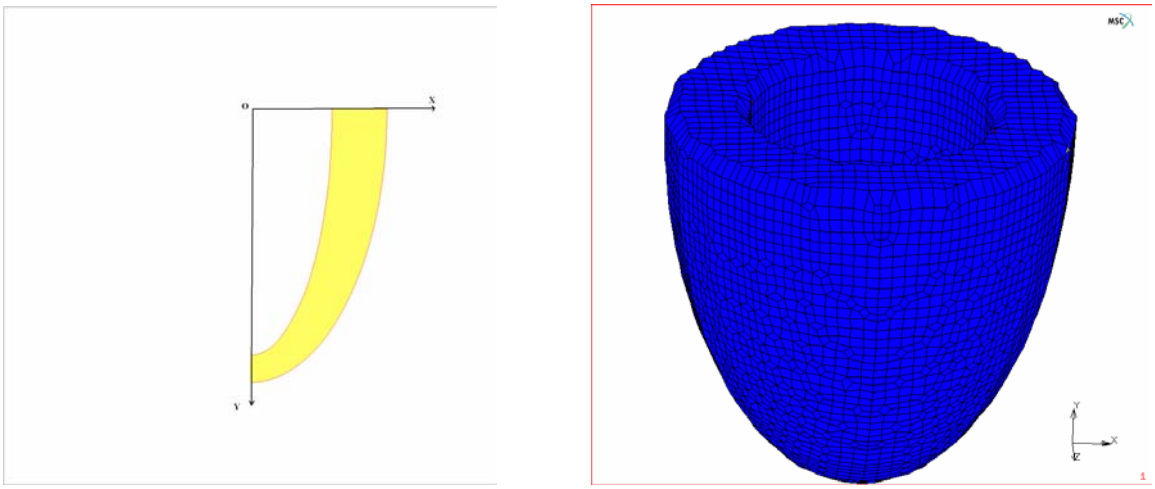

A **B**

Figure 6.5 (A) Connected curves from equation (6.1). (B) generated mesh from prolate spheroidal geometry

Next, the measured fibre trajectory file (Figure 6.6) and the mesh data file were merged into one common data file. With the help of graphical facilities of the applied software the mesh was scaled and the elements were adjusted so that the mesh covered the fibres totally (Figure 6.7). Apparently, with this method, the symmetries of the geometry were lost, yet, the resulting shape was still much smoother than a real geometry of the left ventricle which will be constructed from digitized data later on.

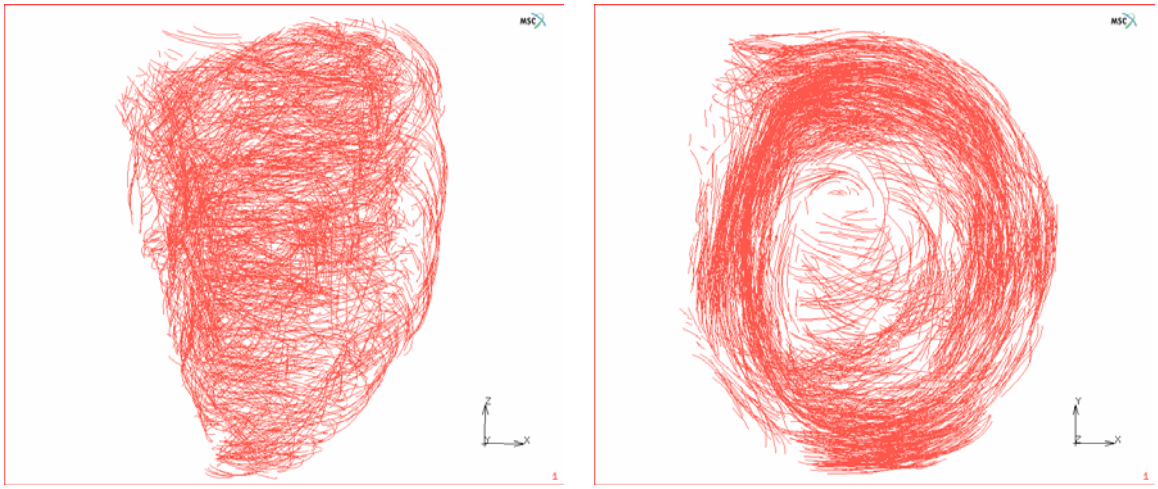

Figure 6.6 Measured fibre trajectories as explained in chapter 3

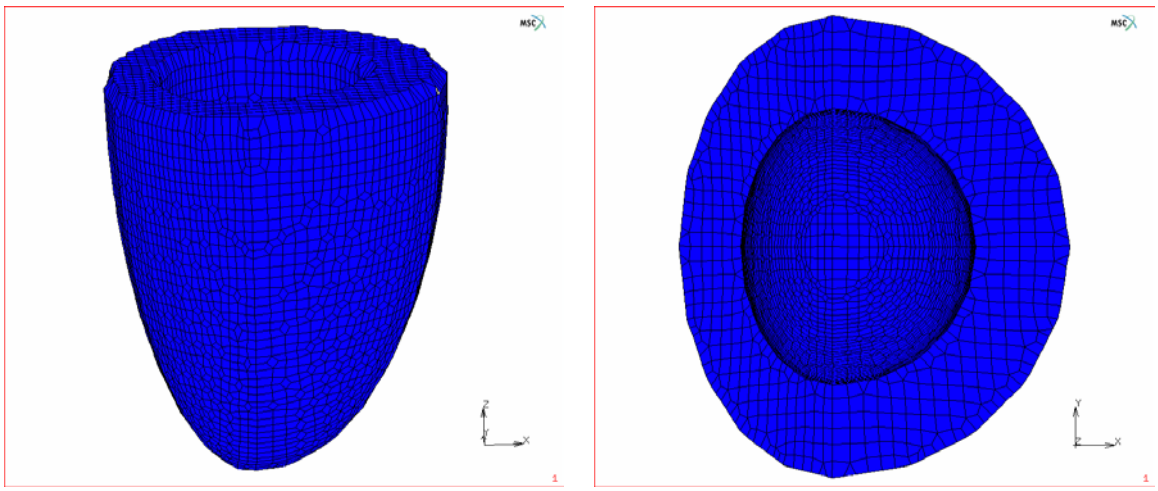

Figure 6.7 Adjusted mesh to the fibres

6.3 Fibre orientation field

In chapter 3 a method was introduced which allows to construct a fibre orientation field for a given mesh from a set of digitized 3D fibre data so that for each element a vector is defined which shows the orientation of the fibres in that element. These vectors are normalized and saved in a file for later numerical use. The advantage of this method is that one can attribute a fibre structure taken from a real heart to an originally prolate spheroidal geometry which is gradually being deformed during this process to accommodate the fibre field but still keeps a smooth outline (Figure 6.7).

6.4 Boundary conditions

The myocardium is surrounded by the pericardial sac. At the basis, furthermore, the left ventricle is restrained by the aorta, the atria and the connections to the right ventricle. Quantitative information on these boundary conditions is not available, so one has to make appropriate assumptions in order to suppress an undesired rigid body displacement of the left ventricle during the finite element calculation. In our model of the left

ventricle, therefore, the motion of the basal plane for the elements which were in sub-epicardial and mid-wall layers was suppressed.

A further boundary condition derives from the intracavital blood pressure acting on the endocardial surface. The blood pressure in a real ventricle depends on time and location. In order to determine the spatial distribution of the pressure as function of time, the fluid dynamics of the blood in the ventricle has to be considered. However, since the pressure gradients in the left ventricle during ejection are mostly small (typically less than 10 mm Hg) in comparison with the absolute pressure, we discarded local variations and assumed a uniform parabolic dependence of the pressure on time. In the literature, the dependence of the blood pressure of the left ventricle on time is reported as shown in Figure (1.7). The curve

$$P = -944.38t^2 + 245.54t \qquad 0 \le t \le 0.2 \tag{6.4}$$

approximates this dependence reasonably well. It has a maximum at

$$\begin{aligned} P_{Max} &= 15.96 \quad \text{kpa} \\ t_{Max} &= 0.13 \quad \text{sec} \end{aligned} \tag{6.5}$$

which corresponds to 120 mmHg, the normal systolic blood pressure for a healthy heart. We assumed that this pressure is uniformly applied to the entire endocardial surface (Figure 6.8).

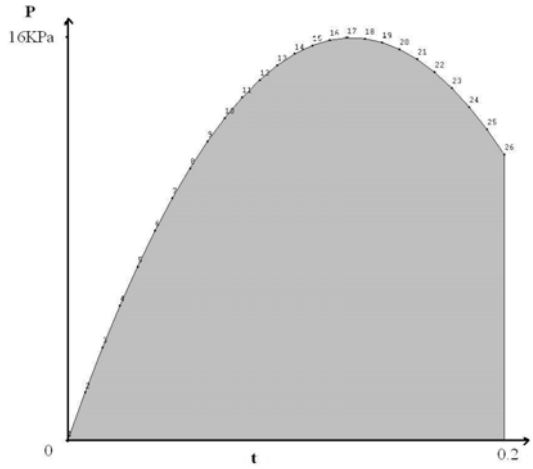

Figure 6.8 Curve of blood pressure according to equation (6.4)

6.5 Strain energy function

In chapter 5 we introduced various strain energy functions for myocardial tissue which have been proposed during the last twenty years. For the simulation of contraction processes, however, the formulation proposed by Lin and Yin (1998) for the active phase of the heart appears to be most appropriate

$$\begin{aligned} W_{act} = C_0 + C_1(I_1 - 3)(I_4 - 1) + C_2(I_1 - 3)^2 \\ + C_3(I_4 - 1)^2 + C_4(I_1 - 3) + C_5(I_4 - 1) \end{aligned} \tag{6.6}$$

where

$$\begin{aligned} I_1 &= \mathrm{tr}\mathbf{C} \\ I_4 &= \mathbf{N} \cdot \mathbf{C} \cdot \mathbf{N} \end{aligned} \tag{6.7}$$

The following values for the material parameters are chosen

$$\begin{aligned} C_1 &= -7.89 \\ C_2 &= 66.20 \\ C_3 &= 51.12 \\ C_4 &= 40.12 \\ C_5 &= 0.0032 \end{aligned} \tag{6.8}$$

The units are given, as in Lin and Yin (1998), in g/cm^2. These material parameters correspond to the phase where the myocardial tissue exhibits its stiffest behaviour during contraction according to the biaxial tests of Lin and Yin (1998). We therefore expect that these values characterize the upper limit for stress tensor in the heart wall.

6.6 Contraction

Systolic contraction is modelled by defining the total second Piola-Kirchhoff stress tensor **S** as the sum of the passive three-dimensional stress tensor $\mathbf{S}_{passive}$ derived from the strain energy function(6.6) and an unknown active three-dimensional stress tensor $\mathbf{S}_{active}$ which

must be defined in the global coordinate system. Accordingly, we can write the total Piola-Kirchhoff stress tensor **S** as follows

$$\mathbf{S} = \mathbf{S}_{passive} + \mathbf{S}_{active} \tag{6.9}$$

We note that $\mathbf{S}_{active}$ has to be given in the global coordinate system because all calculations will be done in the global rectangular coordinate system $(\mathbf{i}, \mathbf{j}, \mathbf{k})$. As mentioned above, for each element, there is a fibre orientation defined as a vector, which we denote by $\mathbf{e}'_1$. We choose this direction as the positive direction of the X_F axis, the axis along which the fibres are oriented in the middle point of the considered element. A second vector $\mathbf{e}'_2$ can be defined as the vector product of $\mathbf{e}'_1$ and the vector $-\mathbf{k}$ as

$$\mathbf{e}'_2 = -\mathbf{e}'_1 \times \mathbf{k} \tag{6.10}$$

because the symmetry axis of the original spheroid was chosen along the Z axis of the global coordinate system $(\mathbf{i}, \mathbf{j}, \mathbf{k})$. $\mathbf{e}'_2$ will therefore be directed toward the inside of the geometry. We choose it as the unit vector along the assumed sheet axis X_S, and it is perpendicular to the X_F and Z axes. The third vector $\mathbf{e}'_3$ can be defined as

$$\mathbf{e}'_3 = \mathbf{e}'_1 \times \mathbf{e}'_2 \tag{6.11}$$

This vector defines the normal axis X_N which is perpendicular to X_F and X_S.

With these three perpendicular unit vectors $\mathbf{e}'_1, \mathbf{e}'_2, \mathbf{e}'_3$ we define the local rectangular coordinate system (X_F, X_S, X_N) in the middle point of each element. The relation between the unit vectors

$$\{\mathbf{e}'_m\} = \begin{Bmatrix} \mathbf{e}'_1 \\ \mathbf{e}'_2 \\ \mathbf{e}'_3 \end{Bmatrix}, \qquad \mathbf{e}'_m \cdot \mathbf{e}'_k = \delta_{mk} \tag{6.12}$$

of the local coordinate system (X_F, X_S, X_N) and the unit vectors

$$\{\mathbf{e}_n\} = \begin{Bmatrix} \mathbf{i} \\ \mathbf{j} \\ \mathbf{k} \end{Bmatrix}, \qquad \mathbf{e}_n \cdot \mathbf{e}_l = \delta_{nl} \tag{6.13}$$

of the global coordinate system (X,Y,Z), is given by the transformation matrix $\mathbf{Q}$

$$\mathbf{Q} = \begin{pmatrix} q_{11} & q_{12} & q_{13} \\ q_{21} & q_{22} & q_{23} \\ q_{31} & q_{32} & q_{33} \end{pmatrix} \tag{6.14}$$

with the components

$$q_{mn} = \mathbf{e}'_m \cdot \mathbf{e}_n \tag{6.15}$$

as follows

$$\{\mathbf{e}'_m\} = \mathbf{Q}\{\mathbf{e}_n\} \qquad m,n = 1,2,3 \tag{6.16}$$

If we denote the second Piola-Kirchhoff stress tensor in the local coordinate system (X_F, X_S, X_N) with $\mathbf{S}'_{active}$, this tensor in the global coordinate system (X,Y,Z) is determined by

$$\mathbf{S}_{active} = \mathbf{Q}^T \mathbf{S}'_{active} \mathbf{Q} \tag{6.17}$$

In order to be able to execute the numerical calculations, we first define the orientation vector for each element, then define the local coordinate system and determine the transformation matrix $\mathbf{Q}$. Subsequently, we can determine the components of the active stress tensor $\mathbf{S}'_{active}$ in the local coordinate system (X_F, X_S, X_N) and apply the transformation (6.17), such that the components of the active stress tensor $\mathbf{S}_{active}$ in the global coordinate system (X,Y,Z) are known. As explained above, furthermore, the blood pressure inside the left ventricle is approximated with a parabola. To determine the values of the components of the stress tensor in the local coordinate system which are necessary in each increment to equilibrate the inside pressure, we introduce small values for the stress components and increase them slowly until the contraction sets in.

The first calculations were performed with an active stress tensor which contained only one component $S'_{active}(F,F)$ in the fibre direction, and it was assessed which minimal value of $S'_{active}(F,F)$ was necessary to overcome the intracavital pressure. In our finite element calculations the pressure increases incrementally whereby the number of

increments can arbitrarily be chosen. The values for the stress component $S'_{active}(F,F)$ have therefore to be determined sequentially according to the pressure increments.

From MRI, among other, we know that there are three main features regarding the deformation process during the contraction of the heart. These features are wall thickening, longitudinal shortening and a twisting rotation. Any realistic simulation of contraction has to reproduce these motions. Accordingly, we began to analyse the components of the active stress tensor and its values in view of these effects. We found in particular that the component $S'_{active}(F,F)$ alone can not produce all of these effects, actually, as we see in Figure 6.9, contraction only with $S'_{active}(F,F)$ caused longitudinal elongation of the left ventricle instead of shortening.

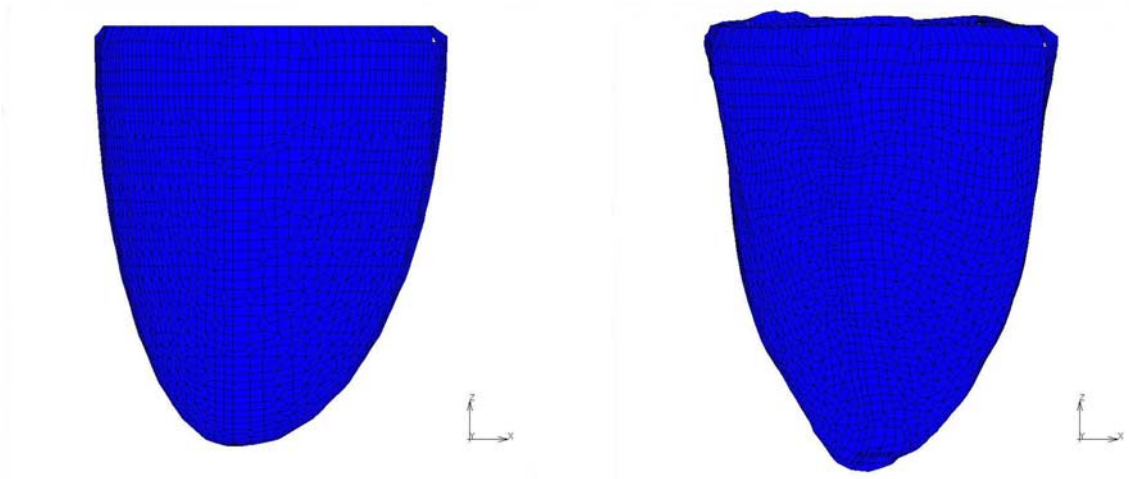

A **B**

Figure 6.9 Active stress tensor is defined only along the fibres. (A) Before contraction. (B) After contraction.

It was therefore necessary to add further components to $\mathbf{S}'_{active}$ which induce longitudinal shortening and rotation. In addition to $S'_{active}(F,F)$, i.e. the active stress along the fibres, a normal component $S'_{active}(N,N)$, i.e. an active stress in cross-fibre direction was introduced which is a function of the active stress along the fibres $S'_{active}(F,F)$. This assumption is in particular in agreement with the biaxial experimental tests in barium-contracted rabbit myocardium (Lin and Yin 1998).

Suitable values for $S'_{active}(F,F)$ and $S'_{active}(N,N)$ were sought by trial and error, but it was thereby taken into account that the biaxial measurements had shown that $S'_{active}(N,N)$ could be between 20% and 62% of the $S'_{active}(F,F)$. The exact relation between $S'_{active}(N,N)$ and $S'_{active}(F,F)$ is however unknown (Lin and Yin 1998). We performed the calculations for different values of the two components of the stress tensor and compared the resulting deformations with MRI measurements of the left ventricle. From these calculations it could finally be concluded that at least one further component of the stress tensor has to be nonzero because with an active stress tensor with fibre and cross-fibre components only as

$$\mathbf{S}'_{active} = \begin{pmatrix} S'_{active}(F,F) & 0 & 0 \\ 0 & 0 & 0 \\ 0 & 0 & S'_{active}(N,N) \end{pmatrix} \tag{6.18}$$

the contraction itself could be simulated but it was associated with some swelling of the geometry, which disturbed the symmetry of the model. To our best knowledge this effect has been never reported and could not be seen in our MRI images either (Figure 6.10).

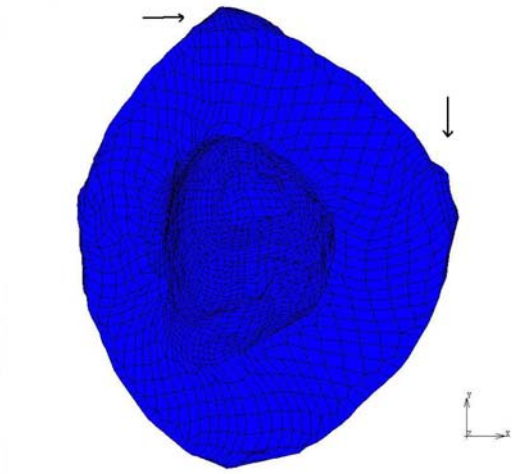

Figure 6.10 Contraction with fibre and cross-fibre component of stress tensor. Swelling are shown in the picture

The dense crosslinking of the myocytes suggested that a shear component exists in the active stress tensor; therefore, we decided to use an active stress tensor $\mathbf{S}'_{active}$ in the following form

$$\mathbf{S}'_{active} = \begin{pmatrix} S'_{active}(F,F) & 0 & 0 \\ 0 & 0 & S'_{active}(S,N) \\ 0 & S'_{active}(N,S) & S'_{active}(N,N) \end{pmatrix} \tag{6.19}$$

This form produced deformations which were essentially in agreement with MRI and MRT sequences (Figure 6.11).

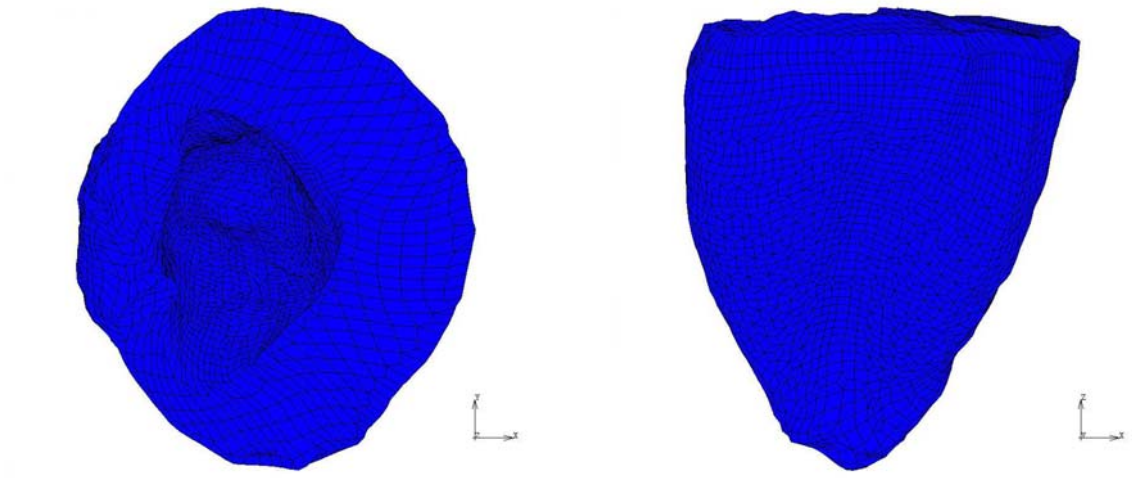

Figure 6.11 Contraction with fibre, cross-fibre and shear component of stress tensor

It should be remembered at this point that (6.19) represents the second Piola-Kirchhoff stress tensor in the local coordinate system of each element which has to be transformed according to equation (6.17) to the global coordinate system and added to the passive second Piola-Kirchhoff stress tensor as outlined in (6.9). Since our material model is purely transversely isotropic, it contains no information with respect to the probable orthotropic structure of the tissue. Accordingly, we can only speculate about the value of the shear component $S'_{active}(S,N)$. We concluded from the simulations that the shear component $S'_{active}(S,N)$ must be between 25% and 50% of the cross-fibre component $S'_{active}(N,N)$.

In a healthy adult heart, the ejection fraction, i.e. the volume of the output stroke to the end diastolic volume, is about 60%. This reduction of the volume is produced primarily by wall thickening, furthermore by radial motion of the epicardium toward the inside of the cavity and longitudinal shortening of the ventricle. It is thereby well known that the wall thickening plays the major role in contraction. Some studies suggest that the laminar architecture of the left ventricular myocardium may in fact be critical for ventricular mechanics, in particular, it has been postulated that, whereas fibre shortening is similar at the epicardium and endocardium and from apex to base (MacGowan and others 1997; Rademakers and others 1994; Waldman and others 1985), local wall thickening increases significantly from subepicardium to subendocardium (Rademakers and others 1994; Sabbah and others 1981; Waldman and others 1985) and may also be greater at the apex and midventricle than at the base (Azhari and others 1995; Rademakers and others 1994; Takeda and others 1992). There are various theories addressing the mechanism of wall thickening.

Some investigators suggested that rearrangement of the lamina in the myocardium is mainly responsible for wall thickening (MacGowan and others 1997; Rademakers and others 1994; Waldman and others 1985). Recently, it was hypothesised that, in addition to sliding of adjacent sheets, the myocardial sheets are dynamic structures that deform during contraction and both mechanisms i.e. sliding and deformation are important for the regional wall thickening (Costa and others 1999). In our model we do not have any laminar structure, so wall thickening during the contraction is the result of the longitudinal shortening and the radial motion of the epicardial surface toward the inside of the model only. Yet, the deformation of the elements can be compared with the suggested deformation of the sheets (Costa and others 1999). In order to reach a realistic amount of ejection which is about 60%, finally, we must apply somewhat higher forces, i.e., correspondingly bigger components of the stress tensor than is necessary for equilibrating the intracavital pressure.

The constitutive equation and the model of contraction were implemented within the framework of the commercial software MSC-Marc Mentat®. In the next chapter the various aspects of the implementation will be studied in detail.

References

Arts T, Reneman RS. 1989. Dynamics of left ventricular wall and mitral valve mechanics. J. Biomech. 22(3):261-271.

Arts T, Veenstra PC, Reneman RS. 1982. Epicardial deformation and left ventricular wall mechanics during ejection in the dog. American Journal of Physiology 243:H379-H390.

Azhari H, Weiss JL, Shapiro EP. 1995. Distribution of myocardial strains: an MRI study. Adv Exp Med Biol 382:319-28.

Beyar R, Sideman S. 1984a. A computer study of left ventricular performance based on fiber structure, sarcomere dynamics, and transmural electrical propagation velocity. Circ Res 55:358-375.

Beyar R, Sideman S. 1984b. Model for left ventricular contraction combining the force length velocity relationship with the time varying elastance theory. Biophys J 45:1167-1177.

Bovendeerd PH, Arts T, Delhaas T, Huyghe JM, van Campen DH, Reneman RS. 1996. Regional wall mechanics in the ischemic left ventricle: numerical modeling and dog experiments. Am J Physiol 270(1 Pt 2):H398-410.

Bovendeerd PH, Arts T, Huyghe JM, van Campen DH, Reneman RS. 1992. Dependence of local left ventricular wall mechanics on myocardial fiber orientation: a model study. J Biomech 25(10):1129-40.

Bovendeerd PH, Huyghe JM, Arts T, van Campen DH, Reneman RS. 1994. Influence of endocardial-epicardial crossover of muscle fibers on left ventricular wall mechanics. J Biomech 27(7):941-51.

Costa KD, Takayama Y, McCulloch AD, Covell JW. 1999. Laminar fiber architecture and three-dimensional systolic mechanics in canine ventricular myocardium. Am J Physiol 276(2 Pt 2):H595-607.

Cryer CW, Navidi-Kasmai H, Lunkenheimer PP, Redmann K. 1997. Computation of the alignment of myocardial contractile pathways using a magnetic tablet and an optical method. Technology and Health Care 5:79-93.

Falsetti HL, Mates RE, Grant C, Greene DG, Bunnell IL. 1970. Left ventricular wall stress calculated from one-plane cineangiography. Circ Res 26:71-83.

Fung YC. 1993. Biomechanics : mechanical properties of living tissues. New York: Springer-Verlag. xviii, 568 p.

Ghista DN, Sandler H. 1969. An analytic elastic-viscoelastic model for the shape and the forces in the left ventricle. J. Biomech. 2:35-47.

Gould P, Ghista DN, Brombolich L, Mirsky I. 1972. In vivo stresses in the human left ventricular wall: analysis accounting for the irregular 3d geometry and comparison with idealised geometry analyses. J. Biomech. 5:521-539.

Horowitz A, Perl M, Sideman S, Ritman E. 1986. Comprehensive model for the simulation of left ventricle mechanics. Part 2. Implementation and results analysis. Med Biol Eng Comput 24(2):150-6.

Huisman RM, Sipkema P, Westerhof N, Elzinga G. 1980. Comparison of models used to calculate left ventricular wall force. Med. Biol. Eng. Comput. 18:133-144.

Hunter PJ, Nielsen PM, Smaill BH, LeGrice IJ, Hunter IW. 1992. An anatomical heart model with applications to myocardial activation and ventricular mechanics. Crit Rev Biomed Eng 20(5-6):403-26.

Huyghe JM, Arts T, van Campen DH, Reneman RS. 1992. Porous medium finite element model of the beating left ventricle. Am J Physiol 262(4 Pt 2):H1256-67.

Janz RF, Waldron RJ. 1978. Predicted effect of chronical apical aneurysms on the passive stiffness of the human left ventricle. Circ Res 42(2):255-263.

LeGrice IJ, Hunter PJ, Smaill BH. 1997. Laminar structure of the heart: a mathematical model. Am J Physiol 272(5 Pt 2):H2466-76.

LeGrice IJ, Smaill BH, Chai LZ, Edgar SG, Gavin JB, Hunter PJ. 1995. Laminar structure of the heart: ventricular myocyte arrangement and connective tissue architecture in the dog. Am J Physiol 269(2 Pt 2):H571-82.

Lin DHS, Yin FC. 1998. A Multiaxial Constitutive law for Mammalian Left Ventricular Myocardium in Steady-State Barium Contracture or Tetanus. Journal of Biomechanical Engineering 120:504-517.

MacGowan GA, Shapiro EP, Azhari H, Siu CO, Hees PS, Hutchins GM, Weiss JL, Rademakers FE. 1997. Noninvasive measurement of shortening in the fiber and cross-fiber directions in the normal human left ventricle and in idiopathic dilated cardiomyopathy. Circulation 96(2):535-41.

Mirsky I. 1969. Left ventricular stresses in the intact human heart. Biophys J 9:189-208.

Nielsen PM, Hunter PJ, Smaill BH. 1991a. Biaxial testing of membrane biomaterials: testing equipment and procedures. J Biomech Eng 113(3):295-300.

Nielsen PM, Le Grice IJ, Smaill BH, Hunter PJ. 1991b. Mathematical model of geometry and fibrous structure of the heart. Am J Physiol 260(4 Pt 2):H1365-78.

Panda SC, Natarjan R. 1977. Finite-element method of stress analysis in the human left ventricular layered wall structure. Med. Biol. Eng. Comput. 15:67-71.

Pao YC, Robb RA, Ritman EL. 1976. Plane-strain finite-element analysis of reconstructed diastolic left ventricular cross section. Ann Biomed Eng 4:232-249.

Perl M, Horowitz A, Sideman S. 1986. Comprehensive model for the simulation of left ventricle mechanics. Part 1. Model description and simulation procedure. Med Biol Eng Comput 24(2):145-9.

Rademakers FE, Rogers WJ, Guier WH, Hutchins GM, Siu CO, Weisfeldt ML, Weiss JL, Shapiro EP. 1994. Relation of regional cross-fiber shortening to wall thickening in the intact heart. Three-dimensional strain analysis by NMR tagging. Circulation 89(3):1174-82.

Sabbah HN, Marzilli M, Stein PD. 1981. The relative role of subendocardium and subepicardium in left ventricular mechanics. Am J Physiol 240(6):H920-6.

Sandler H, Dodge HT. 1963. Left ventricular tension and stress in man. Circ Res 13:91-104.

Streeter DD, Basset JR, Basset DL. 1966. An engineering analysis of myocardial fibre orientation in pig's left ventricle in systole. The Anatomical Record 155:503-511.

Streeter DD, Spotnitz HM, Patel DP, Ross J, Sonnenblick EH. 1969. Fibre orientation in the canine left ventricle during diastole and systole. Circ Res 24:339-347.

Takeda T, Toyama H, Ishikawa N, Satoh M, Masuoka T, Ajisaka R, Iida K, Jin W, Sugishita Y, Itai Y. 1992. Quantitative phase analysis of myocardial wall thickening by technetium-99m 2-methoxy-isobutyl-isonitrile SPECT. Ann Nucl Med 6(2):69-78.

Usyk TP, Mazhari R, McCulloch AD. 2000. Effect of Laminar Orthotropic Myofiber Architecture on regional Stress and Strain in the Canine Left Ventricle. Journal of Elasticity 61:143-164.

Vetter FJ, McCulloch AD. 1998. Three-dimensional analysis of regional cardiac function: a model of rabbit ventricular anatomy. Prog Biophys Mol Biol 69(2-3):157-83.

Vinson CA, Gibson DG. 1979. Analysis of left ventricular behaviour in diastole by means of finite element method. Br. Heart J. 41:60-67.

Waldman LK, Fung YC, Covell JW. 1985. Transmural myocardial deformation in the canine left ventricle. Normal in vivo three-dimensional finite strains. Circ Res 57(1):152-63.

Wong AYK, Rautaharju PM. 1968. Stress distribution within the left ventricular wall approximated as a thick ellipsoidal shell. Am. Heart J. 75:649-662.

Yin FCP. 1985. Applications of the finite-element method to ventricular mechanics. CRC Crit. Rev. Biomed. Eng. 12:311-342.

CHAPTER 7

FINITE ELEMENT MODELING OF THE LEFT VENTRICLE – GEOMETRICAL APPROXIMATIONS II

In the last chapter we constructed a finite element model of the left ventricle. Thereby, we introduced the constitutive equation, the boundary conditions and a method for the implementation of contraction. Furthermore, large displacements were taken into account, i.e., the analysis was nonlinear, and the total Lagrangian method has been used. Therefore, the second Piola-Kirchhoff stress and Green-Lagrange strain tensors had to be used for the calculations.

In this chapter, we introduce the active stress tensor and assess the results of the simulation under the conditions of active contraction. In particular, two important characteristics of contraction will be discussed, i.e., the deformation pattern and the local wall thickening, which are basic determinants for the stroke volume.

7.1 Simulation of contraction

In chapter 5 various constitutive equations were discussed, which during the last decades have been proposed to describe the material behaviour of myocardial tissue. As mentioned in chapter 5, some of them have already been used for finite element

implementations by other investigators. Due to experimental restrictions in most of these approaches, the constitutive equations which were originally proposed for passive material behaviour have consistently been used also for the formulation of FE models of the active (systole) along with the passive state (diastole) of myocardial tissue.

The distribution of active stresses in myocardial tissue has not yet been determined experimentally (Huisman and others 1980b; Yin 1985) which is not astonishing in view of the practical difficulties associated with such a task. Some investigators have nevertheless developed theories about active stresses in the heart wall; they used constitutive equations either of passive myocardium or derived from theoretically based active stress simulations for finite element implementation of contraction (Arts and others 1982; Bovendeerd and others 1992; Huyghe and others 1992; Zahalak and others 1999).

However, these models have only partially been successful in modelling the experimentally measured value of stroke volume or a realistic deformation pattern of the myocardium during contraction; in particular, geometrical effects like wall thickening, longitudinal shortening and rotational motion of the myocardium have not yet been satisfactorily described (Bovendeerd and others 1996; Bovendeerd and others 1994). The published results confirm that more complicated mechanisms are involved in the motion of the heart, which to some extent still defy modelling.

In the following, we try to reproduce realistic and inhomogeneous deformation patterns as they are observed under clinical conditions and study the dependence of them on material behaviour and orientation of the fibres.

For this purpose, we use, as mentioned in the last chapter, a constitutive equation of active myocardial tissue according to Lin and Yin (1998), which was based on biaxial experimental tests (Equation 6.19). This equation describes significantly stiffer material than the other equations, proposed by the same authors for myocardium in passive state (Lin and Yin 1998; Novak and others 1994), but has a little different functional form. Yet, the material behaviour of active tissue changes with the time, an effect, which has

not yet been studied such that we are forced to use the constitutive equation that characterizes the behaviour of the fully contracted tissue. Thereby, we do not assume any laminar structure or fibre rearrangement in the material. The existence of such structures or fibre rearrangements, however, is expected to influence the procedure of contraction significantly. In particular, we expect that the values of the components of the applied second Piola-Kirchhoff active stress tensor $\mathbf{S}'_{active}$, which are necessary to simulate the contraction, are therefore bigger than the real values.

We define now the values of the components that must be added to the passive stress tensor in each increment in order to simulate active contraction. For simplicity, we assume that these values are equal for all elements and they do not have any dependence on time or microstructure of the fibres like sarcomere length or the velocity of sarcomere shortening.

We set the incremental values of the second Piola-Kirchhoff active stress tensor $\mathbf{S}'^{\,inc}_{active}$ as follows

$$\mathbf{S}'^{\,inc}_{active} = \begin{pmatrix} 3 & 0 & 0 \\ 0 & 0 & 0.6 \\ 0 & 0.6 & 1.8 \end{pmatrix} \tag{7.1}$$

Here we assumed that the value of $S'_{active}(N,N)$ is about 60% of $S'_{active}(F,F)$, and the value of $S'_{active}(S,N)$ is about 33% of $S'_{active}(N,N)$. $\mathbf{S}'^{\,inc}_{active}$ will be added to the passive stress tensor in each increment, such that the number of increments determines the final level of active stress. All values of the stress components in $\mathbf{S}'^{\,inc}_{active}$ are given in kPa.

In a first step, the contraction process is modelled with 30 increments. Figures (7.1A) and (7.2A) show the mesh before the onset of the deformation. The results of the simulation are shown in Figures (7.1B) and (7.2B). All values of the maximal principal Cauchy stresses are given in Pa.

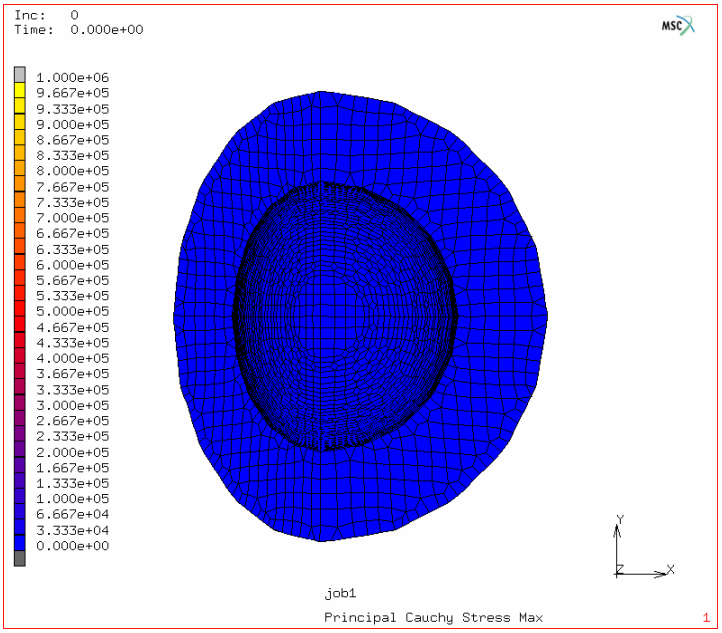

A

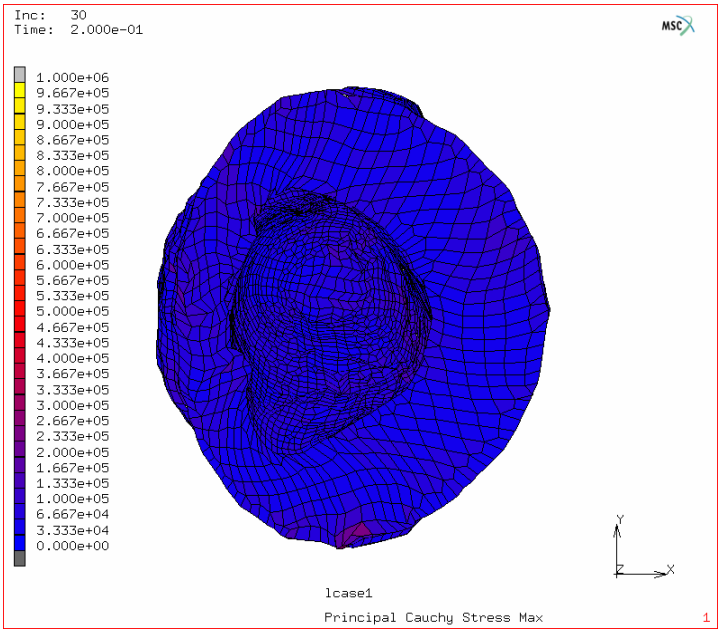

B

Figure 7.1 FE implementation of contraction, up view (A) before deformation (B) after deformation

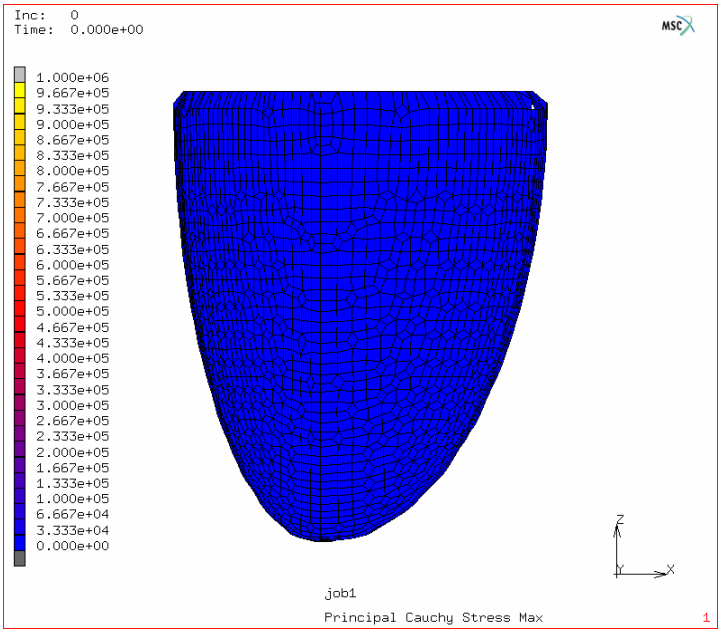

A

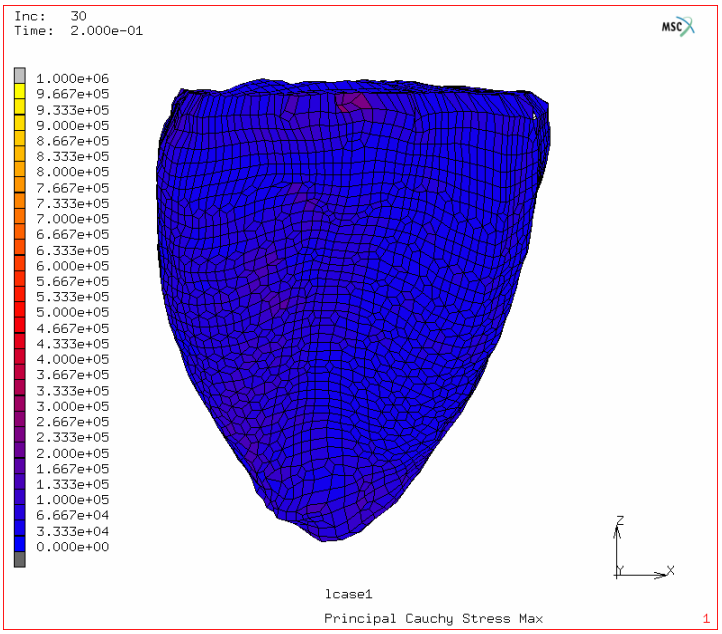

B

Figure 7.2 FE implementation of contraction, front view (A) before deformation (B) after deformation

The deformation of the endocardial surface is shown in Figure (7.3). Here, the volume of the left ventricle reduces from the initial value of 137ml to the final value of 102ml.

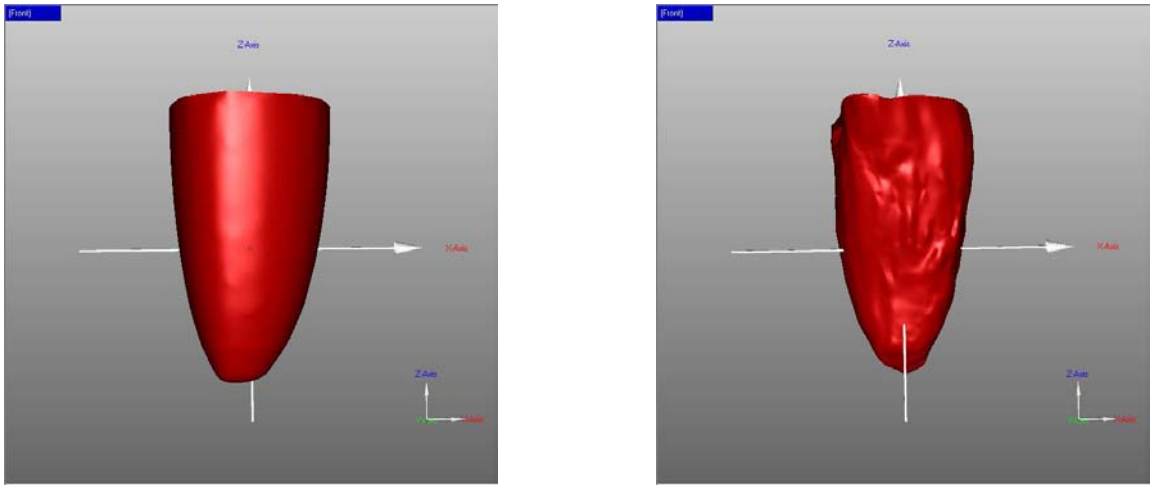

A **B**

Figure 7.3 Deformation of endocardial surface, front view (A) before contraction (B) after contraction with 30 increments

Next, we increase the number of increments to 50 and simulate the contraction again. Figure (7.4) shows the endocardial surface.

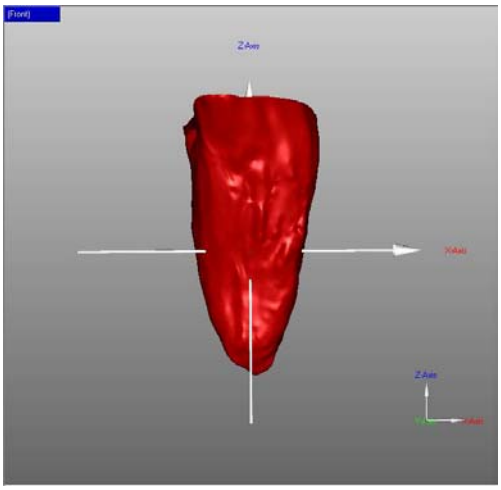

Figure 7.4 Deformation of the endocardial surface after 50 increments

In this case, the volume of the left ventricle reduces from the initial value of 137ml to the final value of 85 ml. The finite element implementation is shown in Figure (7.5).

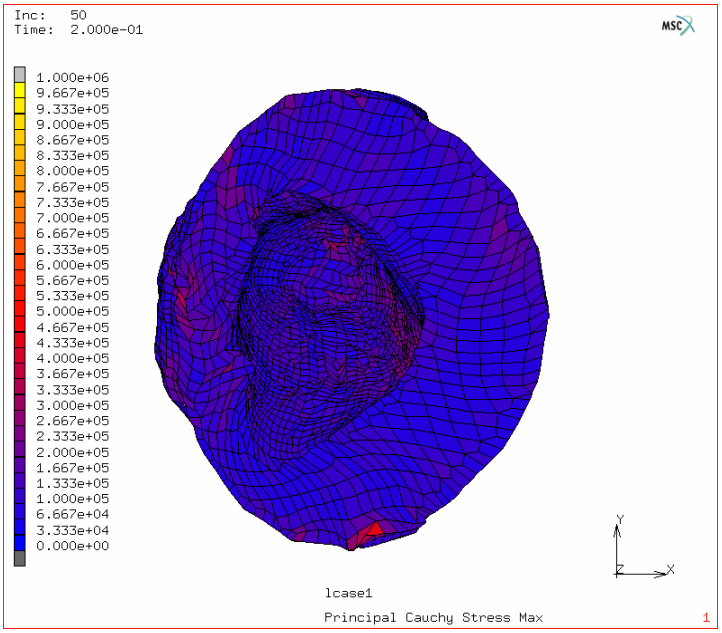

A

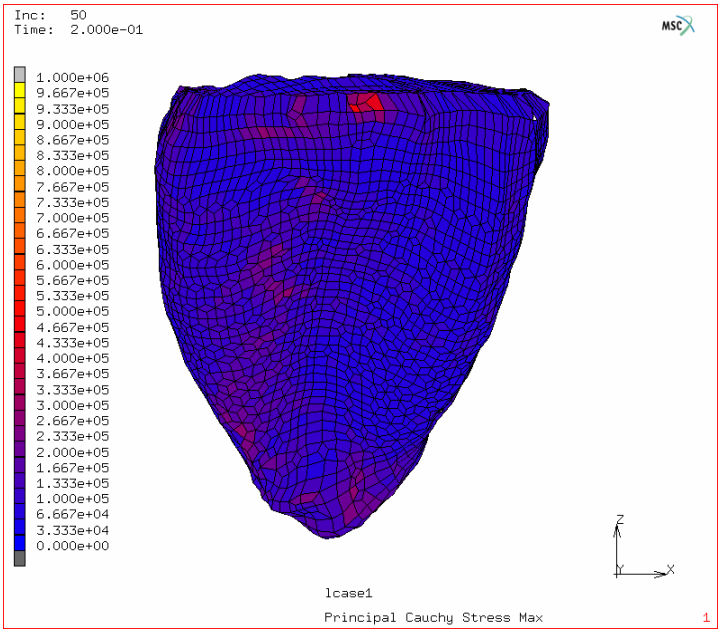

B

Figure 7.5 FE implementation of contraction, front view (A) before deformation (B) after deformation

Finally, we increase the number of increments to 70 and simulate the contraction. The endocardial surface and FE implementation are shown in Figures (7.6) and (7.7), respectively.

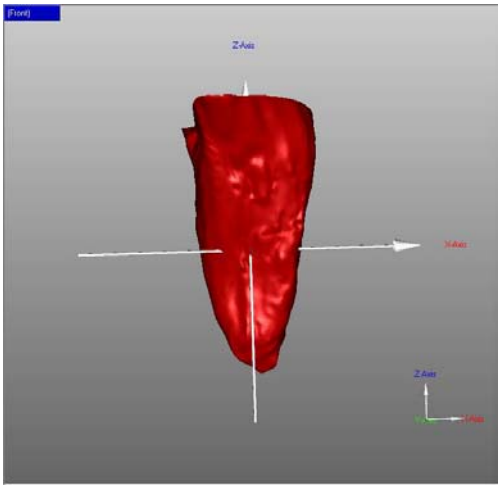

Figure 7.6 Deformation of endocardial surface with 70 increments

In this case, the volume of the left ventricle reduces from the initial value of 137ml to the final value of 75 ml.

It is seen that the ventricular volume does not reduce with the same rate as the number of increments increases, but the rate of volume reduction decreases consistently. This effect can be explained in that more resistance against the deformation develops as the radius of curvature of the ventricle decreases. At the same time, areas exhibiting high stresses develop, which can be seen in red in Figure (7.7). This is particularly well apparent on the endocardial surface.

It has been observed already earlier that the myocardial wall stress can not be measured under *in vivo* conditions. Nevertheless, in a number of published mathematical models attempts have been made to estimate the stress distribution in the ventricular wall. Some of these models give information about the stress distribution over the thickness of the wall as well. Given the experimental uncertainty, it is not astonishing that large differences between the stresses were predicted by the various models for the same cardiac geometry(Huisman and others 1980a; Huisman and others 1980b; Yin 1981; Yin 1985). As a general rule, predicted peak values of the wall stress in most models are around 100 kPa (Bovendeerd and others 1992; Bovendeerd and others 1994; Horowitz and others 1986).

Since the properties of the myocardial tissue change dramatically during the cardiac cycle, serious scepticism concerning the calculated stress distributions is indicated, in particular as a considerable experimental uncertainty exists likewise with respect to the constitutive properties of the cardiac material. If it is attempted to reproduce the inhomogeneous deformation patterns as they are observed under clinical conditions while applying constitutive equations of active myocardial tissue according to Lin and Yin (1998) it is found that the value of the maximal principal Cauchy stress increases in comparison with earlier models using a smoother geometry. This confirms that other mechanisms, for example, possible effects associated with the layered structure of the myocardium suggested by LeGrice and co-workers (1995), are necessary to describe the contraction completely and produce a physiologic stroke volume with lower values of the maximal principal Cauchy stresses.

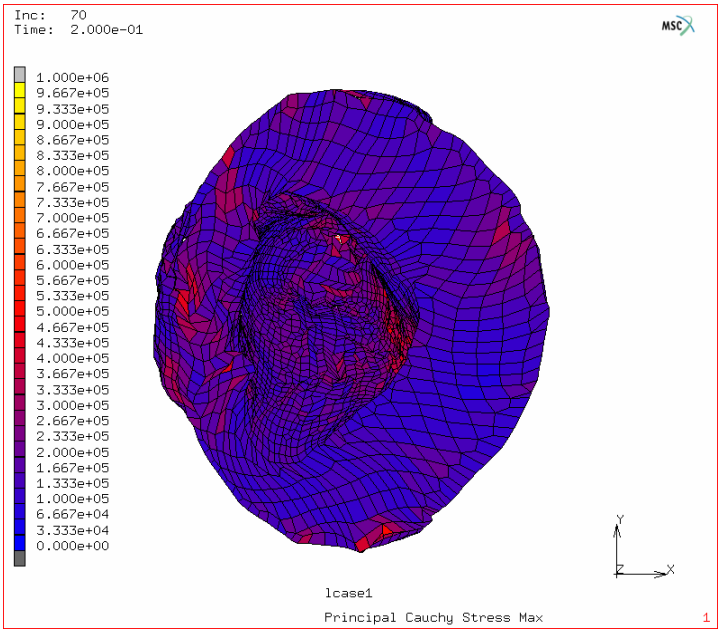

A

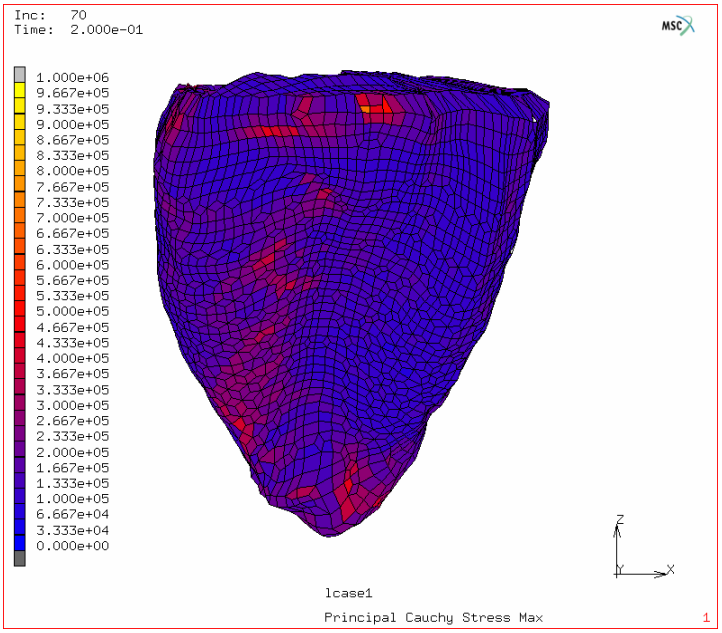

B

Figure 7.7 FE implementation of contraction, front view (A) before deformation (B) after deformation

7.2 Wall thickening

Because of its significant contribution to the stroke volume, wall thickening is of particular interest as a functional measure. In order to assess wall thickening, we consider short axis cross section of parallel equidistant planes exhibiting the geometry of the left ventricle before and after deformation (Figure 7.8). The geometry at the end of contraction is reconstructed from the deformed mesh of Figure (7.7).

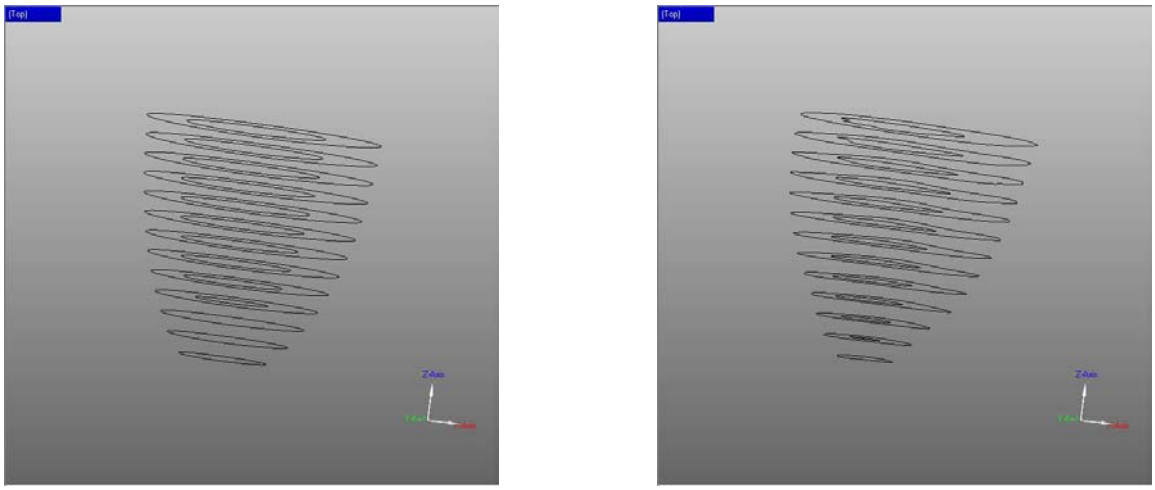

A **B**

Figure 7.8 Cross section of parallel planes with the geometry of the left ventricle (A) before deformation (B) after deformation

We merge both series of cross sections to allow for a comparison (Figure 7.9).
In these Figure, the deformed curves are shown in red.

Figure 7.9 shows that, as a general rule, local wall thickening in each cross section has an irregular distribution but it is remarkable that in cross sections 3, 4, 5 and 6 which are at a distance between 2.4 cm and 4.5 cm underneath the base, maximal wall thickening can be more than 40%. A real heart has a quite complex geometry, especially in the apical area. This area can in particular not be approximated by a deformed spheroid in a straightforward manner and the results of the simulation in this area must therefore be interpreted carefully.

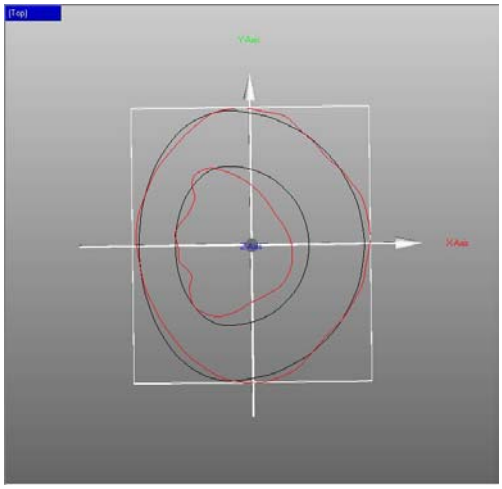
[Top]
YAxis
XAxis

1

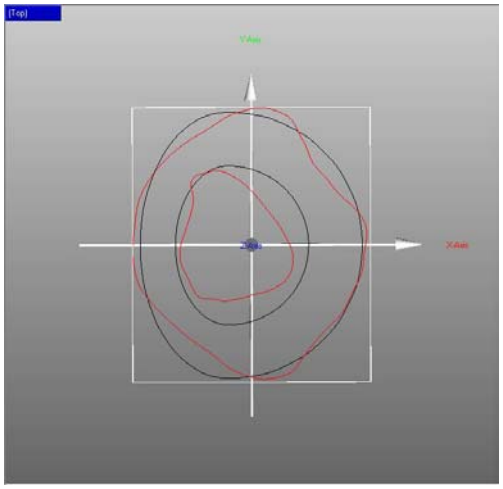
[Top]
YAxis
XAxis

2

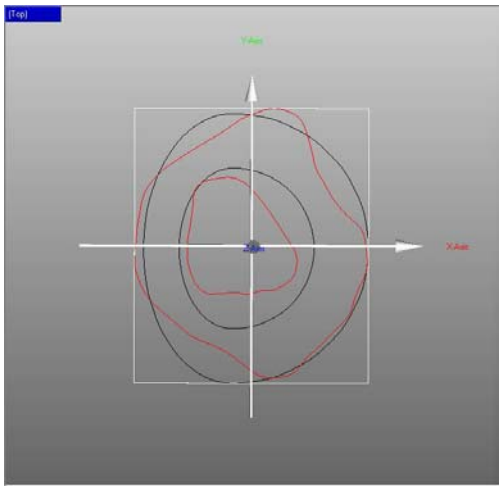
[Top]
YAxis
XAxis

3

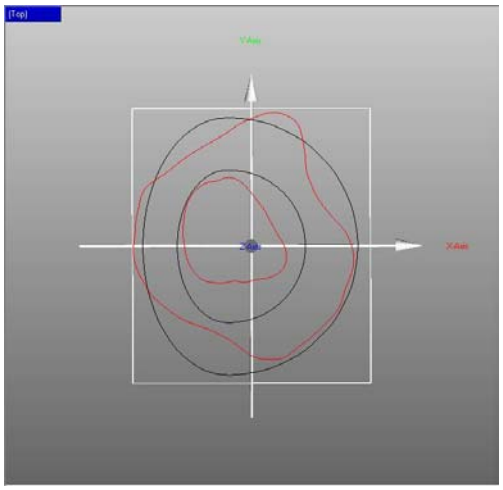
[Top]
YAxis
XAxis

4

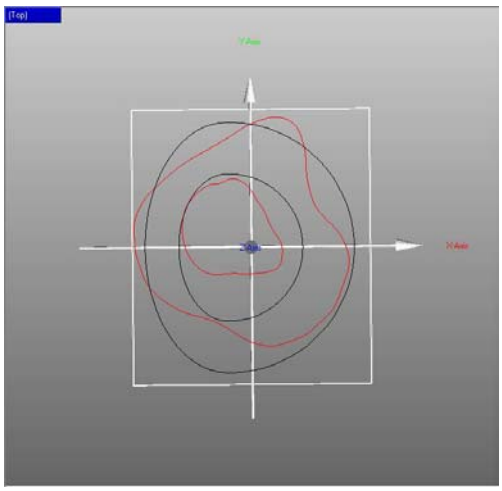
[Top]
YAxis
XAxis

5

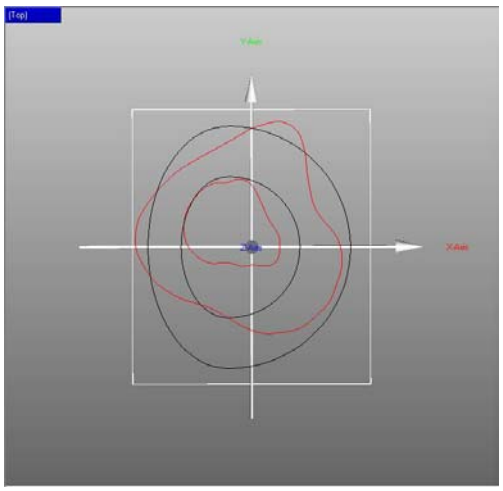
[Top]
YAxis
XAxis

6

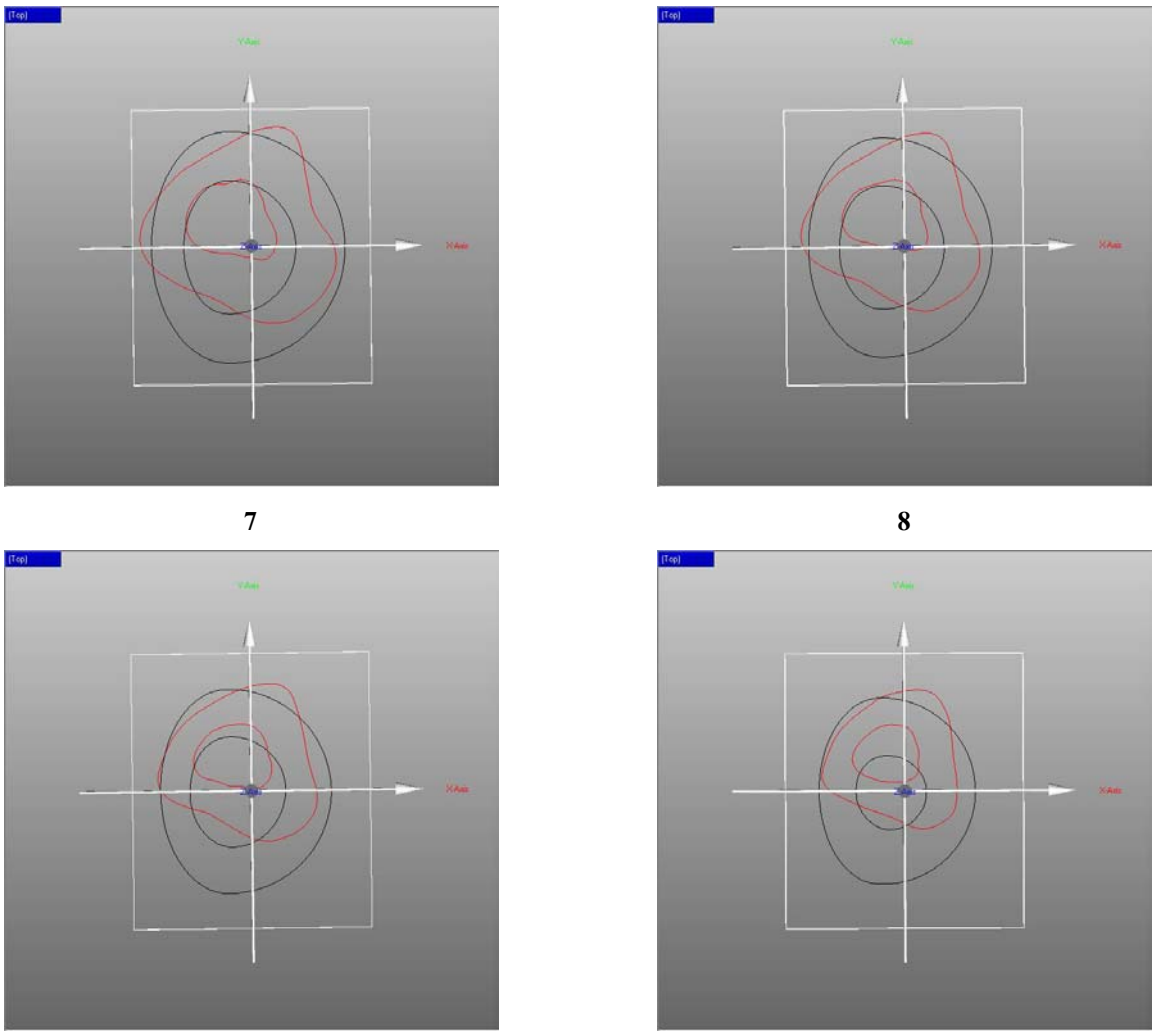

7 **8**

9 **10**

Figure 7.9 Cross sections of deformed (or contracted in red) and undeformed (in black) geometry are compared together

7.3 Material behaviour

In subsection 7.1 we introduced the incremental values of second Piola-Kirchhoff active stress tensor $\mathbf{S}'^{\,inc}_{active}$. It is not always easy to estimate these values; actually large estimated values can quickly cause numerical problems. An alternative method for the simulation of the contraction is to define the total second Piola-Kirchhoff active stress tensor $\mathbf{S}'^{\,total}_{active}$ and improve the subroutine so that the program determines the number of necessary

increments, the time distribution of increments and the best value of incremental second Piola-Kirchhoff active stress tensor $\mathbf{S}'^{\,inc}_{active}$. In this later method the boundary conditions must be corrected and instead of the equation (6.4) for the pressure we must define a constant mean value for the inside pressure. This method reduces the number of increments and the time of calculation remarkably. Because we want to compare the results of simulation of different constitutive equations, we use this later method with constant inter ventricular pressure of 14 kPa and defined total second Piola-Kirchhoff active stress tensor $\mathbf{S}'^{\,total}_{active}$ as in equation (7.2).

$$\mathbf{S}'^{\,total}_{active} = \begin{pmatrix} 140 & 0 & 0 \\ 0 & 0 & 21 \\ 0 & 21 & 84 \end{pmatrix} \tag{7.2}$$

We used the same mesh and boundary conditions as explained in subsection 7.1. Different constitutive equations are implemented, to determine the influence of material behaviour on pattern of deformation, especially irregularities of deformed endocardial surfaces.

The first constitutive equation is equation (6.6), which shows the material behaviour of active myocardium (Lin and Yin 1998) and was used for the simulations of the last subsections (Figure 7.10A).

$$\begin{aligned} W_{active}(I_1, I_4) = {} & C_0 + C_1(I_1 - 3)(I_4 - 1) + C_2(I_1 - 3)^2 \\ & + C_3(I_4 - 1)^2 + C_4(I_1 - 3) + C_5(I_4 - 1) \end{aligned} \tag{7.3}$$

where the material parameters (in g/cm^2) are chosen as follows

$$\begin{aligned} C_1 &= -7.89 \\ C_2 &= 66.20 \\ C_3 &= 51.12 \\ C_4 &= 40.12 \\ C_5 &= 0.0032 \end{aligned} \tag{7.4}$$

The second implemented material behaviour is the constitutive equation of passive myocardium (Equation 5.10)

$$\begin{aligned} W(I_1, \lambda) = {} & C_1(\lambda - 1)^2 + C_2(\lambda - 1)^3 + C_3(I_1 - 3) \\ & + C_4(I_1 - 3)(\lambda - 1) + C_5(I_1 - 3)^2 \end{aligned} \tag{7.5}$$

where the material constants are

$$
\begin{aligned}
C_1 &= 2.753 \quad kPa \\
C_2 &= 15.01 \quad kPa \\
C_3 &= 0.003 \quad kPa \\
C_4 &= -7.356 \quad kPa \\
C_5 &= 5.405 \quad kpa
\end{aligned}
\tag{7.6}
$$

Figure (7.10B) shows the results of simulation.

In chapter 5 we explained that a transversely isotropic material can be idealized as being composed of a noninteracting bundle of fibers and a matrix. The fibers are continuously distributed and can interact with the matrix.

We would like to compare the behaviour of this isotropic matrix with our transversely isotropic constitutive equations. We assume that activated matrix behaves like a Mooney-Rivlin material

$$
\begin{aligned}
W(I_1, I_2) = C_{10}(I_1 - 3) + C_{01}(I_2 - 3) + C_{11}(I_1 - 3)(I_2 - 3) \\
+ C_{20}(I_1 - 3)^2 + C_{30}(I_1 - 3)^3
\end{aligned}
\tag{7.7}
$$

comparison of (7.7) and (7.3) shows that both equations have similar polynomial dependence on I_2 and I_4 respectively, so we decided to choose Mooney-Rivlin material parameters (in $^{g}/_{cm^2}$) as follows (Figure 7.10C)

$$
\begin{aligned}
C_{10} &= 40.12 \\
C_{01} &= 0.0032 \\
C_{11} &= -7.89 \\
C_{20} &= 66.20 \\
C_{30} &= 0.0
\end{aligned}
\tag{7.8}
$$

As the forth material we choose a linear elastic material behaviour for the matrix with assumed *E* modulus and Poisson's ratio as follows (Figure 7.10D)

$$
\begin{aligned}
E &= 200 \quad kPa \\
\nu &= 0.48
\end{aligned}
\tag{7.9}
$$

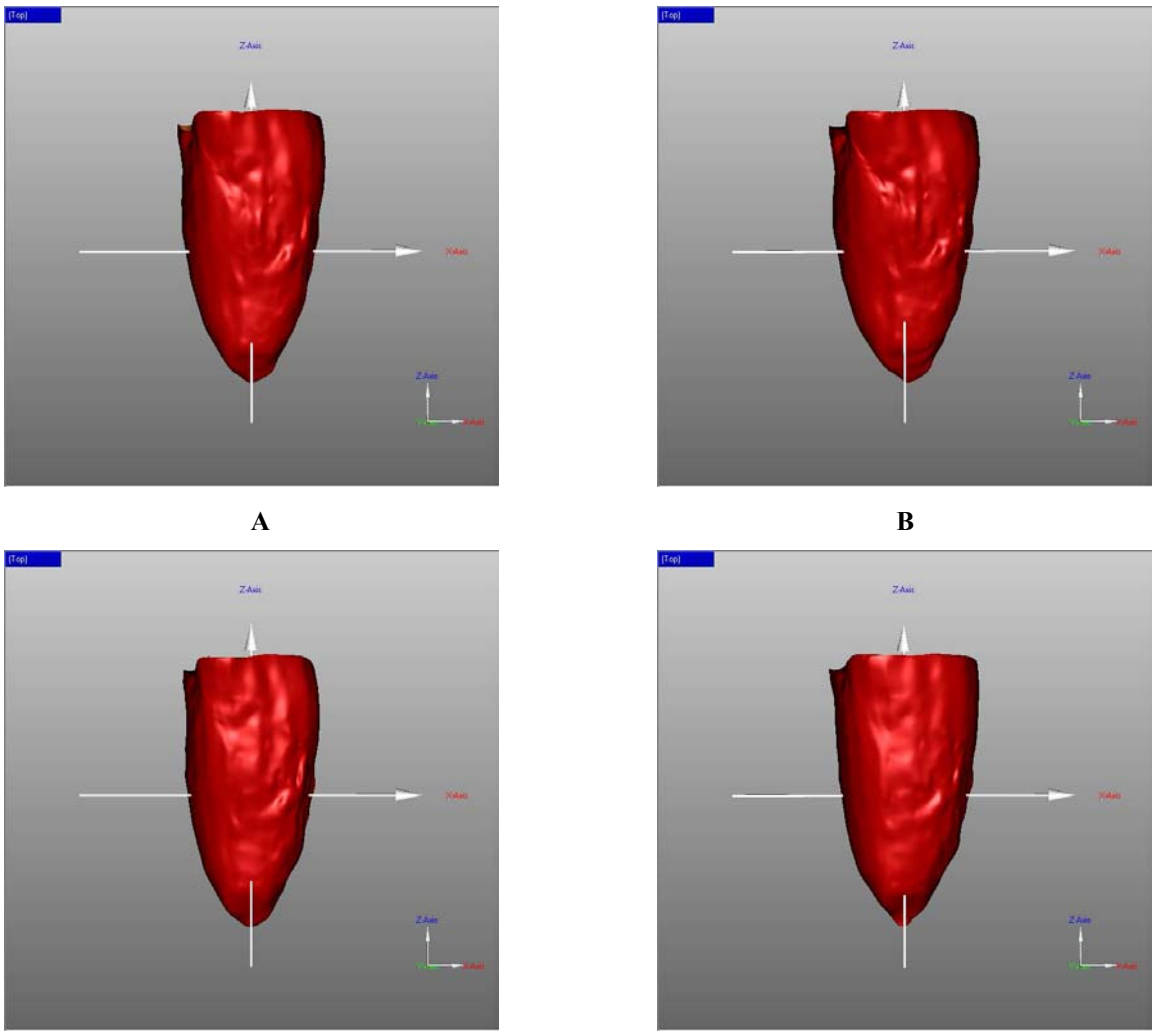

Figure 7.10 (A) Active material, (B) Passive material, (C) Mooney-Rivlin material, (D) Linear elastic material

In these simulations of contraction, the volume of the left ventricle reduces from original value of 137 ml to the final value of 106ml for active material (7.3), 110 ml for passive material (7.5), 107 ml for Mooney-Rivlin (7.7) , and 108 ml for linear elastic material (7.9).

Figure 7.11 shows cross section of the deformed geometry with three planes parallel and about 2cm under the base (Figure 7.11A), 3cm under the base (Figure 7.11B) and 4cm under the base (Figure 7.11C).

Comparison of these Figures show that how material behaviour can influence the pattern of deformation, even though all other conditions are the same.

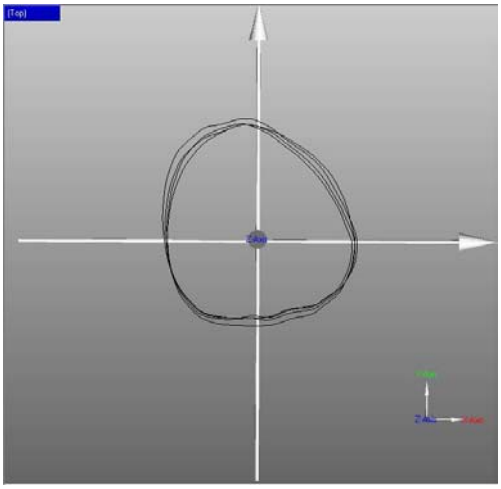

A

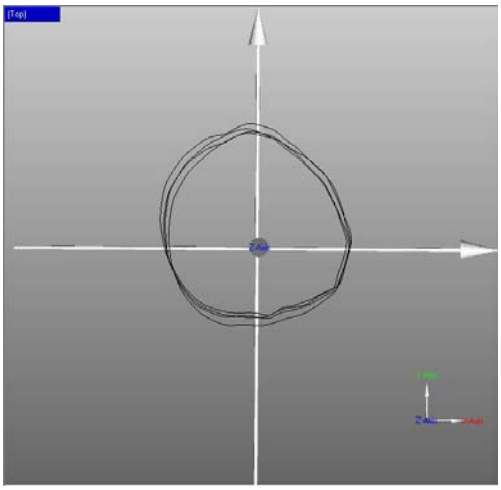

B

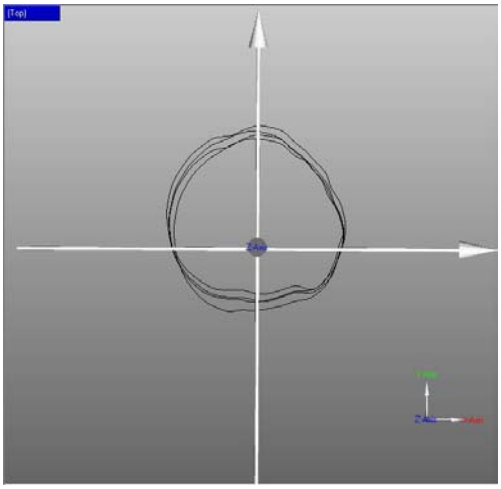

C

Figure 7.11 Cross section of three parallel planes with deformed geometry for different material behaviour

7.4 Fibre orientation

It is instructive to know how fibre orientation can influence the pattern of deformation. We choose another digitalized fibre orientation (Figure 7.12), from a pig heart in systole state, and with the method of chapter 3 produce a new fibre vector field for the same geometry as used in last subsections. Figure 7.12A shows left ventricle of a human heart, where Figure 7.12B shows the left ventricle of a pig heart. Both hearts are digitized in similar spatial situations i.e. the right ventricles in both figures are in the left side. Apparently these two fibre orientations produce different fibre vector fields for the same geometry.

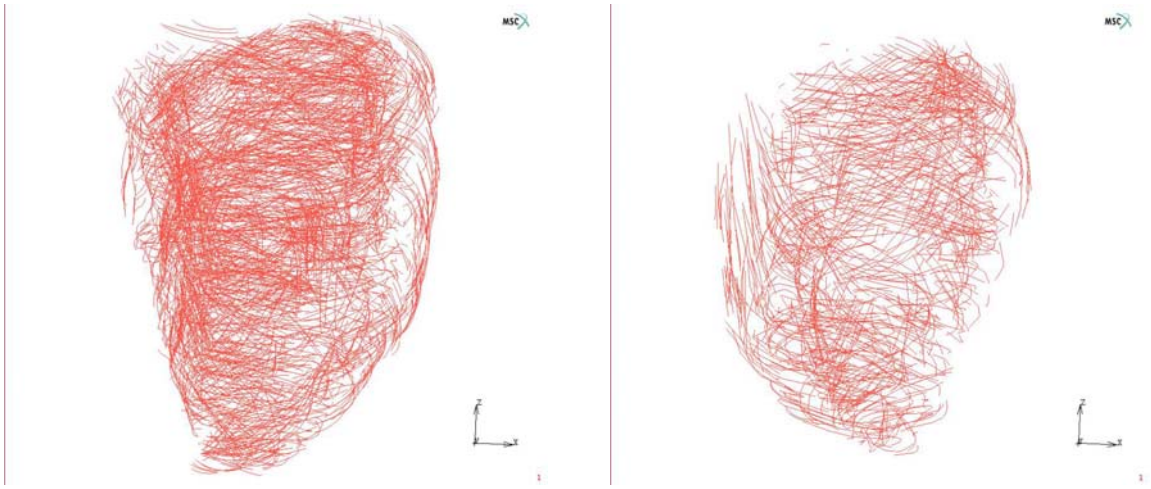

A **B**

Figure 7.12 Fibre orientation of the left ventricle (A) human heart (B) pig heart

We simulate the contraction with the same second Piola-Kirchhoff active stress tensor $\mathbf{S}'^{\,total}_{active}$ as in equation (7.2) and the same boundary conditions as in last subsections. Figure (7.13B) shows the results of simulation for active material (7.3) with coefficients(7.4). Deformed endocardial surface of Figure (7.10A) is shown again for the comparison (Figure 7.13A). These figures show that change in fibre orientation can change the pattern of deformation and the stroke volume significantly. In this case the volume of the left ventricle reduces from the initial value of 137 ml to the final value of 116 ml (Figure

7.13B), which is 10 ml less than the same implementation with last fibre vector field (Figure 7.13A). This means that the stroke volume has been reduced more than 30%.

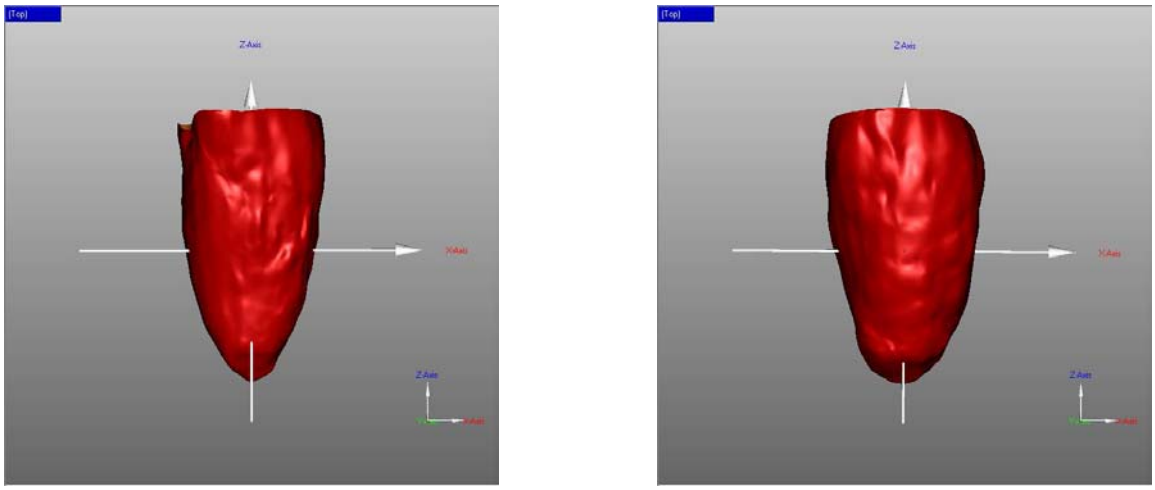

A B

Figure 7.13 Deformed endocardial with the fibre orientation of (A) human heart (B) pig heart

Cross sections of these two deformed endocardial surfaces with three planes parallel to base, and about 2cm, 3cm and 4cm under the base respectively, are shown in Figure (7.14). In these figures red and black curves show cross sections of the deformed geometry with the new and old fibre orientations respectively.

These figures show that even for a very smooth geometry and same boundary conditions and material behaviours, fibre orientation has a remarkable influence on local deformation of the endocardial surface.

Differences in fibre structures of the left ventricle in diastole and systole, as well as the geometrical details of the apex need deeper studies. These details could play an essential role in local wall thickening i.e. stroke volume, and stress distribution in the heart wall.

In the next chapter we begin to study the contraction of a more realistic geometry of the left ventricle.

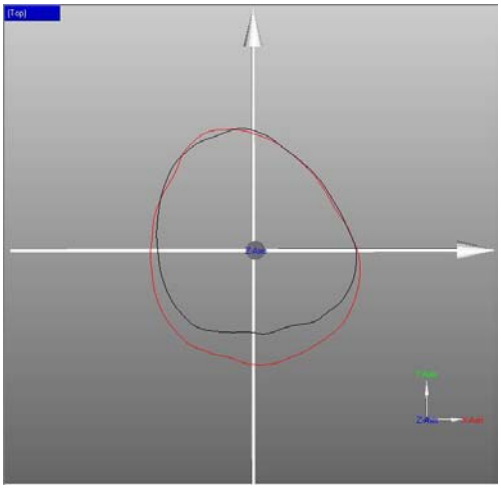

A

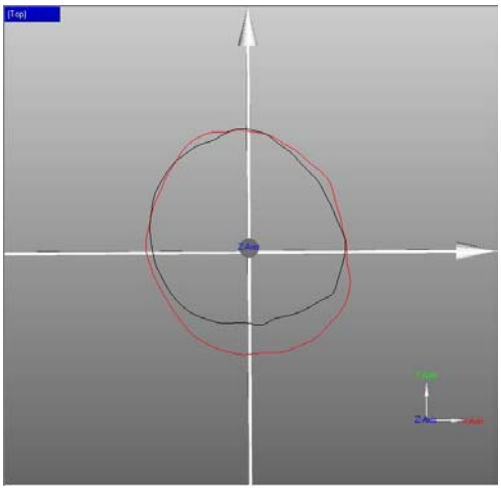

B

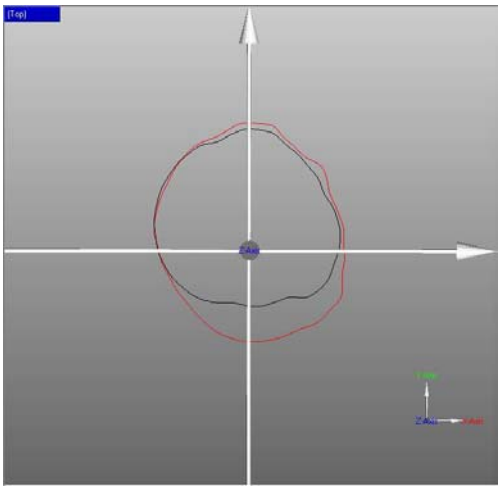

C

Figure 7.14 Cross section of three parallel planes with deformed geometry for different fibre orientations

References

Arts T, Veenstra PC, Reneman RS. 1982. Epicardial deformation and left ventricular wall mechanics during ejection in the dog. American Journal of Physiology 243:H379-H390.

Bovendeerd PH, Arts T, Delhaas T, Huyghe JM, van Campen DH, Reneman RS. 1996. Regional wall mechanics in the ischemic left ventricle: numerical modeling and dog experiments. Am J Physiol 270(1 Pt 2):H398-410.

Bovendeerd PH, Arts T, Huyghe JM, van Campen DH, Reneman RS. 1992. Dependence of local left ventricular wall mechanics on myocardial fiber orientation: a model study. J Biomech 25(10):1129-40.

Bovendeerd PH, Huyghe JM, Arts T, van Campen DH, Reneman RS. 1994. Influence of endocardial-epicardial crossover of muscle fibers on left ventricular wall mechanics. J Biomech 27(7):941-51.

Horowitz A, Perl M, Sideman S, Ritman E. 1986. Comprehensive model for the simulation of left ventricle mechanics. Part 2. Implementation and results analysis. Med Biol Eng Comput 24(2):150-6.

Huisman RM, Elzinga G, Westerhof N, Sipkema P. 1980a. Measurment of the left ventricular wall stress. Cardiovasc Res 14:142-153.

Huisman RM, Sipkema P, Westerhof N, Elzinga G. 1980b. Comparison of models used to calculate left ventricular wall force. Med. Biol. Eng. Comput. 18:133-144.

Huyghe JM, Arts T, van Campen DH, Reneman RS. 1992. Porous medium finite element model of the beating left ventricle. Am J Physiol 262(4 Pt 2):H1256-67.

LeGrice IJ, Takayama Y, Covell JW. 1995. Transverse shear along myocardial cleavage planes provides a mechanism for normal systolic wall thickening. Circ Res 77(1):182-93.

Lin DHS, Yin FC. 1998. A Multiaxial Constitutive law for Mammalian Left Ventricular Myocardium in Steady-State Barium Contracture or Tetanus. Journal of Biomechanical Engineering 120:504-517.

Novak VP, Yin FC, Humphrey JD. 1994. Regional mechanical properties of passive myocardium. J Biomech 27(4):403-12.

Yin FC. 1981. Ventricular Wall Stress. Circ Res 49, No.4(Oct):829-842.

Yin FCP. 1985. Applications of the finite-element method to ventricular mechanics. CRC Crit. Rev. Biomed. Eng. 12:311-342.

Zahalak GI, de Laborderie V, Guccione JM. 1999. The effects of cross-fiber deformation on axial fiber stress in myocardium. J Biomech Eng 121(4):376-85.

CHAPTER 8

FINITE ELEMENT MODELING OF THE LEFT VENTRICLE – REALISTIC GEOMETRY

In the last two chapters we developed a finite element model of the left ventricle. We thereby used a geometrical approximation and studied the pattern of contraction, wall thickening and the effect of different kinds of material behaviour. In this chapter we attempt to refine the geometry and study its effect on local wall thickening. We use the active material behaviour of equation (6.6), the boundary conditions as described in subsection 6.4, and follow the same method as worked out in depth in chapters 6 and 7, respectively.

8.1 Simulation of contraction

In a realistic left ventricular geometry, the local radius of curvature at different locations of the endocardial and epicardial surfaces can be positive or negative and exhibit large variations. Because the local geometry has a significant influence on the stress distribution and the deformation pattern, the geometrical details have to be taken into account in the model. Yet, the construction of a network, i.e. the meshing procedure, will be more difficult as the geometry becomes more complicated. Manual meshing is very time-consuming while automatic meshing requires extensive testing and manual

adaptation. The development of a suitable mesh for a realistic geometry is therefore a nontrivial step.

As a first step towards the model of a real left ventricle, we used the geometry as shown in Figure (8.1). This geometry was produced from digitized points of the endocardial and epicardial surfaces of a human heart, as explained in chapter 3, but the surface was smoothed and truncated at the base. These modifications simplified the application of the boundary conditions at the base as described in subsection 6.4.

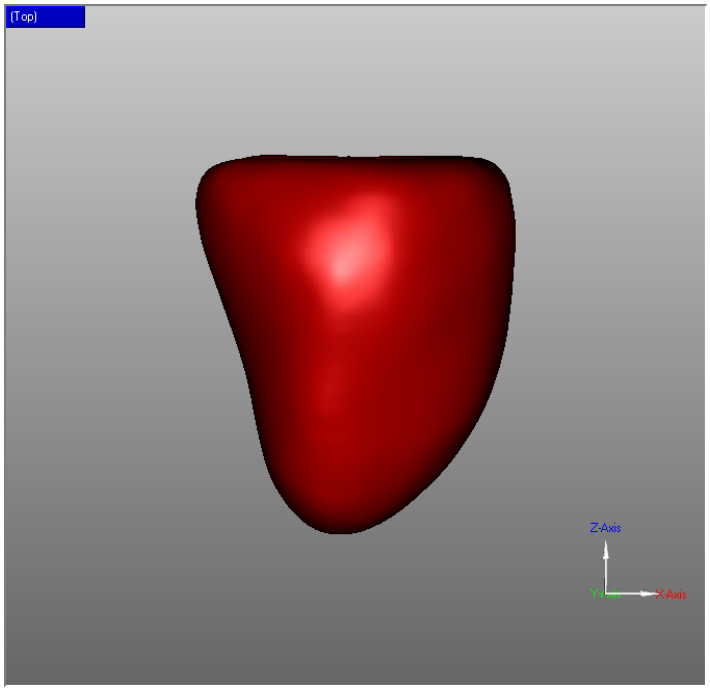

Figure 8.1 Real geometry of a smoothed and truncated (at the base) human heart

A mesh consisting of more than 19,600 eight-node hexahedral elements was created with the help of the hex-mesh generator of the commercial software package MSC-MarcMentat® (Figure 8.2A).

When working with real geometries, care has to be exercised with respect to the modeling of contraction. In the last two chapters we developed two numerically different methods for the simulation of contraction. In the first method we added the incremental

second Piola-Kirchhoff active stress tensor $\mathbf{S}'^{\,inc}_{active}$ to the second Piola-Kirchhoff passive stress tensor and determined the number of increments. In the second method we prescribed the final second Piola-Kirchhoff active stress tensor $\mathbf{S}'^{\,total}_{active}$ and used an adaptive algorithm for the determination of the number of necessary increments along with the incremental value of the stress tensor.

Generally, both of these methods can be used in case of a real geometry, but it was found that automatic meshing leads to models where either one or the other method converges easier, even though by regulating the parameters also the method which is not well suited can be applied after appropriate testing and adaptation.

In this subsection we applied the first method and chose $S'_{active}(F,F)$ equal to 3 kPa and the incremental values of the second Piola-Kirchhoff active stress tensor $\mathbf{S}'^{\,inc}_{active}$ (in kPa) as follows

$$\mathbf{S}'^{\,inc}_{active} = \begin{pmatrix} 3 & 0 & 0 \\ 0 & 0 & 0.3 \\ 0 & 0.3 & 1.8 \end{pmatrix} \tag{8.1}$$

This choice was found to be favourable for convergence up to 70 increments. Theoretically, the number of increments can be increased until the mesh fails, but from a physiological point of view bigger values are not relevant. Results of the simulation are shown in Figure (8.2B).

The local irregularities of the epicardial and endocardial surfaces were seen to cause large deformations associated with high stress regions, especially in subendocardial layers, where the radius of curvature was in general smaller than elsewhere. This effect was indeed expected and already observed by other investigators (Arts and others 1982; Bovendeerd and others 1996; Bovendeerd and others 1992; Bovendeerd and others 1994; Huyghe and others 1992). Subepicardial layers near the apex exhibit some high stress regions likewise. As mentioned in the last chapter, however, the apex has quite an irregular geometry and the accuracy of our digitized data was not sufficient to reproduce

all details of its structure. Accordingly, the stress distribution along with the deformation pattern in the apical region will need further consideration in the future based on more precise geometrical data.

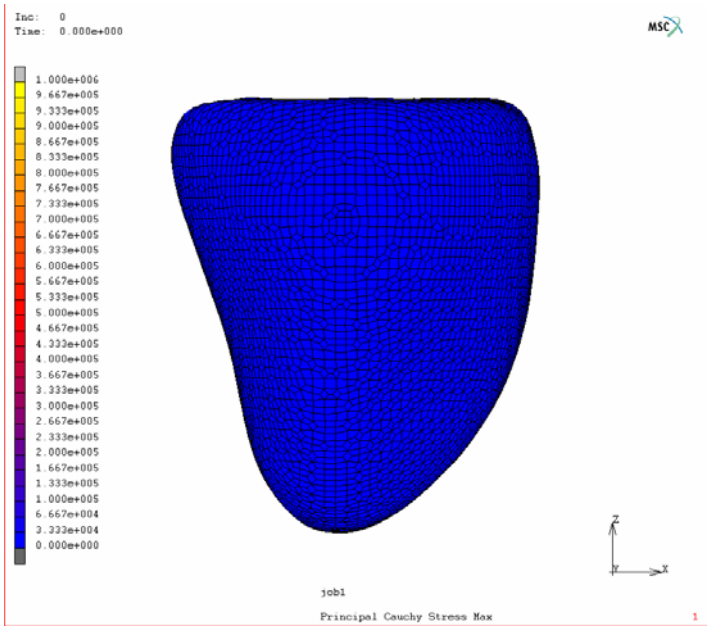

A

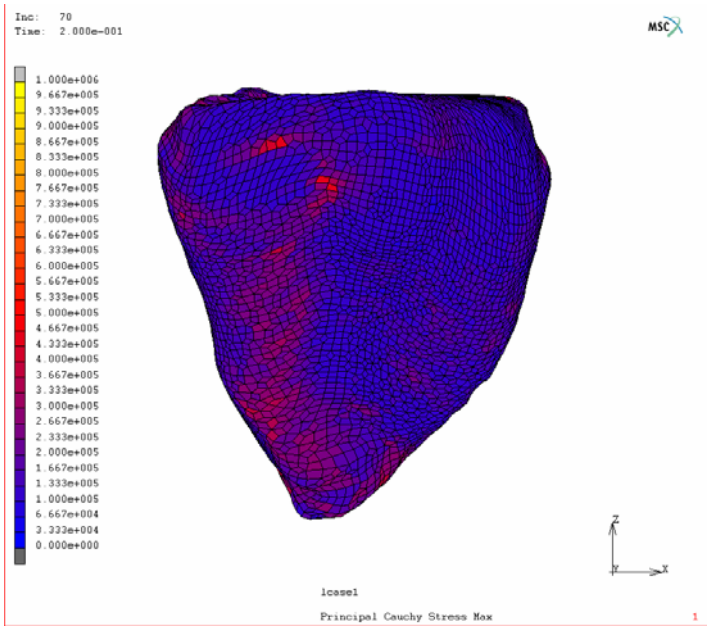

B

Figure 8.2 FE implementation of contraction, front view (A) before deformation (B) after deformation

The deformation of the endocardial surface is shown in Figure (8.3). In this calculation, the volume reduction of the left ventricle, i.e., the stroke volume is about 47%. This result is somewhat less than the physiologic value, but near the results of subsection 7.1 even though in this case a reduced active stress tensor was applied. An important difference between the geometry used here (Figure 8.2A) and the smooth geometrical approximation of the last chapter (Figure 7.2A) is that in Figure (8.2A) the curvature of the septal surface is opposite to the curvature of the septum in the last chapter. This fact confirms that the geometry, especially the local curvature, can reduce the active stress needed for similar deformations.

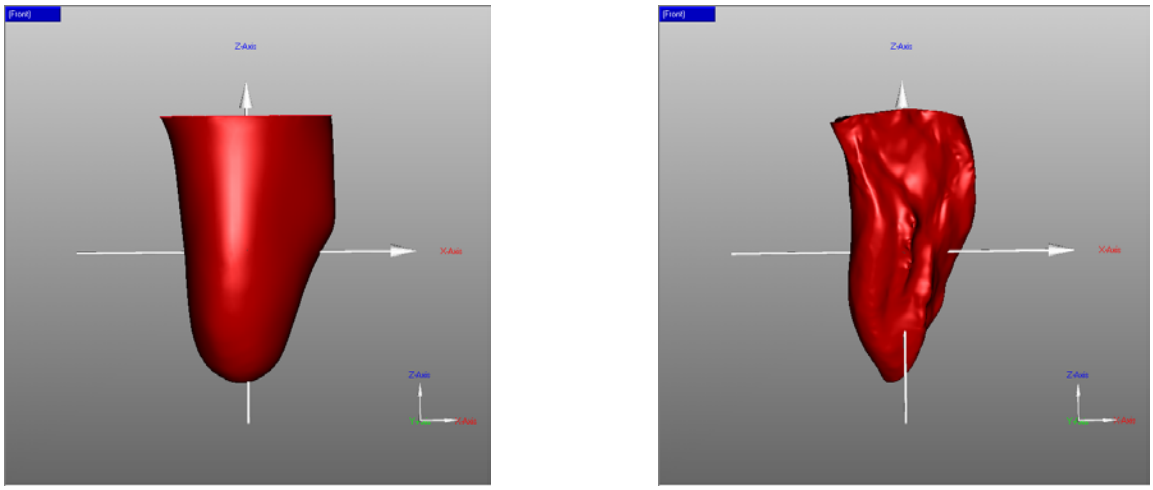

A **B**

Figure 8.3 Deformation of endocardial surface, front view (A) before contraction (B) after contraction

Cross sections showing the ventricular contour in various planes parallel to base (perpendicular to the long axis) can be compared in Figure (8.4). It can be seen again that wall thickening exhibits an irregular distribution around the perimeter. Cross sections 1, 2, 3 and 4 which are between 2 cm and 4 cm under the base show a maximal local wall thickening of about 47%, which is clearly more than the maximal value of the wall thickening in the last chapter. This finding confirms the fact that the geometrical details of the left ventricle can influence the local wall thickening significantly. As mentioned above, comparison of Figure (8.2A) and (7.2A) shows that the septal surfaces have

opposite curvatures. This circumstance influences the pattern of wall thickening directly, so that in Figure (8.4), the minimal wall thickening is found in the septum while in Figure (7.9) the septum shows a remarkably high value of thickening. The maximal wall thickening, in turn, occurs in Figure (8.4) in a posterior and superior region, similar as in Figure (7.9). Measurement of local wall thickening and three dimensional analysis of the heart motion were the matter of discussion and research during the last decades (Bogaert and Rademakers 2001; MacGowan and others 1997; Rademakers and others 1994; Stuber 1997; Waldman and others 1985).

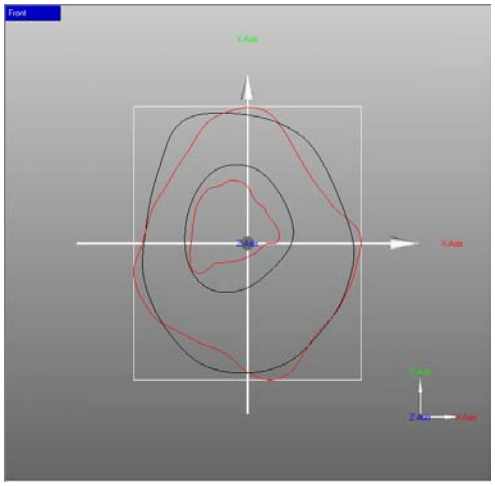

1

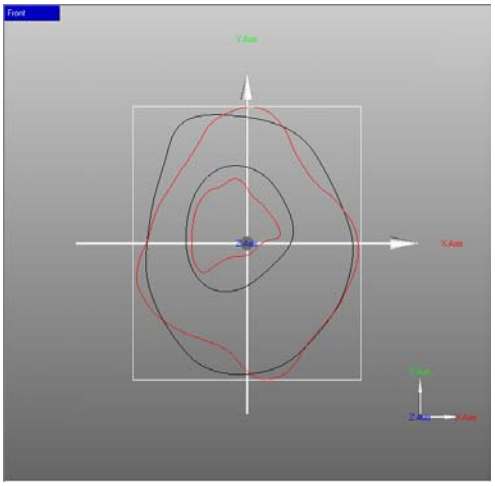

2

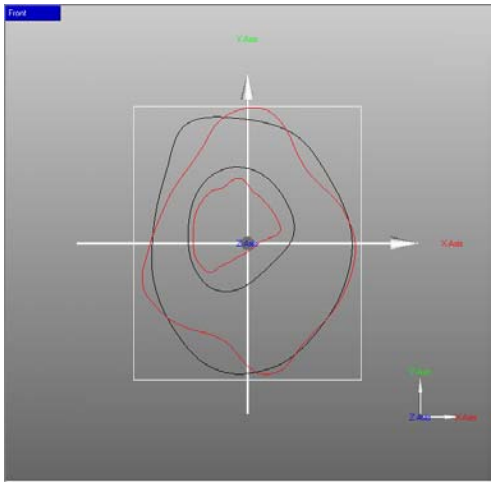

3

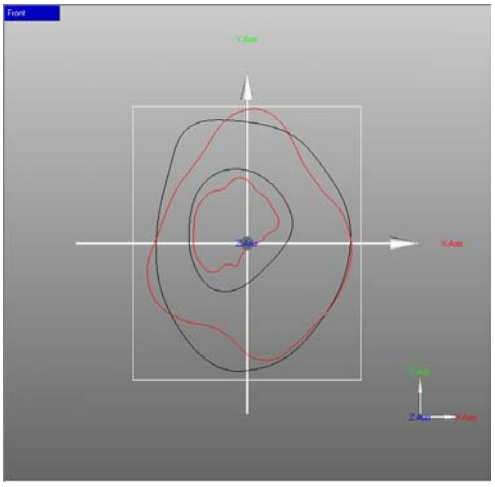

4

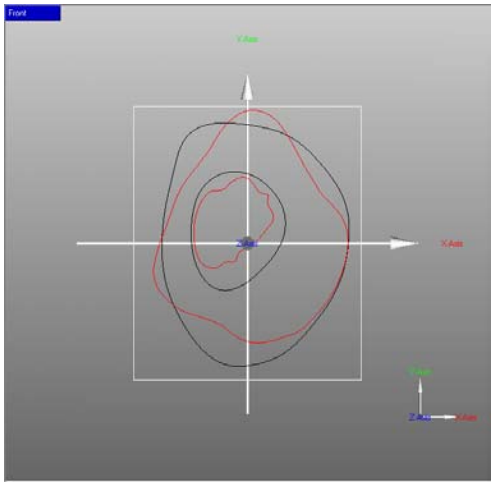

5

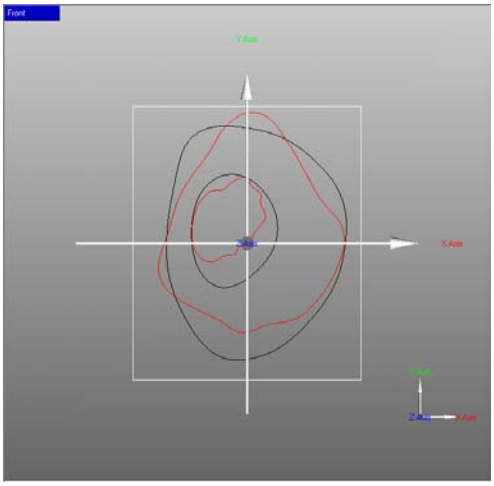

6

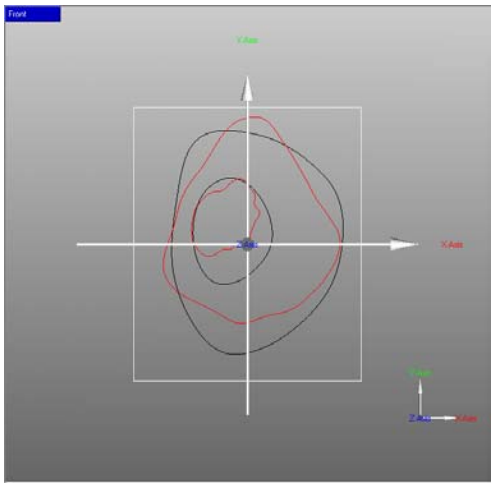

7

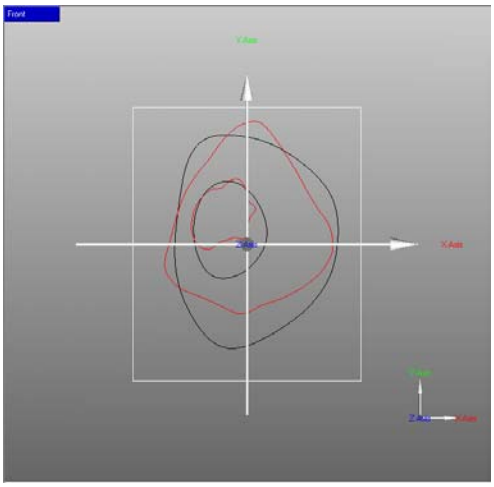

8

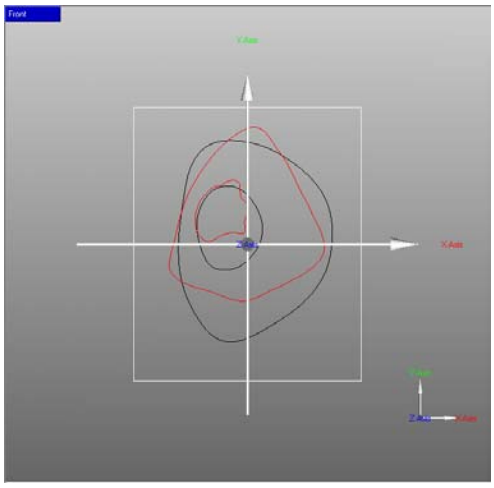

9

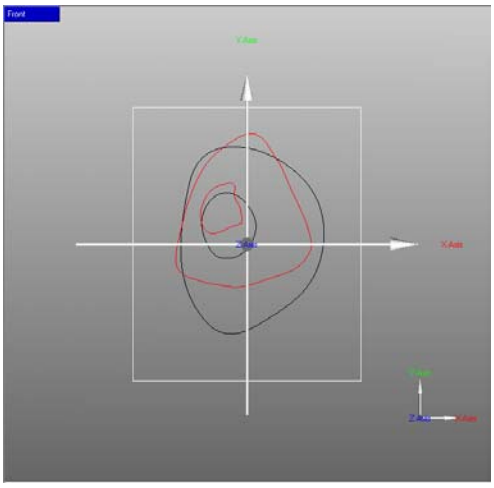

10

Figure 8.4 Cross sections of deformed (or contracted in red) and undeformed (in black) geometry

8.2 A real geometry

In this subsection we begin the study of a real geometry of a human heart. The geometry was constructed from digitized data as explained in chapter 3 (Figure 8.5).

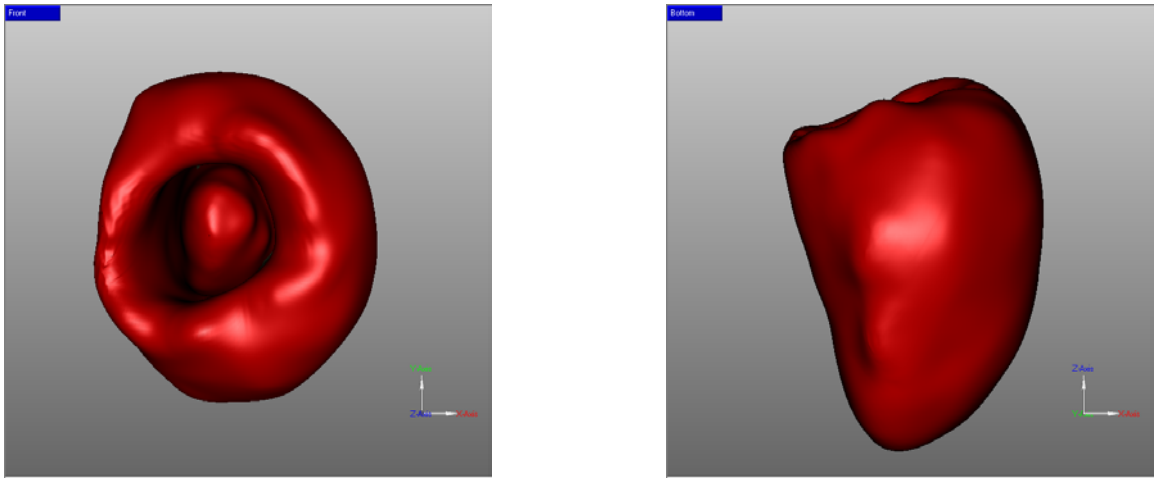

A **B**

Figure 8.5 Real geometry of a smoothed human heart

A mesh consisting of more than 46,700 eight-node hexahedral elements was created with the help of the hex-mesh generator of the commercial software package MSC-MarcMentat® (Figure 8.6A). The fibre orientation was derived from the fibre vector field described in chapter 3, which was used already in the last chapter (Figure 6.6).

In this case the number of elements was relatively high, accordingly, the calculations were time consuming. It was found that the second method for the simulation of contraction was more favourable. The total second Piola-Kirchhoff active stress tensor $\mathbf{S}'^{\,total}_{active}$ (in kPa) was defined as follows

$$\mathbf{S}'^{\,total}_{active} = \begin{pmatrix} 200 & 0 & 0 \\ 0 & 0 & 60 \\ 0 & 60 & 120 \end{pmatrix} \tag{8.2}$$

Here we assumed again that the value of $S'_{active}(N,N)$ is about 60% of $S'_{active}(F,F)$. The value of $S'_{active}(S,N)$, as discussed in chapters 6 and 7, could be estimated between 25% and 50% of $S'_{active}(N,N)$. The good quality of mesh allowed us to apply the upper 50% limit for $S'_{active}(S,N)$.

The simulations revealed furthermore that the boundary conditions influence the pattern of deformation significantly. In the last two models, boundary conditions were always applied at the base. As a result, we could not simulate the contraction in the basal area properly, moreover, longitudinal shortening was prevented because of an inaccurate structure of apex. In this model, however, due to geometrical irregularities at the base, we applied the boundary condition on selected elements of the apical area. A constant value of 14 kPa for the ventricular pressure was defined as in the last chapter. Here, the effect of long-axis shortening is seen clearly; it is about 15%. Figure (8.6B) shows the results of the simulation.

These findings demonstrate that it is important to define a realistic set of boundary conditions. In particular, as discussed in chapters 1 and 6, the heart is contained within the pericardial sac. The pericardial sac, in turn, influences the motion of myocardium during the contraction and dilatation. Accordingly, the role of the pericardium should be studied and taken in to account in future models.

The deformation of the endocardial surface is shown in Figure (8.7).

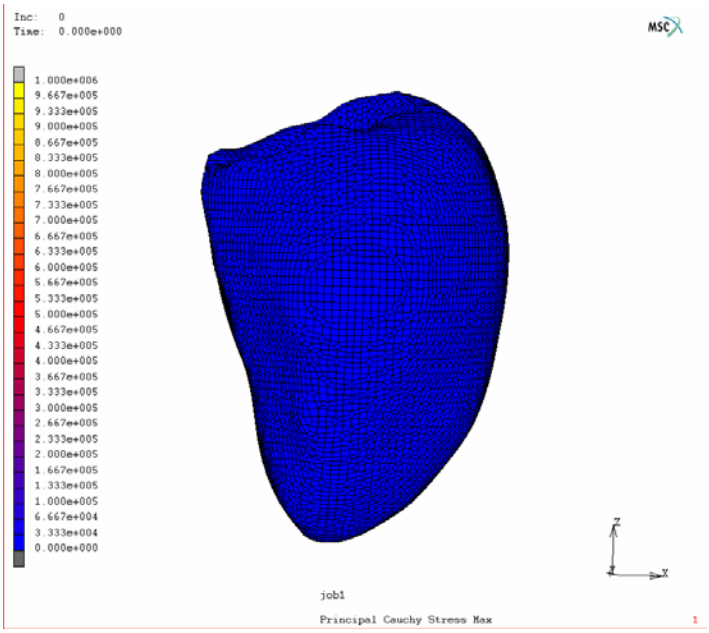

A

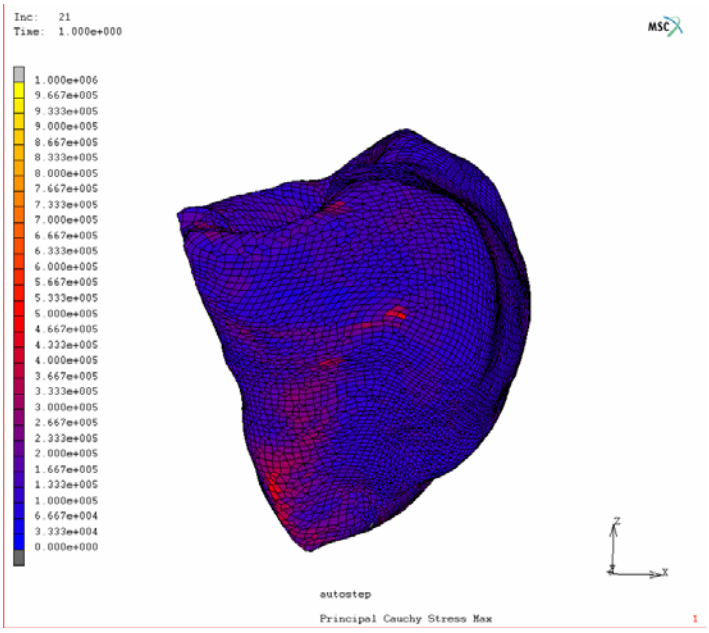

B

Figure 8.6 FE implementation of contraction, front view (A) before deformation (B) after deformation

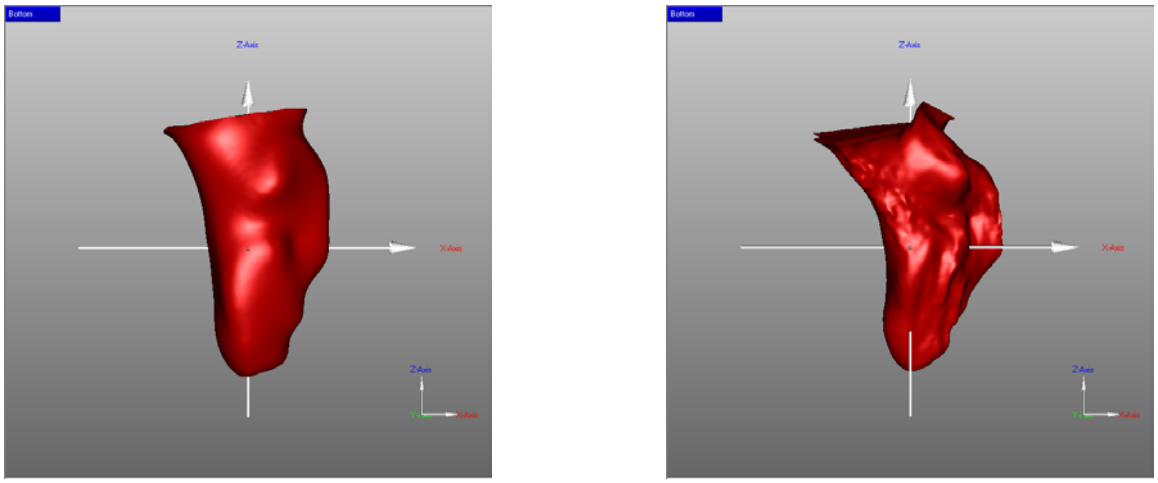

A **B**

Figure 8.7 Deformation of endocardial surface, front view (A) before contraction (B) after contraction

The volume of the left ventricle reduces from an initial value of 102 ml to the final value of 60 ml which corresponds to a stroke volume of about 41%, which is somewhat less than a physiologic value.

Cross sections exhibiting the epi- and endocardial surfaces of deformed geometry within a group of planes parallel to base (in red) are shown in Figure (8.8) and can be compared with the cross sections of undeformed geometry (in black). It can be seen again that wall thickening is distributed in a quite irregular fashion. Basal cross sections thereby show a maximal local wall thickening of about 42%. It confirms again that the boundary conditions can influence the maximal value of wall thickening significantly.

High resolution MRI and MRT imaging techniques become presently available which provide the necessary tools for a quantification of the three dimensional myocardial deformations. The analysis of such measurements will be useful for a validation of our FE models in the future. (Bogaert and others 2000; Bogaert and Rademakers 2001; Mazhari and others 2001; Papademetris and others 2002; Papademetris and others 2001; Sinusas and others 2001).

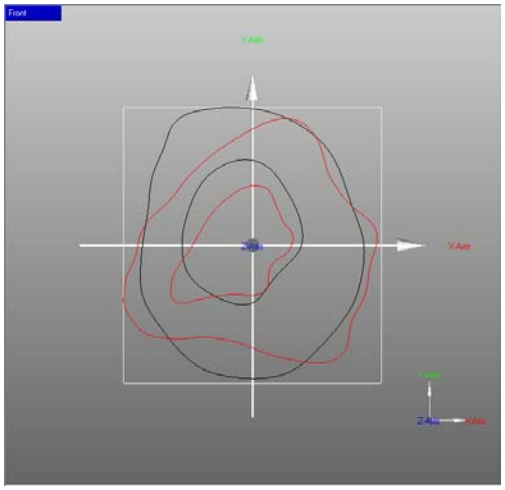
Front
YAxis
XAxis
ZAxis

1

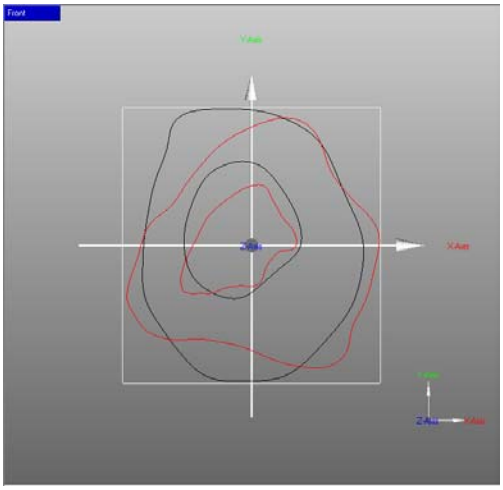
Front
YAxis
XAxis
ZAxis

2

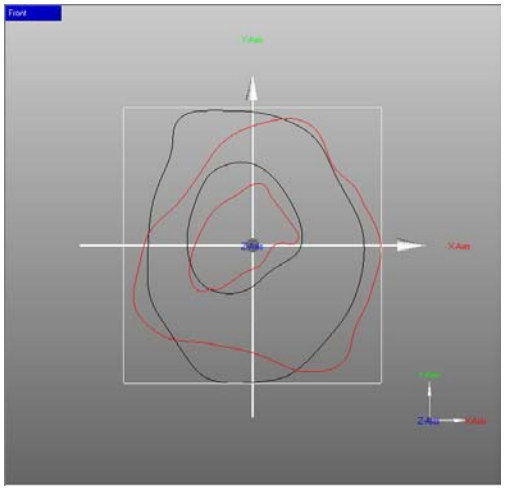
Front
YAxis
XAxis
ZAxis

3

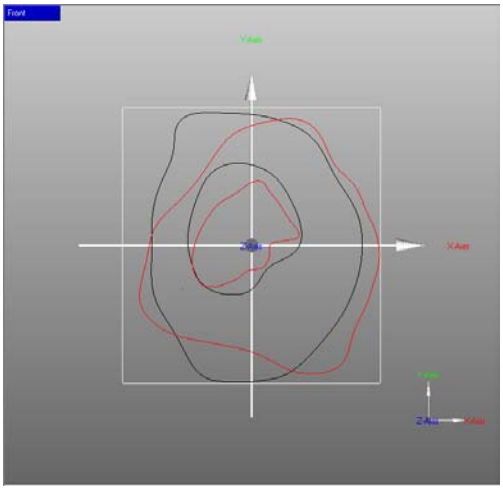
Front
YAxis
XAxis
ZAxis

4

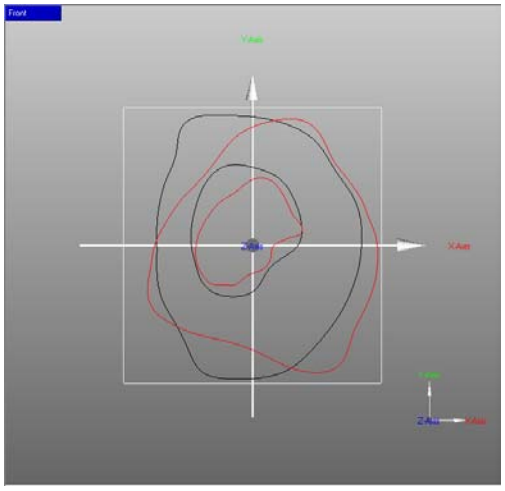
Front
YAxis
XAxis
ZAxis

5

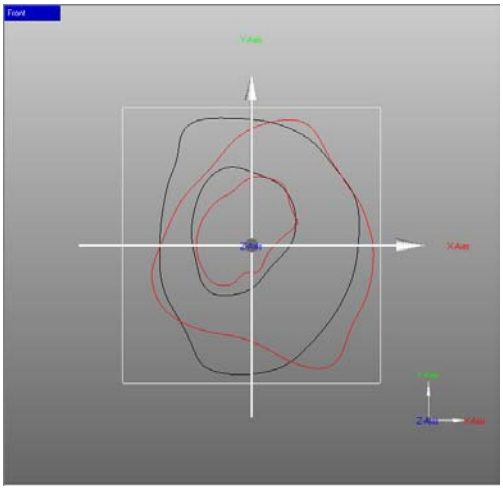
Front
YAxis
XAxis
ZAxis

6

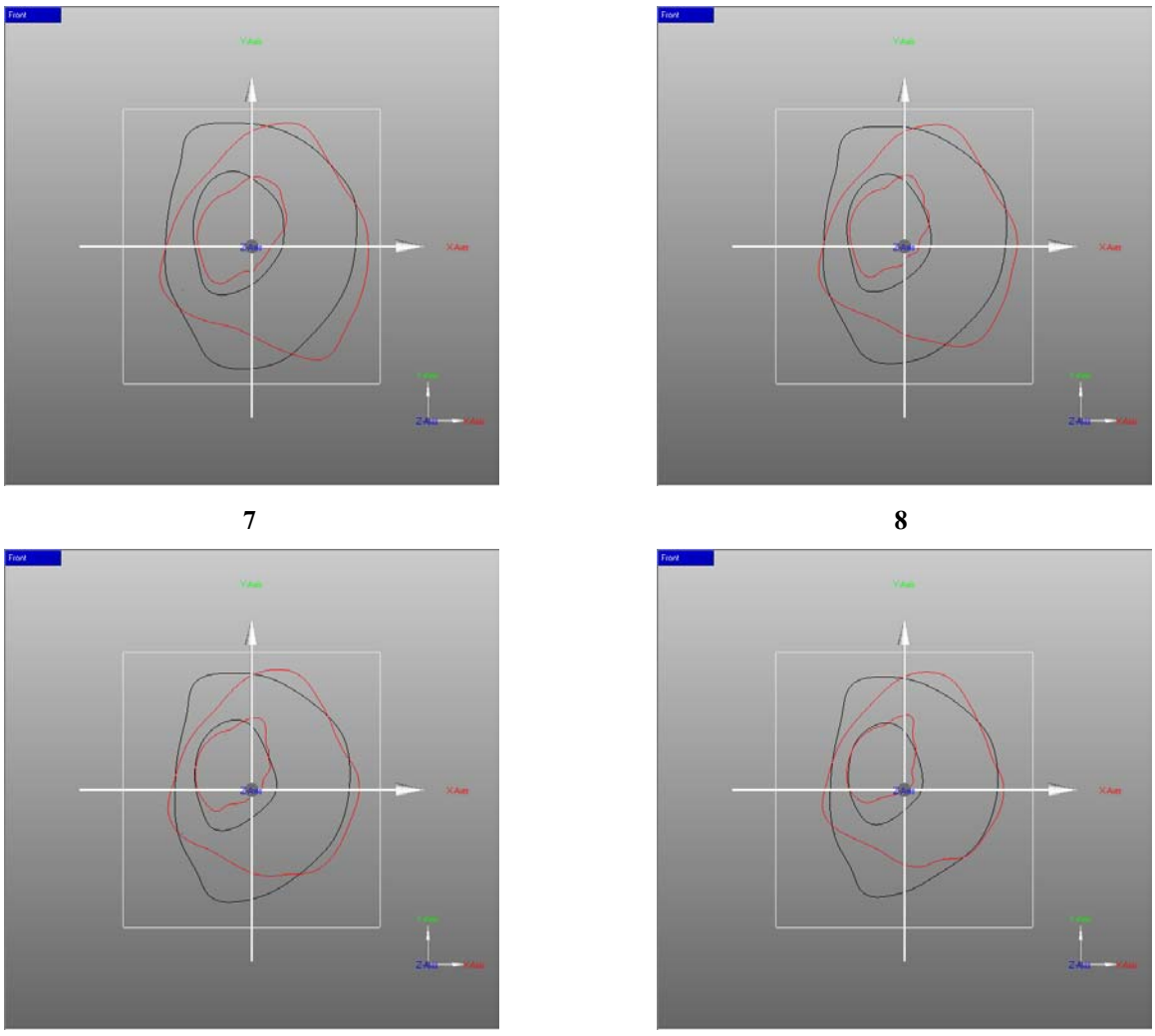

Figure 8.8 Cross sections of deformed (or contracted in red) and undeformed (in black) geometry

8.3 Infarction of the heart

An infarction of the heart causes the death of an area of myocardial tissue, so that depolarization of the cells is not possible. This implies that the infarcted tissue will not contract. The size of the inactive tissue depends on the strength of the infarction. By omitting the application of the total second Piola-Kirchhoff active stress tensor $\mathbf{S}'^{\,total}_{active}$ on the elements of a selected area, we can simulate an infarction with our finite element model. Figure (8.9) shows the selected area (in green) as the infarcted tissue of the heart. All other conditions and $\mathbf{S}'^{\,total}_{active}$ are the same as in the last subsection.

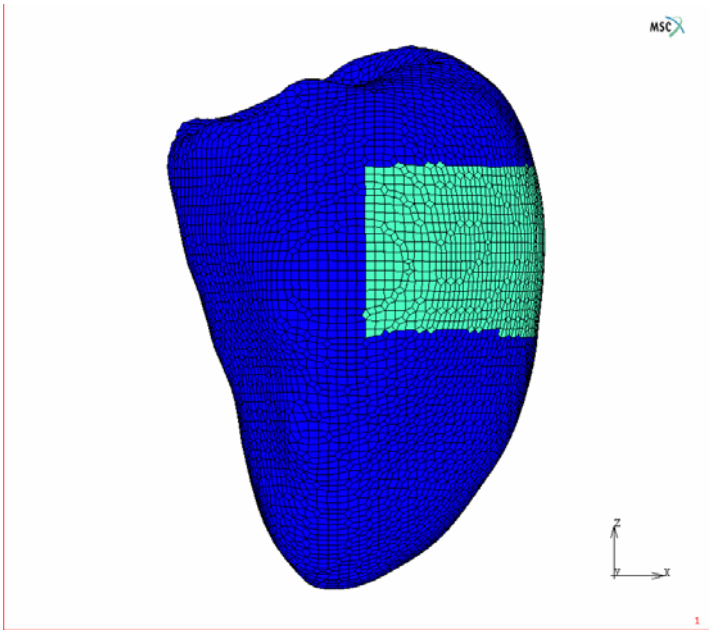

Figure 8.9 Selected area (in green) shows the infarcted tissue

The results of the simulation are shown in Figure (8.10). Negative values of the maximal principal Cauchy stress show that the marked area does not participate in the contraction process. Figure (8.11) exhibits the endocardial surface. Here the volume of the left ventricle does not reduce at all, i.e., there is no contribution to the stroke volume. This finding is in agreement with the clinical observation that a large infarction in the basal area can adversely affect the entire heart and lead to a rapid death. In Figure (8.11) a

significant bulging of the endocardial surface is observed whose extent can be assessed by comparison with Figure (8.7) and which is also in agreement with clinical observations. It is interesting to note that the outside view of the infarcted heart (Figure 8.10) does not show a large difference with a healthy heart (Figure 8.6B).

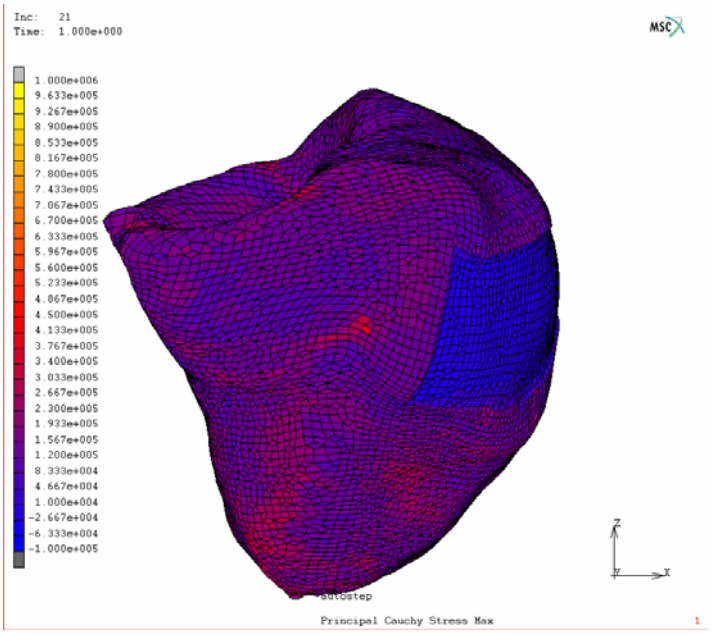

Figure 8.10 FE implementation of heart infarction, front view

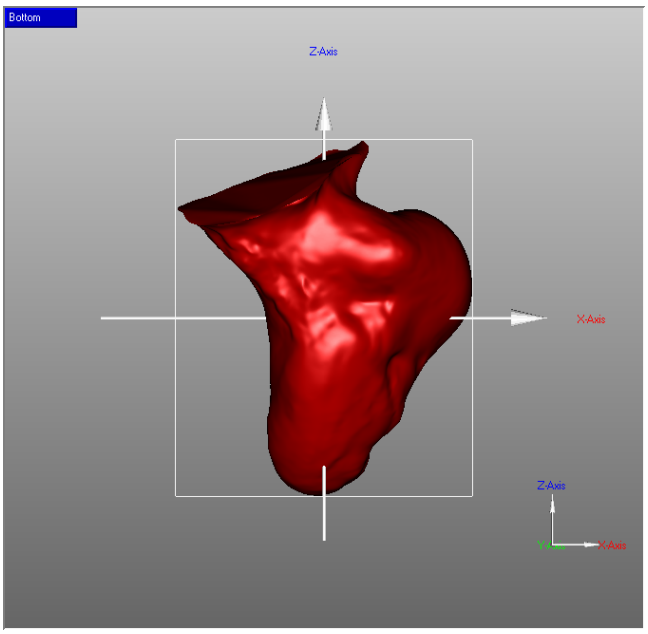

Figure 8.11 Deformation of endocardial surface in an infarcted heart, front view

In Figure (8.12) the cross sections of the health heart (black curves) and infarcted heart (red curves) can be compared. It is seen that the infarction changes the whole pattern of contraction and wall thickening(Bogen and others 1984; Holmes and others 1994; Jogdutt 1985; Summerour and others 1998).

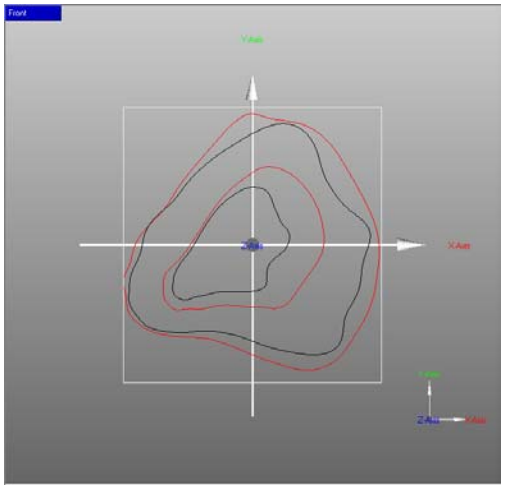

1

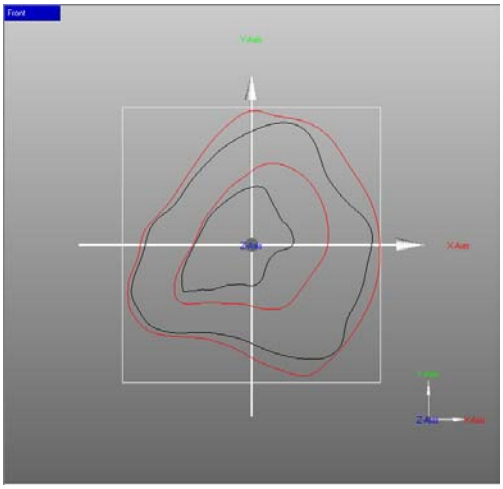

2

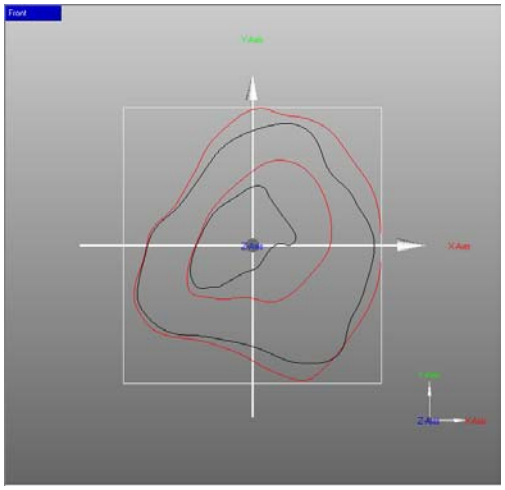

3

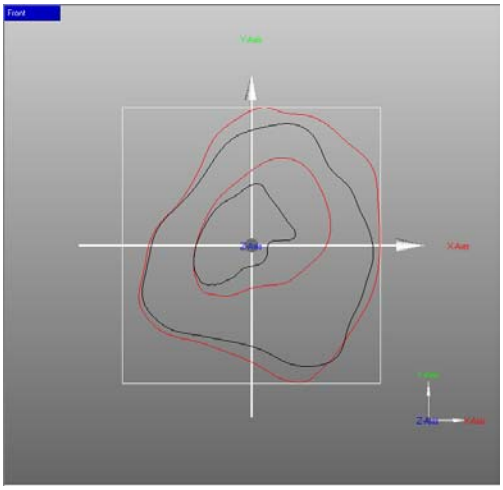

4

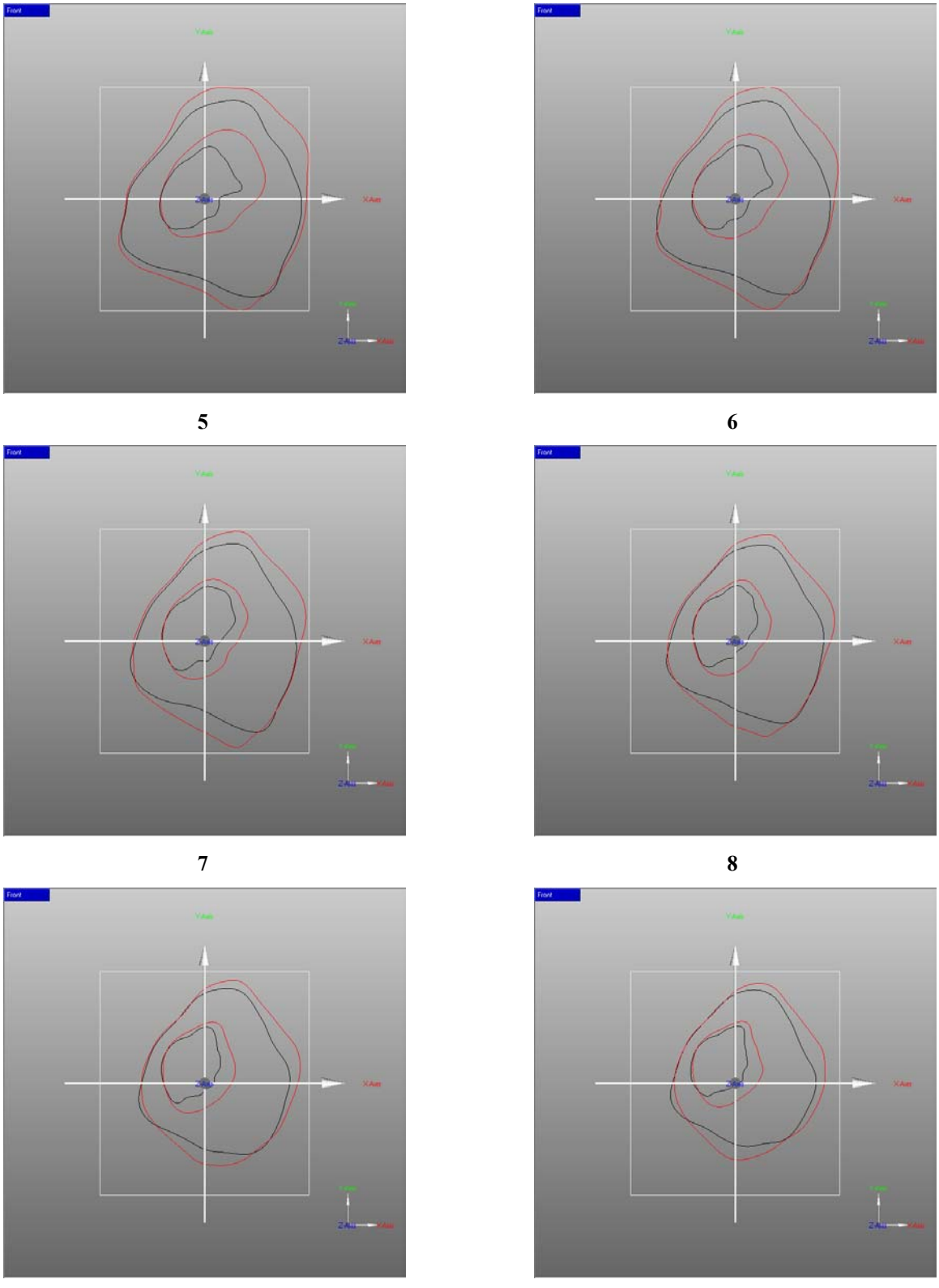

Figure 8.14 Cross sections of deformed (or contracted) geometry for a (A) health heart (in black) (B) infarcted heart

In this chapter we attempted to show the applicability of our approach for the study of heart function under physiological and pathological conditions in realistic cases. We anticipate that this approach will be useful for a deeper understanding of diseases of the heart in general and implantable devices in future.

References

Arts T, Veenstra PC, Reneman RS. 1982. Epicardial deformation and left ventricular wall mechanics during ejection in the dog. American Journal of Physiology 243:H379-H390.

Bogaert J, Bosmans H, Maes A, Suetens P, Marchal G, Rademakers FE. 2000. Remote myocardial dysfunction after acute anterior myocardial infarction: impact of left ventricular shape on regional function: a magnetic resonance myocardial tagging study. J Am Coll Cardiol 35(6):1525-34.

Bogaert J, Rademakers FE. 2001. Regional nonuniformity of normal adult human left ventricle. Am J Physiol Heart Circ Physiol 280(2):H610-20.

Bogen DK, Needleman A, McMahon TA. 1984. An analysis of myocardial infarction: the effect of regional changes in contractility. Circ Res 55:805-815.

Bovendeerd PH, Arts T, Delhaas T, Huyghe JM, van Campen DH, Reneman RS. 1996. Regional wall mechanics in the ischemic left ventricle: numerical modeling and dog experiments. Am J Physiol 270(1 Pt 2):H398-410.

Bovendeerd PH, Arts T, Huyghe JM, van Campen DH, Reneman RS. 1992. Dependence of local left ventricular wall mechanics on myocardial fiber orientation: a model study. J Biomech 25(10):1129-40.

Bovendeerd PH, Huyghe JM, Arts T, van Campen DH, Reneman RS. 1994. Influence of endocardial-epicardial crossover of muscle fibers on left ventricular wall mechanics. J Biomech 27(7):941-51.

Holmes JW, Yamashita H, Waldman LK, Covell JW. 1994. Scar remodeling and transmural deformation after infarction in the pig. Circulation 90:411-420.

Huyghe JM, Arts T, van Campen DH, Reneman RS. 1992. Porous medium finite element model of the beating left ventricle. Am J Physiol 262(4 Pt 2):H1256-67.

Jogdutt BI. 1985. Delayed effects of early infarct-limiting therapies on healing after myocardial infarction. Circulation 72:907-914.

MacGowan GA, Shapiro EP, Azhari H, Siu CO, Hees PS, Hutchins GM, Weiss JL, Rademakers FE. 1997. Noninvasive measurement of shortening in the fiber and

cross-fiber directions in the normal human left ventricle and in idiopathic dilated cardiomyopathy. Circulation 96(2):535-41.

Mazhari R, Omens JH, Pavelec RS, Covell JW, McCulloch AD. 2001. Transmural Distribution of Three-Dimensional Systolic Strains in Stunned Myocardium. Circulation 104:336-341.

Papademetris X, Sinusas AJ, Dione DP, Constable RT, Duncan JS. 2002. Estimation of 3-D left ventricular deformation from medical images using biomechanical models. IEEE Trans Med Imaging 21(7):786-800.

Papademetris X, Sinusas AJ, Dione DP, Duncan JS. 2001. Estimation of 3D left ventricular deformation from echocardiography. Med Image Anal 5(1):17-28.

Rademakers FE, Rogers WJ, Guier WH, Hutchins GM, Siu CO, Weisfeldt ML, Weiss JL, Shapiro EP. 1994. Relation of regional cross-fiber shortening to wall thickening in the intact heart. Three-dimensional strain analysis by NMR tagging. Circulation 89(3):1174-82.

Sinusas AJ, Papademetris X, Constable RT, Dione DP, Slade MD, Shi P, Duncan JS. 2001. Quantification of 3-D regional myocardial deformation: shape-based analysis of magnetic resonance images. Am J Physiol Heart Circ Physiol 281(2):H698-714.

Stuber M. 1997. Quantification of the human heart wall motion by ultra-fast magnetic resonance myocardial tagging techniques [Ph.D. Thesis]. Zurich: Ph.D. Thesis, Swiss Federal Institute of Technology. ethz-bib 12208 p.

Summerour S, Emery J, Fazeli B, Omens JH, McCulloch AD. 1998. Residual strain in ischemic ventricular myocardium. J. Biomech. Engng 120:710-714.

Waldman LK, Fung YC, Covell JW. 1985. Transmural myocardial deformation in the canine left ventricle. Normal in vivo three-dimensional finite strains. Circ Res 57(1):152-63.

General Bibliography

Alexander DC, Pierpaoli C, Basser PJ, Gee JC. 2001. Spatial transformations of diffusion tensor magnetic resonance images. IEEE Trans Med Imaging 20(11):1131-9.

Arts T, Bovendeerd P, Delhaas T, Prinzen F. 2003. Modeling the relation between cardiac pump function and myofiber mechanics. J Biomech 36(5):731-6.

Arts T, Bovendeerd PH, Prinzen FW, Reneman RS. 1991. Relation between left ventricular cavity pressure and volume and systolic fiber stress and strain in the wall. Biophys J 59(1):93-102.

Arts T, Reneman RS. 1989. Dynamics of left ventricular wall and mitral valve mechanics. J. Biomech. 22(3):261-271.

Arts T, Veenstra PC, Reneman RS. 1982. Epicardial deformation and left ventricular wall mechanics during ejection in the dog. American Journal of Physiology 243:H379-H390.

Azhari H, Oliker S, Rogers WJ, Weiss JL, Shapiro EP. 1996. Three-dimensional mapping of acute ischemic regions using artificial neural networks and tagged MRI. IEEE Trans Biomed Eng 43(6):619-26.

Azhari H, Sideman S, Weiss JL, Shapiro EP, Weisfeldt ML, Graves WL, Rogers WJ, Beyar R. 1990. Three-dimensional mapping of acute ischemic regions using MRI: wall thickening versus motion analysis. Am J Physiol 259(5 Pt 2):H1492-503.

Azhari H, Weiss JL, Rogers WJ, Siu CO, Shapiro EP. 1995a. A noninvasive comparative study of myocardial strains in ischemic canine hearts using tagged MRI in 3-D. Am J Physiol 268(5 Pt 2):H1918-26.

Azhari H, Weiss JL, Rogers WJ, Siu CO, Zerhouni EA, Shapiro EP. 1993. Noninvasive quantification of principal strains in normal canine hearts using tagged MRI images in 3-D. Am J Physiol 264(1 Pt 2):H205-16.

Azhari H, Weiss JL, Shapiro EP. 1995b. Distribution of myocardial strains: an MRI study. Adv Exp Med Biol 382:319-28.

Azhari H, Weiss JL, Shapiro EP. 1997. In vivo assessment of regional myocardial work in normal canine hearts using 3D tagged MRI. Adv Exp Med Biol 430:241-8.

Basser PJ. 1995. Inferring microstructural features and the physiological state of tissues from diffusion-weighted images. NMR Biomed 8(7-8):333-44.

Basser PJ. 1997. New histological and physiological stains derived from diffusion-tensor MR images. Ann N Y Acad Sci 820:123-38.

Basser PJ. 2002. Relationships between diffusion tensor and q-space MRI. Magn Reson Med 47(2):392-7.

Basser PJ, Jones DK. 2002. Diffusion-tensor MRI: theory, experimental design and data analysis - a technical review. NMR Biomed 15(7-8):456-67.

Basser PJ, Mattiello J, LeBihan D. 1994a. Estimation of the effective self-diffusion tensor from the NMR spin echo. J Magn Reson B 103(3):247-54.

Basser PJ, Mattiello J, LeBihan D. 1994b. MR diffusion tensor spectroscopy and imaging. Biophys J 66(1):259-67.

Basser PJ, Pajevic S. 2000. Statistical artifacts in diffusion tensor MRI (DT-MRI) caused by background noise. Magn Reson Med 44(1):41-50.

Basser PJ, Pajevic S. 2003. A normal distribution for tensor-valued random variables: applications to diffusion tensor MRI. IEEE Trans Med Imaging 22(7):785-94.

Basser PJ, Pajevic S, Pierpaoli C, Duda J, Aldroubi A. 2000. In vivo fiber tractography using DT-MRI data. Magn Reson Med 44(4):625-32.

Basser PJ, Pierpaoli C. 1996. Microstructural and physiological features of tissues elucidated by quantitative-diffusion-tensor MRI. J Magn Reson B 111(3):209-19.

Basser PJ, Pierpaoli C. 1998. A simplified method to measure the diffusion tensor from seven MR images. Magn Reson Med 39(6):928-34.

Beyar R, Sideman S. 1984a. A computer study of left ventricular performance based on fiber structure, sarcomere dynamics, and transmural electrical propagation velocity. Circ Res 55:358-375.

Beyar R, Sideman S. 1984b. Model for left ventricular contraction combining the force length velocity relationship with the time varying elastance theory. Biophys J 45:1167-1177.

Boehme W. 1936. Ueber den aktiven Anteil des Herzens an der Förderung des Venenblutes. Ergebn. Physiol. 38:252-338.

Bogaert J, Bosmans H, Maes A, Suetens P, Marchal G, Rademakers FE. 2000. Remote myocardial dysfunction after acute anterior myocardial infarction: impact of left ventricular shape on regional function: a magnetic resonance myocardial tagging study. J Am Coll Cardiol 35(6):1525-34.

Bogaert J, Rademakers FE. 2001. Regional nonuniformity of normal adult human left ventricle. Am J Physiol Heart Circ Physiol 280(2):H610-20.

Bogen DK, Needleman A, McMahon TA. 1984. An analysis of myocardial infarction: the effect of regional changes in contractility. Circ Res 55:805-815.

Borelli HS. 1681. De Muto Animalium. Rome.

Bosmans H, Bogaert J, Rademakers F, Marchal G, Laub G, Verschakelen J, Baert AL. 1996. Left ventricular radial tagging acquisition using gradient-recalled-echo techniques: sequence optimization. Magma 4(2):123-33.

Botham MJ, Lemmer JH, Gerren RA, Long RW, Behrendt DM, Gallagher KP. 1984. Coronary vasodilator reserve in young dogs with moderate right ventricular hypertrophy. Ann Thorac Surg 38(2):101-7.

Bovendeerd PH, Arts T, Delhaas T, Huyghe JM, van Campen DH, Reneman RS. 1996. Regional wall mechanics in the ischemic left ventricle: numerical modeling and dog experiments. Am J Physiol 270(1 Pt 2):H398-410.

Bovendeerd PH, Arts T, Huyghe JM, van Campen DH, Reneman RS. 1992. Dependence of local left ventricular wall mechanics on myocardial fiber orientation: a model study. J Biomech 25(10):1129-40.

Bovendeerd PH, Huyghe JM, Arts T, van Campen DH, Reneman RS. 1994. Influence of endocardial-epicardial crossover of muscle fibers on left ventricular wall mechanics. J Biomech 27(7):941-51.

Bradley TD. 2000. Sleep apnea implications in cardiovascular and cerebrovascular disease. New York: Dekker. 554 S. p.

Brutsaert DL. 1987. Nonuniformity: a physiologic modulator of contraction and relaxation of the normal heart. J. Am. Coll. Cardiol. 9:341-348.

Brutsaert DL, Rademakers F, Sys SU. 1984. Triple control of relaxation: implications in cardiac disease. Circulation 69:190-196.

Brutsaert DL, Sonnenblick EH. 1969. Force-velocity-length-time relations of the contractile elements in heart muscle of the cat. Circ Res 24:137-149.

Buchalter MB, Rademakers FE, Weiss JL, Rogers WJ, Weisfeldt ML, Shapiro EP. 1994. Rotational deformation of the canine left ventricle measured by magnetic resonance tagging: effects of catecholamines, ischaemia, and pacing. Cardiovasc Res 28(5):629-35.

Carmeliet E, Vereecke J. 2002. Cardiac cellular electrophysiology. Boston: Kluwer Academic Publishers. 421 S. p.

Chen J, Song S, Liu W, McLean M, Allen J, Tan J, Wickline S, Yu X. 2003. Remodeling of cardiac fiber structure after infarction in rats quantified with diffusion tensor MRI. AmJ Physiol Heart Circ Physiol. 285(3):H946-54.

Chuong CJ, Fung YC. 1986. Residual stress in arteries. In: Schmid-Schönbein GW, Woo Sl-Y, Zweifach BW, editors. Frontiers in Biomechanics. New York: Springer-Verlag. p pp. 117-129.

Costa KD, Holmes JW, McCulloch AD. 2001. Modelling cardiac mechanical properties in three dimentions. The Royal Society 359:1233-1250.

Costa KD, Hunter PJ, Rogers JM, Guccione JM, Waldman LK, McCulloch AD. 1996a. A three-dimensional finite element method for large elastic deformations of ventricular myocardium: I--Cylindrical and spherical polar coordinates. J Biomech Eng 118(4):452-63.

Costa KD, Hunter PJ, Wayne JS, Waldman LK, Guccione JM, McCulloch AD. 1996b. A three-dimensional finite element method for large elastic deformations of ventricular myocardium: II--Prolate spheroidal coordinates. J Biomech Eng 118(4):464-72.

Costa KD, May-Newman K, Farr D, O'Dell WG, McCulloch AD, Omens JH. 1997. Three-dimensional residual strain in midanterior canine left ventricle. Am J Physiol 273(4 Pt 2):H1968-76.

Costa KD, Takayama Y, McCulloch AD, Covell JW. 1999. Laminar fiber architecture and three-dimensional systolic mechanics in canine ventricular myocardium. Am J Physiol 276(2 Pt 2):H595-607.

Creswell LL, Moulton MJ, Cox JL, Rosenbloom M. 1995. Revascularization after acute myocardial infarction. Ann Thorac Surg 60(1):19-26.

Creswell LL, Moulton MJ, Wyers SG, Pirolo JS, Fishman DS, Perman WH, Myers KW, Actis RL, Vannier MW, Szabo BA and others. 1994. An experimental method for evaluating constitutive models of myocardium in in vivo hearts. American Journal of Physiology 267,2pt2:H853-63.

Creswell LL, Pasque MK, Vannier MW. 1993. Three-dimensional cardiac magnetic resonance imaging. American Journal of card. Imaging 7(3):195-208.

Creswell LL, Pasque MK, Vannier MW. 1993. Three-dimensional cardiac magnetic resonance imaging. American Journal of card. Imaging 7(3):195-208.

Cryer CW, Navidi-Kasmai H, Lunkenheimer PP, Redmann K. 1997. Computation of the alignment of myocardial contractile pathways using a magnetic tablet and an optical method. Technology and Health Care 5:79-93.

Das DK. 1999. Heart in stress. New York: New York Academy of Sciences. 438 S. p.

Delhaas T, Arts T, Bovendeerd PH, Prinzen FW, Reneman RS. 1993. Subepicardial fiber strain and stress as related to left ventricular pressure and volume. Am J Physiol 264(5 Pt 2):H1548-59.

Denisova O, Shapiro EP, Weiss JL, Azhari H. 1997. Localization of ischemia in canine hearts using tagged rotated long axis MR images, endocardial surface stretch and wall thickening. Magn Reson Imaging 15(9):1037-43.

Dokos S, LeGrice IJ, Smaill BH, Kar J, Young AA. 2000. A triaxial-measurement shear-test device for soft biological tissues. J Biomech Eng 122(5):471-8.

Dokos S, Smaill BH, Young AA, LeGrice IJ. 2002. Shear properties of passive ventricular myocardium. Am J Physiol Heart Circ Physiol 283(6):H2650-9.

Drake DH, McClanahan TB, Ning XH, Gerren RA, Dunham WR, Gallagher KP. 1987. Changes in contractility fail to alter the size of the functional border zone in anesthetized dogs. Circ Res 61(2):166-80.

Eringen AC. 1962. Nonlinear theory of continuous media. New York: McGraw-Hill. 477 p.

Eringen AC. 1980. Mechanics of continua. Huntington, N.Y.: R. E. Krieger Pub. Co. xv, 592 p.

Falsetti HL, Mates RE, Grant C, Greene DG, Bunnell IL. 1970. Left ventricular wall stress calculated from one-plane cineangiography. Circ Res 26:71-83.

Fung YC. 1990. Biomechanics : motion, flow, stress, and growth. New York: Springer-Verlag. xv, 569 p.

Fung YC. 1993. Biomechanics : mechanical properties of living tissues. New York: Springer-Verlag. xviii, 568 p.

Fung YC. 1997. Biomechanics : circulation. New York: Springer. xvii, 571 p.

Fung YC, Chien S. 2001. Introduction to bioengineering. Singapore ; River Edge, NJ: World Scientific. xvii, 293 p.

Gallagher KP, Buda AJ, Pace D, Gerren RA, Shlafer M. 1986a. Failure of superoxide dismutase and catalase to alter size of infarction in conscious dogs after 3 hours of occlusion followed by reperfusion. Circulation 73(5):1065-76.

Gallagher KP, Gerren RA, Choy M, Stirling MC, Dysko RC. 1987a. Subendocardial segment length shortening at lateral margins of ischemic myocardium in dogs. Am J Physiol 253(4 Pt 2):H826-37.

Gallagher KP, Gerren RA, Ning XH, McManimon SP, Stirling MC, Shlafer M, Buda AJ. 1987b. The functional border zone in conscious dogs. Circulation 76(4):929-42.

Gallagher KP, Gerren RA, Stirling MC, Choy M, Dysko RC, McManimon SP, Dunham WR. 1986b. The distribution of functional impairment across the lateral border of acutely ischemic myocardium. Circ Res 58(4):570-83.

Gallagher KP, Ning XH, Gerren RA, Drake DH, Dunham WR. 1987c. Effect of aortic constriction on the functional border zone. Am J Physiol 252(4 Pt 2):H826-35.

Gallagher KP, Stirling MC, Choy M, Szpunar CA, Gerren RA, Botham MJ, Lemmer JH. 1985. Dissociation between epicardial and transmural function during acute myocardial ischemia. Circulation 71(6):1279-91.

Geerts L, Bovendeerd P, Nicolay K, Arts T. 2002. Characterization of the normal cardiac myofiber field in goat measured with MR-diffusion tensor imaging. Am J Physiol Heart Circ Physiol 283(1):H139-45.

Ghista DN, Sandler H. 1969. An analytic elastic-viscoelastic model for the shape and the forces in the left ventricle. J. Biomech. 2:35-47.

Gielen AW, Oomens CW, Bovendeerd PH, Arts T, Janssen JD. 2000. A Finite Element Approach for Skeletal Muscle using a Distributed Moment Model of Contraction. Comput Methods Biomech Biomed Engin 3(3):231-244.

Goldstein DS. 2001. The autonomic nervous system in health and disease. New York: M. Dekker. xii, 618 p.

Gould P, Ghista DN, Brombolich L, Mirsky I. 1972. In vivo stresses in the human left ventricular wall: analysis accounting for the irregular 3d geometry and comparison with idealised geometry analyses. J. Biomech. 5:521-539.

Green AE, Adkins JE. 1970. Large elastic deformations. Oxford,: Clarendon Press. xiv, 324 illus. p.

Guccione JM, Costa KD, McCulloch AD. 1995. Finite element stress analysis of left ventricular mechanics in the beating dog heart. J Biomech 28(10):1167-77.

Guccione JM, Le Prell GS, de Tombe PP, Hunter WC. 1997a. Measurements of active myocardial tension under a wide range of physiological loading conditions. J Biomech 30(2):189-92.

Guccione JM, McCulloch AD. 1993. Mechanics of active contraction in cardiac muscle: Part I--Constitutive relations for fiber stress that describe deactivation. J Biomech Eng 115(1):72-81.

Guccione JM, McCulloch AD, Waldman LK. 1991. Passive material properties of intact ventricular myocardium determined from a cylindrical model. J Biomech Eng 113(1):42-55.

Guccione JM, Moonly SM, Moustakidis P, Costa KD, Moulton MJ, Ratcliffe MB, Pasque MK. 2001a. Mechanism underlying mechanical dysfunction in the border zone of left ventricular aneurysm: a finite element model study. Ann Thorac Surg 71(2):654-62.

Guccione JM, Moonly SM, Wallace AW, Ratcliffe MB. 2001b. Residual stress produced by ventricular volume reduction surgery has little effect on ventricular function and mechanics: a finite element model study. J Thorac Cardiovasc Surg 122(3):592-9.

Guccione JM, O'Dell WG, McCulloch AD, Hunter WC. 1997b. Anterior and posterior left ventricular sarcomere lengths behave similarly during ejection. Am J Physiol 272(1 Pt 2):H469-77.

Guccione JM, Waldman LK, McCulloch AD. 1993. Mechanics of active contraction in cardiac muscle: Part II--Cylindrical models of the systolic left ventricle. J Biomech Eng 115(1):82-90.

Guyton AC, Hall JE. 2000. Textbook of medical physiology. Philadelphia: Saunders. xxxii, 1064 S. p.

Hasan KM, Basser PJ, Parker DL, Alexander AL. 2001. Analytical computation of the eigenvalues and eigenvectors in DT-MRI. J Magn Reson 152(1):41-7.

Holmes JW, Yamashita H, Waldman LK, Covell JW. 1994. Scar remodeling and transmural deformation after infarction in the pig. Circulation 90:411-420.

Holubarsch CJF. 2002. Mechanics and energetics of the myocardium. Boston: Kluwer Academic Publishers. 216 S. p.

Holzapfel GA. 2000. Nonlinear solid mechanics : a continuum approach for engineering. Chichester ; New York: Wiley. 455 p.

Hooks DA, Tomlinson KA, Marsden SG, LeGrice IJ, Smaill BH, Pullan AJ, Hunter PJ. 2002. Cardiac microstructure: implications for electrical propagation and defibrillation in the heart. Circ Res 91(4):331-8.

Horowitz A, Lanir Y, Yin FC, Perl M, Sheinman I, Strumpf RK. 1988a. Structural three-dimensional constitutive law for the passive myocardium. J Biomech Eng 110(3):200-7.

Horowitz A, Perl M, Sideman S. 1993. Geodesics as a mechanically optimal fiber geometry for the left ventricle. Basic Res Cardiol 88 Suppl 2:67-74.

Horowitz A, Perl M, Sideman S, Ritman E. 1986. Comprehensive model for the simulation of left ventricle mechanics. Part 2. Implementation and results analysis. Med Biol Eng Comput 24(2):150-6.

Horowitz A, Sheinman I, Lanir Y, Perl M, Sideman S. 1988b. Nonlinear incompressible finite element for simulating loading of cardiac tissue--Part I: Two dimensional formulation for thin myocardial strips. J Biomech Eng 110(1):57-61.

Hort W. 1957. Untersuchungen über die Muskelfaserdehnung und das Gefüge des Myokards in der rechten Herzkammerwand des Meerschweinchens. Virchows Arch. path. Anat. Physiol. 239:694-731.

Hort W. 1960a. Makroskopische und mikrometrische Untersuchungen am Myokard verschieden stark gefüllter linker Kammern. Virchows Arch. path. Anat. Physiol. 333:569-581.

Hort W. 1960b. Untersuchungen zur funktionellen Morphologie des Bindegewebsgerüstes und der Blutgefässe der linken Herzkammerwand. Virchows Arch. path. Anat. Physiol. 33:565-581.

Huber ME. 2003. Coronary artery magnetic resonance angiography. Zurich: ETH Diss No. 15196. 123 p.

Huisman RM, Elzinga G, Westerhof N, Sipkema P. 1980. Measurment of the left ventricular wall stress. Cardiovasc Res 14:142-153.

Huisman RM, Sipkema P, Westerhof N, Elzinga G. 1980. Comparison of models used to calculate left ventricular wall force. Med. Biol. Eng. Comput. 18:133-144.

Humphrey JD, Strumpf RK, Yin FC. 1989. A theoretically-based experimental approach for identifying vascular constitutive relations.

Humphrey JD, Strumpf RK, Yin FC. 1990a. Biaxial mechanical behavior of excised ventricular epicardium. Am J Physiol 259(1 Pt 2):H101-8.

Humphrey JD, Strumpf RK, Yin FC. 1990b. Determination of a constitutive relation for passive myocardium: I. A new functional form. Journal of Biomechanical Engineering 112:333-339.

Humphrey JD, Strumpf RK, Yin FC. 1990c. Determination of a constitutive relation for passive myocardium: II. Parameter estimation. Journal of Biomechanical Engineering 112:340-346.

Humphrey JD, Strumpf RK, Yin FC. 1992. A constitutive theory for biomembranes: application to epicardial mechanics. Journal of Biomechanical Engineering 114(4):461-6.

Humphrey JD, Yin FC. 1989. Constitutive relations and finite deformations of passive cardiac tissue II: stress analysis in the left ventricle. Circ Res 65(3):805-17.

Hunter PJ, McCulloch AD, Nielsen PMF, Smaill BH. 1988. A finite element model of passive ventricular mechanics. Computational Methods in Bioengineering 9:387-397.

Hunter PJ, Nielsen PM, Smaill BH, LeGrice IJ, Hunter IW. 1992. An anatomical heart model with applications to myocardial activation and ventricular mechanics. Crit Rev Biomed Eng 20(5-6):403-26.

Huyghe JM, Arts T, van Campen DH, Reneman RS. 1992. Porous medium finite element model of the beating left ventricle. Am J Physiol 262(4 Pt 2):H1256-67.

Ingels NB. 1997. Myocardial fiber architecture and left ventricular function. Technology and Health Care 5:45-52.

Janz RF, Waldron RJ. 1978. Predicted effect of chronical apical aneurysms on the passive stiffness of the human left ventricle. Circ Res 42(2):255-263.

Jogdutt BI. 1985. Delayed effects of early infarct-limiting therapies on healing after myocardial infarction. Circulation 72:907-914.

Kallioniemi A, Kallioniemi OP, Waldman FM, Chen LC, Yu LC, Fung YK, Smith HS, Pinkel D, Gray JW. 1992. Detection of retinoblastoma gene copy number in metaphase chromosomes and interphase nuclei by fluorescence in situ hybridization. Cytogenet Cell Genet 60(3-4):190-3.

Laplace PS. 1806. Marquis de Supplément au Livre X du Traité de Méchanique Céleste.

LeGrice IJ, Hunter PJ, Smaill BH. 1997. Laminar structure of the heart: a mathematical model. Am J Physiol 272(5 Pt 2):H2466-76.

LeGrice IJ, Smaill BH, Chai LZ, Edgar SG, Gavin JB, Hunter PJ. 1995a. Laminar structure of the heart: ventricular myocyte arrangement and connective tissue architecture in the dog. Am J Physiol 269(2 Pt 2):H571-82.

LeGrice IJ, Takayama Y, Covell JW. 1995b. Transverse shear along myocardial cleavage planes provides a mechanism for normal systolic wall thickening. Circ Res 77(1):182-93.

LeGrice IJ, Takayama Y, Holmes JW, Covell JW. 1995c. Impaired subendocardial function in tachycardia-induced cardiac failure. Am J Physiol 268(5 Pt 2):H1788-94.

LeGrice P, Baird E, Hodge L. 1995d. Treatment of basal cell carcinoma with intralesional interferon alpha-2a. N Z Med J 108(1000):206-7.

Lemmer JH, Botham MJ, McKenney P, Gerren RA, Kirsh MM, Gallagher KP. 1984. Norepinephrine plus phentolamine improves regional blood flow during experimental low cardiac output syndrome. Ann Thorac Surg 38(2):108-16.

Lessick J, Sideman S, Azhari H, Shapiro E, Weiss JL, Beyar R. 1993. Evaluation of regional load in acute ischemia by three-dimensional curvatures analysis of the left ventricle. Ann Biomed Eng 21(2):147-61.

Lin DHS, Yin FC. 1998. A Multiaxial Constitutive law for Mammalian Left Ventricular Myocardium in Steady-State Barium Contracture or Tetanus. Journal of Biomechanical Engineering 120:504-517.

Lower R. 1669. Tractatus de Corde. London.

Lunkenheimer PP, Redmann K, Dietl K-H, Cryer C, Richter K-D, Whimster WF, Niederer P. 1997a. The heart's fibre alignment assessed by comparing two digitizing systems. Methodological investigation into the inclination angle toward wall thickness. Technology and Health Care 5:65-77.

Lunkenheimer PP, Redmann K, Florek J, Fassnacht U, Cryer CW, Wübbeling F, Niederer P, Anderson RH. 2004. The forces generated within the musculature of the left ventricular wall. Heart 90:(in press).

Lunkenheimer PP, Redmann K, Scheld H, Dietl K-H, Cryer C, Richter K-D, Merker J, Whimster WF. 1997b. The heart muscle's putative 'secondary structure'. Functional implications of a band-like anisotropy. Technology and Health Care 5:53-64.

MacGowan GA, Burkhoff D, Rogers WJ, Salvador D, Azhari H, Hees PS, Zweier JL, Halperin HR, Siu CO, Lima JA and others. 1996. Effects of afterload on regional left ventricular torsion. Cardiovasc Res 31(6):917-25.

MacGowan GA, Shapiro EP, Azhari H, Siu CO, Hees PS, Hutchins GM, Weiss JL, Rademakers FE. 1997. Noninvasive measurement of shortening in the fiber and cross-fiber directions in the normal human left ventricle and in idiopathic dilated cardiomyopathy. Circulation 96(2):535-41.

Mandarino WA, Pinsky MR, Gorcsan J. 1998. Assessment of left ventricular contractile state by preload-adjusted maximal power using echocardiographic automated border detection. JACC 31(861-868).

Marzilli M, Goldstein S, Sabbah HN, Lee T, Stein PD. 1979. Modulating effect of regional myocardial performance on local myocardial perfusion in the dog. Circ Res 45(5):634-41.

Marzilli M, Levantesi D, Sabbah HN, Taddei L, Dalle Vacche M, Stein PD. 1984. Regional myocardial systolic function. Effects of coronary occlusion and reperfusion. G Ital Cardiol 14(12):1052-61.

Marzilli M, Sabbah HN, Goldstein S, Stein PD. 1985. Assessment of papillary muscle function in the intact heart. Circulation 71(5):1017-22.

Marzilli M, Sabbah HN, Lee T, Stein PD. 1980a. Role of the papillary muscle in opening and closure of the mitral valve. Am J Physiol 238(3):H348-54.

Marzilli M, Sabbah HN, Stein PD. 1980b. Mitral regurgitation in ventricular premature contractions. The role of the papillary muscle. Chest 77(6):736-40.

Marzilli M, Sabbah HN, Stein PD. 1980c. Supply-demand balance of subendocardial muscle: estimation from intramyocardial pressure. J Thorac Cardiovasc Surg 79(6):803-8.

Masuoka T, Ajisaka R, Watanabe S, Yamanouchi T, Iida K, Sato M, Takeda T, Toyama H, Ishikawa N, Itai Y and others. 1995. Usefulness of hyperventilation thallium-201 single photon emission computed tomography for the diagnosis of vasospastic angina. Jpn Heart J 36(4):405-20.

Masuoka T, Ajisaka R, Watanabe S, Yamanouchi T, Saito T, Iida K, Sugishita Y, Takeda T, Ishikawa N, Toyama H. 1993. [Myocardial ischemia detected by isoproterenol stress cardiac blood-pool scintigraphy: significance of asynchrony as an index of myocardial ischemia]. J Cardiol 23(1):9-18.

Mattiello J, Basser PJ, Le Bihan D. 1997. The b matrix in diffusion tensor echo-planar imaging. Magn Reson Med 37(2):292-300.

Mazhari R, Omens JH, Pavelec RS, Covell JW, McCulloch AD. 2001. Transmural Distribution of Three-Dimensional Systolic Strains in Stunned Myocardium. Circulation 104:336-341.

Miranda PC, Hallett M, Basser PJ. 2003. The electric field induced in the brain by magnetic stimulation: a 3-D finite-element analysis of the effect of tissue heterogeneity and anisotropy. IEEE Trans Biomed Eng 50(9):1074-85.

Mirsky I. 1969. Left ventricular stresses in the intact human heart. Biophys J 9:189-208.

Mirsky I, Ellison RC, Hugenholtz PG. 1981. Assesment of myocardial contractility in children and young adults from ventricular pressure recordings. Am. J.Cardiol. 27:359-367.

Mirsky I, Krayenbühl HP. 1981. The role of wall stress in the assessment of ventricular function. Herz 6:288-299.

Moulton MJ, Creswell LL, Actis RL, Myers KW, Vannier MW, Szabo BA, Pasque MK. 1995. An inverse approach to determining myocardial material properties. J Biomech 28(8):935-48.

Moulton MJ, Creswell LL, Downing SW, Actis RL, Myers KW, Szabo BA, Vannier MW, Pasque MK. 1994. Ventricular interaction in the pathologic heart. A model based study. Asaio J 40(3):M773-83.

Moulton MJ, Creswell LL, Downing SW, Actis RL, Szabo BA, Pasque MK. 1996a. Myocardial material property determination in the in vivo heart using magnetic resonance imaging. Int J Card Imaging 12(3):153-67.

Moulton MJ, Creswell LL, Downing SW, Actis RL, Szabo BA, Vannier MW, Pasque MK. 1996b. Spline surface interpolation for calculating 3-D ventricular strains from MRI tissue tagging. American Journal of Physiology 270(1pt2):H281-97.

Moulton MJ, Creswell LL, Mackey ME, Cox JL, Rosenbloom M. 1996c. Obesity is not a risk factor for significant adverse outcomes after cardiac surgery. Circulation 94(9 Suppl):II87-92.

Moulton MJ, Creswell LL, Mackey ME, Cox JL, Rosenbloom M. 1996d. Reexploration for bleeding is a risk factor for adverse outcomes after cardiac operations. J Thorac Cardiovasc Surg 111(5):1037-46.

Moulton MJ, Creswell LL, Mackey ME, Cox JL, Rosenbloom M. 1996a. Obesity is not a risk factor for significant adverse outcomes after cardiac surgery. Circulation 94(9 Suppl):II87-92.

Moulton MJ, Creswell LL, Mackey ME, Cox JL, Rosenbloom M. 1996b. Reexploration for bleeding is a risk factor for adverse outcomes after cardiac operations. J Thorac Cardiovasc Surg 111(5):1037-46.

Moulton MJ, Creswell LL, Ungacta FF, Downing SW, Szabo BA, Pasque MK. 1996c. Magnetic resonance imaging provides evidence for remodeling of the right ventricle after single-lung transplantation for pulmonary hypertension. Circulation 94(9 Suppl):II312-9.

Moulton MJ, Downing SW, Creswell LL, Fishman DS, Amsterdam DM, Szabo BA, Cox JL, Pasque MK. 1995. Mechanical dysfunction in the border zone of an ovine model of left ventricular aneurysm. Ann Thorac Surg 60(4):986-97; discussion 998.

Murali S, Tokarczyk T, Ristich J, McCurry K, MacGowan GA, Rosenblum WD, McNamara DM, Shapiro R, Fung JJ, Kormos RL. 2001. Short-term survival with combined heart-kidney or combined heart-liver transplantation with allografts from a single donor. J Heart Lung Transplant 20(2):168.

Nash MP, Hunter PJ. 2000. Computational mechanics of the heart. journal of Elasticity 61(1-3):113-141.

Nielsen PM, Hunter PJ, Smaill BH. 1991a. Biaxial testing of membrane biomaterials: testing equipment and procedures. J Biomech Eng 113(3):295-300.

Nielsen PM, Le Grice IJ, Smaill BH, Hunter PJ. 1991b. Mathematical model of geometry and fibrous structure of the heart. Am J Physiol 260(4 Pt 2):H1365-78.

Novak VP, Yin FC, Humphrey JD. 1994. Regional mechanical properties of passive myocardium. J Biomech 27(4):403-12.

Ogden RW. 1984. Non-linear elastic deformations. Chichester, New York: E. Horwood ;Halsted Press. xiv, 532 p.

Ohayon J, Usson Y, Jouk PS, Cai H. 1999. Fibre Orientation in Human Fetal Heart and Ventricular Mechanics : A Small Perturbation Analysis. Comput Methods Biomech Biomed Engin 2(2):83-105.

Pajevic S, Aldroubi A, Basser PJ. 2002. A continuous tensor field approximation of discrete DT-MRI data for extracting microstructural and architectural features of tissue. J Magn Reson 154(1):85-100.

Pajevic S, Basser PJ. 2003. Parametric and non-parametric statistical analysis of DT-MRI data. J Magn Reson 161(1):1-14.

Panda SC, Natarjan R. 1977. Finite-element method of stress analysis in the human left ventricular layered wall structure. Med. Biol. Eng. Comput. 15:67-71.

Pao YC, Robb RA, Ritman EL. 1976. Plane-strain finite-element analysis of reconstructed diastolic left ventricular cross section. Ann Biomed Eng 4:232-249.

Papademetris X, Sinusas AJ, Dione DP, Constable RT, Duncan JS. 2002. Estimation of 3-D left ventricular deformation from medical images using biomechanical models. IEEE Trans Med Imaging 21(7):786-800.

Papademetris X, Sinusas AJ, Dione DP, Duncan JS. 2001. Estimation of 3D left ventricular deformation from echocardiography. Med Image Anal 5(1):17-28.

Perl M, Horowitz A. 1987. Mechanical model for the simulation of ischaemia and infarction of the left ventricle. Med Biol Eng Comput 25(3):284-8.

Perl M, Horowitz A, Sideman S. 1986. Comprehensive model for the simulation of left ventricle mechanics. Part 1. Model description and simulation procedure. Med Biol Eng Comput 24(2):145-9.

Perman WH, Creswell LL, Wyers SG, Moulton MJ, Pasque MK. 1995. Hybrid DANTE and phase-contrast imaging technique for measurement of three-dimensional myocardial wall motion. J Magn Reson Imaging 5(1):101-6.

Pierpaoli C, Barnett A, Pajevic S, Chen R, Penix LR, Virta A, Basser P. 2001. Water diffusion changes in Wallerian degeneration and their dependence on white matter architecture. Neuroimage 13(6 Pt 1):1174-85.

Pierpaoli C, Basser PJ. 1996. Toward a quantitative assessment of diffusion anisotropy. Magn Reson Med 36(6):893-906.

Pierpaoli C, Jezzard P, Basser PJ, Barnett A, Di Chiro G. 1996. Diffusion tensor MR imaging of the human brain. Radiology 201(3):637-48.

Pirolo JS, Bresina SJ, Creswell LL, Myers KW, Szabo BA, Vannier MW, Pasque MK. 1993. Mathematical three-dimensional solid modeling of biventricular geometry. Ann Biomed Eng 21(3):199-219.

Potter K, Leapman RD, Basser PJ, Landis WJ. 2002. Cartilage calcification studied by proton nuclear magnetic resonance microscopy. J Bone Miner Res 17(4):652-60.

Rademakers F, Van de Werf F, Mortelmans L, Marchal G, Bogaert J. 2003. Evolution of regional performance after an acute anterior myocardial infarction in humans using magnetic resonance tagging. J Physiol 546(Pt 3):777-87.

Rademakers FE, Buchalter MB, Rogers WJ, Zerhouni EA, Weisfeldt ML, Weiss JL, Shapiro EP. 1992. Dissociation between left ventricular untwisting and filling. Accentuation by catecholamines. Circulation 85(4):1572-81.

Rademakers FE, Rogers WJ, Guier WH, Hutchins GM, Siu CO, Weisfeldt ML, Weiss JL, Shapiro EP. 1994. Relation of regional cross-fiber shortening to wall thickening in the intact heart. Three-dimensional strain analysis by NMR tagging. Circulation 89(3):1174-82.

Rijcken J, Arts T, Bovendeerd P, Schoofs B, van Campen D. 1996. Optimization of left ventricular fibre orientation of the normal heart for homogeneous sarcomere length during ejection. Eur J Morphol 34(1):39-46.

Rijcken J, Bovendeerd PH, Schoofs AJ, van Campen DH, Arts T. 1997. Optimization of cardiac fiber orientation for homogeneous fiber strain at beginning of ejection. J Biomech 30(10):1041-9.

Rijcken J, Bovendeerd PH, Schoofs AJ, van Campen DH, Arts T. 1999. Optimization of cardiac fiber orientation for homogeneous fiber strain during ejection. Ann Biomed Eng 27(3):289-97.

Rogers WJ, Jr., Shapiro EP, Weiss JL, Buchalter MB, Rademakers FE, Weisfeldt ML, Zerhouni EA. 1991. Quantification of and correction for left ventricular systolic long-axis shortening by magnetic resonance tissue tagging and slice isolation. Circulation 84(2):721-31.

Rohde GK, Barnett AS, Basser PJ, Marenco S, Pierpaoli C. 2004. Comprehensive approach for correction of motion and distortion in diffusion-weighted MRI. Magn Reson Med 51(1):103-14.

Sabbah HN, Marzilli M, Liu ZQ, Stein PD. 1986a. Coronary extravascular compression influences systolic coronary blood flow. Heart Vessels 2(3):140-6.

Sabbah HN, Marzilli M, Liu ZQ, Stein PD. 1986b. Relation of intramyocardial pressure to coronary pressure at zero flow. Clin Exp Pharmacol Physiol 13(6):477-86.

Sabbah HN, Marzilli M, Stein PD. 1980. Intracardiac phonocardiography in experimental left ventricular cavity obliteration: potential clinical applicability for the distinction of obliterating left ventricle from hypertrophic obstructive cardiomyopathy. Am Heart J 100(1):77-80.

Sabbah HN, Marzilli M, Stein PD. 1981a. The relative role of subendocardium and subepicardium in left ventricular mechanics. Am J Physiol 240(6):H920-6.

Sabbah HN, Marzilli M, Stein PD. 1981b. Ultraminiature strain gauge transducer for assessing regional intramyocardial pressure. Med Instrum 15(2):121-4.

Sacks MS, Chuong CJ. 1993. A constitutive relation for passive right-ventricular free wall myocardium. J Biomech 26(11):1341-5.

Sandler H, Dodge HT. 1963. Left ventricular tension and stress in man. Circ Res 13:91-104.

Schmid-Schönbein GW, Fung Y-C. 1986. Frontiers in biomechanics (symposium entitled "Frontiers of applied mechanics and biomechanics" held in honor of the 65th birthday of Professor Y(uan)-C(heng) Fung; San Diego - Calif., July 1984). New York a. o.: Springer. XVIII, 395 p.

Shapiro EP, Rademakers FE. 1997. importance of oblique fiber orientation for left ventricular wall deformation. Technology and Health Care 5:21-28.

Shrager RI, Basser PJ. 1998. Anisotropically weighted MRI. Magn Reson Med 40(1):160-5.

Sinusas AJ, Papademetris X, Constable RT, Dione DP, Slade MD, Shi P, Duncan JS. 2001. Quantification of 3-D regional myocardial deformation: shape-based analysis of magnetic resonance images. Am J Physiol Heart Circ Physiol 281(2):H698-714.

Spencer AJM. 1972. Deformations of fibre-reinforced materials. Oxford: Clarendon Press. 6,128 p.

Spencer AJM. 1984. Continuum theory of the mechanics of fibre-reinforced composites. Wien: Springer. viii, 284 -- p.

Sperelakis N. 1995. Physiology and pathophysiology of the heart. Boston [etc.]: Kluwer. XVI, 1173 S. p.

Sperelakis N. 2001. Heart physiology and pathophysiology. San Diego: Academic Press. 1261 S. p.

Stein PD, Davis Z, Sabbah HN, Marzilli M. 1979. Reduction of coronary flow in the native circulation after bypass. Observations in a hydraulic model of the cardiovascular system. J Thorac Cardiovasc Surg 78(5):772-8.

Stein PD, Marzilli M, Sabbah HN, Lee T. 1980. Systolic and diastolic pressure gradients within the left ventricular wall. Am J Physiol 238(5):H625-30.

Stein PD, Davis Z, Sabbah HN, Marzilli M. 1979a. Reduction of coronary flow in the native circulation after bypass. Observations in a hydraulic model of the cardiovascular system. J Thorac Cardiovasc Surg 78(5):772-8.

Stein PD, Marzilli M, Sabbah HN, Lee T. 1980a. Systolic and diastolic pressure gradients within the left ventricular wall. Am J Physiol 238(5):H625-30.

Stein PD, Sabbah HN, Anbe DT, Marzilli M. 1979b. Performance of the failing and nonfailing right ventricle of patients with pulmonary hypertension. Am J Cardiol 44(6):1050-5.

Stein PD, Sabbah HN, Anbe DT, Marzilli M. 1980b. The pulmonary component of the second sound in right ventricular failure. Henry Ford Hosp Med J 28(1):79-4.

Stein PD, Sabbah HN, Marzilli M. 1985. Intramyocardial pressure and coronary extravascular resistance. J Biomech Eng 107(1):46-50.

Stein PD, Sabbah HN, Marzilli M, Blick EF. 1980c. Comparison of the distribution of intramyocardial pressure across the canine left ventricular wall in the beating heart during diastole and in the arrested heart. Evidence of epicardial muscle tone during diastole. Circ Res 47(2):258-67.

Stevens C, Remme E, LeGrice I, Hunter P. 2003. Ventricular mechanics in diastole: material parameter sensitivity. J Biomech 36(5):737-48.

Streeter DD, Basset JR, Basset DL. 1966. An engineering analysis of myocardial fibre orientation in pig's left ventricle in systole. The Anatomical Record 155:503-511.

Streeter DD, JR. 1983. Gross morphology and fibre geometry in the heart wall. Handbook of Physiology, Section 2: The Cardiovascular System Vol. 1:pp. 61-109.

Streeter DD, JR., Basset DL. 1966. An engineering analysis of myocardial fibre orientation in pig's left ventricle in systole. The Anatomical Record 155:503-511.

Streeter DD, JR., Power WE, Ross MA, Torrent-Guasp F. Three-Dimentional fiber orientation in the mammalian left ventricular wall. In: Vally Forge P, 1975, Baan, j., A. Noordergraaf, J. Raines (eds.), editor; 1978; London. The MIT Press, Cambridge (Massachusets). p 73-84.

Streeter DD, JR., Spotnitz DPP, Ross JJ, Sonnenblick EH. 1969a. Fiber orientation in the canine left ventricle during diastole and systole. Circ Res 24:339-347.

Streeter DD, Spotnitz HM, Patel DP, Ross J, Sonnenblick EH. 1969b. Fibre orientation in the canine left ventricle during diastole and systole. Circ Res 24:339-347.

Strumpf RK, Humphrey JD, Yin FC. 1993. Biaxial mechanical properties of passive and tetanized canine diaphragm. American Journal of Physiology 265(2pt2):H469-75.

Stuber M. 1997. Quantification of the human heart wall motion by ultra-fast magnetic resonance myocardial tagging techniques [Ph.D. Thesis]. Zurich: Ph.D. Thesis, Swiss Federal Institute of Technology. ethz-bib 12208 p.

Stuber M, Scheidegger MB, Fischer SE, Nagel E, Steinemann F, Hess OM, Boesiger P. 1999. Alternations in the local myocardial motion pattern in patients suffering from pressure overload due to aortic stenosis. Circulation 100:361-368.

Summerour S, Emery J, Fazeli B, Omens JH, McCulloch AD. 1998. Residual strain in ischemic ventricular myocardium. J. Biomech. Engng 120:710-714.

Takayama Y, Costa KD, Covell JW. 2002. Contribution of laminar myofiber architecture to load-dependent changes in mechanics of LV myocardium. Am J Physiol Heart Circ Physiol 282(4):H1510-20.

Takayama Y, Holmes JW, LeGrice I, Covell JW. 1996. Enhanced regional deformation at the anterior papillary muscle insertion site after chordal transsection. Circulation 93(3):585-93.

Takeda T, Toyama H, Iida K, Masuoka T, Ajisaka R, Kuga K, Satoh M, Sugahara S, Jin W, Ishikawa N and others. 1991. A study of ventricular contraction sequence in complete right bundle branch block by phase analysis. Ann Nucl Med 5(1):19-27.

Takeda T, Toyama H, Ishikawa N, Masuoka T, Ajisaka R, Iida K, Satoh M, Jin W, Saitou T, Yamanouchi T and others. 1992a. Perfusion and mechanical analysis with

technetium-99m 2-methoxy-isobutyl-isonitrile in a case of dilated cardiomyopathy. Ann Nucl Med 6(2):103-10.

Takeda T, Toyama H, Ishikawa N, Satoh M, Masuoka T, Ajisaka R, Iida K, Jin W, Sugishita Y, Itai Y. 1992b. Quantitative phase analysis of myocardial wall thickening by technetium-99m 2-methoxy-isobutyl-isonitrile SPECT. Ann Nucl Med 6(2):69-78.

Torrent-Guasp F, Buckberg GD, Clemente C, Cox JL, Coghlan HC, Gharib M. 2001. The structure and function of the helical heart and its buttress wrapping. I. The normal macroscopic structure of the heart. Seminars in Thoracic and Cardiovascular Surgery 13:301-319.

Torrent-Guasp F, Whimster WF, Redmann K. 1997. A silicone rubber mould of the heart. Technology and Health Care 5:13-20.

Truesdell C, Noll W. 1992. The non-linear field theories of mechanics. Berlin ; New York: Springer-Verlag. x, 591 p.

Usyk TP, Mazhari R, McCulloch AD. 2000. Effect of Laminar Orthotropic Myofiber Architecture on regional Stress and Strain in the Canine Left Ventricle. Journal of Elasticity 61:143-164.

van Doorn A, Bovendeerd PH, Nicolay K, Drost MR, Janssen JD. 1996. Determination of muscle fibre orientation using Diffusion-Weighted MRI. Eur J Morphol 34(1):5-10.

Vendelin M, Bovendeerd PH, Arts T, Engelbrecht J, van Campen DH. 2000. Cardiac mechanoenergetics replicated by cross-bridge model. Ann Biomed Eng 28(6):629-40.

Vendelin M, Bovendeerd PH, Engelbrecht J, Arts T. 2002a. Optimizing ventricular fibers: uniform strain or stress, but not ATP consumption, leads to high efficiency. Am J Physiol Heart Circ Physiol 283(3):H1072-81.

Vendelin M, Bovendeerd PH, Saks V, Engelbrecht J. 2002b. Cardiac mechanoenergetics in silico. Neuroendocrinol Lett 23(1):13-20.

Vetter FJ, McCulloch AD. 1998. Three-dimensional analysis of regional cardiac function: a model of rabbit ventricular anatomy. Prog Biophys Mol Biol 69(2-3):157-83.

Vetter FJ, McCulloch AD. 2000. Three-dimensional stress and strain in passive rabbit left ventricle: a model study. Ann Biomed Eng 28(7):781-92.

Vetter FJ, McCulloch AD. 2001. Mechanoelectric feedback in a model of the passively inflated left ventricle. Ann Biomed Eng 29(5):414-26.

Vinson CA, Gibson DG. 1979. Analysis of left ventricular behaviour in diastole by means of finite element method. Br. Heart J. 41:60-67.

Vis MA, Bovendeerd PH, Sipkema P, Westerhof N. 1997. Effect of ventricular contraction, pressure, and wall stretch on vessels at different locations in the wall. Am J Physiol 272(6 Pt 2):H2963-75.

Waldman LK, Fung YC, Covell JW. 1985. Transmural myocardial deformation in the canine left ventricle. Normal in vivo three-dimensional finite strains. Circ Res 57(1):152-63.

Weiss, j. A., Maker BN, Govindjee S. 1996. Finite element implementation of incompressible, transversely isotropic hyperelasticity. Computer methods in applied mechanics and engineering 135:107-128.

Weiss JA. 1994. A constitutive model and finite element representation for transversely isotropic soft tissue. Ph.D. Thesis: The University of Utha.

Wong AYK, Rautaharju PM. 1968. Stress distribution within the left ventricular wall approximated as a thick ellipsoidal shell. Am. Heart J. 75:649-662.

Wu J, Takeda T, Toyama H, Ajisaka R, Masuoka T, Satoh M, Ishikawa N, Sugishita Y, Itai Y. 1995. Resting asynchronous left ventricular contraction abnormality analyzed by a phase method in spastic angina pectoris. J Nucl Med 36(6):1003-8.

Wu J, Takeda T, Toyama H, Ajisaka R, Masuoka T, Watanabe S, Sato M, Ishikawa N, Itai Y. 1999. Phase changes caused by hyperventilation stress in spastic angina pectoris analyzed by first-pass radionuclide ventriculography. Ann Nucl Med 13(1):13-8.

Yin FC. 1981. Ventricular Wall Stress. Circ Res 49, No.4(Oct):829-842.

Yin FCP. 1985. Applications of the finite-element method to ventricular mechanics. CRC Crit. Rev. Biomed. Eng. 12:311-342.

Zahalak GI, de Laborderie V, Guccione JM. 1999. The effects of cross-fiber deformation on axial fiber stress in myocardium. J Biomech Eng 121(4):376-85.